THESIS

WASTE HEAT DRIVEN TURBO-COMPRESSION COOLING

Submitted by
Shane Daniel Garland
Department of Mechanical Engineering

In partial fulfillment of the requirements
For the Degree of Master of Science
Colorado State University
Fort Collins, Colorado
Spring 2018

Master's Committee:

Advisor: Todd M. Bandhauer

Anthony J. Marchese
Kenneth H. Carlson

ABSTRACT

WASTE HEAT DRIVEN TURBO-COMPRESSION COOLING

Waste heat recovery systems utilize exhaust heat from power generation systems to produce mechanical work, provide cooling, or create high temperature thermal energy. One waste heat recovery application is to use the exhaust heat from a Natural Gas Combined Cycle Power Plant (NGCC) to drive a heat activated cooling system that can offset a portion of the plant condenser load. There are several heat activated cooling systems available including absorption, adsorption, ORVC, and ejector, but each has disadvantages. One system that can overcome the disadvantages of typical heat activated cooling systems is a turbo-compression cooling system (TCCS). In this system, the exhaust heat enters an organic Rankine cycle at the boiler and vaporizes the fluid that passes through a turbine. The turbine power is directly transferred to a compressor via a hermetically sealed shaft that is made possible by a magnetic coupling. The compressor operates a vapor-compression system which provides a cooling effect in the evaporator. The hermetic seal between the turbine and compressor allows for two separate fluids on the power and cooling cycles, which maximizes the efficiency of the turbine and compressor simultaneously.

This study presents a thermodynamic modeling approach that makes system performance predictions for the baseline design case, and for off-design performance conditions. The off-design modeling approach uses turbo-compressor performance maps and a heat exchanger *UA* scaling methodology to accurately simulate system operation for a broad range of temperatures and cooling loads. A 250 kW_{th} cooling capacity TCCS was constructed and tested to validate the modeling approach. The test facility simulates a 138:1 scaled NGCC power plant configuration in

which the TCCS extracts 106°C waste heat from the flue gases and produces a cooling effect that offsets a portion of the NGCC condenser load. The design target for the test facility was to achieve a COP of 2.1 while chilling water from 17.2°C to 16°C at an ambient temperature of 15°C. Although the final design point was not tested for this study due to facility limitations, the off-design performance methodology was utilized to predict the performance for an ambient condition of 27.5°C and power and cooling cycle mass flow rate range between 0.35 kg s^{-1} - 0.5 kg s^{-1} and 0.65 kg s^{-1} – 0.85 kg s^{-1}, respectively. The comparison between the experimental and modeling data suggested strong correlation over the data range presented with a maximum error in COP of only 2.0% among the selected data points. Future experimental data over a larger range of ambient temperatures and system conditions is suggested to further validate the system modeling. Regardless, the results in the present study show that the TCCS compares favorably with other heat activated cooling systems.

ACKNOWLEDGEMENTS

First and foremost, I would like to thank Dr. Todd Bandhauer for advising me during my graduate research. I appreciate his positive attitude and wholehearted belief from the beginning that I had the capabilities to take the lead on the project. Throughout my entire graduate career, Dr. Bandhauer has challenged me to produce high quality and professional work and I have grown immensely as an engineer.

The project certainly would not be possible without the never ending support of my Interdisciplinary Thermal Science (ITS) Lab Members. Torben Grumstrup provided immense support during the design of the facility; I learned a great deal from his professional opinion. I cannot thank Alex Grauberger, John Simon, and Derek Young enough for their contributions to the project. Their fabrication expertise and tireless work ethic was the only reason the project was completed in a timely manner. Other members of the lab that deserve special recognition include Achyut Paudel, Spencer Gibson, Katie Johnson, and Sean Moser.

In addition, everyone at the Powerhouse Energy Campus has been extremely supportive during the project. I would particularly like to recognize Kirk Evans, Mark James, and James Tillotson, for allowing me to constantly pester them with questions and for their irreplaceable support with the electrical, instrumentation, and Labview programming work. Erik Larson also deserves recognition for his work on the mezzanine and general facilities support.

Recognition should be given to our project partners at Barber-Nichols, Inc., and Modine Manufacturing. I would specifically like to thank Kevin Eisemann, Jeff Noall, and Bob Fuller from Barber-Nichols, and Ranga Sami and Mike Reinke from Modine. Their technical expertise and

professional competence not only increased my knowledge of both turbo-machinery and heat exchanger design, but also allowed the project to proceed on schedule.

I would also like to thank the Department of Energy Advanced Research Projects Agency – Energy (ARPA-E) for their innovative thinking and financial support of the project under contract DE-AR0000574. Without their creative foresight this project may not exist and I am grateful they have been patient with our progress throughout my time on the project.

Finally, I would like to recognize my family and friends for their constant support during my entire graduate education. They have kept me lighthearted during my research and have reminded me to get out of the lab and have fun enjoying Colorado.

TABLE OF CONTENTS

LIST OF TABLES

LIST OF FIGURES

NOMENCLATURE

Symbol	Description	Units
A	Area	m^2
Bo	Boiling number	-
CAT	Closest approach temperature	°C
COP	Coefficient of Performance	-
C_l	Louvered fin geometric constant	-
C	Heat capacity rate	$kW\ K^{-1}$
Cp	Heat capacity, constant pressure	$kJ\ kg^{-1}\ K^{-1}$
Cr	Heat capacity ratio	-
Cv	Heat capacity, constant volume	$kJ\ kg^{-1}\ K^{-1}$
D	Diameter	m
Ds	Specific diameter	$lb_f^{1/4}\ s^{1/2}\ lb_m^{-1/4}\ ft^{-1/4}$
f	Factor	-
F_p	Fin pitch	mm
F_l	Fin length	mm
Fr	Froude number	-
G	Mass flux	$kg\ s^{-1}\ m^{-2}$
g	Acceleration due to gravity	$m\ s^{-2}$
h	Enthalpy	$kJ\ kg^{-1}$
Δh	Enthalpy change	$kJ\ kg^{-1}$
ht	Heat transfer coefficient	$W\ m^{-2}\ K^{-1}$
H	Head	$ft\ lb_f\ lb_m$

j	Colburn factor	-
k	Thermal conductivity	$W\ m^{-1}\ K^{-1}$
L	Length	m
L_l	Louver length	mm
L_p	Louver pitch	mm
$\dot{m}$	Mass flow rate	$kg\ s^{-1}$
MW	Molecular weight	$kg\ kmol^{-1}$
N	Speed	RPM
No	Number	-
Ns	Specific speed	$ft^{3/4}\ lb_m^{3/4}\ min^{-1}\ s^{-1/2}$
Nu	Nusselt number	-
NTU	Number of transfer units	-
ΔP	Differential pressure	kPa
P	Pressure	kPa
Pr	Prandlt number	-
Q	Volumetric flow rate	$m^3\ s^{-1}$
$\dot{Q}$	Heat duty	kW
R	Gas constant	$kJ\ kmol^{-1}\ K^{-1}$
Re	Reynolds number	-
Rs	Resistance	$kW\ K^{-1}$
T	Temperature	°C
T_d	Tube depth	mm
T_p	Tube pitch	mm
UA	Heat transfer conductance	$kW\ K^{-1}$

V	Velocity	m s^{-1}
$\dot{V}$	Volumetric flow rate	m^3 hr^{-1}
$\dot{W}$	Work	kW
x	Fluid quality	-
X_{tt}	Turbulent-turbulent Martinelli parameter	-
Z	Compressibility factor	-
ZR	Compressibility-Gas Constant factor	kJ kg^{-1} K^{-1}
Greek Symbols		
δ	Pressure ratio	-
δ_f	Fin thickness	mm
ε	Effectiveness	-
ε_γ	Compressibility factor	-
η	Efficiency	-
γ	Specific heat ratio	-
μ	Dynamic viscosity	kg m^{-1} s^{-1}
ν	Kinematic viscosity	m^2 s^{-1}
ρ	Density	kg m^{-3}
θ	Angle	deg
θ_{cr}	Critical velocity ratio	-
Subscripts		
a	Air	
abs	Absorption	
act	Actual	
alt	Alternate	

amb	Ambient	
axis	Axis	
base	Baseline desing case	
b	Boiler	
bf	Boiler fan	
C	Cold temperature reservoir	
c	Cooling cycle	
cf	Condenser fan	
church	Churchill friction factor	
comp	Compressor	
cond	Condenser	
cr	Critical	
exh	Exhaust	
e	Evaporator	
eq	Equivalent	
f	Cycle fluid	
fg	Heat of vaporization	
fin	Fin	
finrow	Fin rows	
g	Glycol	
gp	Glycol pump	
H	High temperature reservoir	
HEX	Heat exchanger	
ht	Heat transfer coefficient	

hyd	Hydraulic diameter	
ideal	Ideal	
in	Inlet	
liq	Liquid	
lp	Louvered fin	
M	Medium temperature reservoir	
max	Maximum	
min	Minimum	
o	Outlet	
off	Off-design case	
p	Power cycle	
per	Percent	
prim	Primary	
pump	Pump	
Q	Heat duty	
R134a	Fluid R134a	
R152a	Fluid R152a	
ref	Reference conditions	
sat	Saturation	
sec	Heat exchanger section (sub-cooled, two-phase, or superheated)	
secon	Secondary	
shaft	Shaft	
sc	Sub-cooled	
sh	Super-heated	

sp	Single-phase	
total	Total	
t	Turbine	
thickness	Thickness	
tp	Two-phase	
tube	Tube	
univ	Universal	
vap	Vapor	

CHAPTER 1. INTRODUCTION

1.1. Background

Each year, Lawrence Livermore National Laboratory compiles a comprehensive chart showing the flow of energy in the United States (Figure 1-1). The total energy from each generation source (i.e., Natural Gas, Coal, Petroleum, etc.) is tracked from generation to end use, where it is shown as either rejected energy or energy services. Due to thermodynamic limitations and efficiency losses, nearly 70% (66.4 Quadrillion BTUs) of all energy produced ends up rejected as wasted energy. A large portion (70% or 46.9 Quadrillion BTUs) of the wasted energy is low grade heat in the form of exhaust gas or engine coolant from the two major contributors of the wasted energy: electricity generation and transportation [2]. Although this rejected heat is low temperature, there is still a tremendous amount of energy that can be salvaged by using a waste heat recovery (WHR) system. By utilizing energy that is normally wasted, the entire energy

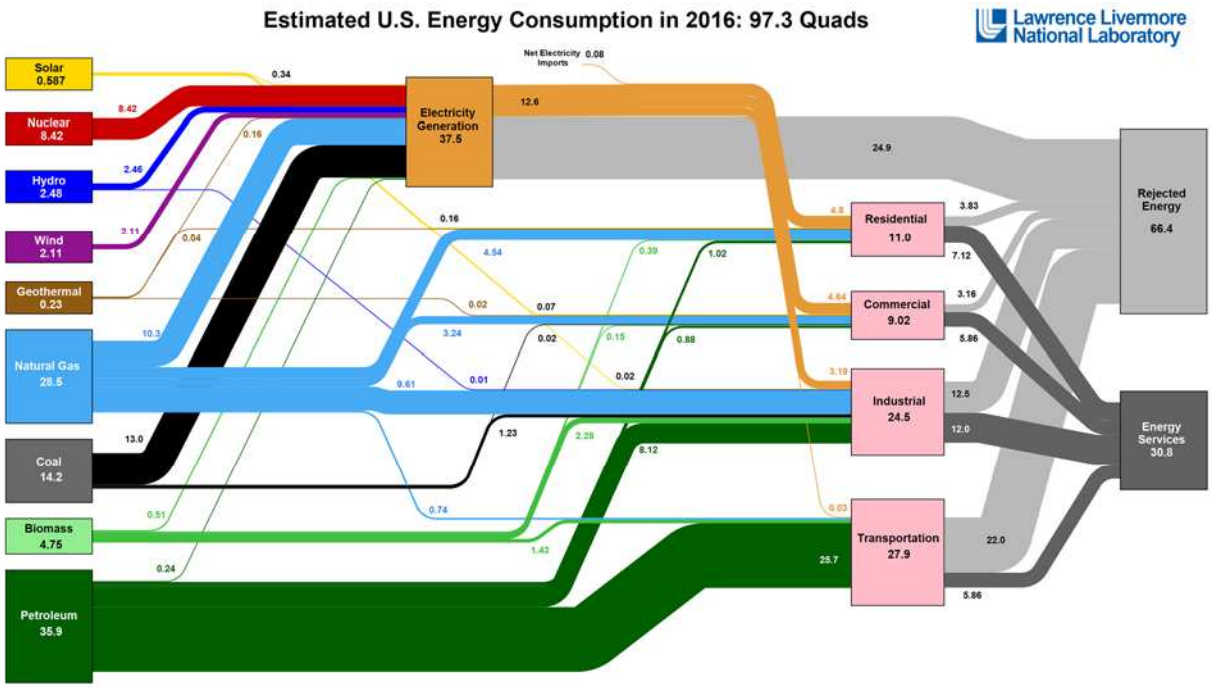

Figure 1-1. Lawrence Livermore National Laboratory energy flow chart [2].

ecosystem becomes more efficient and there is potential to make significant reductions in the amount of CO_2 dissipated into the atmosphere. Developing countries are of particular interest to reducing worldwide emissions due to their growing populations and reliance on diesel generators to provide power. For example, India in particular is set for rapid growth in the power generation sector as the country contains 18% of the world's population, but uses only 6% of the world's primary energy [56].

WHR systems are used to convert waste thermal energy into some other useable form such as mechanical work, cooling, or high temperature thermal energy [3]. WHR systems are not new, and engineers for centuries have been employing methods to increase the efficiency of thermal systems by utilizing waste heat. In fact, WHR systems are typically variations of typical thermal conversion systems that were developed in the industrial revolution alongside the steam engine.

The invention and development of steam and internal combustion engines was highly influenced by the strides made in thermodynamic theory by Sadi Carnot. In 1824, Carnot developed a theoretical cycle governing all thermodynamic processes and defined the upper efficiency limit a system can achieve when converting heat into work [57]. Figure 1-2 is a graphical display of an engine operating between two heat reservoirs. Any thermodynamic system is defined by heat transfer from high temperature to low temperature thermal reservoirs. If work is done by the system, the power transferred is determined by the difference in thermal energy between the

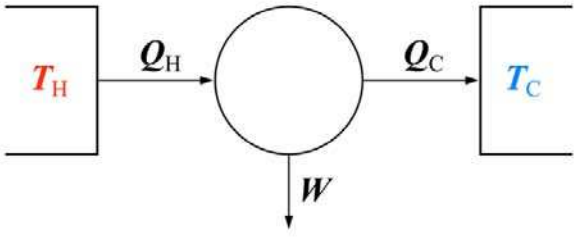

Figure 1-2. A heat engine includes a hot reservoir and cold reservoir and some work output to the surroundings [5].

two reservoirs. Carnot defined an equation showing the maximum efficiency of any heat engine can be simplified to a function of the hot and cold reservoir temperatures [5].

$$\eta = \frac{W}{Q_H} = 1 - \frac{T_C}{T_H} \tag{1.1}$$

Since equation (1.1) is derived from a completely reversible process, it does not represent any real heat engine, but instead describes the maximum possible efficiency a heat driven cycle can achieve. Figure 1-3 shows the variation in Carnot efficiency as a function of the reservoir temperature difference. From the figure, it is clearly seen that as the temperature difference increases, the Carnot efficiency also increases, but has diminishing returns for very high temperature differences. The Carnot cycle can also be reversed to determine the theoretical performance of a refrigeration cycle, defined as the coefficient of performance (COP) [5].

$$COP = \frac{Q_C}{W} = \frac{T_C}{T_H} - 1 \tag{1.2}$$

These two equations are very beneficial to cycle thermodynamics and provide a baseline for overall system comparison. In the case of heat engines, the relevance of Carnot's work is that each

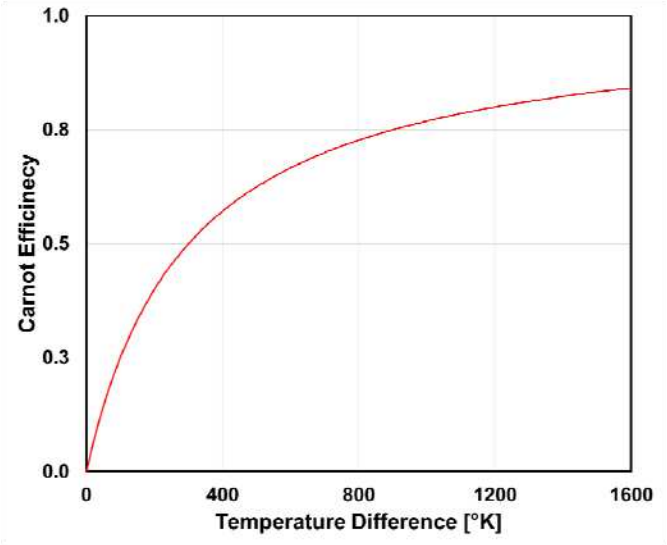

Figure 1-3. Carnot efficiency as a function of reservoir temperature difference for a heat engine.

thermodynamic process must reject heat into a low temperature thermal reservoir to generate work. The processes can never be thermodynamically perfect, however, because there are no completely reversible processes, and losses are always present. Thus, there will always be room to improve thermodynamic cycles by attempting to completely utilize the energy available. As long as there is a temperature difference between the hot and cold reservoirs, the energy can be utilized; although, in some cases, the efficiency gains will be small [57].

Most modern processes include a thermodynamic cycle, with the most prominent being power plants, internal combustion engines, chemical manufacturing processes, furnaces, boiler exhausts, and other manufacturing processes. Due to the Carnot efficiency limitations mentioned

Table 1-1. Temperature ranges and applications for various sources of waste heat [3].

Temp. Range	Sources	Temp. (°C)	Typical Recovery Methods
High [>600°C]	Nickel/Steel refining furnace Basic oxygen furnace Aluminum reverberatory furnace Copper refining furnace Steel heating furnace Copper reverberatory furnace Hydrogen plants Fume incinerators Glass melting furnace Coke oven Iron cupola	1370 - 1600 1200 1100 - 1200 760 - 820 930 - 1040 900 - 1090 600 - 980 600 - 1430 1300 - 1540 600 - 1000 820 - 980	• Combustion air preheat • Process heating • Mechanical work • Electrical power • Furnace preheating • Transfer to med-low temperature processes
Medium [200 - 600°C]	Steam boiler exhaust Gas turbine exhaust Reciprocating engine exhaust Heat treating furnace Drying & baking ovens Cement kiln	230 - 480 370 - 540 320 - 590 430 - 600 230 - 590 450 - 600	• Combustion air preheat • Process heating • Mechanical work • Electrical power • Furnace preheating • Feedwater preheating
Low [<200°C]	Exhaust gases exiting recovery devices in gas-fired boilers, ethylene furnaces, etc. Process steam condensate Cooling water from: furnace doors annealing furnaces air compressors internal combustion engines air conditioning and refrigeration condensers Drying, baking, and curing ovens Hot processed liquids/solids	70 - 200 50 - 90 30 - 50 70 - 200 30 - 50 70 - 120 30 - 40 90 - 200 30 - 200	• Space heating • Domestic water heating • Temperature upgrading • ORC cycles – electrical power • Water condensation

above, each of these processes must reject energy to a low temperature reservoir, and there is often wasted energy in those energy flows. The wasted heat from these sources comes in the form of exhaust gases, engine coolant, or other low temperature fluid flows [3]. There is a broad range of temperatures classified in the waste heat realm, from high temperature sources (600°C to 1600°C) to medium temperature (200°C to 600°C) to low temperature (30°C to 200°C) [3]. Table 1-1 shows some processes that produce high, medium, and low temperature exhaust ranges. The flow rate and temperature of the exhaust source is critical to WHR because, due to the Carnot efficiency, they set the maximum amount of extractible energy from the system. Exhaust sources at high temperatures can transfer more heat and produce more usable energy than low grade heat sources [3].

The most prominent WHR systems are heat pumps, systems used to generate electricity (Rankine and Kalina), and heat activated cooling systems. Heat activated cooling systems are the main focus of this research due to the lack of research in the field and considerable growth opportunities. These systems typically use a thermodynamic cycle to generate a cooling effect. Often the systems generate cold process water that can be used in some other location of the process, for air conditioning, or for refrigeration purposes [3]. One application for heat driven chillers which is of particular interest to this research is the reduction of water use in power plant applications by supplying supplemental cooling driven by exhaust gas. To address this need, a program was devised by the Advanced Research Projects Agency Energy (ARPA-e) to target the particular goal of water reduction by removing evaporative cooling towers and replacing them with dry air cooling towers. The utilization of waste heat in power plants is discussed in the next section.

1.2. Heat Activated Cooling for Power Plants

One of the largest freshwater users in the U.S. are electric power generating facilities, which consume approximately 38% of the total each year. Most of the water (90%) is used to cool thermoelectric power plants [58, 59] and, although a majority of the water is recycled within the plant or rejected to the environment at an elevated temperature, a large amount of water is evaporated in cooling towers. In fact, 42% of power plants in the U.S. utilize evaporative cooling, resulting in 4.3 billion gallons per day of freshwater consumption [58, 60]. In certain locations in the U.S., drought conditions have burdened the freshwater resources available. California is one example where droughts have ravaged the fresh water sources: in 2014, it was reported that 82% of the state experienced extreme drought conditions [61].

One method to significantly reduce water withdrawals is to use a dry-air cooled heat exchanger. Unfortunately, dry-air systems are implemented in less than 1% of U.S. power plants because of high cost and potentially reduced power plant efficiency [62, 63]. The primary driver behind evaporative cooling towers is that because of water's high density and thermal conductivity compared to air, the heat transfer characteristics of an evaporative cooling tower are better. These characteristics allow the heat exchangers for evaporative cooling towers to have a much smaller surface area compared to dry-air systems which has a direct impact on capital costs.

One possibility that might allow dry-air cooling in many applications is to use a heat activated cooling system to offset some power plant cooling load. If a significant fraction of the cooling load is offset, a dry air heat exchanger could become more economically feasible because the heat exchanger area required would be reduced. Figure 1-4 shows the proposed concept with a 555 MW Natural Gas Combined Cycle (NGCC) Case 13 in a recent DOE/NETL report. Case 13 lists the flue gas temperature at the outlet of the steam bottoming cycle at a 106°C with an ambient

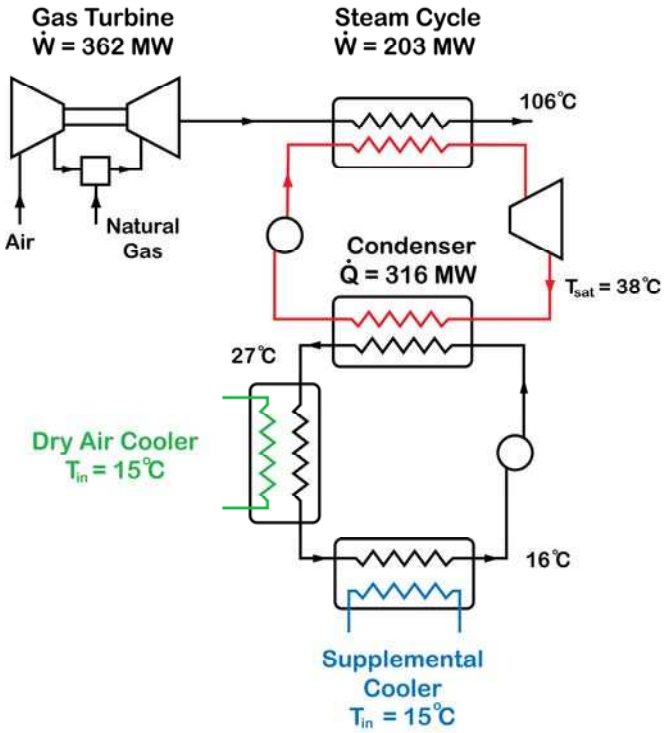

Figure 1-4. Proposed system configuration for a 555 MW NGCC power plant.

temperature of 15°C [64]. Case 13 would normally route water from the condenser to the evaporative cooling towers, but, in the alternative proposed system, a dry air cooler followed by a heat activated cooling system would be used. The heat activated cooling system takes advantage of a "free" waste heat source to provide cooling with an elevated temperature lift. As a result, condensers in the supplemental cooler could operate at higher fluid to ambient temperature difference compared with a single dry air cooler, which means the condensers operate more efficiently and reduces the heat exchange area. One study has been conducted to determine the feasibility of the proposed power plant configuration. The study calculated the dry air heat exchange *UA* for a single dry cooler to reject all of the power plant load and compared it with the heat exchange area for a reduced dry air cooler plus the heat exchangers for a supplemental cooling system. The maximum reduction in *UA* shown in the study was 26% [6]. These results show a heat activated system has potential benefits in the reduction of power plant capital cost as compared to

single dry air coolers. One of the main reasons a heat activated cooling system would be successful in the proposed power plant application is the high COP for the TCCS. The COP calculated for the study was 2, which is high compared to other state of the art cooling systems. However, the high COP for a heat activated cooling system is driven by the high, medium, and low heat reservoir temperatures.

1.3. Research Objectives

Although there has been considerable research on heat activated cooling systems, there has been little research on using these systems for power plant applications. The main objective of this effort is to investigate using a heat activated cooling system for a power plant cooling application. As shown in previous research, a high COP (>2) is required for a heat activated cooling system to be cost effective while reducing water consumption at a NGCC power plant [6]. Therefore, the specific targets of this research were to model a system to utilize 106°C exhaust gas to meet a COP of 2.1 while chilling water from 17.2°C to 16°C at an ambient temperature of 15°C. One further goal of this research was to develop a simple modeling technique to calculate the system performance at off-design conditions. A test facility was designed and constructed to validate the baseline and off-design modeling approaches. The final design target was not achieved during testing due to facility design restrictions. However, the off-design modeling approach was validated so that future investigations into power plant cooling can be explored.

1.4. Thesis Organization

In the following chapters, the motivation, thermodynamic modeling, design, and experimental results for a 250 kW_{th} turbo-compression cooling system are presented. Chapter two provides relevant background information for state-of-the-art heat activated cooling systems and presents the technological gaps that motivated the current research. Chapter three outlines the

thermodynamic modeling procedure that predicts TCCS performance at any design condition. The modeling includes thermodynamic modeling, turbo-machine Cordier analysis, fluid selection techniques, heat exchanger size calculations, and a comprehensive off-design performance methodology that integrates turbo-machine efficiency maps and a heat exchanger *UA* scaling methodology. Chapter four presents the design and construction of the test facility used to validate the thermodynamic modeling technique. In Chapter five, a summary of the experimental test data is given, followed by comparisons to the thermodynamic modeling, and concluding with an uncertainty analysis for the important experimentally measured and calculated values. The conclusions and recommendations for the present and future work are presented in Chapter six, while Chapter seven gives the references cited in this thesis. Appendix A provides sample calculations for the baseline thermodynamic state, the heat exchanger *UA* calculations, and the off-design performance calculation. Appendices B-F present relevant test facility documentation including the P&ID, equipment list, valve list, instrument list, and the operating and safety procedures.

CHAPTER 2. LITERATURE REVIEW

The previous chapter discussed the need to reduce or eliminate water consumption in thermoelectric power plant. One approach is to power a heat activated cooling system by waste heat and provide additional cooling to the plant. The purpose of this chapter is to provide a detailed literature review on state-of-the-art heat activated cooling systems. To guide the discussion, the theoretical maximum COP for a three reservoir cooling system is derived first, which will aide in making comparisons between systems with different heat reservoir temperatures. The next section delves into the status of heat activated cooling system performances, including absorption, adsorption, ejectors, and ORVCs. This discussion allows the needs for further research to be identified in heat activated cooling systems for power plant waste heat recovery. Finally, after these are discussed, the focus of the present investigation to address the research needs is given at the end of the chapter.

2.1. Theoretical Carnot Efficiency for Three-Reservoir Heat Activated Cooling Systems

The maximum theoretical efficiency for a thermodynamic cycle is determined from the reservoir temperatures. Heat engines and heat pumps typically operate by exchanging heat between two reservoirs, and the efficiency has been previously described in equations (1.1) and (1.2), respectively. In contrast, heat activated cooling systems exchange heat between three reservoirs, and, as a result, require a different expression to determine the theoretical performance limit. Figure 2-1 is a graphical representation of the three reservoir system. The three thermal reservoirs in the two graphics represent the heat rejection temperatures as they interact with a heat activated cooling system. Figure 2-1 (a) represents a system with only three temperature reservoirs and no

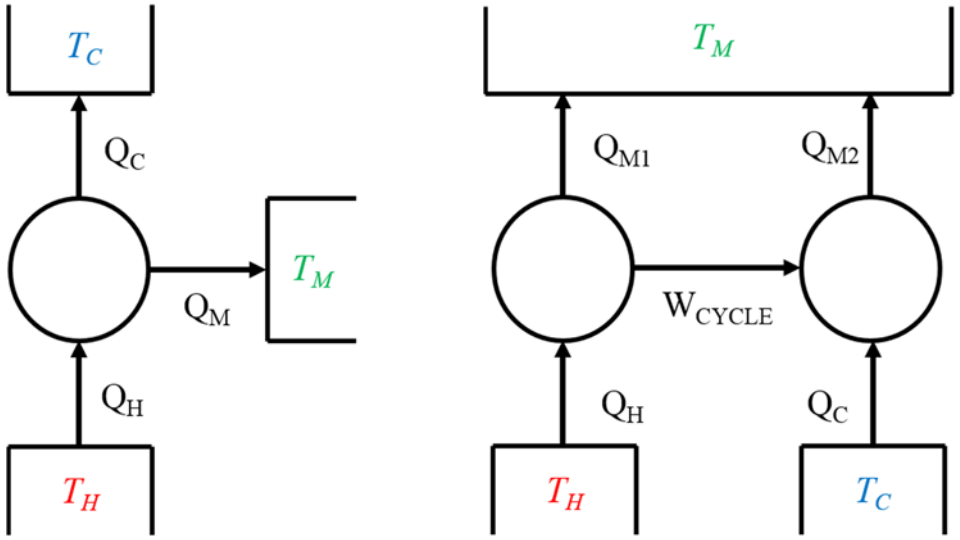

Figure 2-1. Three-reservoir heat rejection for (a) fully thermal exchange system and (b) two cycle system with work exchange. These two cycles are thermodynamically equivalent with a fully reversible assumption.

work exchange, while Figure 2-1 (b) represents the TCCS where work is exchanged between two separate cycles operating within the thermal reservoir limits. T_H represents the high temperature reservoir created by the waste heat source and in contact with a boiler heat exchanger. T_M is the medium temperature reservoir, which is the ambient environment temperature in contact with the condensing heat exchangers. Finally, the cold temperature reservoir (T_C) is the chilling load for the application and is in contact with the chiller heat exchanger. If these two cycles are internally reversible, they are thermodynamically equivalent, and yield the same maximum theoretical COP In the following example, conservation of energy equations and the Kelvin temperature scale are applied to the cycle shown in Figure 2-1 (b). First, the COP is defined as the cooling output divided by the heat input as follows:

$$COP = \frac{Q_C}{Q_H} \tag{2.1}$$

Even though, in many cases, the heat source for a heat activated cooling system is waste or 'free' energy, the COP is a useful comparison metric because it allows for a direct comparison between

systems. There is only a certain amount of energy available in a waste heat stream, and the COP determines how much cooling that can be done with this energy. Conservation of energy is applied to control volumes around each reversible cycle in the three reservoir system as follows:

$$Q_{\mathrm{H}} - Q_{\mathrm{M1}} = W_{\mathrm{cycle}} \tag{2.2}$$

$$Q_{\mathrm{M2}} - Q_{\mathrm{C}} = W_{\mathrm{cycle}} \tag{2.3}$$

If the cycle work is transferred with no losses, equations (2.2) and (2.3) are set equal to each other to yield:

$$Q_{\mathrm{H}} - Q_{\mathrm{M1}} = Q_{\mathrm{M2}} - Q_{\mathrm{C}} \tag{2.4}$$

Equation (2.4) can now algebraically manipulated and inserted into equation (2.1) to derive the COP of the system based on the heat duties to the three reservoirs.

$$COP = \frac{Q_{\mathrm{C}}}{Q_{\mathrm{H}}} = \frac{\left(1 - \frac{Q_{\mathrm{M1}}}{Q_{\mathrm{H}}}\right)}{\left(\frac{Q_{\mathrm{M2}}}{Q_{\mathrm{C}}} - 1\right)} \tag{2.5}$$

Finally, by applying the assumption of fully reversible processes, and using the Kelvin temperature scale, the final form of the maximum theoretical COP is as follows:

$$COP_{\mathrm{MAX}} = \frac{\left(1 - \frac{T_{\mathrm{M}}}{T_{\mathrm{H}}}\right)}{\left(\frac{T_{\mathrm{M}}}{T_{\mathrm{C}}} - 1\right)} \tag{2.6}$$

The medium reservoir temperatures are assumed equal in this case because the medium heat rejection temperature is equal for both sides of the cycle.

Equation (2.6) is very useful to make comparisons across many different heat activated cooling systems because it provides a comparison metric for systems with significantly different temperature reservoirs. For instance, in comparing two LiBr-H_2O absorption studies, one by Gomri

and the other by Izquierdo et al., the COPs were 0.79 and 0.64, respectively [17, 41]. One might select the Gomri system, because the COP is higher, thus appearing to have better performance. However, although the medium and low temperature reservoirs having similar temperatures, the waste heat input temperature in study by Gomri was 115°C, while for Izquierdo et al. it was only 99°C. By employing equation (2.6) the maximum theoretical COP for Gomri and Izquierdo et al. are calculated to be 3.02 and 1.97, respectively. Thus, although the study by Gomri provides a better COP, the maximum theoretical COP is also higher, and it is not clear which system utilizes the available heat in a more effective manner. As an alternative, these systems can be compared based on their fraction of maximum theoretical COP.

$$f_{\mathrm{COP}} = \frac{COP}{COP_{\mathrm{MAX}}} \tag{2.7}$$

The systems by Gomri and Izquierdo et al. yield COP fractions of 0.26 and 0.33, respectively. This suggests that Izquierdo et al. utilizes the available heat more effectively, which implies that if both systems were operated at the same temperatures it is possible that Izquierdo et al. would have better performance.

However, this conclusion does not tell the complete story of the effects of reservoir temperature on system performance because the difference between COP fraction and maximum theoretical COP does not change linearly. Figure 2-2 shows a plot of the maximum theoretical COP and the COP fraction for many types of heat activated cooling systems. The figure shows that most systems follow a similar trend, where at low maximum theoretical COPs the performance approaches the maximum, while at high theoretical COPs performance is a low fraction of the maximum. This implies that the highest performing system would be one in which there is a high maximum COP and a high COP fraction. This can be seen when comparing double effect and single effect absorption systems. The blue triangles indicate single-effect LiBr-H_2O absorption

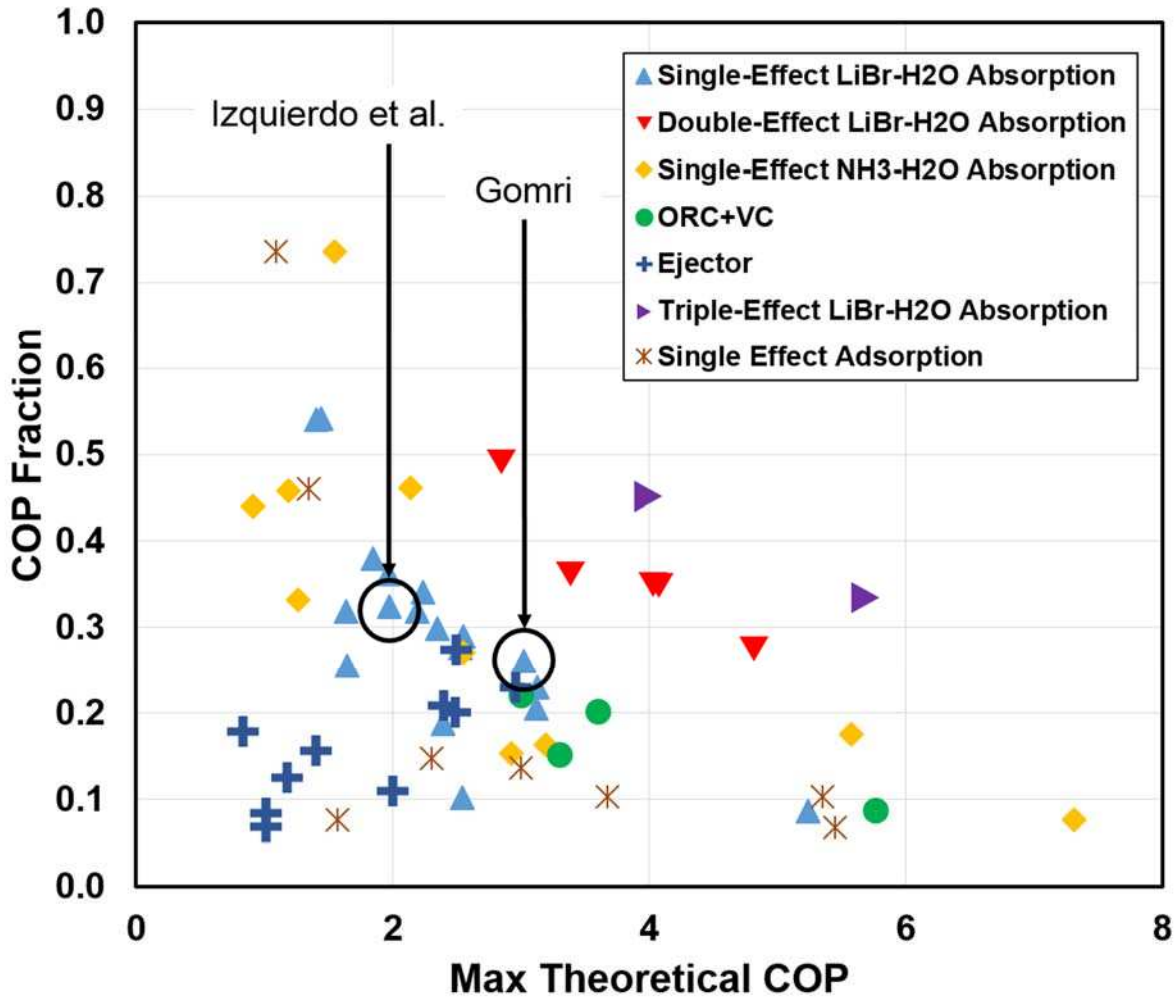

Figure 2-2. Heat activated cooling system performance represented by the comparison between maximum theoretical COP and COP fraction. (Data taken from multiple references [4, 9] [11-13] [7, 18-52].)

systems, while the red triangles indicate double effect LiBr-H_2O systems. Although in most cases the double effect systems have a higher maximum theoretical COP (due to increased waste heat temperature) the COP fraction is also higher, which shows in the shift upward and to the right on the plot. This shows that double effect absorption systems generally outperform single effect, but those performance benefits generally come from additional components. Based on these observations, Figure 2-2 can be used to inform decisions for implementing heat activated cooling systems, because it compares systems operating with different waste heat, ambient, and cold reservoir temperatures.

Returning to the previous example between Gomri and Izquierdo et al., both points can be located on Figure 2-2. The points follow a typical trend for single-effect LiBr-H_2O systems. Thus, although Gomri shows a higher COP and Izquierdo et al. shows a higher COP fraction, the performance of the two systems is likely very similar at all conditions. Selection of an appropriate system would be determined by a cost analysis between the two systems. Further research on this topic would be to develop an economic metric to determine the cost of a system for a given performance. This metric would provide a selection technique for choosing the most optimal heat activated cooling system at any condition.

2.2. State-of-the-Art Heat Activated Cooling Systems

As mentioned in Chapter one, heat activated cooling systems could be useful for thermoelectric power plant applications because they have potential to eliminate evaporative cooling towers, significantly reducing water consumption. The four major heat activated cooling systems are absorption, adsorption, ejector, and ORVC. This section reviews the literature and presents the advantages and disadvantages for each system. The system performance for each study can be compared using the metrics presented in Section 2.1 and by referencing Figure 2-2. By using these metrics, systems with different high, medium, and low reservoir temperatures can be compared directly. All of this information helps inform the system selection for the power plant application.

2.2.1. Absorption System

Absorption systems are the most prevalently used and studied heat activated systems due to their high performances and environmentally friendly refrigerant options. The working fluid for absorption systems is generally a binary solution mixture of an absorbent and a refrigerant. Although approximately 40 refrigerants and 200 absorbents have been studied, the most common

combinations are ammonia-water and LiBr-water. Ammonia-water combinations are favorable because both fluids are highly stable for a wide range of conditions and ammonia has a high heat of vaporization, which improves heat exchanger performance. Furthermore, by using ammonia as the refrigerant, the system can provide cooling below 0°C. LiBr-water systems use water as the refrigerant, which limits the application above 0°C. However, neither of these two fluids are toxic or flammable, and water has a very high heat of vaporization [65].

Figure 2-3 is a process flow diagram for an absorption refrigeration cycle. The cycle begins when a strong mixture of refrigerant and absorbant are pumped to a high pressure where they enter a generator. At the generator, heat is added which causes more volatile fluid to evaporate. The refrigerant is directed to a condenser where is rejects heat to the environment while the "weak" solution of refrigerant-absorbant goes back to the absorber. The refrigerant exiting the condenser operates in a similar fashion as a typical vapor-compression cycle, where it is expanded and then provides the cooling effect at the evaporator. After the evaporator, the refrigerant vapor goes to the absorber where it meets the "weak" refrigerant-absorber solution which restarts the process [5]. Multi-effect absorption system operate in a similar manner as single effect, but there are

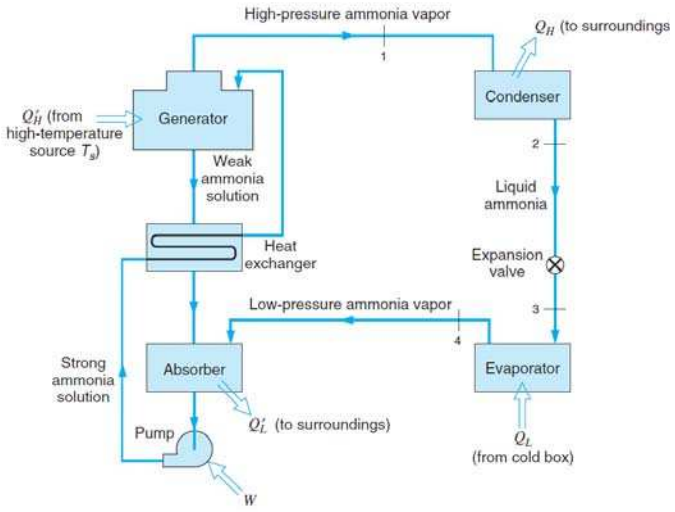

Figure 2-3. Process flow diagram for a typical absorption system [5].

multiple generators to heat the fluid mixture to a higher temperature and concentrate the refrigerant more [17]. The COP for these absorption systems is calculated in a similar manner as typical vapor-compression systems, but the work input is replaced with the heat input as follows:

$$COP_{\text{abs}} = \frac{\dot{Q}_{\text{C}}}{\dot{Q}_{\text{H}}} \tag{2.8}$$

The pump work is often negligible as compared with the heat input so it can be neglected without much error [3].

One efficiency benefit for absorption systems is that the number of desorption stages can be increased depending on the exhaust temperature. Single and double effect absorption systems are the most prevalently available with representative heat source temperatures of 90°C and 120°C, respectively [17]. Triple effect systems are theoretically feasible for even higher waste heat stream temperatures, but are economically limited due to the complexity and cost [66]. The performance of a heat activated cooling system is described by the COP, which in this case is the cooling output of the system divided by the heat and work inputs. For single and double effect absorption systems, typical values for the COP are 0.75 and 1.6, respectively, when chilling water from 14°C to 7°C [52].

Single effect absorption systems are the most common due to their relative simplicity and high COP compared to other heat activated cooling systems. Ammonia-water systems follow the same basic schematic as shown in Figure 2-3, but, due to the high volatility of the ammonia-water mixture, a rectifier is required between the desorber and condenser. There have been many studies on ammonia-water systems for a variety of applications. Several studies have focused on theoretical thermodynamic modeling, including Chua et al. who employed the Colburn-Drew mass transfer equations to model the absorption process and found a COP of 0.52 for boiler, condenser, and chiller temperatures of 125°C, 30°C, and 8.7°C, respectively [29]. Kim and Park also

t_G (°C)	t_E (°C)	t_S (°C)	$(COP)_{Conventional\ cycle}$	$(COP)_{Proposed\ cycle}$	Percentage improvement
120	−10	25	0.588	0.719	22.3
		35	0.496	0.610	22.9
		45	0.295	0.402	36.3
120	0	25	0.676	0.970	43.5
		35	0.592	0.715	20.8
		45	0.480	0.583	21.4
120	10	25	0.775	1.135	46.4
		35	0.685	0.917	33.8
		45	0.593	0.699	17.8
150	−10	25	0.576	0.895	55.4
		35	0.501	0.646	28.9
		45	0.417	0.543	30.2
150	0	25	0.657	0.982	49.5
		35	0.578	0.838	44.9
		45	0.499	0.628	25.8
150	10	25	0.754	0.977	29.6
		35	0.663	0.893	34.7
		45	0.581	0.773	33

Figure 2-4. Improvement in COP by optimizing the heat exchangers through a pinch point analysis [13].

performed a theoretical analysis through a lumped parameter dynamic model and found similar results with a thermodynamic COP of 0.56. However, the analysis by Kim and Park considered extremely hot flue gas of 870°C, which generates a large amount of heat at the generator and potentially increases its COP [31].

Jawahar et al. attempted to optimize the heat exchangers of an ammonia-water absorption cycle by performing a pinch point analysis. The results of the analysis are presented in Figure 2-4 and showed fairly high COP increases (maximum of 55.4%) for every combination over a traditional cycle [13]. Le Lostec et al. also investigated some thermodynamic modeling improvements by adding a mass transfer coefficient in the absorber and multi-component condensation effects in the condenser. With these changes implemented in their modeling approach, the COP was 0.60 for boiler, condenser, and chiller temperatures of 87°C, 35°C, and 22.3°C, respectively. The modeling approach was compared with experimental results with minimal reported error [32].

A few other papers have also performed actual experiments to validate their thermodynamic modeling approaches. Said et al. designed a solar activated chiller system used in Saudi Arabia. The team focused on providing ice with evaporator saturation conditions between -2°C and -7°C. Even at very high ambient conditions of 45°C, the system had a COP of 0.42 (generator and chilled water at 140°C and -4°C, respectively) [33]. This result is promising for a device with such high ambient temperatures. Han et al. also focused on creating an ice producing chiller, and, with a cooling output of 11.7 kW_{th}, showed a COP of 0.47 [28]. Although both results are fairly low, when considering the maximum theoretical COP is also low (i.e., 1.26 to 2.92), they have similar performance to typical ammonia-water based systems.

Single effect LiBr-Water absorption systems are very popular in the commercial sector and most are rated for ambient and chilled water temperatures of 30°C and 7°C, respectively, but operate over a broad range of heat source temperatures. Table 2-1 lists the COPs for five commercially available single effect systems and their respective heat source temperatures. Each of these systems have very similar COPs which indicates it is challenging to dramatically increase the efficiency. The cooling capacities for commercial production are generally above 175 kW_{th} and can be powered by a variety of sources. In addition, some theoretical studies have investigated improvements for LiBr-Water system performance. Joudi and Lafta aimed to simplify previous modeling approaches by introducing a new model for the absorber when considering simultaneous

Table 2-1. Performance of commercially available single-effect LiBr-Water absorption systems.

System/Manufacturer	Generator Temperature [°C]	COP
Trane – CoGenie LT5 [4]	132	0.64
Carrier – Unit 16LJ [9]	95	0.7
Yazaki – SC50 [19]	88	0.7
Broad X – Unit 20 [54]	98	0.76
Carrier – Unit 16TJ [55]	100.6	0.7

heat and mass transfer. They found a COP of 0.71 when the system operated with heat source, ambient, and cooling water temperatures of 85°C, 30°C, and 8°C, respectively [42]. By comparing their theoretical results with published literature similar to the data in Table 2-1, the authors found excellent correlation to validate their modeling. Salmi et al. presented a modeling analysis for an absorption system used for a ship application in tropical conditions. The heat source for their application was engine jacket water or exhaust gases and, by assuming a COP of 0.5, the total fuel savings for the ship were calculated while offsetting the cooling load. The authors discovered 61% of the cooling load was delivered by waste heat, saving approximately 95 tons of fuel per year [43]. Other studies included utilizing solar thermal energy as the heat source. Izquierdo et al. focused on an absorption chiller for residential use and found an overall system COP of 0.37 [41]. Lizarte et al. expanded on the previous work of Izquierdo et al. by powering the cooling system from solar thermal power. The results of that modeling approach found a COP of 0.53 for generator, ambient, and chiller temperatures of 105°C, 37.5°C, and 17°C, respectively. The study found a large area was devoted to solar thermal energy generation (42.2 m^2) to only deliver 4.5 kW_{th} of energy. Although the trial results show positive potential, the economic and space aspects of the modeling will be challenging [39].

One disadvantage to using LiBr-Water systems is the potential for LiBr crystallization at high generator temperatures. After the desorption process, the weak solution is sent back the absorber where it will begin to cool. If the temperature is too high, the LiBr solution will pass through a crystallization region and block the system passages [65]. Gilani and Ahmed presented a crystallization detection technique that can be applied to modeling approaches to identify the problem [67]. If higher generator temperatures are to be achieved for LiBr-Water absorption, double effect systems must be employed. The double effect system has an additional generator

that allows the weak solution less temperature drop to eliminate the crystallization and give advantages to using the higher exhaust temperature. Figure 2-5 shows a schematic of a double effect system. Double effect chillers have higher COPs as compared with single effect, but much of the increase is due to the higher boiler temperatures, which increases the theoretical COP [65]. It is postulated that other heat activated cooling systems with high heat inputs would have similar COPs. Figure 2-6 shows an analysis comparing single, double and triple effect system COPs at various generator and evaporator temperatures for a constant condenser temperature of 33°C. It is clear that multi-effect systems have an increased COP, but operate poorly at very low generator temperatures. Several researchers have presented data for double effect systems that match well with the data presented by Gomri. Xu et al. presented a study on a LiBr-Water double effect system and found a COP of 1.23 with steam at a pressure of 680 kPa [50]. Irmanesh and Mehrabian performed a similar study and found a COP of 1.33 with a heat source of 150°C and chilled water temperature of 5°C [51]. Additionally, some researchers have investigated slight performance modifications to the standard double effect cycle. Farshi et al. studied a LiBr-Water system in three absorbent flow configurations (series, parallel, and reverse parallel) under similar temperature conditions. The operating configurations are based on the flow direction of absorbent between the

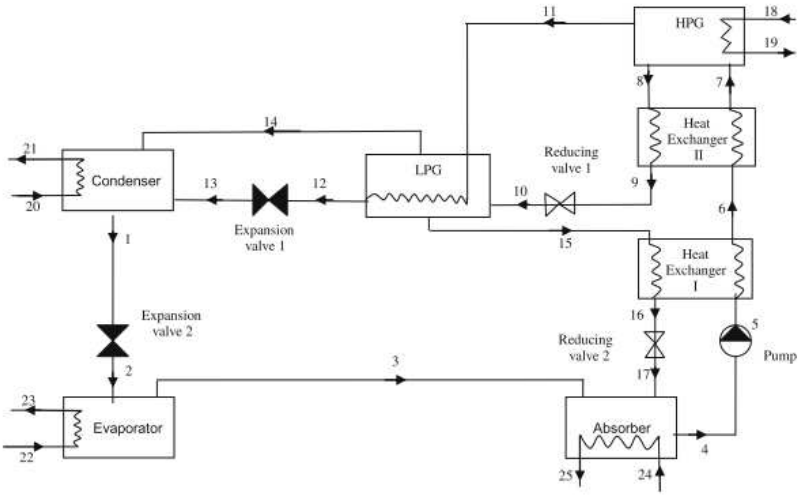

Figure 2-5. Double effect absorption system schematic [17].

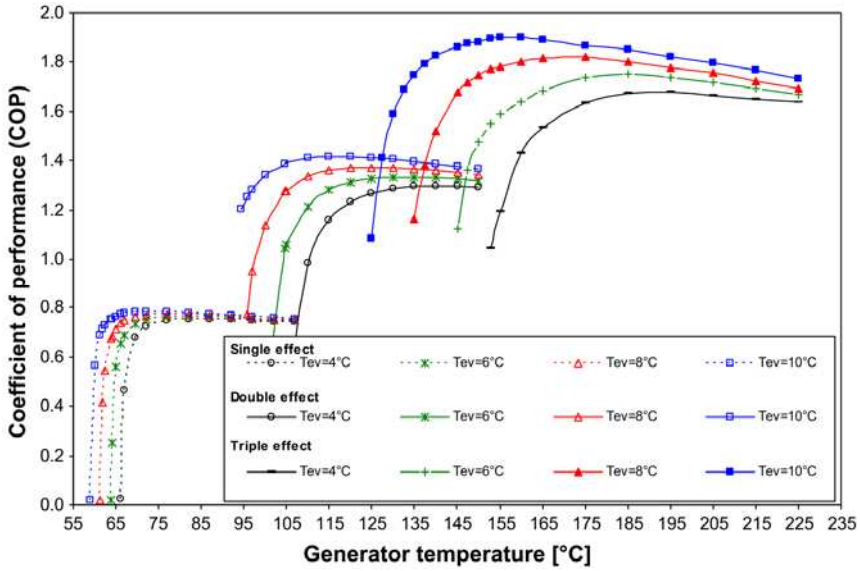

Figure 2-6. COP comparison for single and multi-effect absorption over a range of temperatures [17].

components. The results of the study were that systems with parallel and reverse parallel had very similar COPs, but that both were higher than in series [68].

The increase in components for the double effect system manifests itself in an increase in capital cost and size over single effect systems. These cost and size increases can be prohibitive for high order systems such as double and triple effect. One study, by Shirazi et al. performed a techno-economic analysis of single and multi-effect LiBr-Water absorption systems. The study found that for double and triple effect systems, the direct radiance index (measure of sun exposure) needs to be very high (above 70%) for a triple effect system to be cost-competitive [66]. The sun exposure is a proxy for heat exchanger size, so the result indicates very large and expensive systems. Thus, although triple effect systems have superior performance – for example, Gomri et al. show an approximate 30% COP increase [17] – the component cost and general system complexity can make multi-effect systems prohibitively expensive.

There are several strengths to absorption systems that make them the most popular heat activated cooling technology. The absorption process does not require any rotating components

besides a simple pump to elevate the pressure. Furthermore, the cooling capacity of absorption systems can be high because the relative component simplicity allows for easy scaling of the components for high loads. Most commercial absorption systems operate with cooling loads well above 100 RT, and in some cases as high as 4000 RT [69]. The maintenance costs can be low due to the basic and stationary components. There are other performance benefits to absorption chilling as well. The systems have high COPs compared with other heat activated cooling technologies, which makes absorption highly marketable. Most single effect absorption system operate with COPs of 0.6 - 0.8 while double effect systems can achieve COPs between 1.0 and 1.4. The working fluids used for the systems are another benefit to absorption systems. The most commonly used fluids are ammonia-water and LiBr-water, all of which have minimal environmental impact, are easily obtainable, and have a low cost.

The weaknesses of absorption systems involve the fluid properties and large footprint of the systems. The two main absorbent-fluid combinations have several disadvantages. The LiBr-water system uses water as the refrigerant, thus limiting the application to above 0°C due to potential for freezing. Thus, the systems can only be used for air conditioning applications where the evaporator temperature is nominally 5°C. The concentrated LiBr also presents issues due to high corrosiveness and potential for crystallization. The LiBr corrosion reduces the system life by degrading the piping and heat exchangers which accelerates replacement time [65]. For higher temperature applications, the LiBr can easily crystallize in the heat exchangers which clogs them and slows or stops performance of the system. Careful design is required to ensure the system can operate at the full range of heat sources. Although the ammonia-water systems do not have the same crystallization issues as LiBr-water, there are problems associated with using ammonia as the refrigerant. Ammonia has a high toxicity, a high pressure, and readily corrodes copper. The

high pressure of ammonia in the generator causes the components, lines, and pressure vessels to be rated at a high pressure, thus increasing capital cost. Perhaps the largest issue with absorption systems is the large footprint which can drive a large capital cost. The heat exchange components tend to be large to maximize the efficiency of the system which leads to high capital costs. For instance, Little and Garimella showed that an absorption system footprint would be 3.8 m^2 at 120°C waste heat temperature. In contrast, an ORVC unit would have a footprint of 3.07 m^2 for the same heat source temperature which implies a lower cost for the ORVC [15]. Multi-stage systems require several additional components, such as additional generators and heat exchangers, to achieve their high COPs, which adds additional capital cost.

2.2.2. Adsorption Systems

Adsorption systems operate with three primary components as shown in Figure 2-7: an adsorption bed, an evaporator, and a condenser. The cycle works in a batch process driven by the adsorption and desorption phases in the generator (adsorption bed in Figure 2-7). At the start of the cycle, all three valves are closed and the adsorption bed is heated by waste heat. When the pressure and temperature of the adsorption bed reaches the desired condenser saturation pressure,

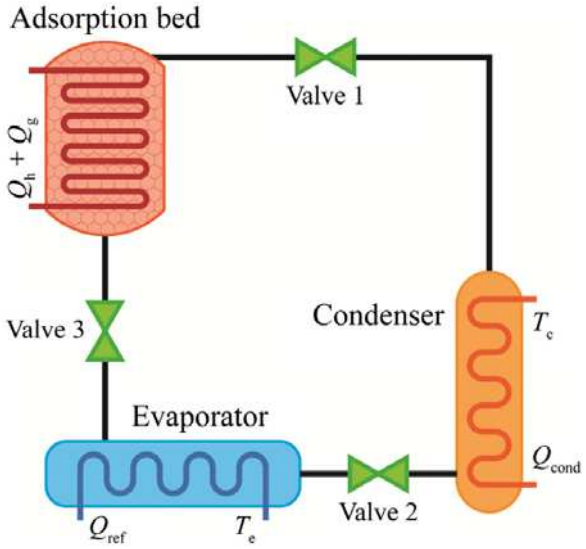

Figure 2-7. Single stage adsorption system diagram [11].

valve 1 is opened which starts the fluid desorption from the bed. The next phase begins by opening valve 2 to allow the vapor to flow into the evaporator. When the pressure reaches the evaporation pressure, valve 3 is opened, causing the fluid to flow through the evaporator into the adsorption bed where it is adsorbed to restart the process [11]. Double effect and triple effect adsorption systems operate with multiple sorption beds to take advantage of higher waste heat temperatures. In these multi-effect applications, there has been considerable research on increasing thermal energy recovery because heating of the sorption bed requires approximately 41% of the heating load and there is considerable energy wasted as the sorption bed cools between cycles. The need for thermal recovery has driven multi-effect innovations such as cascading, internal heat recovery, and the thermal wave concept [70].

The design of the adsorbent bed is critical because the adsorption process depends on the interaction between the working fluid and the adsorbent bed. This process is dominated by Van de Waals forces. In many simulations, adsorption is assumed to be a reversible process, where the adsorbed molecules adsorb and desorb with no losses. In reality, the process is not completely reversible, and there is deterioration of the adsorptive material during cycles. Some causes of deterioration are fragmentation of the absorbent material at high adsorption rates, material impurities from unwanted oxidation, and the amount of coagulated water trapped within the absorber [71]. Wang et al proposed two possible solutions to decrease adsorbent deterioration. The first option is to restore the adsorbent capabilities by washing it with a ph-solution while under pressurization. The second option is to enhance the adsorbent bed through surface modifications by implementing metallic particles into the adsorbent that can counteract the deterioration effects [71].

Incorporating various materials into the adsorbent bed also addresses another common issue: the thermal conductivity of the sorbent is very low. Heat is transferred into and out of the sorption bed primarily through conduction. Low thermal conductivity sorbents are not conducive to high transfer rates and, therefore, achieving an efficient cycle is challenging [71]. By incorporating conductive materials into the adsorbent bed, the conductivity can be increased which enhances heat transfer. In one study, graphite and copper powders were added to an activated carbon absorption bed, yielding a 25% increase in heat transfer performance [72]. In another study, Guilleminot et al. created an adsorption bed with 35% metallic foam and 65% zeolite adsorbent, and the effective heat transfer coefficient of the adsorbent increased from 20 W m^{-2} K^{-1} to 180 W m^{-2} K^{-1} [73]. Although these major increases in heat transfer coefficient help to increase system efficiency, the addition of materials to sorbent bed can decrease the mass transfer surface area. Often, sorbent beds with infused conductors will employ some other method to limit the decrease in mass transfer. The most common method is to reduce thickness of the sorbent layer [71].

There are several common adsorption bed-fluid pairs depending on the application: activated carbon-methanol, activated carbon-ammonia, zeolite-water, and silica gel-water. Each combination listed above has advantages and disadvantages. The carbon-methanol pairing has high adsorption capacity and low adsorption/desorption temperature. Methanol has a high latent heat of evaporation, which provides good heat transfer characteristics in the heat exchangers. One of the primary disadvantages with carbon-methanol is the poor thermal conductivity of activated carbon. Several modeling attempts have investigated improving the adsorption and heat transfer performance of the carbon adsorption bed [71]. Teng et al. developed a purely theoretical model based on the well-known Dubinin-Radushkevich equation. The study presented simulation results for a variety of heat exchanger temperatures and working pair combinations and found fairly high

COPs, upwards of 0.6 for evaporator, condenser, and generator temperatures of -10°C, 30°C, and 90°C. The authors do note, however, that experiments will be required to validate the modeling approach [22]. Cacciola et al. focused on developing techniques for carbon adsorbent material shaping and metal powder infusion to increase the adsorption capability and thermal conductivity. They used PTFE as a binding agent to create a powder infused adsorption brick with a smooth surface to create good contact with the heat source and fluid. The PTFE binding agent did have a minor negative effect on the thermal conductivity, but significant gains in the adsorption capabilities (40% increase over baseline) offset this challenge [74]. One other team investigated carbon-fiber as the activated carbon sorbent, which increased the COP by 10-20% and the adsorption capacity by 2-3 times [75]. One final disadvantage with activated carbon-methanol is the use of methanol as the working fluid. Methanol breaks down at temperatures above 150°C, which limits realistic system operation to temperatures below 120°C. Additionally, methanol is listed as highly toxic fluid, and extreme care must be taken during system design and operation to minimize hazardous leaks [71].

Activated carbon-ammonia systems have similar advantages and disadvantages to activated carbon-methanol. The system has good heat transfer characteristics in the component heat exchangers, and has a similarly high adsorption capability, but it still suffers from the low conductivity sorbent. Ammonia can also operate at low temperatures, and the system is often used to create ice. By using ammonia as the working fluid, the system can be operated at high temperatures because ammonia does not chemically break down at as low a temperature as methanol. However, ammonia is a toxic fluid and reacts poorly to some powder additives for increased thermal conductivity [71]. Tamainot-Telto and Critoph experimentally validated a thermodynamic model with a generator and evaporator temperatures of 102°C and -12.5°C,

respectively, and found a COP of 0.12. Their theoretical modeling showed a 90% increase in performance by using monolithic carbon compared to granular carbon and recommended using monolithic carbon for future studies with any activated carbon system [23]. Xu et al. simulated the carbon-ammonia cycle for ice making applications with an evaporating temperature of -18°C. Their most significant contribution was modeling the system at a variety of conditions to determine the best performing system for each condition. The study found that multi-stage adsorption is appropriate for some of the more extreme conditions. Table 2-2 shows the system performance for a condenser temperature of 30°C, but the complete table also includes 20°C and 40°C condenser temperatures. The range of COPs for the various conditions was 0.01 to 0.55 [11].

Table 2-2. Selection of COP points for the optimum adsorbent cycle under various heat reservoir temperatures [11].

T_c/°C	T_e/°C	Optimum	T_{g2}/°C										
			50	60	70	80	90	100	110	120	130	140	150
30	−25	Cycle	/	III	III	II	II	II	II	I	I	I	I
		COP	/	0.07	0.08	0.10	0.11	0.11	0.11	0.12	0.13	0.14	0.15
		Δx	/	0.03	0.05	0.04	0.06	0.07	0.08	0.04	0.05	0.06	0.07
	−15	Cycle	III	III	II	II	II	I	I	I	I	I	I
		COP	0.05	0.09	0.12	0.13	0.14	0.15	0.18	0.19	0.20	0.20	0.20
		Δx	0.01	0.05	0.05	0.07	0.09	0.04	0.06	0.07	0.09	0.10	0.10
	−5	Cycle	III	II	II	I	I	I	I	I	I	I	I
		COP	0.10	0.14	0.16	0.17	0.22	0.25	0.26	0.26	0.26	0.26	0.26
		Δx	0.04	0.05	0.08	0.04	0.06	0.09	0.10	0.12	0.13	0.14	0.15
	5	Cycle	II	II	I	I	I	I	I	I	I	I	I
		COP	0.16	0.19	0.27	0.31	0.33	0.33	0.33	0.33	0.32	0.32	0.31
		Δx	0.04	0.08	0.06	0.09	0.12	0.14	0.16	0.17	0.19	0.20	0.20
	15	Cycle	I	I	I	I	I	I	I	I	I	I	I
		COP	0.26	0.39	0.41	0.42	0.42	0.41	0.40	0.39	0.38	0.37	0.37
		Δx	0.03	0.08	0.13	0.16	0.19	0.21	0.23	0.24	0.26	0.27	0.27

Zeolite-water combinations have advantages over carbon based systems due to the higher latent heat of water as compared to methanol or ammonia. The water based system is also advantageous because it allows for a wide range of adsorbent bed temperatures, with a typical range being between 80°C and 200°C [71]. Since the temperatures at the adsorption bed can be fairly high, the system is often considered for automobile applications with high temperature exhaust. Zhang designed and tested a Zeolite 13-water system operating with an adsorption heat exchanger enhanced by fins. The study found a good correlation between simulation and

experimental results (3.2% maximum error) with the best COP and specific cooling power being 0.38 and 25.7 W/kg, respectively. The author points out that these are promising results for an adsorption system, but that the waste heat temperatures are fairly high, which is increasing the performance [24]. Poyelle et al. investigated enhancing the adsorbent material to increase the thermal conductivity of the material. They produced an adsorbent with a fifty times higher thermal conductivity (0.1 W m^{-1} K^{-1} to 5 W m^{-1} K^{-1}) and a wall heat transfer coefficient increase by twenty times (30 W m^{-2} K^{-1} to 500 W m^{-2} K^{-1}). Although the mass transfer of the adsorbent did decrease, the COP obtained was 0.41 and specific cooling power was 97 W kg^{-1} for generator and evaporator temperatures of 240°C and 4°C [25]. One disadvantage of a zeolite-water system is that the application cannot be below 0°C because water will freeze. Therefore, many zeolite-water systems are used for air conditioning applications. Another disadvantage is the poor adsorbent mass transfer caused by the low evaporator pressure of water [71]. To summarize, zeolite-water systems tend to have strong heat transfer capabilities but have weak mass transfer characteristics which tend to counteract each other.

One final frequently studied adsorption bed-fluid combination is silica gel-water. These systems have similarities to zeolite-water systems, including that they are generally only used for air conditioning applications due to the high freezing point of water. However, silica gel-water systems can operate at lower desorption temperatures (as low as 60°C) due to the properties of silica gel [71]. Najeh et al. investigated the performance for use in a solar thermal cooling application, and, with a solar collector temperature between 60°C and 100°C, they showed a reliable cooling duty of 5.64 kW and a COP of 0.62 [27]. Cho and Kim also presented work in which a low temperature adsorption source was used between 60°C and 80°C, but focused on improving the refrigeration capacity and cycle time. The study predicted that increasing the heat

transfer rates in each of heat exchangers would significantly increase cycle time and cooling capacity. The cooling capacity had the largest increase at about three times the baseline [76]. One further study, by Alam et al., investigated a two-bed adsorption system that optimized the bed switching frequency and heat exchanger properties to overcome the batch limitation. The switching frequency was critical for system performance and the results showed the specific cooling capacity and COP could not be optimized simultaneously. The maximum COP (0.45) occurred at a switching frequency of approximately 0.25 while the specific cooling capacity occurred at 0.43. This result indicates that the design conditions should be carefully considered when designing an appropriate adsorption system [26].

As noted in several studies above, the advantages to using adsorption systems are their low complexity and ability to operate with very low temperature heat streams. In the basic adsorption system, there are only three components to construct and three control valves to operate the system. Most adsorption systems do not require any primary power to circulate the fluid because the systems are driven by pressure differences and actuated valves. This simple design allows the system to have significant operational cost savings as compared with heat activated cooling system competitors. Another advantage of adsorption systems is their ability to operate with very low heat streams. The heat source is simply used to desorb the fluid from the sorbent bed, and in some cases, such as silica gel-water combinations, desorption can be achieved with temperatures as low as 60°C [27, 76]. This low temperature waste heat gives a distinct advantage over other heat activated cooling systems that have minimum operating temperatures near 80°C. A common application for adsorption includes a solar thermal heat source rather than waste heat.

Although there are advantages to adsorption in simple construction and low operating temperatures, there are several prohibitive disadvantages. The adsorption bed in the system has to

operate in a batch process, creating a challenge for practical applications. Most applications require continuous cooling, and either multiple adsorption units or multiple adsorption beds are required for continuous operation. Although the systems generally have low maintenance costs, the adsorbent bed has been shown to deteriorate, causing the system performance to degradation. Beyond the complexity required for system operation, there are also some fundamental issues if the system is going to compete with other state of the art heat activated cooling systems. As shown in the studies above, the COPs are typically on the low end of the spectrum when plotted on Figure 2-2. The low COPs are generally caused by deficiencies in the adsorbent material, which have poor heat and mass transfer characteristics. Some attempts have been made at increasing the heat transfer properties by infusing metals into the adsorbent material, but, those methods have not yielded major COP increases. One further issue related to the adsorbent performance is the low cooling power density of the adsorbent which can lead to higher footprints and bulkier components. In one study, Kim and Ferreira compare an adsorption and absorption system and find adsorption is 4.6 times heavier and 5.4 times bulkier than the absorption. They conclude that for small to medium systems, wide spread adoption of adsorption is hindered by the considerable bulk and expense [77]. The fluids used for these systems presents yet one final challenge because many of the working fluids are toxic. Each of these disadvantages will need to be addressed for adsorption systems to become more prevalent in the heat activated cooling market.

2.2.3. ORVC Systems

ORVC systems, as the name suggests, are a combination of organic rankine and vapor compression cycles. There are several configurations of the system, but most use the heat source to power an expansion device that drives a compression device to generate a cooling effect. The most common ORVC employs a turbo-compressor and a shared condenser as shown in Figure 2-

8. The shared condenser requires the fluid to be the same for the ORC and VC cycles. State points 1 – 9 are the same as in a standard Rankine cycle where the waste heat stream is absorbed at the boiler. The turbine in the Rankine cycle drives a compressor and the outlet streams are combined before entering the condenser. At point 7 the flow splits and a portion is sent through the Rankine cycle while the other portion is sent to the vapor-compression cycle. The fluid at point 10 is expanded to a lower pressure and then heated to vapor in the evaporator before compression. ORVC systems are typically less complicated as compared to absorption and have competitive COPs [15].

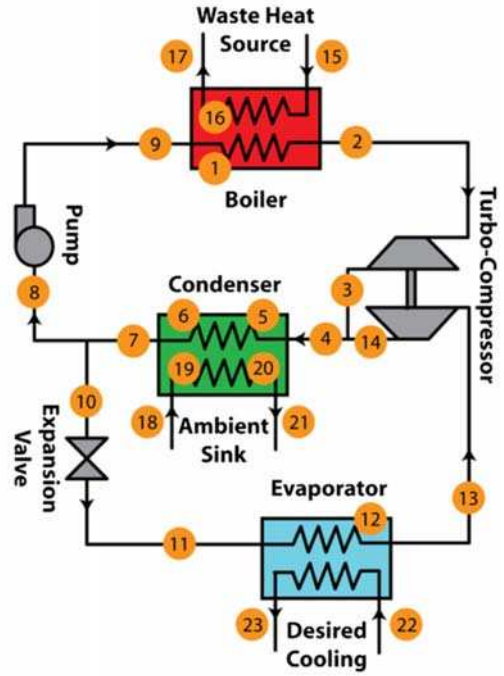

Figure 2-8. ORVC cycle schematic [15].

For low cooling duties, a positive displacement device is used, such as the alternating piston cylinder presented by Aphornratana and Sriveerakul (Figure 2-9). By controlling a series of valves, the high pressure fluid from the boiler generates work to drive the compression for the vapor-compression cycle. Their study analyzed the performance of the system over a range of operating temperatures using fluid R22 and R134a. One representative data point at generator,

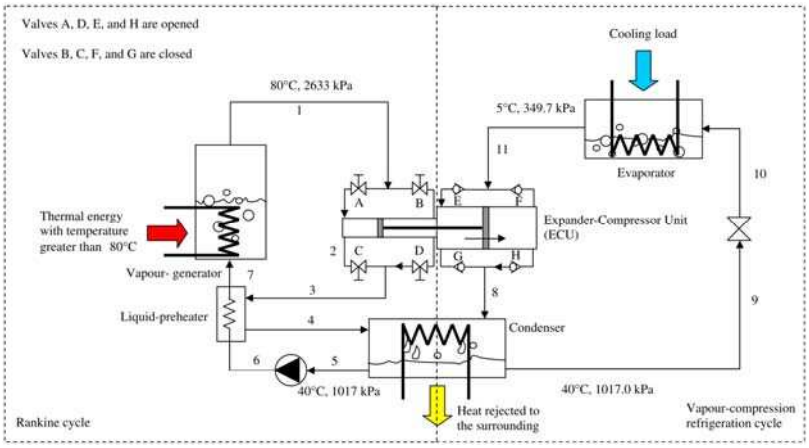

Figure 2-9. Dual piston expansion/compression device shown in center with associated valve positioning [16].

condenser, and evaporator temperatures of 90°C, 35°C, and 5°C, respectively, yielded a COP of 0.55 for R22 and 0.45 with R134a [16]. The theoretical maximum COP for these temperatures is 1.4, which aligns well with competitor absorption systems. However, the efficiency for the dual piston device is not presented, and significant efficiency gains could be realized by decoupling the power and cooling cycles.

Recognizing the environmental impacts in operating with high global warming potential refrigerants, Li et al. analyzed several hydrocarbons (propane, butane, isobutane, and propylene) in a single fluid configuration and showed some promising results. Butane typically had higher COPs, with a representative value being 0.47 for generator, condenser, and evaporator temperatures of 90°C, 40°C, and 5°C. The COP was calculated by assuming expander and compressor isentropic efficiencies of 80% and 75%, respectively. The authors also provided some analysis on the effect of expander and compressor efficiency to the COP [12]. The black lines in Figure 2-10 and Figure 2-11 show the COP while the turbine and compressor efficiencies are increased. It is clear that increasing the efficiencies has a large effect on COP, however, their modeling approach is purely theoretical, and the authors do not present any turbo-machine options or do any calculations to prove these high efficiencies are possible for a system operating with a

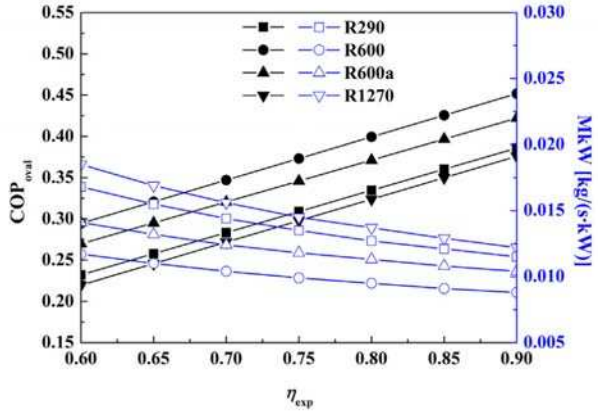

Figure 2-10. COP increase as expander efficiency varies from 60-90% [12].

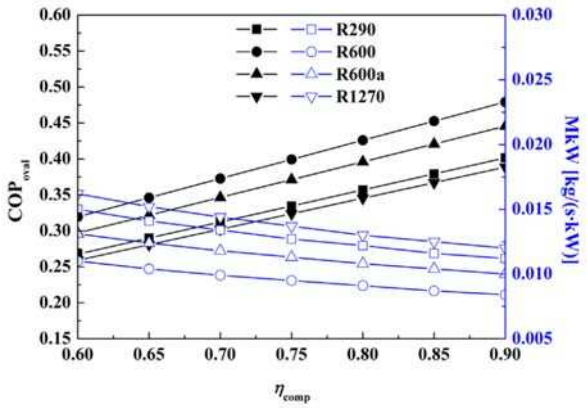

Figure 2-11. COP increase as compressor efficiency varies from 60-90% [12].

single fluid. One final issue with operating with hydrocarbon fluids is their flammability, which make operation of the facility more challenging. Extreme care must be taken to ensure minimal leaks occur during install and operation.

One other single fluid study, presented by Wang et al., also displays the lack of system optimization driven from fluid selection. Their system analyzed an ORVC for a desert military application with a high ambient temperature of 48.9°C. They compensated for the performance losses from the high ambient by increasing the heat input and evaporator chiller temperatures. The fluid selected for this application was R245fa, which is common for organic Rankine cycle systems, but does not perform exceptionally well for refrigeration applications. They first analyzed a baseline cycle and found a COP of 0.54 for the boiler, condenser, and evaporator conditions of 190°C, 48.7°C, and 18°C, respectively. These temperature ranges yield a theoretical maximum COP of 2.89. They then considered adding a power cycle recuperator and sub-cooler which resulted in an increased COP to 0.66. Similar to previous studies, the expander and compressor efficiencies were set at 75% and 80%, and the authors speculate that a two fluid system would have efficiency benefits over a single fluid system [20].

Building on the previous study, two papers, Dubey et al. and Jeong and Kang, investigated using multi-stage expanders and compressors to achieve higher pressure ratios and produce more work. By using multi-stage machinery, they also added an economizer between compressor stages, a recuperator between the pump and boiler, and a boiler with a reheating loop. For the system to work, the boiling input temperature was very high, with both studies simulating ranges between 200°C–300°C. Figure 2-12 shows the system configuration for both studies. Dubey et al. showed a high COP under all conditions, with one representative point being 1.42 at boiler, condenser, and evaporator temperatures of 220°C, 30°C, and 5°C [78]. Jeong and Kang found similar results with a representative point being 1.37 at boiler, condenser, and evaporator temperatures of 250°C, 40°C, and 6°C [53]. Although both systems were able to achieve high COPs, the boiler inlet temperatures were very high (≥200°C), which yields a high maximum COP. By plotting the data on Figure 2-2, the systems do have better performance than single effect absorption, but align similarly with double effect. The other disadvantage behind these systems is the trade-off between increased

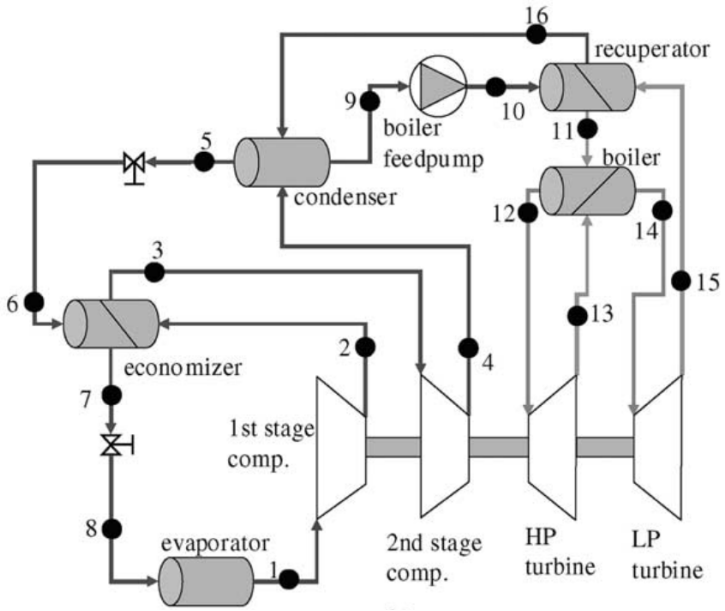

Figure 2-12. ORVC with multiple stages, an economizer, recuperator, and reheater [53].

performance and cost. Adding additional heat exchangers and a multi-stage turbo-machine will add complexity and cost that might be uneconomical.

As mentioned in several of the ORVC cycles previously, one major downfall for the single fluid options is the lack of optimization for the turbine and compressor efficiencies. The reason for the unoptimized components is that the fluid is required to perform optimally at the relatively high temperatures for the Rankine cycle while also performing optimally for the low temperatures of the vapor-compression cycle. Several researchers have noticed this phenomenon and have designed systems with potential to overcome the efficiency losses associated with single fluid systems. Prigmore and Barber were one of the first to create an ORVC system with different fluids. Their system, shown in Figure 2-13, used a flat plate solar thermal collector with a temperature of

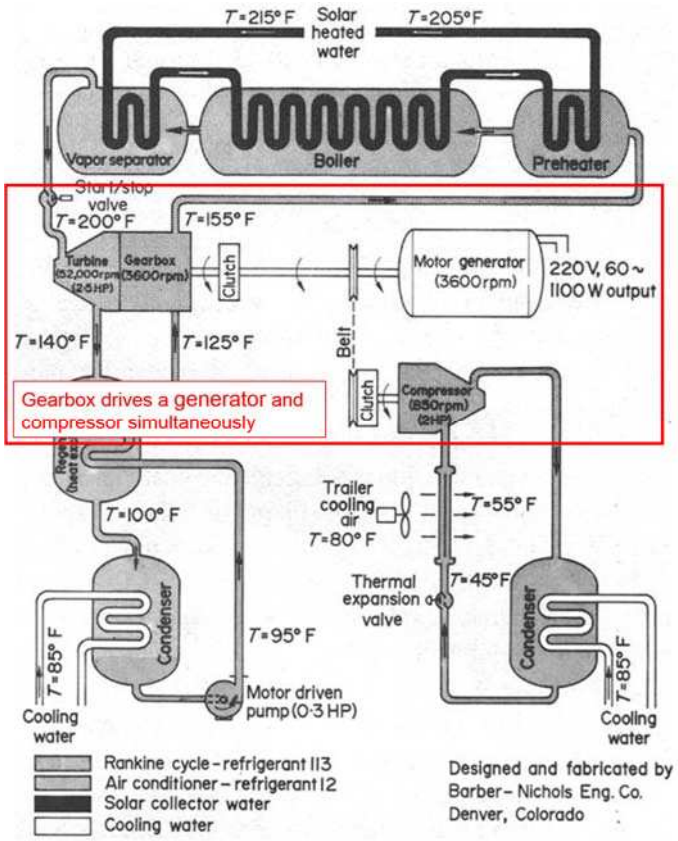

Figure 2-13. Prigmore and Barber's system design with the high speed turbine driving a generator and compressor [7].

approximately 100°C. The turbine spun at a high speed with power transfer of 25 horsepower that could generate electricity through a motor generator combination and also drive a 2 horsepower on a vapor-compression cycle. The power cycle fluid was R113 and the cooling cycle fluid R12 (both fluids have since been banned due to harmful environmental effects) and found a maximum COP of 0.5 during test conditions. The gear box and clutch system added some transmission losses, although the authors do not quantify the amount lost. There was also a higher chance of refrigerant leaks through the gear box and clutch system, releasing harmful fluids to the environment. The authors note that although the system performs fairly well, the cost of the system did not outweigh the benefits. A detailed economic analysis would be required with up to date cost information to determine if a similar system would be economically feasible in the current market.

Wang et al. built on the previous research by Prigmore and Barber by eliminating the gear box and directly driving the compressor from the turbine work. Figure 2-14 shows the results from their effort. The application focused not only on the performance of the system, but also on the size and weight of the systems. The authors selected aluminum brazed micro-channel heat exchangers that were light-weight and had high heat transfer capabilities. The fluids selected for

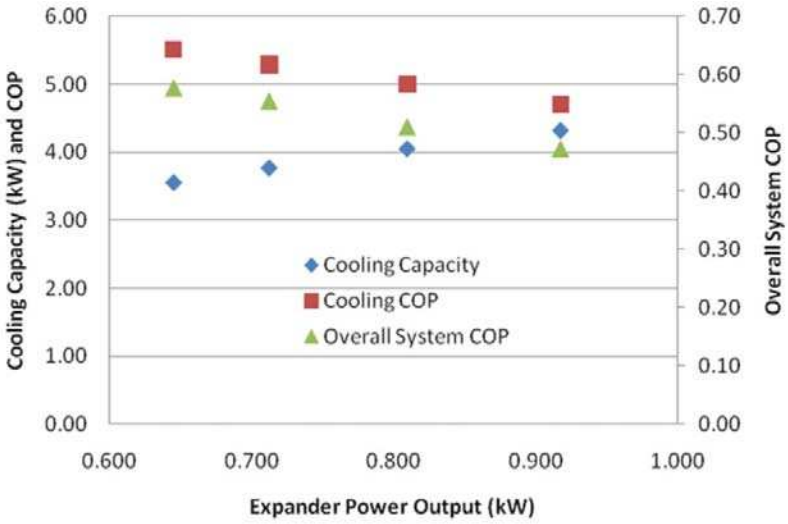

Figure 2-14. Cooling capacity and overall system COP for various expander power outputs [21].

the Rankine and vapor-compression cycles were R245fa and R134a due to their favorable properties at the desired test conditions. Additionally, both fluids are commercially available, have low toxicity, are nonflammable, and noncorrosive. The system was designed for a small scale application, so scroll machinery was used to optimize the efficiency of the turbine and compressor. The results of the testing are shown Figure 2-14. The modeling results were not compared with the test data because the test conditions were not the same as the baseline modeling conditions. The design specifications were for the system to produce 5.3 kW with boiler, condenser, and evaporator temperatures of 200°C, 48.9°C, and 32°C. However, during testing, the temperature conditions for the condenser and evaporator were significantly lower, both being approximately 22°C. The authors speculate that the low condenser and evaporator temperature did not generate a large enough driving force across the thermostatic expansion valve to achieve the required mass flow rate and, therefore, the cooling capacity did not reach the design condition. This prevented the team from validating their modeling approach. This lack of prediction methodology will be discussed in a later section, but presents an opportunity to create a modeling approach that predicts system performance at off-design conditions. One further note by the authors is the performance of the heat exchangers, particularly the boiler. The test facility used a standard plate style heat exchanger which suffered efficiency losses and only had a 75% effectiveness. They postulated that a micro-channel plate-fin heat exchanger would generate a much higher effectiveness and increase the overall efficiency of the system [21].

Each successive research effort on ORVC systems has followed a positive efficiency trend by selecting more optimal system configurations and fluid selections. The COPs for ORVC systems are fairly competitive with absorption technologies in the commercial market. ORVC systems may have cost benefits as compared to absorption, due to the lack of complex absorption

technology and additional components such as the absorbers and generators. The system also has distinct advantages in the range of heat source temperatures over other systems. Rankine cycle fluids can handle a wide variety of temperatures without major modification. Absorption systems, conversely, require multi-stage devices to operate at high temperatures, which causes a large increase in cost and complexity. The fluids used for ORVC systems are typically well known fluids with low toxicity which means leak tolerances can be relaxed and system construction costs reduced. In addition, Rankine and vapor-compression cycles are well understood, thus making costs and components widely available.

The weaknesses of ORVC systems are the lack of cycle optimization, the semi-complex operation modes, and the inability to operate at very low temperature ranges. In previous ORVC studies, the Rankine and vapor-compression cycles have not been optimized simultaneously. In many cases, either the turbine or the compressor have a high efficiency, but not both. This leads to a sub-optimal COP for the entire cycle, but also presents an opportunity for future system improvement by focusing on fluid selection. Because the systems operate with positive displacement devices or turbo-machinery, there are some operational challenges as compared with other heat activated cooling systems with more basic operation principles. The added complexity could lead to slightly higher maintenance costs, but it is possible that the initial capital cost could outweigh this challenge. One final disadvantage to ORVC systems is operation at low heat inputs. Some adsorption systems have the capability to operate at very low temperatures, but, due to a superheating requirement for the turbine, it can be challenging to operate at such low heat source temperatures. The lowest temperature range of most ORVC applications is 80°C, compared to some adsorption systems operating with temperatures are low as 60°C.

2.2.4. Ejector Systems

Ejector systems operate in a similar manner as ORVC systems, but the turbo-machine is replaced with an ejector as shown in Figure 2-15. At state point one vapor exiting the vapor generator passes into the supersonic nozzle of the ejector which creates a vacuum at the inlet of the mixing chamber, thus pulling secondary vapor into the chamber from the evaporator. The two fluid streams mix and then the diffuser expands the fluid to the desired condensation pressure. After rejecting heat in the condenser, the fluid is split with some fluid expanding through the expansion valve while the other portion is pumped to a high pressure. The fluid through the expansion valve (point 5) provides the cooling effect while the fluid after the pump (point 4) is vaporized by adding heat from the waste heat stream [15].

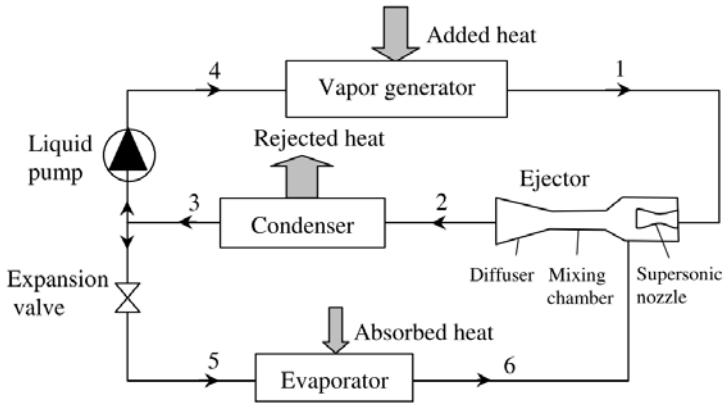

Figure 2-15. Typical ejector system [14].

The COP calculation for an ejector system is similar to many heat activated cooling systems, in which the refrigeration effect at the evaporator is divided by the heat input of the boiler. A pump is typically used to increase the pressure of the liquid heated to the boiler. Some studies included the pump work in the COP, while others neglect it because the work is small compared to the boiler heat input. One study, by Eames et al., found the pump work for an ejector system is typically less than 1% of the boiler heat input, and, thus, can be neglected with minimal computation error [45]. A study by Nguyen et al. attempted to create a purely passive system by

eliminating the pump and instead relying on gravitational effects to drive the condensate to the boiler [79]. None of the analyzed ejector studies included auxiliary power loads (e.g. secondary side fan or pump power) in the COP calculation.

Because the turbo-machinery typical of ORVC systems is replaced by an ejector, the overall efficiency of a jet refrigeration system is largely dependent on ejector performance. Ejectors tend to have poor performance compared to turbo-machinery due to high irreversibilities and small operating ranges in the ejection process. Figure 2-16 shows the main processes in an ejector. The high pressure fluid enters the nozzle and is accelerated, thus creating a low pressure region at point 1 and drawing the secondary fluid into the mixing chamber. At the end of the mixing chamber the fluids are at supersonic speeds and create a normal shock at the throat to cause a compression effect. The flow then sub-sonically diffuses to further increase the pressure [8]. The main sources of irreversibilities are due to pure mixing, kinetic energy losses, and normal shock wave losses [80]. Many papers have focused on ejector geometry changes in an attempt to optimize performance. Korres et al. investigated the characteristic efficiency of the ejector as function of the compression ratio of the system. The study found a strong relation between the overall efficiency and the pressure ratio. They noted the efficiency factor increases for increasing compression ratios, but after a certain point the efficiency reaches a maximum. Beyond this maximum the efficiency decreases which implies the ejector is not as efficient at off-design

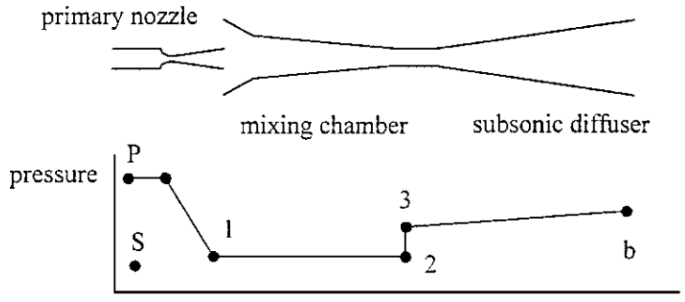

Figure 2-16. Primary regions and pressure characteristics of an ejector [8].

conditions [81]. In 1985, Huang et al. characterized the performance of ejector systems by analyzing the choking phenomenon in the secondary vapor stream. They generated performance maps from empirical data that show the distinct choking effect for ejectors operating with back pressures below the critical value [47]. Figure 2-17, presented by Chunnanond et al. shows the flow choking graphically and describe the performance effects [10]. It is clear from Figure 2-17, that ejectors have difficulty operating over a wide range of conditions due to their fixed geometric conditions. Sun looked to rectify this problem by introducing an ejector with variable geometric configurations that could be adjusted based on design requirements. The study found that optimizing geometries is critical to perform at a range of conditions. However, all of the results presented are strictly theoretical, and the actual system designs are not discussed [82]. Further geometric studies to reduce efficiency losses include Eames and Watanawanavet. Eames produced a new method that accounts for a constant momentum change and helped to eliminate shock wave losses [83]. Watanawanavet performed a geometric simulation through computational fluid modeling software to optimize the length, throat size, and curvature of the converging section [84].

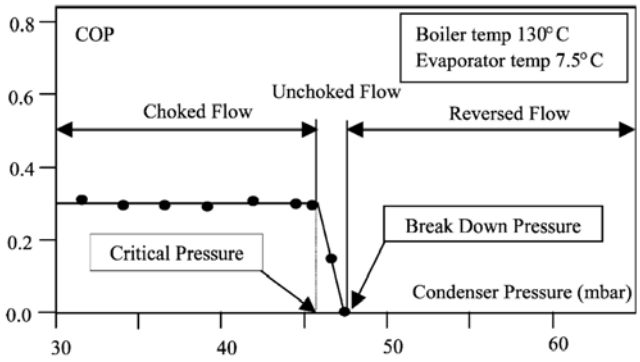

Figure 2-17. Operating regions for a typical ejector refrigeration system [10].

Jet refrigeration systems use the ejector to drive the cooling cycle flow. The system operates by accelerating a high pressure and temperature fluid through a nozzle to create a low pressure region. The secondary vapor inlet port is located just before the mixing region (position

of low pressure) such that the fluid is entrained into the accelerated fluid. The entrainment is the driver to move the secondary fluid which enables evaporation. The fluid selection is critical to not only the ejector performance, but also the saturation conditions of the heat exchangers. Chunnanon and Aphornratana provide a detailed fluid selection methodology and made recommendations for particular fluids [10]. Previous work by Holton has shown that high molecular weight fluids tend to have small ejector sizes for the same system capacity, but also have a higher entrainment ratio and ejector efficiency [85]. Steam (18.02 kg $kmol^{-1}$) was one early fluid used for ejector cycles, but efficiency improvements can be made by using a larger molecule refrigerant such as R123 (176.8 kg $kmol^{-1}$). Another important factor is the fluid pressure at the waste heat temperature required for testing. Water has a low pressure at 100°C (101 kPa) while fluids like R134a have a very high pressure (3972 kPa). The high pressure refrigerants require heavy constructions to withstand the high pressures, which can be costly [10].

Several studies have theoretically or experimentally determined the performance of ejector systems. Eames et al. have provided a study on a steam jet refrigeration with a wide variety of operating conditions and cooling duties (400 to 1000 kW) while maintaining a chilled water temperature of 5°C. The results of the study varied depending on the conditions specified, but the best condition achieved a COP of 0.68 [45]. One interesting note which is well exemplified by this study is the decrease in COP at higher waste heat temperatures. The decrease is driven by the ejector design, which is unable to perform well at conditions outside of the design point due to choked flow or reversed flow conditions as shown in Figure 2-17. Chunnanond and Aphornratana present similar data in Figure 2-18, showing an ejector designed to operate at 130°C [10]. It is clear from the figure that the effective operation region for the system is limited to a small range of condenser pressures and that there is a very small window for optimal COP. The figure also

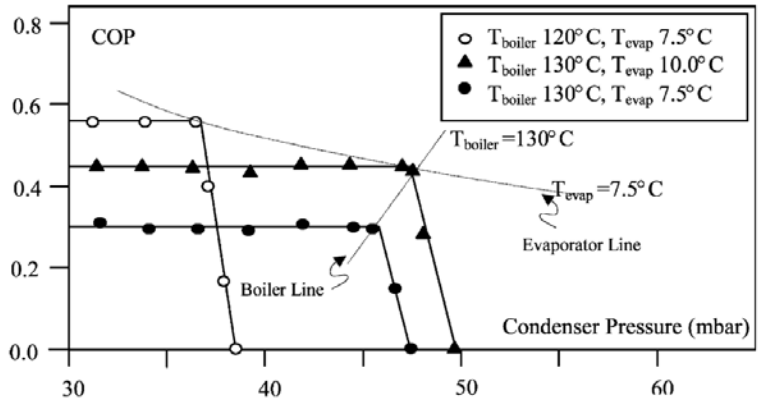

Figure 2-18. Ejector performance at various boiler and evaporator temperatures [10]

suggests that at higher boiler temperatures the COP actually decreases, and would continue to decrease as long as the condenser pressure was high enough for the system to operate. This phenomenon is further explained in Figure 2-19 which shows a full performance map for a range of boiler and evaporator temperatures.

Another study, by Yapici and Yetisen analyzed the performance of an ejector system with fluid R11. They constructed a test facility with a maximum cooling capacity of 900W_{th} to make direct comparisons with modeling efforts. The results of the study showed a maximum COP of 0.25 at waste heat and chilled water temperatures of 100°C and 12°C, respectively. Their experimental COP is fairly low which can be explained by the fluid selection. The authors selected

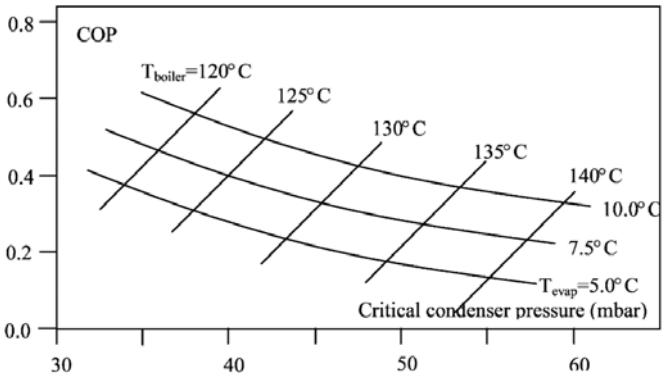

Figure 2-19. Performance map for a steam jet ejector [10].

a refrigerant based on its purchasing availability and did not make their selection based on the most efficient system possible. They do provide some commentary on potential increases in performance for the current fluid selection. For instance, by increasing the evaporator temperature or lowering the condenser pressure, the primary flow will choke at the low vapor generator pressure, thus creating a higher COP and cooling capacity. However, although they modeled this effect, this change would be challenging to implement in practice [14]. These issues exemplify the inherent problems with ejector systems: they have small operational windows and low efficiencies.

Several studies have built on the previous research by analyzing a variety of a hydrocarbon based fluids to optimize system performance. Cizungu et al. investigated four refrigerant options with the same operating conditions and ejector geometry: R123, R134a, R152a, and R717. The results of the study showed that for low heat temperature sources between 70°C and 85°C the most optimal fluids are R134a and R152a [46]. A separate study by Sun et al. also compared a variety of CFC, HCFC, or HFC refrigerants subjected to various evaporator and boiler operating conditions. The most optimal fluid in nearly all cases was R152a with a representative plot shown in Figure 2-20. The authors attributed the performance of the system to the high molecular weight and high latent heat for R152a. The latent heat in particular helps to maximize performance of the phase change heat exchangers in the boiler, condenser, and evaporator [18].

Although ejector systems can be used for many waste heat applications, one promising application is coupling the heat source with a solar thermal collector. A schematic of a solar powered jet refrigeration system is shown in Figure 2-21. A couple investigations have been performed on the feasibility and performance of such as system. Huang et al. simulated and constructed a R141b solar powered system with the addition of a heat regenerator and precooler. They first modeled and tested an ideal cooling system powered by an electric heater and found an

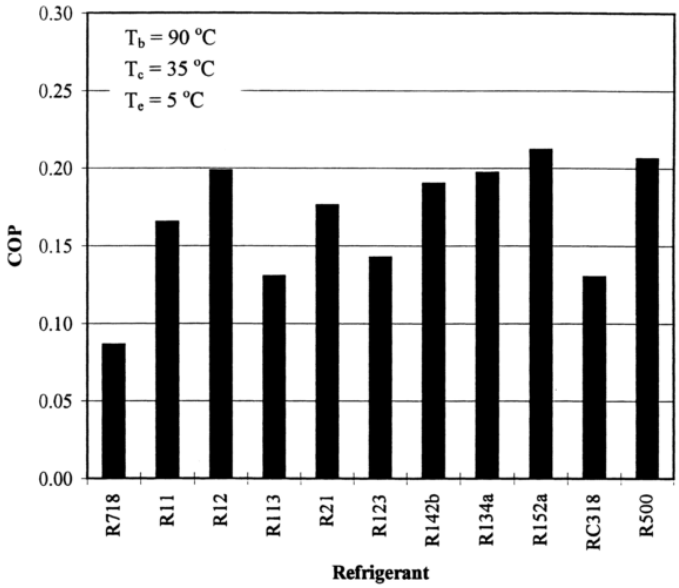

Figure 2-20. Performance of hydrocarbon refrigerants for low temperature ejector systems [18].

experimental COP of 0.5 for generator, condenser, and evaporator temperatures of 95°C, 32°C, and 8°C, respectively. Next, the study designed and tested a solar powered system and found a COP of 0.22 [48]. Khattab and Barakat also performed a detailed study on a solar jet refrigerator and found similar results, but used steam as the working fluid. As with many previous ejector studies, the system was modeled over a range of temperatures to determine optimal performance.

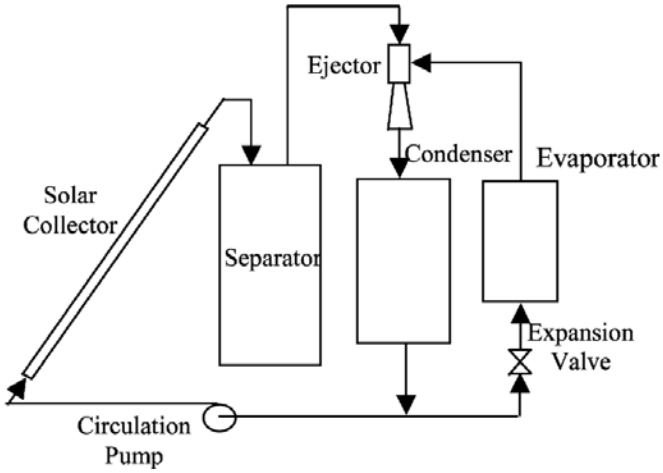

Figure 2-21. Schematic of a solar thermal jet refrigeration system [10].

The COPs reported by Khattab and Barakat are fairly high in comparison to Huang et al. with a maximum of nearly 0.6 with generator, condenser, and evaporator conditions of 50°C, 17°C, and 15°C. These are promising results, although, a full validation would be required to confirm the modeling approach, because, as shown in the study by Huang et al., achieving an experimentally high COP is challenging. Both solar jet refrigeration studies could have difficulties operating during cloudy or cold ambient conditions. Khattab and Barakat suggested adding an additional electric heater to provide heating for the system during low temperature periods [86]. As with any solar powered system, another option is to employ some form of thermal energy storage to improve system operation during non-sunny hours.

The advantages of jet-refrigeration systems over other heat activated cooling systems are their simplistic designs and ease of operation. The passive nature of the ejector provides the cooling effect at the evaporator without use of additional positive displacement or rotating turbo-machinery used in ORVC systems. This advantage means the ejector refrigeration system can operate with minimal additional power input or control. The only primary loop power source required is the minimal power required for the pump that increases the pressure upstream of the waste heat boiler. These simplistic designs also have the potential advantage of low operational costs [8].

However, the simplistic design leads to some major system disadvantages. Because the ejector geometry is typically fixed, the performance of the system is limited to a small range of conditions. Outside of these specified design conditions, the system either operates at a poor efficiency or is unable to generate cooling. The other significant disadvantage of ejector technologies is their poor efficiencies. Because there are high irreversibilities in the ejector, the system COP is often significantly lower than other heat activated cooling systems. As shown in

Figure 2-2, it is clear that ejector systems reside in the lower left corner of the chart, indicating a low theoretical COP and fractional COP. The system is then classified as one of the worst efficiency performers compared with other waste heat cooling systems. The disadvantages in efficiency and operational range do not outweigh the low cost and ease of operation benefits, and is the primary reason why ejector based refrigeration has not had commercial success.

2.3. Research Needs for Thermally Activated Cooling Systems

Many current state-of-the-art heat activated cooling systems suffer from fundamental weaknesses which limit their operation capabilities. The primary limitations of heat activated cooling systems this study aims to address are shown in the following list:

- Several technologies cannot meet a high COP target over a broad range of operating conditions.
- Many heat activated cooling technologies use highly corrosive fluids, high working pressures, or complex system designs.
- Several technologies cannot operate over a broad range of temperatures or struggle to operate at conditions outside their design point.
- Current prediction methodologies do not allow current heat activated cooling systems to be analyzed simplistically in off-design conditions.

Table 2-3 compares the most common heat activated cooling systems over a range of categories similar to the bulleted list above. Absorption systems are the most common heat activated cooling systems due to their high COPs and fair operating temperature ranges. These systems are fairly easy to control, but suffer from high complexities. This system complexity coupled with the large number of cumbersome components causes a high capital cost. This is especially true with multi-effect absorption systems: these systems achieve high efficiencies, but

Table 2-3. Heat activated cooling system comparison.

System	COP	Source Temperature	Corrosive Fluids	Working Pressure	Complexity	Commercially Available?
NH_3-H_2O Absorption	High	>100°C	Yes	High	Moderate	Yes
LiBr-H_2O Absorption	High	<90°C	Yes	Low	Moderate	Yes
Multi-Effect Absorption	High	>120°C	Yes	Low, High	High	Yes
Solid-Vapor Adsorption	Low	<90°C	No	Low	High	Yes
ORVC	High	<90°C	No	Moderate	Low	No
Ejector Cycle	Low	<90°C	No	Moderate	Low	No

require more components and, as a result, high capital costs. Furthermore, the primary working fluid pairs – ammonia-water and LiBr-water – are corrosive, which can reduce component life. Adsorption systems are simpler than absorption, but have low COPs which has made widespread adoption of adsorption systems unsuccessful. Additionally, adsorption systems operate in a batch process and, because cooling applications require continuous operation, multi-stage systems are required. ORVC systems have shown similar performance as absorption and come with less complex system configurations. The lower complexity and smaller size, as shown by Little and Garimella [15], can lead to low capital costs that could be disruptive to absorption technologies. The systems can operate for a wide range of heat sources, but the turbo-machinery required can be a hindrance due to its more complicated operating modes. However, system optimization has been lacking compared with the more mature absorption technologies, and the systems have not been commercialized. By optimizing the turbo-machinery geometry and selecting high performance working fluids more efficient designs can be achieved. Ejector systems are one variant of ORVC systems which attempt to reduce the operational costs and general complexity of typical ORVC systems. Ejector systems have been limited by poor efficiencies that have not been outweighed by the low cost and ease of operation.

One other disadvantage with all of the aforementioned heat activated cooling studies is the inability of the researchers to predict system performance at off-design conditions. Most studies perform a sensitivity analysis based on the primary control variables in the system: the heat stream, condenser inlet, and chiller outlet temperatures. When these temperatures change, the theoretical studies do not consider that the heat exchangers in their systems would change in performance. The experimental studies typically make comparisons to their modeling approaches at the specified design condition, but do not compare the results at off-design conditions. In one heat activated cooling study, by Wang et. al, an ORVC system was simulated for a military application in which the system produced 5.3 kW of cooling with boiler, condenser, and evaporator temperatures of 200°C, 48.9°C, and 32°C, respectively. During testing, however, the conditions at the condenser and evaporator were significantly lower, both being approximately 22°C. This prevented the team from validating their modeling approach [87]. This deficiency was addressed by Wang et al. by simply stating the experimental system should be modified until the temperatures match the modeling. This response is unsatisfying and provides an avenue for additional research in heat activated cooling systems. One method to solve this problem without complex heat exchanger design models is to first calculate a baseline thermodynamic model, and then apply scaling factors to the heat exchanger *UAs* that can predict performance for any off-design condition. This modeling methodology could provide useful off-design insight for heat activated cooling systems, and could be extended to any thermodynamic system with heat exchangers. There has been one study, by Domanski and McLinden, which created a simplified refrigeration system model, named Cycle11, which uses fixed heat exchanger sizes and an entering temperature difference approach to calculate the saturation conditions in the heat exchangers. One issue with the Cycle11 model is the lack of robust compressor modeling that could led to inaccurate predictions [88].

As mentioned in Section 1.2 water consumption is a major issue for power plants, and one possible solution is to implement a waste heat recovery system that can produce a cooling effect while being powered by a low temperature exhaust stream. Although there are many possible heat activated cooling systems that could be used for this application, ORVC systems are one technology with performance and cost benefits that make it a strong potential candidate. However, the previous studies have been unable to maximize the potential of ORVCs.

2.3.1. Turbo-Compression Cooling

One other heat activated cooling system, similar to ORVCs, which has not been fully explored is a recuperative TCCS. The TCCS has similarities to the previously described ORVC systems. A simplified process flow diagram (PFD) for the TCCS is shown Figure 2-22.

The TCCS operates with a recuperative Rankine cycle (power cycle) directly coupled to a vapor-compression cycle (cooling cycle) through a magnetically coupled turbo-compressor. The power cycle has five main components: a pump, a dry air condenser, a recuperator, a turbine, and a waste heat boiler. The power cycle operates in the exact same manner as an ORVC discussed in Section 2.2.3, but a recuperator is added for efficiency benefits. The waste heat source is typically low-temperature exhaust gas added at the waste heat boiler and the condensers reject their heat to

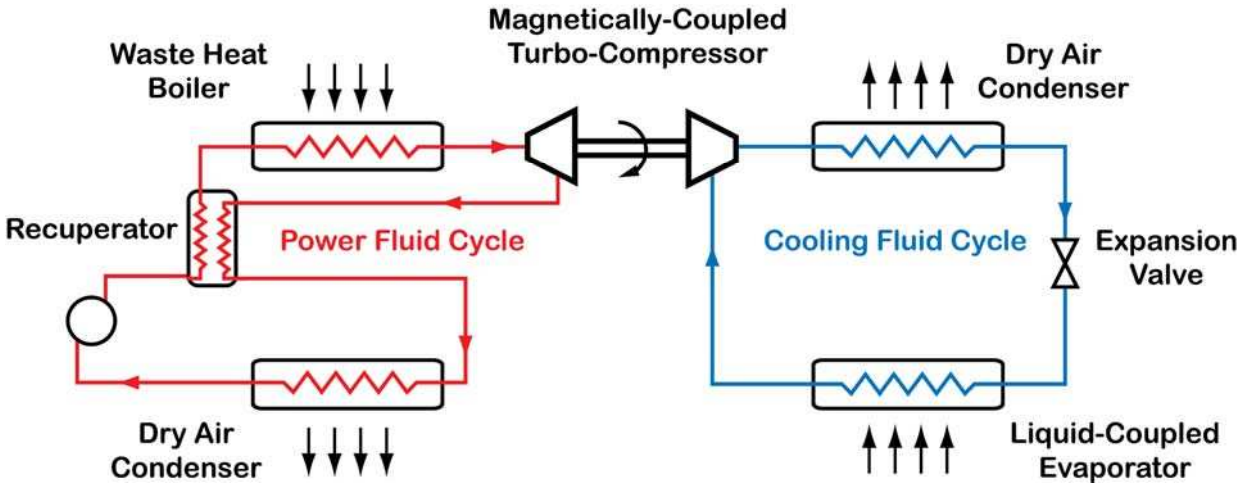

Figure 2-22. Basic PFD for the TCCS.

a dry air source. The cooling cycle is operated just like a vapor-compression cycle as discussed in Section 2.2.3. The cooling effect is generated at the cooling cycle evaporator. The turbine and compressor are connected on the same magnetically coupled shaft, so the power of the turbine is directly transmitted to the compressor with minimal efficiency losses. The magnetic coupling is a critical component to the design because it provides a hermetic shaft seal between the power and cooling cycles. This leak free seal allows for two separate fluids to be used on the power and cooling cycles which maximizes the efficiency of the turbine and compressor simultaneously. A turbo-compression cooling system where the turbine and compressor efficiencies are maximized simultaneously will be able to improve on previous ORVC designs by optimizing the fluid selection to drive a high COP.

There are several other benefits to the TCCS compared to other heat activated cooling technologies. The system has minimal complexity, moderate to low working pressures, and no corrosive working fluids. The selection of working fluids also allows the system to avoid crystallization issues that can effect absorption systems. Furthermore, the temperature range of the system is better than absorption and will allow the system to operate over high temperature waste heat streams without adding additional components. Finally, the system operation is simple, meaning the system can start-up and change operating conditions quickly. This is a distinct advantage over most other heat activated cooling technologies that usually require operation at a constant load.

2.4. Focus of Current Investigation

The current research seeks to improve upon state of the art heat activated cooling technologies, and investigate the integration of a TCCS into power plant cooling application. One distinct advantage of the TCCS compared to other ORVC systems is the magnetically coupled

turbo-compressor, which allows two separate fluids for the power and cooling cycles to maximize the turbine and compressor efficiencies simultaneously. In addition, highly effective aluminum brazed heat exchangers used in the system provide optimal heat transfer at a low cost. These two factors result in a system with a competitive COP at a potentially low cost. The TCCS also has a less complex system design than absorption and adsorption systems, and can be operated with benign fluids. The system also does not suffer crystallization issues that occur at high temperatures for absorption based systems. All of these factors demonstrate that the TCCS is a promising system for heat activated cooling. However, the performance of the system has not been fully exploited to date, and further investigation into its performance over a broad range of operating conditions is warranted. In this study, a performance methodology was created to make direct comparisons with the experimental approach. By validating the thermodynamic model with experimentation, the TCCS can overcome the deficiencies of current heat activated cooling technologies. The following chapter will fully describe the thermodynamic performance model used for experimental comparison.

CHAPTER 3. SYSTEM PERFORMANCE MODELING

As discussed in the previous chapter, the TCCS is one system that could have performance improvements over other heat activated cooling systems. The current study also seeks to determine the performance of the TCCS over a range of ambient temperatures and cooling loads and then make comparisons to experimental data. Although there have been many studies on various thermodynamic systems, very few have modeled these systems at off-design conditions with fixed heat exchanger sizes. The major issue with simulation at off-design conditions is that the heat exchanger sizes are generally fixed, but the conditions within the heat exchangers change. For this reason, complex heat exchanger modeling is required to predict the saturation temperatures and pressures in the heat exchangers. The change in saturation conditions often impacts the efficiency of system turbo-machinery, further increasing modeling complexity. The modeling approach presented in this study improves upon off-design prediction techniques by utilizing heat exchanger scaling and turbo-compressor efficiency methodologies to predict system performance without complex heat transfer models. This model can be used to make informed decisions on operation in off-design conditions and can help optimize thermodynamic systems.

In this chapter, the modeling approach is presented for a 250 kW_{th} cooling system which includes a turbo-machinery Cordier analysis and an optimal fluid selection process. The COP for the optimal design point is described for the system first. Next, the system is modeled for various mass flow rates and temperatures to create an off-design performance map. The performance map is used in Chapter 5 to make direct comparisons with the test results. The system performance model was written in Engineering Equation Solver (EES) in conjunction with the fluid thermodynamic and transport property database REFPROP Version 9.1 created by the National

Institute of Standards and Technology (NIST). A complete sample calculation for the model is shown in Appendix A.

3.1. Baseline thermodynamic state modeling

The model for the TCCS includes a set of thermodynamic equations linking the power and cooling cycles at a 250 kW_{th} cooling scale. This portion of the model was used to optimize the system during the test facility design. This optimization included a fluid selection process and Cordier analysis that allowed the system to meet the target COP of 2.1. The model includes pressure drop calculations for the major components and the fluid piping. Modeling was performed in conjunction with the design of the turbo-machine by Barber-Nichols (BNI) and the heat exchangers by Modine Manufacturing to ensure the results would be feasibly constructed. A process flow diagram is shown in Figure 3-1 and the state points used for modeling are shown in Tables 3-1 and 3-2. The process flow diagram provides a map to understand the thermodynamic modeling equations. The points selected in each cycle were chosen because they represent an

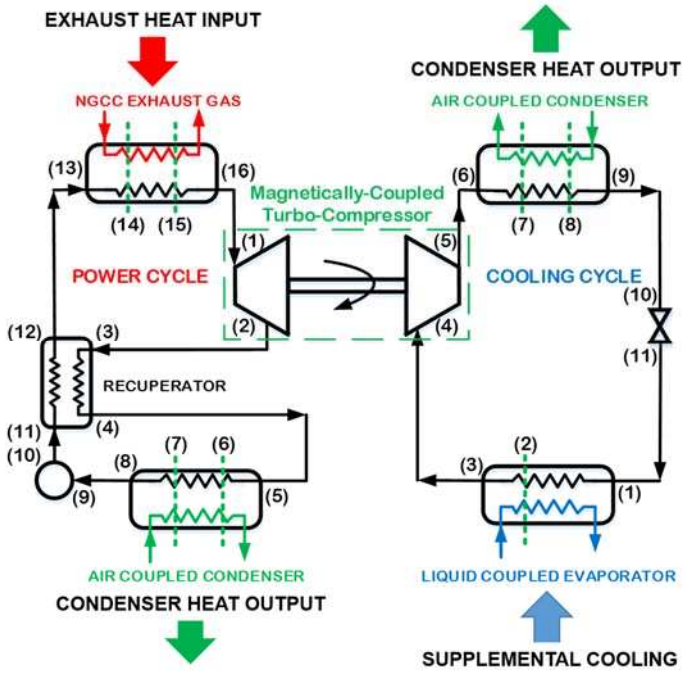

Figure 3-1. PFD showing the cycle state points used for sample calculations.

Table 3-1. Power cycle state points.

State Point	Location
1	Turbine Inlet
2	Turbine Outlet
3	Recuperator Inlet
4	Recuperator Outlet
5	Condenser Inlet
6	Condenser Saturated Vapor
7	Condenser Saturated Liquid
8	Condenser Outlet
9	Pump Inlet
10	Pump Outlet
11	Recuperator Inlet
12	Recuperator Outlet
13	Boiler Inlet
14	Boiler Saturated Liquid
15	Boiler Saturated Vapor
16	Boiler Outlet

Table 3-2. Cooling cycle state points.

State Point	Location
1	Evaporator Inlet
2	Evaporator Saturated Vapor
3	Evaporator Outlet
4	Compressor Inlet
5	Compressor Outlet
6	Condenser Inlet
7	Condenser Saturated Vapor
8	Condenser Saturated Liquid
9	Condenser Outlet
10	Expansion Valve Inlet
11	Expansion Valve Outlet

important state point required to understand system operation. There is a point at the inlet and outlet of each component so that the component can be modeled thermodynamically. Having a point at the inlet and outlet also gives a complete thermodynamic analysis of the connection lines. In addition to points at the inlets and outlets, the phase change heat exchangers are divided based on the phase change regions (sub-cooled, two-phase, and superheated). The boiler and condensers each have three regions, while the evaporator has a two regions. By dividing the heat exchangers into regions, the *UA* can be calculated per region which gives an approximation of the heat exchanger size.

In the following subsections, the assumptions and thermodynamic energy balance equations for the model are discussed first, which is then followed by a discussion of the turbo-machine Cordier analysis. These are then used to select an optimal fluid combination and system operation point that maximizes COP for the system. The final subsection describes how the design point is used to predict the heat exchanger *UA*s.

3.1.1. Assumptions

Many of the assumptions (Table 3-3) used in the baseline modeling approach are based on power plant operating conditions. The waste heat source conditions (106°C exhaust temperature, and 31,363 m^3 hr^{-1} flow rate) were based on 138:1 scale of a DOE/NETL Case 13 NGCC power plant [64]. In addition, the cooling water temperature was set at 17.2°C to 16°C and the ambient temperature was assumed to be 15°C to simulate the power plant conditions as shown in Figure 1-4. By using these conditions, a power plant simulation was performed to determine if the addition of the TCCS could provide *UA* savings in the replacement of evaporative cooling towers. The TCCS *UA* plus required dry air heat exchanger *UA* was compared with replacement of the evaporative cooling towers with a single dry air cooler. If the addition of a TCCS could reduce the dry-air heat exchanger *UA* significantly, then the technology would be feasible for power plant applications. Subcritical and supercritical Rankine cycle turbo-compression cooling systems (TCCSs) were compared and the results are shown in Figure 3-2. The results of the simulation show that for a COP of 2, the dry air heat exchanger *UA* was reduced by 26% (i.e., 111 MW K^{-1} from 150 MW K^{-1}) as compared with a baseline dry air condenser [6]. The results of the study also

Table 3-3. TCCS assumptions derived from scaled version of DOE/NETL Case 13 power plant operating conditions.

Component	***Assumption***
Waste Heat Boiler	T_{exh} = 106°C $\dot{V}_{exh}$ = 31,363 m^3 hr^{-1}
Evaporator (Liquid Coupled)	$\dot{Q}_{c,e}$ = 250 kW $T_{e,g,in}$ = 17.2°C $T_{e,g,o}$ = 16°C
Ambient temperature	T_{amb} = 15°C
System COP	*COP* = 2.1

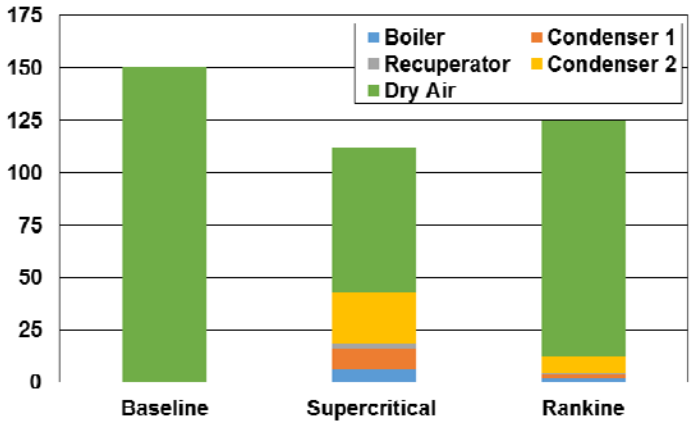

Figure 3-2. Dry air heat exchanger *UA*s for evaporative cooling tower replacement for a single dry air heat exchanger (baseline), a supercritical TCCS, and a subcritical TCCS.

show that the system COP must be high to make the power plant application feasible. For this research, the target COP was set at 2.1 under the power plant operating conditions.

The operating conditions for the baseline thermodynamic system modeling are listed in Table 3-4. These conditions are the necessary inputs required to solve the thermodynamic model and meet the required power plant assumptions made in Table 3-3. The conditions were determined based on discussions with Barber-Nichols and Modine Manufacturing and the components described in Chapter four were designed to meet the design criteria. The temperatures of the power cycle boiler outlet temperature, boiler liquid saturation condition, and condenser outlet temperature were all fixed: 103.5°C, 92.5°C, and 23.9°C, respectively. The temperatures of the chilled water were assumed to enter and exit the liquid-coupled evaporator at 17.2°C and 16°C, respectively. The cooling cycle condenser and evaporator saturation conditions were set at 23.2°C and 13.9°C, respectively. In addition, the sub-cooling condition out of the condenser was set to 22.7°C and the superheating condition out of the evaporator was set to 16.3°C. All of the pressure drops for the heat exchangers were based on Modine Manufacturing estimates to approximate realistic system performance, and the pressure drop in the connecting lines was assumed to be 1 kPa. The

Table 3-4. Operating conditions for baseline thermodynamic cycle and heat exchanger *UA* modeling.

Component	***Assumption***
Waste Heat Boiler	$\Delta P_{b,sc}$ = 0.2 kPa $\Delta P_{b,tp}$ = 1.2 kPa $\Delta P_{b,sh}$ = 0.2 kPa $\Delta P_{p,exh}$ = 0.2 kPa $T_{p,b,sat}$ = 92.5°C $T_{p,b,sh}$ = 103.5°C
Evaporator (Liquid Coupled)	$\Delta P_{e,tp}$ = 19 kPa $\Delta P_{e,sh}$ = 1 kPa $\Delta P_{e,g}$ = 30.2 kPa $T_{e,sat,o}$ = 13.9°C $T_{e,sh}$ = 16.3°C
CC Condenser (Air Cooled)	$\Delta P_{c,cond,sh}$ = 0.2 kPa $\Delta P_{c,cond,tp}$ = 1.71 kPa $\Delta P_{c,cond,sc}$ = 0.2 kPa $T_{c,cond,sat,o}$ = 23.2°C $T_{c,cond,sc}$ = 22.7°C $\dot{V}_{c,cond,a}$ = 135,000 m^3 hr^{-1}
PC Condenser (Air Cooled)	$\Delta P_{p,cond,sh}$ = 1 kPa $\Delta P_{p,cond,tp}$ = 8.8 kPa $\Delta P_{p,cond,sh}$ = 1 kPa $T_{p,cond,sat,o}$ = 23.9°C $T_{p,cond,sc}$ = 23.1°C $\dot{V}_{p,cond,a}$ = 39,000 m^3 hr^{-1}
Recuperator	$\Delta P_{r,liq}$ = 1.45 kPa $\Delta P_{r,vap}$ = 4.74 kPa $T_{p,cond,sh}$ = 2°C
Line pressure drops	ΔP = 1 kPa
Component Efficiencies	$\eta_{p,pump}$ = 32% $\eta_{p,bf}$ = 45% $\eta_{p,gp}$ = 45%
Turbo-machine	η_t = 80% η_{comp} = 80% η_{shaft} = 93% N = 30,000 RPM

compressor and turbine efficiencies were both assumed to be 80% and the Cordier calculations in Section 3.1.3 validate this assumption. Because the turbine and compressor both operate on the same shaft, the speed of the two are equal, and, based on BNI design experience the mechanical

transmission efficiency from the turbine to the compressor was assumed to be 93% for the magnetic coupling. Finally, the component efficiencies for the power cycle pump, boiler circulation fan, and glycol pump were set to calculate the power requirement for each. With these parameters set, enough information is given to proceed with the basic thermodynamic modeling.

3.1.2. Baseline Thermodynamic Analysis

The thermodynamic state for the baseline case was determined by using the assumptions listed in Table 3-3. The fluids modeled in the baseline analysis were HFE-7000 and R152a for the power and cooling cycles, respectively. A description of the fluid selection process is outlined in Section 3.1.4. The process flow diagram (Figure 3-1) and cycle state points (Table 3-1 and Table 3-2) provide a summary for the baseline thermodynamic analysis. A temperature-entropy diagram showing the cycle is provided (Figure 3-3) for provide further clarity. As is noted in Table 3-4, there are several temperature inputs required to solve the thermodynamic system. The most important temperatures are the saturation conditions for the waste heat boiler, the power and cooling cycle condensers, and the chiller. These temperatures are important because they set the state points around the cycle which allows the entire system to be solved. If the saturation temperatures of each heat exchanger are set, the pressure can be found at the saturated liquid and

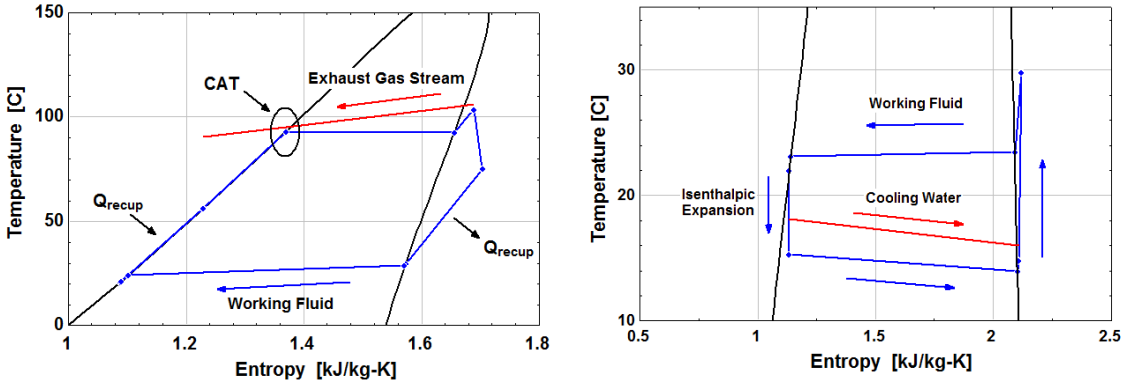

(a) **(b)**

Figure 3-3. Temperature-entropy diagrams for the Rankine TCCS powered by a waste heat source while providing chilled water at 16°C and an ambient temperature of 15°C: **(a)** Power fluid HFE7000 **(b)** Cooling fluid R152a.

vapor dome by using that temperature and a quality (i.e., 0 at saturated liquid and 1 at saturated vapor). The pressure is used with the pressure drop inputs of the components to resolve each state point around the heat exchangers. The pressures are also useful because they set the pressure ratio for the turbine and compressor and allow the turbo-machine efficiency, size, and spin speed to be calculated. The following discussion describes the order in which the thermodynamic state is resolved.

The first step is to determine the cooling cycle mass flow rate by an energy balance at the cooling cycle evaporator:

$$\dot{Q}_{c,e} = \dot{m}_c \left(h_{c,3} - h_{c,1} \right) \tag{3.1}$$

The vapor saturation and outlet superheating temperatures are inputs set at 13.9°C and 16.3°C, respectively. By using the saturation pressure at the vapor region (quality of 1) and subtracting the pressure drop through the superheated region, the enthalpy at the outlet of the evaporator is found ($h_{c,3}$) via a property relationship. The inlet enthalpy is found by using the saturation pressure and by assuming an ideal enthalpy change across the expansion valve.

$$h_{c,10} = h_{c,11} \tag{3.2}$$

The enthalpy at the expansion valve inlet ($h_{c,11}$) is found by using a property relationship at the cooling cycle condenser outlet. The CC condenser liquid saturation temperature is used to find the pressure and the sub-cooling temperature at the condenser exit is used to find the temperature. Now that the enthalpy at the inlet and outlet of the evaporator is known, and by using the assumed evaporator heat duty, the CC mass flow rate is found.

The next step is to determine the compressor work by applying an energy balance across the compressor.

$$\dot{W}_{c,comp} = \dot{m}_c \left(h_{c,5} - h_{c,4} \right) \tag{3.3}$$

The compressor inlet enthalpy ($h_{c,4}$) is known from the evaporator outlet conditions while including the pressure drop across the connecting line (assumed to be 1 kPa). The mass flow is known from equation (3.1), so the remaining parameter is the enthalpy at the outlet which relies on the compressor isentropic efficiency.

$$\eta_{c,comp} = \frac{\left(h_{c,s,5} - h_{c,4}\right)}{\left(h_{c,5} - h_{c,4}\right)} \tag{3.4}$$

Since the compressor efficiency is an assumption and the ideal enthalpy at the outlet ($h_{c,s,5}$) is found from the inlet conditions and outlet pressure, the outlet enthalpy ($h_{c,5}$) can be calculated. Equation (3.3) is solved to find the compressor work. The compressor outlet condition now allows the heat duty for the CC condenser to be calculated using conservation of energy:

$$\dot{Q}_{c,cond} = \dot{m}_c \left(h_{c,6} - h_{c,9}\right) \tag{3.5}$$

The individual section (sub-cooled, two-phase, or superheated) heat duties for the cooling cycle are found by applying an energy balance as shown in the general equation below:

$$\dot{Q}_{sec} = \dot{m}\Delta h_{sec} \tag{3.6}$$

Now that the CC state points are known, the next step is to determine the power cycle conditions. The turbine work is found by dividing the compressor work by the shaft efficiency:

$$\dot{W}_t = \frac{\dot{W}_c}{\eta_{shaft}} \tag{3.7}$$

The PC mass flow rate is calculated by applying an energy balance at the turbine.

$$\dot{W}_t = \dot{m}_p \left(h_{p,1} - h_{p,2}\right) \tag{3.8}$$

The inlet and outlet enthalpies require calculation since the turbine work is found from equation (3.7). The inlet enthalpy is found from the inputs made at the PC boiler heat exchanger. The pressure at the turbine inlet is found by knowing the liquid saturation pressure (from saturation temperature at quality of 0) and the pressure drop through the heat exchanger sections and

connection lines (1.2 + 0.2 + 1 kPa for tp, sh, and lines, respectively). The temperature at the inlet is set as the superheating temperature from the boiler. Using the inlet temperature and pressure, the enthalpy at the inlet of the turbine is found using the property relationships. The outlet enthalpy is found by using the isentropic efficiency across the turbine.

$$\eta_{\mathrm{t}} = \frac{\left(h_{\mathrm{p},1} - h_{\mathrm{p,s},2}\right)}{\left(h_{\mathrm{p},1} - h_{\mathrm{p},2}\right)} \tag{3.9}$$

The turbine efficiency is an assumption (80%), and the ideal enthalpy at the outlet ($h_{\mathrm{p,s},2}$) is found by a property relation with the outlet pressure (found from setting saturation pressure at condenser and including pressure drops through components) and the inlet conditions. From these to values, the outlet enthalpy ($h_{\mathrm{p},2}$) is calculated. Now that the outlet enthalpy is known, equation (3.8) is used to find the PC mass flow rate.

The recuperator heat duty is the next component calculation because the vapor inlet and outlet states are known from equation (3.9) and the PC condenser superheated temperature input, respectively.

$$\dot{Q}_{\mathrm{p,recup}} = \dot{m}_{\mathrm{p}}\left(h_{\mathrm{p},3} - h_{\mathrm{p},4}\right) \tag{3.10}$$

The heat exchanger calculations in Section 3.1.5 show the recuperator effectiveness is realistic. Now, the PC condenser heat duty is determined by employing an energy balance.

$$\dot{Q}_{\mathrm{p,cond}} = \dot{m}_{\mathrm{p}}\left(h_{\mathrm{p},5} - h_{\mathrm{p},8}\right) \tag{3.11}$$

Since everything on the right hand side (RHS) of the equation is known or is found through property relationships (based on temperature inputs), the heat duty of the PC condenser calculated. The PC boiler heat duty is calculated in a similar manner by applying an energy balance with known inlet and outlet conditions.

$$\dot{Q}_{\mathrm{p,b}} = \dot{m}_{\mathrm{p}}\left(h_{\mathrm{p},16} - h_{\mathrm{p},13}\right) \tag{3.12}$$

The enthalpy at the liquid inlet of the recuperator ($h_{p,11}$) is calculated because the recuperator heat duty is already known (equation (3.10)) and the outlet enthalpy ($h_{p,12}$) is known from the boiler inlet state and the pressure drop through the connection lines.

$$\dot{Q}_{p,recup} = \dot{m}_p \left(h_{p,12} - h_{p,11} \right) \tag{3.13}$$

The final step to complete the state points is it to determine the work across the PC pump by an energy balance.

$$\dot{W}_{p,pump} = \dot{m}_p \left(h_{p,9} - h_{p,10} \right) \tag{3.14}$$

The inlet and outlet enthalpies of the pump were determined from the known inlet and outlet conditions of the recuperator and condenser. The individual section (sub-cooled, two-phase, or superheated) heat duties for the power cycle are found in a similar manner as the cooling cycle, by applying equation (3.6).

Now that the thermodynamic state points are known for the power and cooling cycles, the COP is calculated with the following equation.

$$COP = \frac{\dot{Q}_{c,evap}}{\dot{Q}_{p,b} + \dot{W}_{p,pump} + \dot{W}_{aux}} \tag{3.15}$$

The CC evaporator heat duty is an assumption, the PC boiler heat duty is calculated from equation (3.12), the pump work is found through equation (3.14), and the auxiliary power ($\dot{W}_{aux}$) is a summation of the auxiliary power loads of the TCCS (boiler fan, condenser fans, glycol pump).

$$\dot{W}_{aux} = \dot{W}_{p,bf} + \dot{W}_{p,cf} + \dot{W}_{c,cf} + \dot{W}_{c,gp} \tag{3.16}$$

The condenser fan power is a summation of the number of fans required ($No_{p,cf} = 2$ and $No_{c,cf} = 6$) and the power requirement for each fan ($\dot{W}_{p,cf}$ = 0.915 kW and $\dot{W}_{c,cf}$ = 1.13 kW).

$$\dot{W}_{cf,total} = No_{cf} \dot{W}_{cf} \tag{3.17}$$

The boiler fan and glycol pump power are calculated by dividing the ideal head by the efficiency.

$$\dot{W} = \frac{\dot{V}\Delta P}{\eta} \tag{3.18}$$

The volumetric flow rate, pressure drop, and efficiency are all specific inputs which allows for easy calculation. Once the power of each auxiliary component is known, the total auxiliary power is found with equation (3.16), and then the COP is calculated with equation (3.15). Calculation of the thermodynamic state points provides the required information to determine the performance of the turbine and compressor.

3.1.3. Turbo-Machine Cordier Analysis

After the thermodynamic state points are determined, a Cordier analysis was performed to validate the efficiency assumptions (η = 80%) for the turbine and compressor. The Cordier analysis is a turbo-machine prediction technique that employs an empirical chart to relate the diameter, flow rate, isentropic head, and speed of a turbo-machine to the efficiency. The charts are plotted on a log scale with the specific speed (Ns) on the x-axis and the specific diameter (Ds) on the y-axis. The specific speed and specific diameter equations are shown below and are fucnctions of actual speed, diameter, volumetric flow rate, and head:

$$Ns = \frac{N\sqrt{\dot{V}}}{H^{3/4}} \tag{3.19}$$

$$Ds = \frac{DH^{1/4}}{\sqrt{\dot{V}}} \tag{3.20}$$

BNI has generated plots for compressors and turbines using the equations above which are shown in Figure 3-4 and Figure 3-5. By knowing the specific speed and specific diameter, a point is placed on the chart which will fall within a contour that approximates the efficiency given the flow characteristics. For this research, the target efficiency for both the turbine and compressor is 80%. The 80% contour line is highlighted in Figure 3-4 and Figure 3-5. The density used to calculate

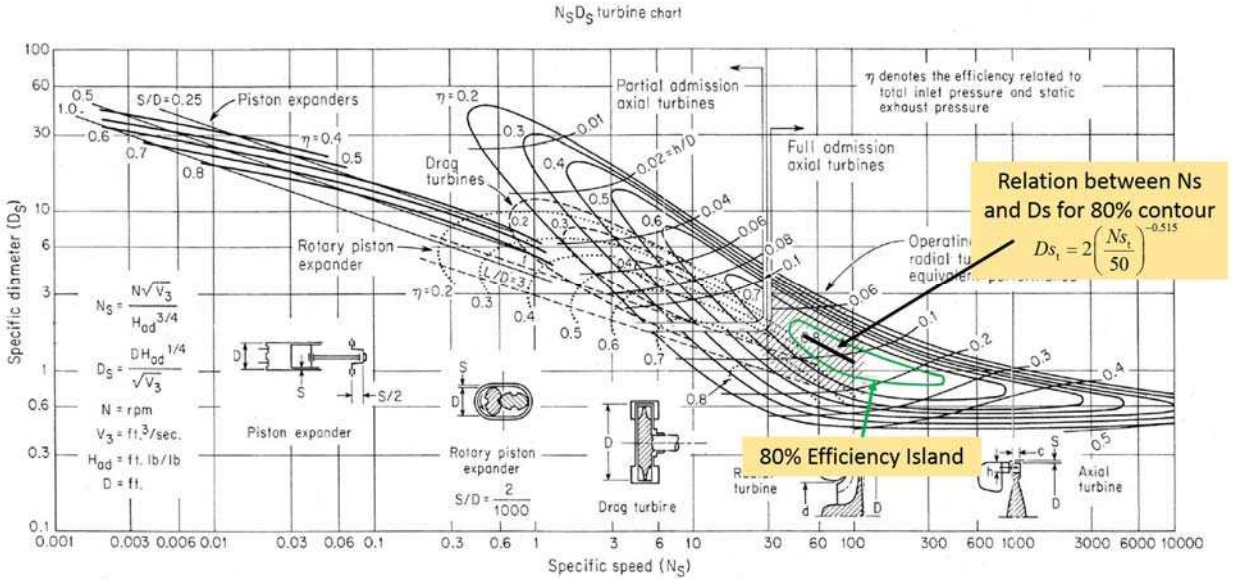

Figure 3-4. Empirically generated turbine Ns-Ds chart for Cordier analysis [1].

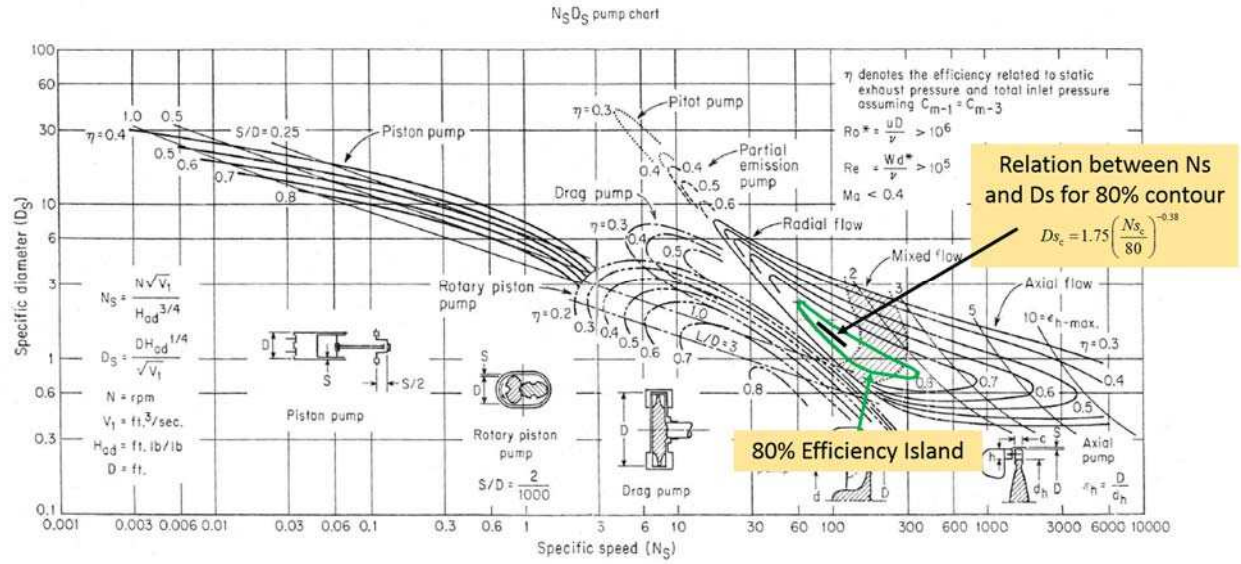

Figure 3-5. Empirically generated compressor Ns-Ds chart for Cordier analysis [1].

volumetric flow in equations (3.19) and (3.20) are calculated using the inlet conditions for compressors and the outlet condition for turbines.

In the present modeling approach, the efficiency for the turbine and compressor were first assumed to be 80% to complete the thermodynamic evaluation. Next, it was appropriate to determine the actual efficiency for comparison by calculating the specific speed and specific diameter and finding the location on the BNI charts. The specific speed and diameter equations

are also useful because they can provide the approximate key dimensions of the turbo-machine for comparison with the BNI design.

The first step is to determine the volumetric flow rate at the turbine outlet by dividing the PC mass flow rate by the density (determined from property relationship).

$$\dot{V}_{\mathrm{p},2} = \frac{\dot{m}_{\mathrm{p}}}{\rho_{\mathrm{p},2}} \tag{3.21}$$

The units for the volumetric flow rate for the diagrams is $ft^3\ s^{-1}$, and appropriate unit conversions should be applied. The adiabatic head for the turbine is calculated using the equation below:

$$H_{\mathrm{t}} = \left(h_{\mathrm{p},1} - h_{\mathrm{p,s},2}\right) \tag{3.22}$$

The units for the ideal head of the turbine are $ft^2\ s^{-2}$, and appropriate conversions should be applied. Now that the ideal head and volumetric flow rate at the outlet are known and the specific speed is assumed, the specific speed is computed using equation (3.19). The units for specific speed are $ft^{3/4}\ lbm^{3/4}\ min^{-1}\ s^{-1/2}$.

The specific speed is related to the specific diameter by an empirical correlation. The correlation describes the approximate relationship between specific speed and diameter for "good" turbo-machines. In this modeling approach, the black line on Figure 3-4 shows the turbine correlation lies within the 80% efficiency contour as follows:

$$Ds_{\mathrm{t}} = 2\left(\frac{Ns_{\mathrm{t}}}{50}\right)^{-0.515} \tag{3.23}$$

The diameter for the turbine, in ft, can now be determined by employing equation (3.20). The calculated specific speed and diameter are used to read the Cordier diagram and determine if the turbine will operate within the predicted 80% efficiency contour.

The compressor specific speed and diameter equations are calculated similarly to the turbine, but, the volumetric flow rate is calculated at the inlet instead of the outlet:

$$\dot{V}_{c,4} = \frac{\dot{m}_c}{\rho_{c,4}} \tag{3.24}$$

The adiabatic head for the compressor is calculated using the equation below:

$$H_c = \left(h_{c,s,5} - h_{c,4} \right) \tag{3.25}$$

The units for the ideal head of the compressor should be in $ft^2\ s^{-2}$ so appropriate conversions should be applied. Now that the ideal head and volumetric flow rate at the outlet are known and by using the speed assumption, the specific speed is computed using equation (3.19). The units for specific speed are $ft^{3/4}\ lbm^{3/4}\ min^{-1}\ s^{-1/2}$.

Next, similar to the turbine, there is an empirical correlation for compressors that relates the specific speed and diameter for "good" turbo-machines. As is shown in Figure 3-5, the correlation lies in the center of the 80% efficiency contour and is described by the equation below:

$$Ds_c = 1.75 \left(\frac{Ns_c}{80} \right)^{-0.38} \tag{3.26}$$

Equation (3.20) for specific diameter is used to calculate the actual diameter of the compressor, in ft. The calculated diameter is used for comparison with the actual compressor design by BNI. The calculated specific speed and diameter are used to iterate the compressor Cordier diagram and determine if the turbine will operate within the assumed 80% efficiency contour.

If either the turbine or compressor were not within the designated efficiency contours, the cycle conditions require modification, or different fluids were selected to ensure the turbo-machine was operating at optimal performance. The fluid selection for both cycles was the most critical aspect to achieving a high efficiency system and the procedure for selection is described in the following section.

3.1.4. Fluid Selection Process

The fluid selection for the TCCS was performed by analyzing all of the fluids in the Engineering Equation Solver and REFPROP databases. The fluid combinations were narrowed based on a set of reduction criteria presented in this section. The first step in the fluid selection process was to analyze single fluid options with the turbine and compressor operating on the same shaft. The aforementioned thermodynamic modeling approaches were applied while assuming the same power and cooling cycle fluid. The turbine and compressor isentropic efficiencies were both assumed to be 80% and a Cordier analysis was performed for each fluid. Based on the turbine and compressor efficiency plots (Figure 3-4 and Figure 3-5), the range for the specific speed to be within the 80% efficiency contour was 80 to 140 and 45 to 100 for compressors and turbines, respectively. By setting the compressor specific speed to 140, the maximum turbine specific speed would be calculated. The result of the single fluid analysis was that no single fluid was met the target turbine specific speed range because the high pressure ratio across the turbine yielded a low speed. Figure 3-6 shows several representative fluids where the specific turbine speed was unable to reach the required threshold (45) to achieve an 80% isentropic efficiency. At this point, two

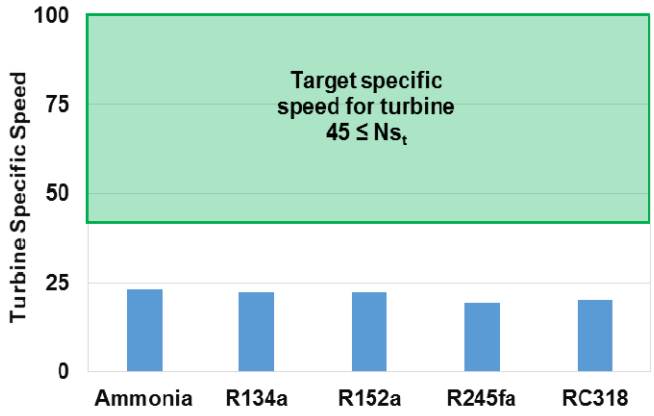

Figure 3-6. Turbine specific speeds for several representative fluids at a compressor specific speed of 140 [6].

options were evaluated as solutions to the efficiency problem: a single fluid with speed change via gearing and using two different fluids.

The main criteria used to evaluate these two solutions is presented in Table 3-5. The COP target for power plant cooling was 2.1, so the first criteria was to eliminate low COP solutions. The second criteria is to keep the compressor pressure ratio below 2.5. This limit was implemented to reduce the high side refrigerant pressure in the system, and to help the performance of the bearings. At pressure limits above 2.5, ball bearings used in the turbo-compressor in the present study begin to wear down at an appreciably higher rate, and an alternate bearing configuration would be required. The next elimination criteria was related to the speed and specific speed of the turbo-machine. For the single fluid applications with a gear box, the speed for either side was limited to 100,000 RPM when the specific speed of the compressor was set at the lowest limit of 80. This limit kept the speed from exceeding BNI's design experience for operating speed. The dual fluid criteria are set to keep the efficiency within the desired range, and to keep the speed under 50,000 RPM. The speed is reduced for the dual fluid application due to the magnetic coupling between the turbine and compressor. Barber-Nichols does not have design experience at high speeds with a magnetic coupling, where shaft decoupling is more likely to occur. The final criteria are the turbine and compressor diameters. If the diameter of the turbo-machine becomes too small, efficiency losses tend to be significant. One of the main losses for small wheel sizes is

Table 3-5. Fluid elimination criteria for the TCCS.

Variable	Criteria
COP	< 2.1
Pressure ratio, compressor	> 2.5
Specific turbine speed, dual fluid	≥ 100 when Nsc = 80
	≤ 45 when Nsc = 140
	≤ 45 when Speed = 50,000 RPM
	$\geq 25{,}000$ RPM when Nsc = 80
Single fluid turbine speed	$\geq 100{,}000$ RPM when Nsc = 80
Single fluid compressor speed	$\geq 100{,}000$ RPM when Nsc = 80

windage at the blade tip due to the relatively small tip clearances compared to the blade length. If the blades become too small compared to the clearances, manufacture of the wheels becomes difficult as well.

The modeling approach also accounted for the pressure drop through the heat exchangers. In some cases, the pressure drop had a significant impact on COP because high pressure drops change the properties at the outlet of the heat exchangers. In one early modeling condition with fluids HFE7100 and R1234ze(Z), the COP decreased from 2.25 to 1.35 as the cooling cycle evaporator pressure drop increased from 0 to 30 kPa (Figure 3-7). Similar effects occurred for the other heat exchangers as well with the power cycle condenser having a large impact on performance.

The single fluid option uses a gear box so the turbine can spin faster than the compressor. By applying the fluid selection criteria and using realistic heat exchanger pressure drops, the single fluid combinations were narrowed to several options presented in Table 3-6. Each option met the required criteria, but the diameters of the turbine and compressor were small because the enthalpy

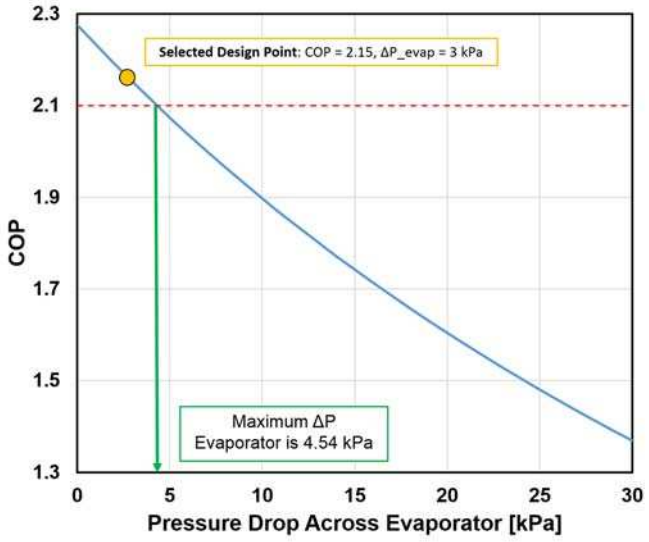

Figure 3-7. COP decrease due to cooling cycle evaporator pressure drop for fluids HFE7100 (power) and R1234ze(Z) (cooling).

Table 3-6. Single fluid combinations with gear reduction at 250 kW_{th}, a compressor specific speed of 120, and a turbine specific speed of 50.

Fluid	COP	Speed Ratio [RPM]	Speed Comp [RPM]	Speed Turb [RPM]	PC Mass Flow [kg/s]	CC Mass Flow [kg/s]	Turb. Diam. [in]	Comp. Diam. [in]	ΔP PC Cond. [kPa]	ΔP CC Evap. [kPa]
SES36	2.21	0.39	15,080	38,667	0.33	0.93	1.35	2.97	20	3
r245fa	2.16	0.39	25,078	64,301	0.30	0.81	0.96	2.06	20	4
R1233zd(E)	2.17	0.39	23,374	59,934	0.29	0.80	1.02	2.21	20	3
R1234ze(Z)	2.15	0.40	28,300	70,749	0.27	0.85	0.89	1.88	20	4
R236ea	2.17	0.39	24,475	62,757	0.36	1.0	0.89	1.89	20	4
R236fa	2.11	0.40	26,444	66,110	0.39	1.1	0.81	1.70	20	6
R1234ze(E)	2.12	0.40	38,150	95,376	0.35	0.95	0.60	1.25	20	7

change across each side of the turbo-machine was small. Even though the pressure ratios were fairly large, the enthalpy change across the turbine was small. The volumetric flow rate was not high enough to compensate for this low flow rate, and, as a result, the turbine spins at a high rate and a small diameter. In addition, although the gear boxes are highly efficient, they require oil and are not necessarily leak free. Due to the lack of hermetic seal, oil could leak into either cycle, thus degrading performance and requiring complex oil circulation equipment. As a result, two fluid options were explored.

To create a hermetic seal, a synchronous magnetic coupling can be used. Based on the advice from Barber-Nichols, the speed was limited to less than 30,000 RPM to ensure that the mechanical power transmission efficiency between the turbine and the compressor is sufficiently high. The results for a few fluid combinations at the 250 kW_{th} design case are shown in Table 3-7. Dual fluids were the only options considered due to the complications involved with the gearing for a single fluid application. At the 250 kW_{th} scale, few fluid combinations met the turbo-machine size and COP requirements. One fluid combination that met all requirements was HFE-7000 for the power cycle and R152a for the cooling cycle. The combination had specific speeds for the turbine and compressor of 62.1 and 107.1 ($ft^{3/4}$ $lbm^{3/4}$ min^{-1} $s^{-1/2}$), respectively, which both fell

Table 3-7. Dual fluid combinations at 250 kW_{th}.

Power Fluid	Cooling Fluid	COP	Turb. Specific Speed	Comp. Specific Speed	PC Mass Flow [kg/s]	CC Mass Flow [kg/s]	Turbine Diam. [in]	Comp. Diam. [in]	ΔP CC Cond. [kPa]	ΔP CC Evap [kPa]
R114	R152a	2.25	41.0	107.1	0.61	0.92	3.36	3.90	16	20
R236fa	R152a	2.05	39.8	107.1	0.61	0.92	3.30	3.90	16	20
HFE7000	R152a	2.10	62.1	107.1	0.61	0.92	4.09	3.90	16	20
R245fa	R152a	2.17	42.0	107.1	0.61	0.92	2.6	3.90	16	20

within the ideal range to meet the 80% efficiency contour. The specific diameter for the turbine and compressor were 1.79 and 1.57 ($lbf^{1/4}$ $s^{1/2}$ $lbm^{-1/4}$ $ft^{-1/4}$), respectively. The wheel diameters for the turbine and compressor were 4.05 in and 3.86 in, respectively, with a power transfer of 12.4 kW. The mechanical transmission losses were calculated by BNI to be 804 W which provides a mechanical efficiency of 93%. The primary transmission losses at full load are windage on the wheels (i.e., 285 W and 90 W for the turbine and compressor, respectively), shaft bearing viscous fluid drag (i.e., 146 W and 105 W for the turbine and compressor, respectively), and windage around the magnetic coupling (i.e., 98 W and 80 W for the turbine and compressor, respectively). The fluid selection process resulted in determining optimal fluids used in the thermodynamic cycle. The final step to modeling the baseline case was to find each of the heat exchanger *UA*s.

3.1.5. Heat Exchanger *UA* Calculations

After the baseline thermodynamic conditions were set for the two working fluids, the next phase in the modeling approach was to calculate the overall thermal conductance (*UA*) for each heat exchanger. The *UA* for a heat exchanger is the overall heat transfer coefficient (*U*) multiplied by an area (*A*), and it provides a proxy for heat exchanger size without employing detailed heat transfer correlations. The *UA* is useful for this research because once the basic thermodynamic calculation is made, the off-design performance is found by scaling the *UAs* based on the new operation conditions. Hand calculations for the heat exchangers are shown in Appendix A.

In this modeling approach, the $\varepsilon - NTU$ method for determining heat exchanger *UA* was used, as shown below [89]:

$$UA = NTU \times C_{min} \tag{3.27}$$

The number of transfer units (*NTUs)* are calculated separately for each heat exchanger using correlations based on the style (i.e., cross-flow, counterflow, etc.) and operating regime (i.e., sub-cooled, two-phase, or superheated) of the particular heat exchanger. The heat exchanger configurations are shown in Figure 3-8. The condensing heat exchangers are a single pass cross-flow arrangement. The flow enters as a superheated vapor, transitions to a two-phase flow. The two-phase mixture then returns back to the first header using a baffle in the second header. When the fluid exits the heat exchanger, it is a subcooled liquid. The boiler heat exchanger is a similar style cross flow heat exchanger, but in a two pass arrangement. The subcooled liquid at the inlet is heated as it travels through the passes and exits as a superheated vapor at the outlet. In both of these cases the secondary flow is air that passes through the finned tube gaps. The chiller and recuperator are both globally counterflow heat exchangers. The primary flow enters the heat exchanger and flows straight through, while the secondary fluid snakes through a series of channels as it travels to the outlet. For the chiller, the fluid passes through multiple cross flow passages, but the two fluids – the cooling cycle fluid and the power plant cooling water – flow in global counter flow to one another.

The *NTUs* are found by correlations depending on the style and fluid regime of the heat exchanger. The condensers and boiler are cross-flow dry air condensers that operate in two different regimes: between dry air and a single-phase fluid, and between dry air and a two-phase working fluid. For the two-phase section, the *NTU* is calculated as follows:

$$NTU_{tp} = -\ln\left(1 - \varepsilon_{tp}\right) \tag{3.28}$$

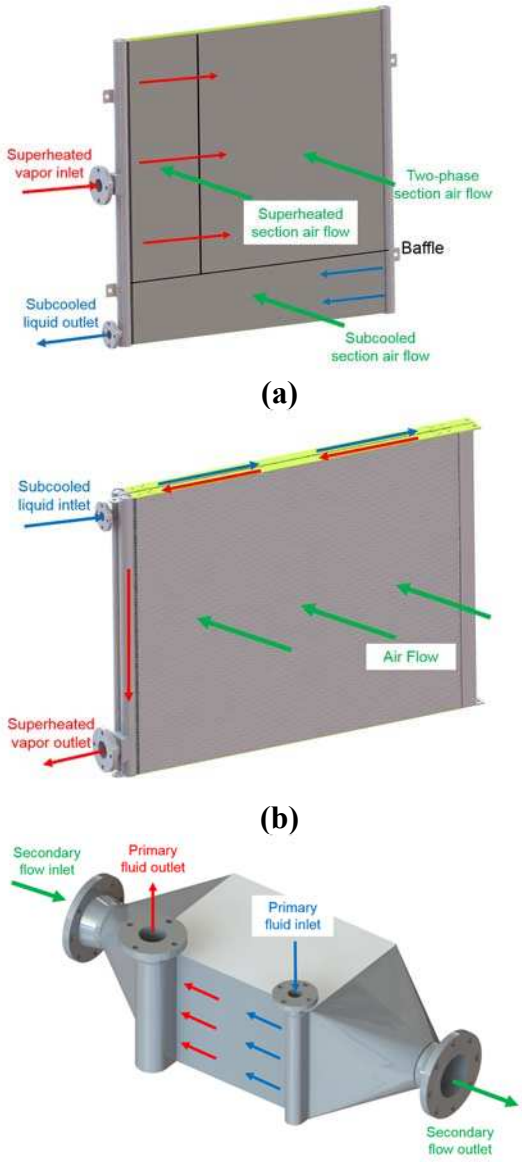

Figure 3-8. Heat exchanger designs for **(a)** single pass cross-flow (condensers), **(b)** two-pass cross-flow (boiler), and **(c)** cross-counterflow (recuperator and chiller).

The NTUs for the single phase regions are determined iteratively by the following equation and assuming both fluids are unmixed:

$$\varepsilon_{da} = 1 - \exp\left\{\frac{NTU^{0.22}}{Cr}\left[\exp\left(-CrNTU^{0.78}\right) - 1\right]\right\} \tag{3.29}$$

The CC evaporator, PC boiler, and recuperator are all counter-flow heat exchangers, and, thus, employ different correlations relating effectiveness and *NTUs*. The two-phase regions for the CC evaporator and PC boiler are calculated in the same manner as the cross-flow. The single-phase regions, however, are calculated as follows:

$$NTU_{sp} = \begin{cases} \dfrac{\varepsilon_{sp}}{1-\varepsilon_{sp}} & for\ Cr_{sp} = 1 \\ \dfrac{1}{Cr_{sp}-1}\ln\left(\dfrac{\varepsilon_{sp}-1}{\varepsilon_{sp}Cr_{sp}-1}\right) & for\ Cr_{sp} \neq 1 \end{cases} \tag{3.30}$$

Each of the *NTU* correlations shown above require a calculation of heat capacity ratio and effectiveness. The heat capacity ratio (*Cr*) is defined as the ratio between the minimum and maximum heat capacity ratios as follows:

$$Cr = \frac{C_{min}}{C_{max}} \tag{3.31}$$

The heat exchanger effectiveness (ε) for each section was calculated using equation (3.32) and the heat capacity ratio was calculated using equation (3.31).

The effectiveness for each heat exchanger region is found as follows:

$$\varepsilon = \frac{\dot{Q}}{C_{min}\left(\Delta T_{in}\right)} \tag{3.32}$$

where the heat duty ($\dot{Q}$) and temperature difference (ΔT) are determined from the basic thermodynamic modeling, and the minimum heat capacity rate (C_{min}) is determined by comparison between primary and secondary sides:

$$C_{min} = \dot{m}\ Cp \tag{3.33}$$

The primary fluid for the boiling and condensing heat exchangers is always the working fluid for the cooling and power cycles. The secondary fluid for the boiler, chiller, and condensers are the exhaust air, a 30:70 mixture of propylene-glycol:water, and the ambient air, respectively.

Table 3-8. Baseline modeling area percentages for cross-flow heat exchangers.

Heat Exchanger Section	Area Percentage
Waste Heat Boiler	
Sub-cooled	0.15
Two-Phase	0.49
Superheated	0.36
Power Cycle Condenser	
Superheated	0.02
Two-Phase	0.91
Sub-cooled	0.07
Cooling Cycle Condenser	
Superheated	0.02
Two-Phase	0.87
Sub-cooled	0.11

For the recuperator in the power cycle, the primary flow is the vapor phase working fluid flowing to the condenser, and the secondary flow is liquid phase flowing to the boiler. The secondary side mass flow rate for each fluid section is calculated differently for cross-counterflow vs. cross-flow heat exchangers. For cross-flow heat exchangers (condensers and boiler) the secondary mass flow rate is defined by the frontal area the air is passing through. Each section of the heat exchanger (sub-cooled, two-phase, or superheated) has a fraction of the total air mass flow that is proportional to the heat transfer area required for the heat duty of that section. The heat transfer area depends on the primary side conditions because the primary fluid side heat transfer coefficient for each section can change dramatically. For instance, the two-phase heat transfer coefficient is significantly higher (often an order of magnitude) than the single-phase section, so less heat transfer area is required in the two-phase region to obtain the same heat duty. The baseline areas for the cross-flow heat exchangers were known from a proprietary heat exchanger design model (shown in Table 3-8). Although the boiler is a two-pass configuration, the area calculation method was assumed to be single pass to simplify the calculation procedure. Therefore, a simple factor is used to determine the secondary mass flow:

$$\dot{m}_{a,sec} = \dot{m}_{a,total} A_{per,sec} \tag{3.34}$$

Unfortunately, this method cannot be applied to counter-flow exchangers (chiller and recuperator) with multiple passes because the heat transfer area for each section utilizes the same fluid for subsequent sections. For simplicity, the secondary fluid mass flow rate is assumed to rely only upon on heat duty for the counter flow heat exchangers as follows:

$$\dot{m}_{a,sec} = \dot{m}_{a,total} \left(\frac{\dot{Q}_{sec}}{\dot{Q}_{total}} \right) \tag{3.35}$$

This simplification should not have a major effect on the results because, for the chiller, the two-phase region has a large portion of the overall *UA*, and, for the recuperator, there is only one fluid regime so the changing heat duty has no effect on other regions. The heat exchanger area percentages for the cross-flow heat exchangers are shown in Table 3-8. A complete tabulation of the heat exchanger *UA*s as calculated in this section are shown in Table 3-9.

Table 3-9. Heat exchanger *UA* calculation results for the basic thermodynamic model (15°C ambient).

Component	Section	UA [kW K^{-1}]	Number of HEX	Dimensions Each L×W×H [m]	Mass Each [kg]
Waste Heat Boiler	$UA_{b,sc}$	4.14	2	1.24×1.5×0.12	120
	$UA_{b,tp}$	4.80			
	$UA_{b,sh}$	1.11			
	UA_{b}	10.1			
Evaporator (Liquid Coupled)	$UA_{e,tp}$	209.3	2	0.37×0.38×0.5	77.4
	$UA_{e,sh}$	2.7			
	UA_{e}	212			
Power Cycle Condenser (Air Cooled)	$UA_{p,cond,sc}$	0.08	3	1.4×1.3×0.05	49
	$UA_{p,cond,tp}$	10.05			
	$UA_{p,cond,sh}$	0.03			
	$UA_{p,cond}$	10.2			
Cooling Cycle Condenser (Air Cooled)	$UA_{co,cond,sc}$	0.11	6	1.4×1.7×0.05	67.5
	$UA_{co,cond,tp}$	79.4			
	$UA_{co,cond,sh}$	1.34			
	$UA_{co,cond}$	80.9			
Recuperator	UA_{recup}	2.53	1	0.16×0.16×0.45	21.8

In all cases the two-phase region of the heat exchanger has the largest *UA* because, in general, the heat duty in the two-phase region is the largest. For example, the heat duty for the cooling cycle chiller is 247.6 kW for the two phase region and only 2.4 kW for the superheated vapor region. This difference is caused by the large enthalpy of vaporization required to heat the fluid from liquid to vapor as compared with the low amount of energy required to superheat the vapor. The largest *UA* among the five heat exchangers is the cooling cycle chiller while the smallest is the recuperator. The chiller has the largest *UA* because it has a large heat duty requirement (250 kW) and a small temperature lift (1.2°C). In addition, the chiller saturation temperature is very close to the chilled water temperature (T_{sat} = 15.3°C while chilling 17.2°C - 16°C water in power plant configuration) which increases the effectiveness and causes the *UA* to be large. The strict requirements for the chiller (causing the high *UA*) are necessary due to the power plant operating conditions. The recuperator is the smallest heat exchanger because it operates with single phase fluids and has a low heat duty. Furthermore, the entering temperature difference is fairly high between the hot vapor inlet and the cold liquid inlet (ΔT = 52°C), which drives a lower effectiveness than some of the other heat exchangers, thus causing a lower *UA*.

Although the cooling and power cycle condensers have similar saturation conditions and both interact with the same environment temperature, Table 3-9 shows they have radically different *UA*s (i.e., 80.9 kW K^{-1} and 10.2 kW K^{-1} for the cooling and power, respectively). This difference is primarily due to the large cooling duty required for the cooling cycle as compared with the power cycle. The cooling cycle condenser has a heat duty of nearly 263 kW, while the power cycle condenser is only 86 kW. This difference in *UA* also manifests itself in a physically larger heat exchanger for the cooling cycle as noted in Table 3-9.

The sizes and masses of the heat exchangers are another interesting point because although the chiller has the largest *UA*, it has a small size and weight as compared with the boiler and condensers. The difference occurs due to the secondary fluid for the heat exchangers: the boiler and condensers are all air coupled, while the chiller is liquid coupled. Since the heat transfer characteristics for the liquid are far better than air, the surface area required can be smaller. Since each heat exchanger is constructed with aluminum, the total size and mass of the chiller will be smaller than the air coupled heat exchangers. For instance, the heat duty to mass ratio for the chiller is 1.61 kW kg^{-1}, while for the boiler, CC condenser, and PC condenser they are 0.41 kW kg^{-1}, 0.65 kW kg^{-1}, and 0.58 kW kg^{-1}, respectively. So, although the chiller heat duty is 250 kW, and the power cycle condenser heat duty is 86 kW, they have roughly the same total mass (154 kg vs. 147 kg for the chiller and PC condenser, respectively). The *UAs* that have been discussed in this section are used to set the system size for the off-design condition methodology shown in the following section.

3.2. TCCS Off-Design Performance

The TCCS will not always operate at the specified design point as described in Section 3.1 because the thermal reservoir temperatures and compressor loads have an effect on the system performance. Therefore, a modeling analysis was performed to determine system performance over a range of conditions, and is described in the following sections. Section 3.2.1 describes the compressor and turbine performance maps showing the turbo-machine efficiency and speed for various state conditions. Section 3.2.2 describes the heat exchanger scaling methodology, and Section 3.2.3 outlines the off-design methodology for predicting performance. The result of the modeling is a performance map predicting system COP as a function of power and cooling cycle

mass flow rates. The performance map is used to compare with the actual test facility data presented in Chapter 5.

3.2.1. Turbo-Machine Performance Maps

To predict the efficiency of the turbine and compressor at any operating condition, compressor and turbine maps were generated. The maps were developed by BNI for the specific turbo-compressor used in the test facility. The compressor and turbine performance maps are shown in Figure 3-9 and Figure 3-10, respectively. Both maps include the reference conditions, which are also listed in Table 3-10. The reference conditions are used to predict off-design performance as shown in Section 3.2.3. For reference, the green diamond on both plots are the design conditions. In this section, the maps will be described in general terms, followed by the theory for off-design performance, and then the presentation of the equation required to predict performance.

The x-axis of the compressor map is the corrected mass flow in kg s^{-1}, which is a relationship between the actual mass flow and the original design mass flow. The y-axis is the corrected ideal specific enthalpy rise across the compressor in kJ kg^{-1}, which is a relationship between the actual enthalpy rise and the original design enthalpy rise. The efficiency contours and corrected speeds are plotted as a function of the corrected mass flow and corrected ideal specific enthalpy rise. Therefore, if the turbo-machine conditions are known, the efficiency and speed can be estimated by interrogating the plot. A linear interpolation between speed and efficiency lines is utilized in this study. The black line at the left of the compressor map is the stall line. If the compressor is operating to the left of this line, the compressor will stall. A compressor is typically unable to operate in the stall region because, at low mass flow rates and high speeds, the fluid can separate from the blades and create large vibrations, leading to possible blade failure [90]. The

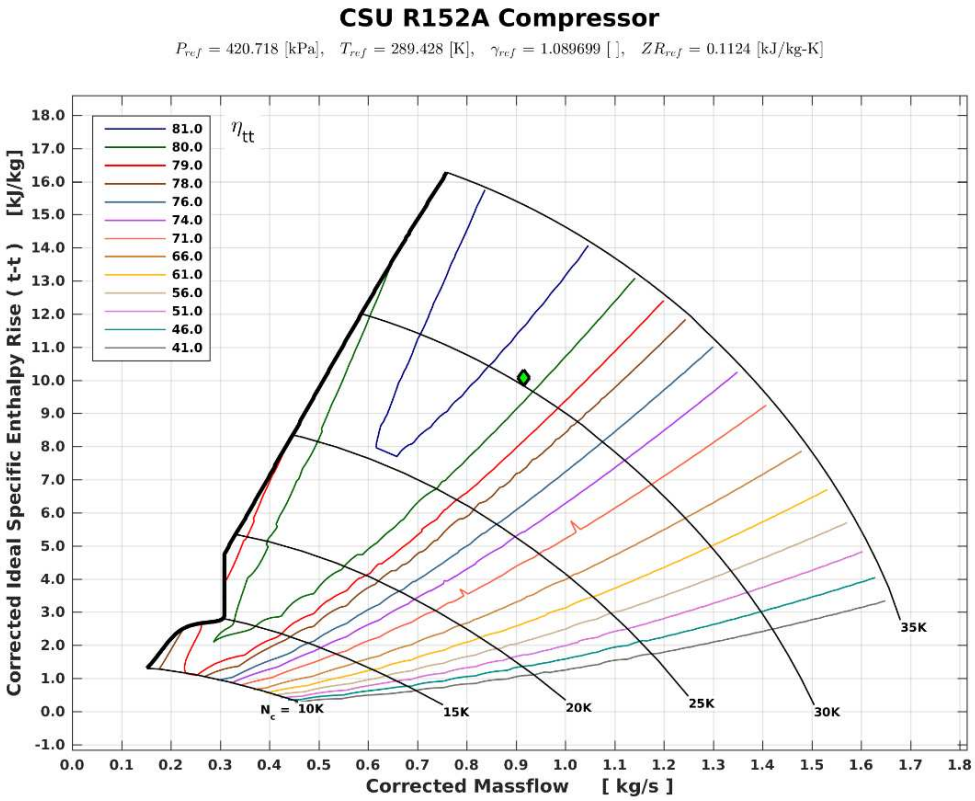

Figure 3-9. Compressor efficiency map.

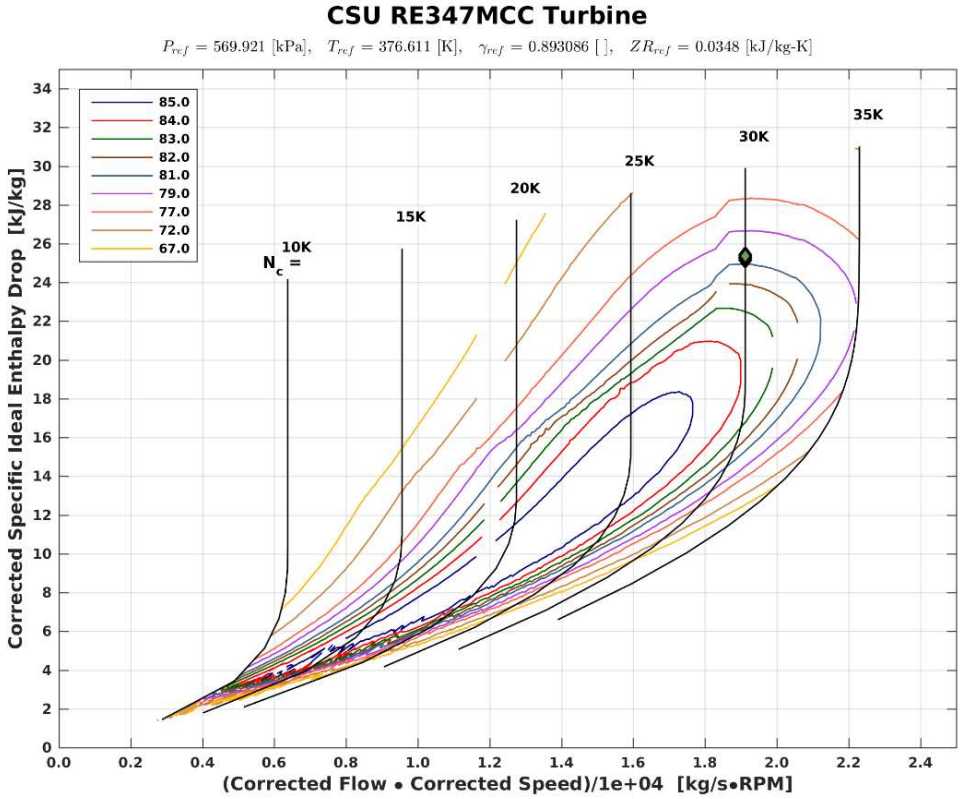

Figure 3-10. Turbine efficiency map.

Table 3-10. Reference conditions for the turbo-compressor.

Reference Condition	*Value*
Turbine temperature	$T_{t,ref} = 376.611°K$
Turbine pressure	$P_{t,ref} = 569.921$ kPa
Turbine specific heat ratio	$\gamma_{t,ref} = 0.893086$
Turbine ZR	$ZR_{t,ref} = 0.0348$ kJ kg^{-1} K^{-1}
Compressor temperature	$T_{comp,ref} = 289.428°K$
Compressor pressure	$P_{comp,ref} = 420.718$ kPa
Compressor specific heat ratio	$\gamma_{comp,ref} = 1.089699$
Compressor ZR	$ZR_{comp,ref} = 0.1124$ kJ kg^{-1} K^{-1}

design speed for the turbo-compressor is 30,000 RPM and it is not recommended to operate the machine at over 35,000 RPM due to potential decoupling of the magnetically coupled shaft.

The turbine map is different from the compressor because the turbine can operate over a range of pressure ratios when the flow is choked. This characteristic of turbines causes the speed lines to become vertical as the flow chokes, and those vertical speed lines will collapse to a single curve when plotted against the mass flow rate. These two complications cause a change in display of the turbine map because it becomes impossible to resolve the efficiency contours when operating in the choked flow region. The x-axis of the turbine is multiplied by the corrected speed of the machine to separate the choked flow lines. The division by 10,000 is for easier display. Similar to the compressor, the y-axis of the turbine map is the corrected ideal enthalpy drop across the turbine in kJ kg^{-1}. Due to the vertical nature of the speed lines in the choked flow region, the data from the turbine map is extracted using different inputs than the compressor. On the compressor map, a mass flow rate and enthalpy rise will always produce a unique point on the map. However, that is not true for the turbine map because there are infinite possible enthalpy drops for a given mass flow rate. Turbine maps must be interrogated using a known speed and corrected ideal enthalpy drop to predict the efficiency and mass flow. These compressor conditions

should be resolved first to find the required shaft speed, and the turbine enthalpy drop is found from the PC saturation assumptions.

The equations to calculate the corrected values used for the turbo-compressor maps are derived for a machine that is operating under dynamic similarity. Dynamic similarity assumes the fluid velocities of the design case and the off-design case are equivalent at every location in the flow field. Because both the magnitude and direction of the velocity vectors are equal, the amount of flow-turning will also be equal. Another important limitation of the performance maps is that predictions should not be made for values close to the critical point because the correction equations tend produce very large errors due to the high sensitivity of *CpT*. There can also be calculation errors associated with compressibility effects and differences in the ratio of specific heats between the conditions of interest.

To ensure the off-design calculation is meeting the dynamic similarity requirements, specific conditions should be met: (1) the off-design point should have the same value of specific speed and diameter and (2) the relative and absolute frame Mach numbers in the flow field should be small (<0.3). Condition one can be satisfied by equating the design conditions with the off-design conditions for the head and flow coefficients.

$$\frac{Q_{\mathrm{d}}}{N_{\mathrm{d}} D_{\mathrm{d}}^3} = \frac{Q_{\mathrm{alt}}}{N_{\mathrm{alt}} D_{\mathrm{alt}}^3} \tag{3.36}$$

$$\frac{H_{\mathrm{d}}}{N_{\mathrm{d}}^2 D_{\mathrm{d}}^2} = \frac{H_{\mathrm{alt}}}{N_{\mathrm{alt}}^2 D_{\mathrm{alt}}^2} \tag{3.37}$$

By solving equation (3.36) and (3.37) simultaneously, it is possible to achieve dynamic similarity in the turbo-machine. However, these equations show that condition 1 implies the physical diameter of the turbo-machine changes in the off-design condition modeling, which may seem counter-intuitive, but is a result of the turbo-machine being designed for one particular condition.

For alternate conditions, a change in turbo-machine geometry is almost always required, so, as long as the blade tip clearances maintain their relative proportions with the flow-path dimensions, then the prediction is accurate. If the blade tip clearances become a large portion of the wheel dimensions, the component map gives overly optimistic predictions.

There are several reference parameters required to calculate the performance in off-design conditions. For both the compressor and turbine, each of the following parameters can be found by comparing the actual conditions at the inlet of the turbo-machine with the reference conditions. The pressure ratio between the reference condition and current condition is defined as follows:

$$\delta = \frac{P_{\text{act}}}{P_{\text{ref}}} \tag{3.38}$$

The actual specific gas constant is found by dividing the universal gas constant by the molecular weight of the fluid.

$$R_{\text{act}} = \frac{R_{\text{univ}}}{MW} \tag{3.39}$$

The actual compressibility factor (Z) is a function of the properties at the inlet of the compressor and is shown in the following equation:

$$Z_{\text{act}} = \frac{P_{\text{act,in}} \upsilon_{\text{act,in}}}{R_{\text{univ}} T_{\text{act,in}}} \tag{3.40}$$

The actual specific heat ratio is defined as the specific heat at constant pressure divided by the specific heat at constant volume (each evaluated at the inlet with property relationships).

$$\gamma_{\text{act}} = \frac{Cp_{\text{act}}}{Cv_{\text{act}}} \tag{3.41}$$

The critical velocity for the reference and actual conditions are calculated using the same equation which includes the specific heat ratio, gravitational constant, compressibility factor, specific gas constant, and temperature.

$$V_{cr} = \sqrt{\frac{2\gamma}{\gamma+1} gZRT} \tag{3.42}$$

The critical velocity ratio and compressibility factors between reference and actual condition can now be determined as follows:

$$\theta_{cr} = \left(\frac{V_{cr,act}}{V_{cr,ref}} \right)^2 \tag{3.43}$$

$$\varepsilon_{\gamma} = \frac{\gamma_{ref} \left(\frac{2}{\gamma_{ref}+1} \right)^{\frac{\gamma_{ref}}{\gamma_{ref}-1}}}{\gamma_{act} \left(\frac{2}{\gamma_{act}+1} \right)^{\frac{\gamma_{act}}{\gamma_{act}-1}}} \tag{3.44}$$

With each of these factors determined, the x-axis and y-axis of the compressor is found. The corrected mass flow rate for the compressor (x-axis of efficiency map) is found by using the actual CC mass flow rate in the equation below:

$$\dot{m}_{eq} = \frac{\dot{m}\varepsilon_{\gamma}\sqrt{\theta_{cr}}}{\delta} \tag{3.45}$$

The corrected ideal enthalpy rise (y-axis of efficiency map) is the ideal enthalpy rise divided by the critical velocity ratio.

$$\Delta h_{eq} = \frac{\Delta h_{ideal}}{\theta_{cr}} \tag{3.46}$$

These values allow the compressor efficiency map to be interrogated to find the predicted speed and efficiency of the compressor. A sample compressor map is shown in Figure 3-11 to demonstrate the interrogation technique. The speed determined from the compressor map is not the actual compressor speed, but is a corrected speed. The equation to convert the corrected speed to actual speed is shown below:

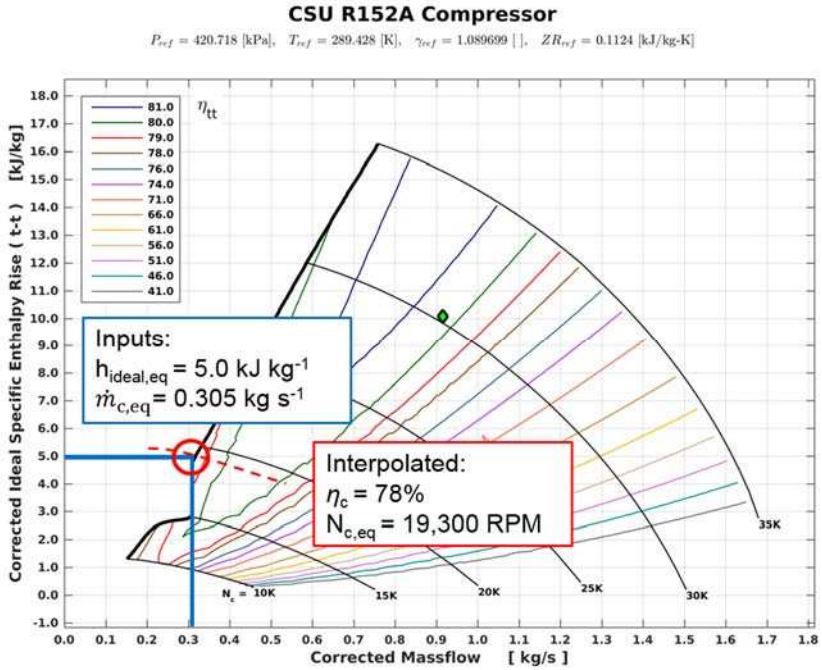

Figure 3-11. Sample compressor map demonstrating the technique to read data based on the corrected mass flow and corrected ideal specific enthalpy rise.

$$N = N_{\text{eq}}\sqrt{\theta_{\text{cr}}} \tag{3.47}$$

The turbine performance map is interrogated by using the corrected speed and the corrected specific ideal enthalpy drop to find the efficiency of the turbine and the x-axis value (corrected flow times corrected speed). The speed (N) calculated from equation (3.47) is the actual spinning speed, but not the corrected speed required to read the turbine map. Equations (3.38) through (3.44) should be used to calculate the actual parameters at the turbine inlet, and then the turbine corrected speed is calculated using equation (3.47). The next step is to find the corrected ideal enthalpy drop across the turbine, which is calculated similarly to the compressor using equation (3.46). A sample turbine map is shown in Figure 3-12 to demonstrate the technique used to read data with the corrected speed and corrected ideal specific enthalpy drop.

The result of the turbine map interrogation are the turbine efficiency and the x-axis value. From the x-axis value, the turbine corrected mass flow rate is calculated using the equation below:

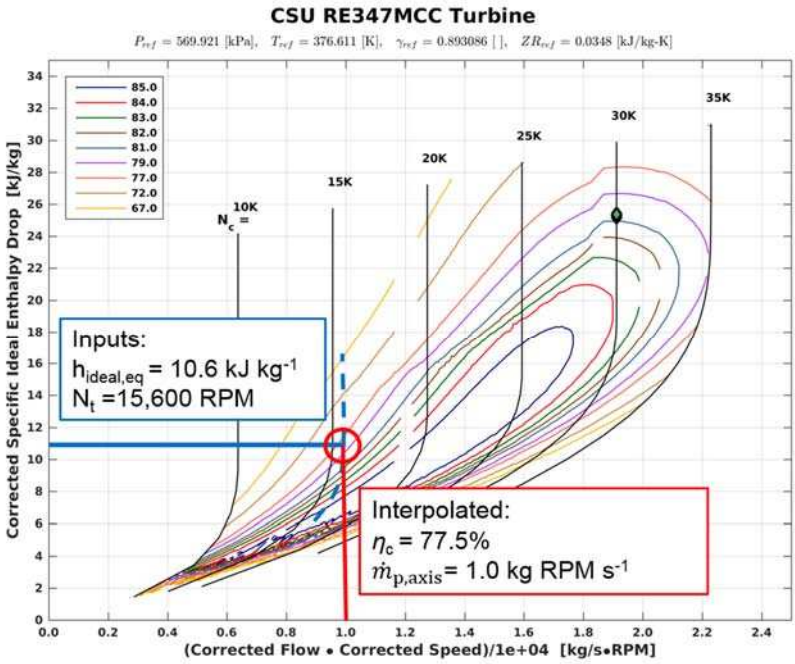

Figure 3-12. Sample turbine map demonstrating the technique to read data based on the corrected speed and corrected ideal specific enthalpy drop.

$$\dot{m}_{\mathrm{p,t,axis}} = \frac{\dot{m}_{\mathrm{p,t,eq}} N_{\mathrm{p,t,eq}}}{10,000} \tag{3.48}$$

The actual power cycle mass flow rate is calculated by using the corrected mass flow in equation (3.45). This subsection provided the interrogation technique to determine off-design performance of the turbo-machine. The following section describes the heat exchanger *UA* scaling methodology that is used to find the performance of the heat exchangers in off-design conditions.

3.2.2. *UA* Scaling Methodology

Determining the heat exchanger performance is critical to accurately predicting the system COP in off-design conditions because the fluid flow rates and temperatures change so the heat exchanger will perform differently than in the baseline condition. The *UA* is one aspect that changes in off-design conditions because although the area remains constant, the overall heat

transfer coefficient changes. The heat transfer coefficient could be determined from detailed heat transfer models, but the equations add computational complexity. In the present study, a *UA* scaling methodology is employed for each heat exchanger to enable simulation over a wide range of conditions with a lower degree of computational fire-power.

In this method, the temperature inputs from the baseline case (Table 3-4) are removed and replaced with scaled heat exchanger *UAs* that are dependent on the iteratively solved fluid conditions. By inputting the *UA,* the heat exchangers set the sub-cooling, saturation, and superheating temperatures. Table 3-11 shows the previous temperature assumption from the basic modeling and the *UA* replacement used for the off-design modeling. There are nine temperature assumptions required to solve the baseline model, and each of these assumptions needs to be replaced by a single *UA* value. Due to the heat exchangers used, there are twelve section *UAs*, so if all twelve values were input, the system of equations would be over constrained and could not solve. In three cases, two *UA* values were combined to produce nine *UA* values that would replace the nine temperature inputs. The combinations were for the boiler and condensers and involved combining the two-phase *UA* with either the subcooled or superheated *UA*. For example, the set temperatures for the basic modeling approach at the cooling cycle condenser are the saturation and

Table 3-11. UA-Temperature replacement combinations

Component	***Temperature input***	***UA replacement***
Waste Heat Boiler	$T_{p,b,sat}$	$UA_{p,b,sc} + UA_{p,b,tp}$
	$T_{p,p,sh}$	$UA_{p,b,sh}$
Evaporator	$T_{c,evap,sat,o}$	$UA_{c,evap,tp}$
	$T_{c,evap,sh}$	$UA_{c,evap,sh}$
CC Condenser	$T_{c,cond,sc}$	$UA_{c,cond,sc}$
	$T_{c,cond,sat,o}$	$UA_{c,cond,tp} + UA_{c,cond,sh}$
PC Condenser	$T_{p,cond,sc}$	$UA_{p,cond,sc}$
	$T_{p,cond,sat,o}$	$UA_{p,cond,tp} + UA_{p,cond,sh}$
Recuperator	$T_{p,cond,sh}$	$UA_{p,recup}$

sub-cooling temperatures, but there are three *UA* regimes for the heat exchanger. The sub-cooled *UA* replaces the sub-cooled temperature, while the *UAs* for the two-phase and superheated regions were combined to replace the saturation temperature.

The scaling methodology multiplies the baseline resistances (*Rs*) by heat transfer coefficient, area, and fluid scaling factors to determine the new *UA*. A general form of the equation used to calculate the off-design *UA* is as follows:

$$UA_{\text{off}} = \left(\frac{1}{Rs_{\text{prim}} f_{\text{h,prim}} f_{\text{A,sec}} f_{\text{f}}} + \frac{1}{Rs_{\text{secon}} f_{\text{h,sec}} f_{\text{A,sec}} f_{\text{f}}} \right)^{-1} \tag{3.49}$$

There are three scaling factors used in the equation (3.49): heat transfer coefficient scaling (f_{h}), area change scaling (f_{A}), and fluid scaling (f_{f}). The following two sections describe the *UA* scaling methodology in detail. The first section discusses the baseline heat exchanger resistance values (*Rs*) and the second section outlines the *UA* scaling factors.

3.2.2.1. Determining Baseline Heat Exchanger Resistances

The first step to finding the new *UA* is to determine the heat transfer resistances (*Rs*) on the primary and secondary sides of the heat exchanger during the baseline design case. Equation (3.50) is the resistance of the primary and secondary sides set equal to the *UA* from the baseline modeling case [89]. The wall resistance was neglected for this modeling approach because it had minimal effect on the total *UA* and was assumed to have negligible change in the off-design cases.

$$UA_{\text{model}} = \left(\frac{1}{Rs_{\text{prim}}} + \frac{1}{Rs_{\text{secon}}} \right)^{-1} \tag{3.50}$$

In the present study, the inverse of the traditional thermal resistance (*Rs*) was used for convenience and is defined as the heat transfer coefficient multiplied by the area:

$$Rs = ht \times A \tag{3.51}$$

The secondary side resistance value is found by calculating the secondary side heat transfer coefficient and heat exchange area. As noted in Figure 3-8, there are three different styles of heat exchanger in the TCCS. For air coupled heat exchangers with louvered fin geometries (condensers and boiler) the heat transfer coefficient has been well characterized, and can be calculated with the Chang and Wang correlation [91]. For the recuperator and chiller, the secondary heat transfer coefficient is either a constant or determined from the Gnielinski correlation [92]. The secondary resistance is then calculated by multiplying the heat transfer coefficient by the air side heat transfer area.

Calculating the secondary resistance allows for calculation of the primary resistance because the baseline *UA* is known. The following two subsections describe in detail the Chang and Wang and single phase correlations and are followed by a description of the air side heat exchanger area calculation as an example.

Chang and Wang Correlation for Air Coupled Heat Exchangers

For the tube and fin style heat exchangers (condensers, PC boiler), the secondary fluid flow was air passing over louvered fins and the Chang and Wang correlation was employed [91]. The Chang and Wang heat transfer coefficient correlation was derived by analyzing 91 heat exchangers with varying geometries. The final correlation is a calculation of the Colburn factor which is used to find the heat transfer coefficient:

$$j_a = C_1 Re_{lp}^{-0.49} \tag{3.52}$$

The variable C_1 is a function of the various geometric inputs from the heat exchanger and Re_{lp} is the Reynolds number for louvered fin geometry.

$$C_1 = \left(\frac{\theta}{90}\right)^{0.27}\left(\frac{F_p}{L_p}\right)^{-0.14}\left(\frac{F_l}{L_p}\right)^{-0.29}\left(\frac{T_d}{L_p}\right)^{-0.23}\left(\frac{L_l}{L_p}\right)^{0.68}\left(\frac{T_p}{L_p}\right)^{-0.28}\left(\frac{\delta_f}{L_p}\right)^{-0.05} \tag{3.53}$$

Each geometric constant listed in equation (3.53) was based on the heat exchangers designed by Modine but is proprietary and is not disclosed in this document.

$$Re_{\mathrm{lp}} = \frac{G_{\mathrm{a}} Re_{\mathrm{lp}}}{\mu_{\mathrm{air}}} \tag{3.54}$$

The viscosity, μ_{air}, is determined from the average fluid properties, and the mass flux, G_{a}, is calculated as follows:

$$G_{\mathrm{a}} = \frac{\dot{m}_{\mathrm{a,total}}}{A_{\mathrm{surface}}} \tag{3.55}$$

By using equation (3.52), the Colburn factor is calculated and then used with the following equation to find the heat transfer coefficient of air in the baseline case as follows:

$$ht_{\mathrm{a}} = \frac{j_{\mathrm{a}} Cp_{\mathrm{a}} G_{\mathrm{a}}}{Pr^{2/3}} \tag{3.56}$$

The air side heat transfer coefficient (ht_{a}) is assumed to be equal across the entire heat exchanger. One study by Kim et al. investigated the effect of heat transfer coefficient change due heat exchanger tilt. The condensers in the TCCS are tilted at a 45° angle, and the boiler is horizontal. Kim et al. found the heat transfer coefficient effect from exchanger tilt was negligible and pressure drop was a more significant factor [93]. Because the heat exchanger pressure drop was developed from proprietary heat exchanger models, the pressure drop correction was not applied.

Single-Phase Heat Exchangers Resistances

For the two counter-flow heat exchangers (chiller and recuperator), the heat transfer coefficient in the baseline case was calculated by using two different approaches for Nusselt number. In both cases the secondary side fluid flow was used because of a simpler flow pattern. The secondary fluid for the chiller is the propylene-glycol:water mixture, and the secondary fluid for the recuperator was assumed to be the vapor. In the following equations, the Reynolds number

was calculated by using the hydraulic diameter of flow through one fin section. For the chiller, the Reynolds number was 197, indicating the flow was laminar. The length to width ratio of the individual channel was 4, so a Nusselt number of 5.33 was selected. The Reynolds number for the recuperator was 4706, so the Gnielinski correlation was selected as shown below [89]:

$$Nu = \frac{\left(\frac{f}{8}\left(Re - 1000\right)Pr\right)}{\left(1 + 12.7\left(\frac{f}{8}\right)^{0.5}\left(Pr^{2/3} - 1\right)\right)} \tag{3.57}$$

The next section presents a sample method for secondary side heat exchanger area calculations.

Heat Exchanger Area Calculation

Figure 3-13 shows some geometric considerations used to calculate area for an air coupled heat exchanger. Similar considerations were applied to the recuperator and chiller. The heat transfer area is a summation of the exposed tube and the fin areas to the air flow. The tube base area is simply the length of each tube multiplied by the width:

$$A_{\text{tube}} = 2T_{\text{l}}T_{\text{d}}No_{\text{tube}} \tag{3.58}$$

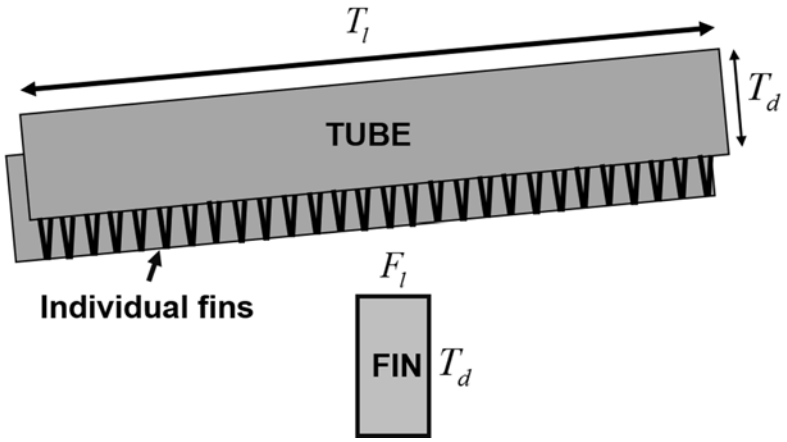

Figure 3-13. Single fin row geometric considerations for air side of cross-flow heat exchangers

Since each tube has two heat transfer sides, the product of the length and width is multiplied by the number of tubes and a factor of two. The fin area was calculated by simplifying the louver geometry to a flat fin and calculating the area multiplied by the total number of fins.

$$A_{\text{fin}} = 2T_{\text{d}}F_{\text{l}}N_{\text{finrow}}(No_{\text{tube}} - 1) \tag{3.59}$$

The factor of two is once again used because each fin has two sides. The number of tubes is subtracted by one because there is one less fin row as compared to tube rows. The total number of fins per fin row is found by dividing the length of each tube by the fin pitch.

$$No_{\text{finrow}} = \frac{L_{\text{t}}}{F_{\text{p}}} \tag{3.60}$$

The thickness of the fins is calculated to find the tube base area removed by adding in the fins:

$$A_{\text{thickness}} = 2\delta_{\text{f}}T_{\text{d}}No_{\text{finrow}}(No_{\text{tubes}} - 1) \tag{3.61}$$

The air side heat transfer area is now calculated by summing the results of equations (3.58) - (3.61):

$$A_{\text{a}} = N_{\text{HEX}}\left(A_{\text{tube}} - A_{\text{thickness}} + A_{\text{fin}}\right) \tag{3.62}$$

Each geometric constant used in equations (3.58) - (3.60) were based on proprietary Modine designs for the heat exchangers in the TCCS and are not disclosed in this document. Similar equations were also applied to calculate the secondary side area and heat transfer coefficients for the chiller and recuperator. Both of these heat exchangers are plate-fin style and the vapor side was used for the recuperator. The following section outlines the use of the baseline primary and secondary resistance values to find the *UA*s in off-design conditions.

3.2.2.2. *UA* Off-Design Scaling Parameters

For any off-design calculation, the primary and secondary resistances (found from equation (3.50)) are fixed at the baseline and then multiplied by scaling factors calculated from the off-design mass flow rates, temperatures, and pressures. This section describes the three scaling factors (heat transfer, area, and fluid) in detail.

Heat Transfer Coefficient Scaling

The heat transfer scaling factor is needed because in off-design conditions, the temperatures, pressures, and flow rates change within the heat exchanger, causing the heat transfer coefficient to change. The heat transfer scaling factor (f_{ht}) is calculated by dividing the heat transfer coefficient of the off-design case by the heat transfer coefficient of the baseline case.

$$f_{\text{ht}} = \frac{ht_{\text{off}}}{ht_{\text{base}}} \tag{3.63}$$

In this research, equation (3.63) is often simplified because the heat transfer calculations can be computationally heavy for many of the heat exchange regimes. In most cases, the heat transfer coefficient can be reduced to a function of Nusselt numbers as shown in the following equations.

The heat transfer coefficient is a function of the conductivity, Nusselt number, and length:

$$ht = \frac{kNu}{L} \tag{3.64}$$

By employing equation (3.63), the heat transfer coefficient for the off-design is divided by the baseline case as shown below:

$$\frac{ht_{\text{off}}}{ht_{\text{base}}} = \frac{\frac{k_{\text{off}} Nu_{\text{off}}}{L_{\text{off}}}}{\frac{k_{\text{base}} Nu_{\text{base}}}{L_{\text{base}}}} \tag{3.65}$$

For this analysis, it was assumed that the conductivity of the fluid had minimal change from the baseline to off-design case and that the geometry was constant which simplifies equation (3.65) to the following:

$$\frac{ht_{\text{off}}}{ht_{\text{base}}} \propto \frac{Nu_{\text{off}}}{Nu_{\text{base}}} \tag{3.66}$$

Equation (3.66) is the basis of the simplifications for each heat exchanger regime. There are three regimes in the heat exchangers: single phase, condensing, and boiling. Each of the specific cases are described in the sections below.

Single Phase Regimes

The single phase heat transfer regimes include secondary side flow, sub-cooled liquid flow, superheated vapor flow, and both sides of the recuperator. The secondary side heat transfer mediums are air (condensers and boiler) or a glycol-water mixture (chiller). The air side heat transfer coefficient is a relatively simple calculation so a Nusselt number simplification was not used. Instead, the heat transfer coefficient in the off-design was calculated directly by using the Chang and Wang correlation as presented in equation (3.56). The off-design heat transfer coefficient is then divided by the baseline as shown in equation (3.63).

The glycol-water heat transfer coefficient is more complicated and the properties have minimal change, so equation (3.66) can be simplified. The Dittus-Boelter correlation for single phase flow Nusselt number in a tube is used [92]:

$$Nu = CRe^{a}Pr^{b} \tag{3.67}$$

Inserting equation (3.67) into equation (3.66) yields:

$$\frac{ht_{\text{off}}}{ht_{\text{base}}} \propto \frac{CRe_{\text{off}}^{a}Pr^{b}}{CRe_{\text{base}}^{a}Pr^{b}} \tag{3.68}$$

The constants and Prandtl numbers can cancel because there is minimal property change for the single phase glycol-water mixture between the baseline and off-design cases. This leaves the Reynolds number in the off-design case divided by the baseline case. The Reynolds number is defined as:

$$Re = \frac{\rho V D_{hyd}}{\mu} = \frac{\dot{m}\frac{D_{hyd}}{A}}{\mu} \tag{3.69}$$

By implementing the Reynolds number into equation (3.68), the geometric factors and viscosity cancel to finally yield a relationship relying only on the change in glycol flow rate.

$$\frac{ht_{off}}{ht_{base}} \propto \left(\frac{\dot{m}_{off}}{\dot{m}_{base}}\right)^{a} \tag{3.70}$$

For the glycol-water mixture, the constant 'a' was assumed to be 0.6.

Single phase regimes for the primary fluid (i.e., sub-cooled, superheated, and recuperator) were calculated by using a modification of equation (3.68). In these cases, the geometric parameters were set equal, but the fluid properties were not, resulting in the relationship below:

$$\frac{ht_{off}}{ht_{base}} \propto \left(\frac{\frac{\dot{m}_{off}}{\mu_{off}}}{\frac{\dot{m}_{base}}{\mu_{base}}}\right)^{a} \left(\frac{Pr_{off}}{Pr_{base}}\right)^{b} \tag{3.71}$$

The constants 'a' and 'b' were assumed at 0.8 and 0.3, respectively. This equation was applied to any single phase regime including the liquid and vapor sides of the recuperator.

Condensing Regimes

The condensing regimes of the heat exchangers include the regions in the power and cooling cycle condensers. Condensing regimes were computed using a modified Dobson and Chato correlation. The complete correlation is shown below [94]:

$$Nu = 0.023 Re^{0.8} Pr^{0.4} \left[1 + \frac{2.22}{X_{tt}^{0.89}}\right] \tag{3.72}$$

The turbulent-turbulent Martinelli parameter is defined as a function of densities, viscosities, and quality. The quality was assumed to be 0.5, and differences in quality did not have a major effect on Martinelli parameter.

$$X_{tt} = \left(\frac{\rho_g}{\rho_l}\right)^{0.5} \left(\frac{\mu_l}{\mu_g}\right)^{0.1} \left(\frac{1-x}{x}\right)^{0.9} \tag{3.73}$$

Similarly to the single phase correlation reduction method, equation (3.72) can be simplified due to geometric similarities.

$$Nu = \left(\frac{\dot{m}}{\mu}\right)^{0.8} Pr^{0.4} \left[1 + \frac{2.22}{X_{tt}^{0.89}}\right] \tag{3.74}$$

The baseline and off-design Nusselt numbers are calculated using equation (3.74) and inserted into equation (3.66) to find the heat transfer scaling factor.

Boiling Regimes

The boiling regimes include the two-phase regions of the cooling cycle chiller and power cycle boiler. Boiling regimes were calculated by using a modified Gungor and Winterton correlation. This correlation was selected due to its relative simplicity as compared with other boiling heat transfer correlations and high accuracy [95]. The general correlation takes the form [96]:

$$ht_{TP} = ht_{liq}\left(1 + 3000 Bo^{0.86} Fr^{(0.1-2Fr)} + 1.12 Fr^{0.5}\left[\frac{x}{1-x}\right]^{0.75}\left[\frac{\rho_{liq}}{\rho_{vap}}\right]^{0.41}\right) \tag{3.75}$$

The densities are found via property relationships, the quality is set to 0.5, and the boiling number, *Bo*, is found by the following equation:

$$Bo = \frac{\dot{Q}_{TP}}{\dot{m} h_{fg}} \tag{3.76}$$

The liquid heat transfer is calculated similarly to the Dittus-Boelter relation from equation (3.67):

$$ht_{liq} = \frac{0.023 Re^{0.8} Pr_{liq}{}^{0.4} k_{liq}}{L} \tag{3.77}$$

As shown previously, the Reynolds number can be simplified by removing constant and geometric parameters:

$$ht_{\text{liq}} = \left(\frac{\dot{m}}{\mu}\right)^{0.8} Pr^{0.4} k_{\text{liq}} \tag{3.78}$$

Gungor and Winterton also suggest including the Froude number will provide more accurate results for horizontal tube configurations in equation (3.75).

$$Fr = \frac{\dot{m}^2}{\rho_{\text{liq}} g} \tag{3.79}$$

The heat transfer change factor is calculated by computing the modified heat transfer coefficient for the baseline and off-design and inserting them into equation (3.63).

Area Change Scaling

The area change factor is included in equation (3.49) because the amount of area for a particular heat exchanger regime will change depending on off-design conditions. For instance, having a lower mass flow rate than the baseline will cause a smaller heat duty in the two-phase region of the heat exchangers, which implies the area for that region would also be smaller. The area scaling factor rectifies this problem by first relating the heat duties of the baseline and off-design sections. The first step to calculate the area factor is to find the ratio between the individual section heat duty and the total heat duty.

$$f_{\text{sec}} = \frac{\dot{Q}_{\text{sec}}}{\dot{Q}_{\text{total}}} \tag{3.80}$$

The ratio between the baseline and off-design cases will give the percent change in heat duty:

$$f_{Q,\text{sec}} = \frac{f_{\text{sec,off}}}{f_{\text{sec,base}}} \tag{3.81}$$

Now, consider that as the heat duty of each individual section changes, the heat transfer coefficient also changes. For the off-design conditions, both the heat transfer area of the heat exchanger and

the heat transfer coefficient change. Therefore, equation (3.81) would not be adequate to determine the true area of each section because only scaling by the heat duty does not fully account for the change in mass flow rate and therefore heat transfer coefficient through the section. For example, if the heat transfer coefficient is lower than expected on either side, additional cross-sectional area and, therefore, secondary fluid mass flow is needed. To account for the change in flow through the heat exchanger, the product of the heat duty and heat transfer coefficient scaling factors are multiplied as follows:

$$f_{A,sec} = f_{Q,sec} f_{ht,sec} \tag{3.82}$$

The only heat exchanger the area scaling factor does not apply is the recuperator, because there is only one single phase regime on both sides which means their area remains constant for the baseline and design case. One will notice that in equation (3.82), the heat transfer factor is multiplied twice, once in the actual factor and once within the area factor. As noted above the heat transfer factor is required in the area scaling equation because it helps determine the correct area of each heat exchanger section.

Fluid Change Correction Factor

One additional correction factor is required for the cooling cycle heat exchangers due to the change in fluids. This factor was used because the difference in the enthalpy of vaporization can be significant. For example, the flow rate required for R134a in the baseline case is 1.4 kg s^{-1}, versus 0.91 kg s^{-1} in the R152a design case. The enthalpy of vaporization for R152a is approximately 1.5× an R134a system (Figure 3-14); therefore, at the same heat duty, the R134a system requires a flow rate 1.5× that of R152a. This difference causes the percentage of the baseline heat transfer area to be less for R134a, which causes the area factor in equation 8 to over-predict performance. As an example, if an R134a system had a cooling cycle mass flow of 0.75 kg

s^{-1}, the fraction of baseline mass flow for R152a would be 82%, but for R134a, it would be only 53%. The fluid factor seeks to correct this area by finding the percentage difference between the two mass flows compared to their theoretical baselines (R152a: 0.91 kg s^{-1} and R134a: 1.4 kg s^{-1}).The factor takes the form:

$$f_{\mathrm{f}} = \frac{f_{\mathrm{r134a}}}{f_{\mathrm{r152a}}} \tag{3.83}$$

Where the factors f_{r134a} and f_{r152a} are provided by the following two equations:

$$f_{\mathrm{r134a}} = \frac{\dot{m}_{\mathrm{off}}}{\dot{m}_{\mathrm{base,r134a}}} \tag{3.84}$$

$$f_{\mathrm{r152a}} = \frac{\dot{m}_{\mathrm{off}}}{\dot{m}_{\mathrm{base}}} \tag{3.85}$$

Where the baseline mass flow rates for R134a and R152a systems would be 1.4 kg s^{-1} and 0.91 kg s^{-1}, respectively.

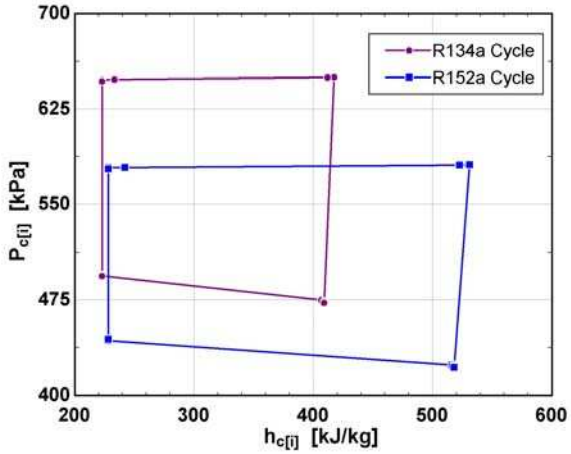

Figure 3-14. P-h diagrams for R152a and R134a vapor-compression cycles at the same baseline conditions.

Now, equation (3.49) is used to find the off-design *UA* for all heat exchangers by assuming the same resistance ratio from the baseline case and multiplying by the area, heat transfer, and fluid change factors. The recuperator would not require area scaling factors and the fluid factor for

all power cycle heat exchangers is equal to one. The next section presents the off-design performance method which employs the turbo-machine efficiency maps and heat exchanger *UA* calculations.

3.2.3. Off-Design Prediction Methodology

The off-design performance methodology is used to scale the performance of the system when it operates under conditions different than in the baseline condition. The approach described here is simpler than using detailed heat exchanger and turbomachinery modeling, but still captures the appropriate physics. This approach is validated with the experimental results gathered on the facilities described in Chapter four. As a result of the model validation, additional system operation points can be predicted, guiding future efforts. In this section, an overview of the methodology that incorporates both turbo-machine and heat exchanger performance scaling are given.

In this model, the temperature assumptions are replaced by heat exchanger *UAs* that are scaled appropriately from the baseline thermodynamic modeling approach. This allows the heat exchanger *UAs* to set the system performance instead of using the assumed sub-cooling, saturation, or superheating temperatures for these fluids. Therefore, as the ambient conditions increase, the saturation temperatures change to meet the *UA* requirements. Now, recall that the saturation conditions have a direct effect on cycle mass flow rate and enthalpy rise across the turbo-machine. Therefore, in off-design conditions, the saturation temperatures will change the conditions (i.e. enthalpy rise, mass flow) for the compressor and turbine, which will change the efficiency. By using the off-design performance maps described in Section 3.2.1 and employing the methodology in this section, the efficiency of the turbo-machine can be found.

The major change in inputs from the previous baseline modeling case is the removal of the temperature inputs and replacement with heat exchanger *UAs*. Table 3-11 shows the previous

temperature input from the basic modeling and the *UA* replacement used for the off-design modeling. There are nine temperature inputs required to solve the baseline model, and each of these inputs needs to be replaced by a single *UA* value. However, there are twelve heat exchanger section *UAs*, and inputting these would over constrain the system of equations. Therefore, for the boiler and two condensers, two *UA* values were combined to produce nine *UA* values that that replace the nine temperature inputs. For example, in the baseline performance calculation, the saturation and sub-cooled outlet temperatures were set for the condensers, but there are three *UA* regimes for this heat exchanger. Thus, the sub-cooled *UA* replaces the sub-cooled temperature, while the combined *UA* for the two-phase and superheated replaced the saturation temperature.

For simplicity, the pressure drop inputs for the components and connection lines are all assumed to be the same in the off-design and baseline model. The exhaust inlet temperature and flow rate were set to match the test facility operating condition. In some cases, maintaining a consistent exhaust temperature during experimentation was challenging, so the prediction methodology can vary to meet facility demand. The volumetric flow rates for the condenser fans were set equal to the design case because the fan speed was set at the maximum rate and did not change. The model does allow the flow rate to change. However, the fan and heat exchanger combination must allow the flow rates to be achieved. The component efficiencies for the pump, boiler fan, and glycol pump are assumed to be the same as in in the baseline modeling case. The shaft efficiency for the turbo-machine would possibly change due to higher windage losses at different design conditions, but an efficiency prediction was beyond the scope of this work and was set at 93%. For the system to iterate, an initial guess for compressor and turbine efficiency was input. The efficiency guesses were selected by using the estimated speed and state points with

the Cordier diagram. The speed was also omitted as an assumption because the off-design speed is found using the off-design methodology.

Figure 3-15 shows a flow chart describing the steps taken during the modeling iterations. The model begins at a known thermodynamic state with initial guesses for all values. The iteration begins by inputting a cooling cycle mass flow, power cycle mass flow, exhaust temperature, cooling water temperature, and ambient temperature. Guesses for the compressor and turbine efficiencies are also input and are the primary iteration variables in the code. A good assumption for efficiency could be determined for a previous solution with similar state points. The next step is to use the guessed conditions to calculate the scaled *UA*s for each heat exchanger. The heat exchanger scaling methodology is presented in Section 3.2.2, with equation (3.49) being the final form to calculate the off-design *UA*.

The scaled heat exchanger *UAs* are used to calculate the temperatures for each heat exchanger by using the *ε-NTU* equations shown in equation (3.27). The section areas for the cross-flow heat exchangers are updated by multiplying the area change factor and fluid factor (cooling cycle exchangers only), by the original area percent.

$$A_{\text{per,sec,off}} = f_{\text{A,sec}} f_{\text{f}} A_{\text{per,sec,base}} \tag{3.86}$$

The off-design area percent would then be used to find the air side mass flow rate.

$$\dot{m}_{\text{a,sec}} = \dot{m}_{\text{a,total}} A_{\text{per,sec,off}} \tag{3.87}$$

Using equation (3.86) has the potential to create a scenario in which the model would predict the heat exchanger is under or over utilizing the heat exchanger area because the sum of the three

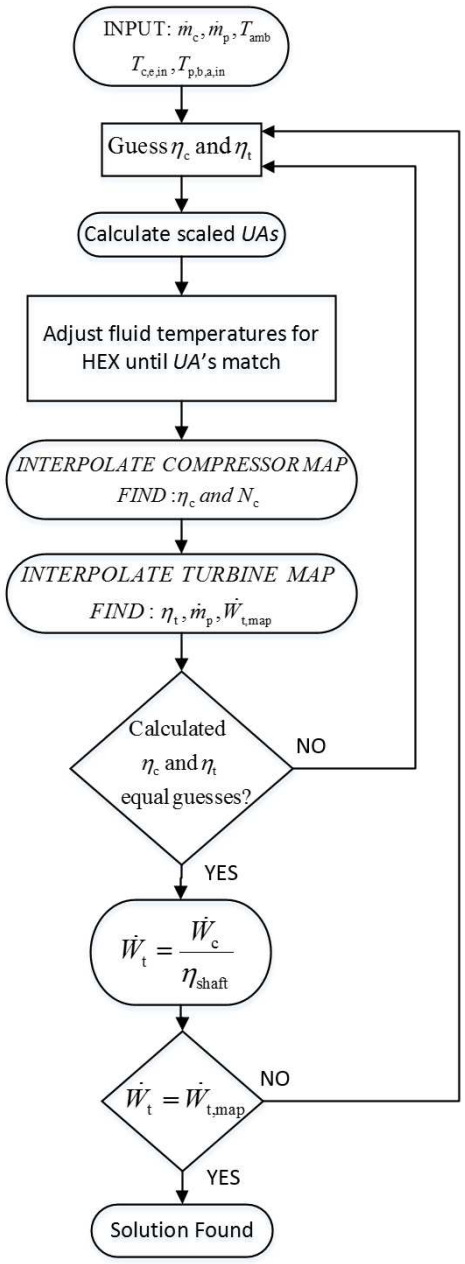

Figure 3-15. Off-design performance methodology flow chart.

sections might not necessarily be equal to one. To account for this change a system of equations was developed for the three sections of the heat exchanger.

$$f_{A,sh} f_f A_{per,sh,base} = A_{per,sh,off} \tag{3.88}$$

$$f_{A,tp} f_f A_{per,tp,base} = A_{per,tp,off} \tag{3.89}$$

$$f_{A,sc} f_f A_{per,sc,base} = A_{per,sc,off} \tag{3.90}$$

$$A_{per,sh,off} + A_{per,tp,off} + A_{per,sc,off} = 1 \tag{3.91}$$

With equation (3.91), the area percentages must always add to one, but the inclusion of this equation over-constrains the solution. One parameter must be removed for each heat exchanger to allow the full system of equations to solve. For the power cycle condenser and boiler the heat duty for the superheated region was removed, while for the cooling cycle condenser, the liquid region heat duty was removed. By removing these variables, the area percentages set the heat duties for those regions and the solution is found iteratively.

After updating the heat exchanger *UA*s in the off-design model, the cycle temperatures will change to meet the new requirements, causing the saturation pressure and enthalpy to also change. Since these values set the conditions around the compressor and turbine the cooling cycle properties should be updated by solving equations (3.1) through (3.6). Using the method described in Section 3.2.1, the corrected mass flow and corrected ideal enthalpy rise are calculated for the compressor. The off-design performance map is interrogated and the results are compared with the initial guess. If the interrogated efficiency does not match the original guess, the compressor efficiency guess should be updated and the cooling cycle state points resolved. Once the map prediction matches the cycle performance, the cooling cycle state points are set.

Establishing the power cycle state points is the next step for the modeling approach. The turbine map must be read by using the speed and corrected ideal enthalpy. The speed is determined by equating the compressor speed with the turbine speed. However, the speed from the compressor map is not the actual speed, and the correction methodology described in Section 3.2.1 (i.e., equation (3.47)) is used to find the actual speed. Based on the speed and correct ideal enthalpy, the map can be interrogated which produces the turbine efficiency and power cycle mass flow rate. If

the turbine efficiency does not match the original guess, the guess should be updated and the power cycle state points resolved. Similarly, if the mass flow rates do not match the input flow rate, the guess for its efficiency is updated until the guessed and calculated mass flow rates are equal. Once the efficiencies and mass flows match, the turbine operational conditions are set. Now, the turbine power ($\dot{W}_{p,t}$) is calculated using equation (3.8). The power transferred from the turbine to the compressor is calculated using equation (3.7) using the assumed shaft efficiency. If the calculated transmitted power and the calculated compressor power are not the same, then all of the saturation temperatures should be adjusted and the entire model is iterated until this is the case. Once the turbine power is found, the rest of the power cycle state points are easily calculated by using equations (3.10) through (3.14), and the overall cycle COP is calculated using equations (3.15) through (3.18).

This chapter provided a complete system model that can be used to calculate the TCCS performance at any operating condition. First, the baseline thermodynamic modeling approach was presented. The baseline modeling approach uses general thermodynamic equations to predict system performance at one individual design condition. A turbo-compressor Cordier analysis was presented, which confirmed the efficiency assumptions. The fluid selection procedure was outlined to show the impact of fluid combinations on the turbo-machine performance and heat exchanger pressure drops. The baseline heat exchanger *UA* calculations were shown, which are critical for the off-design performance modeling.

Next, the off-design performance methodology was presented in detail. The turbo-machine performance maps, generated by Barber-Nichols, were described and required parameters were explained. The *UA* scaling methodology was introduced and the heat transfer and area scaling factors were described. Finally, the complete methodology was outlined which allows for

performance predictions at any off-design condition. The next chapter will describe the design and construction of the test facility used to validate the modeling approach presented in this chapter.

CHAPTER 4. TEST FACILITY DESIGN AND CONSTRUCTION

The test facility was constructed to measure the performance of the system and to validate modeling methodology discussed in Chapter 3. The layout of the facility and pipe routing was modeled in Solidworks before the initial construction. A complete piping and instrumentation diagram (P&ID) is shown in Appendix B, and will be referenced throughout this chapter to aid in the description of various facility components.

Figure 4-1 shows an overview photo of the facility. The facility uses an approximate space of 25 × 45 × 20 ft (width × length × height) and the bulk construction was completed on the mezzanine level of the Powerhouse Energy Campus from August 2016 to February 2017. The facility was designed with two primary fluid loops, one exhaust gas simulation loop, four

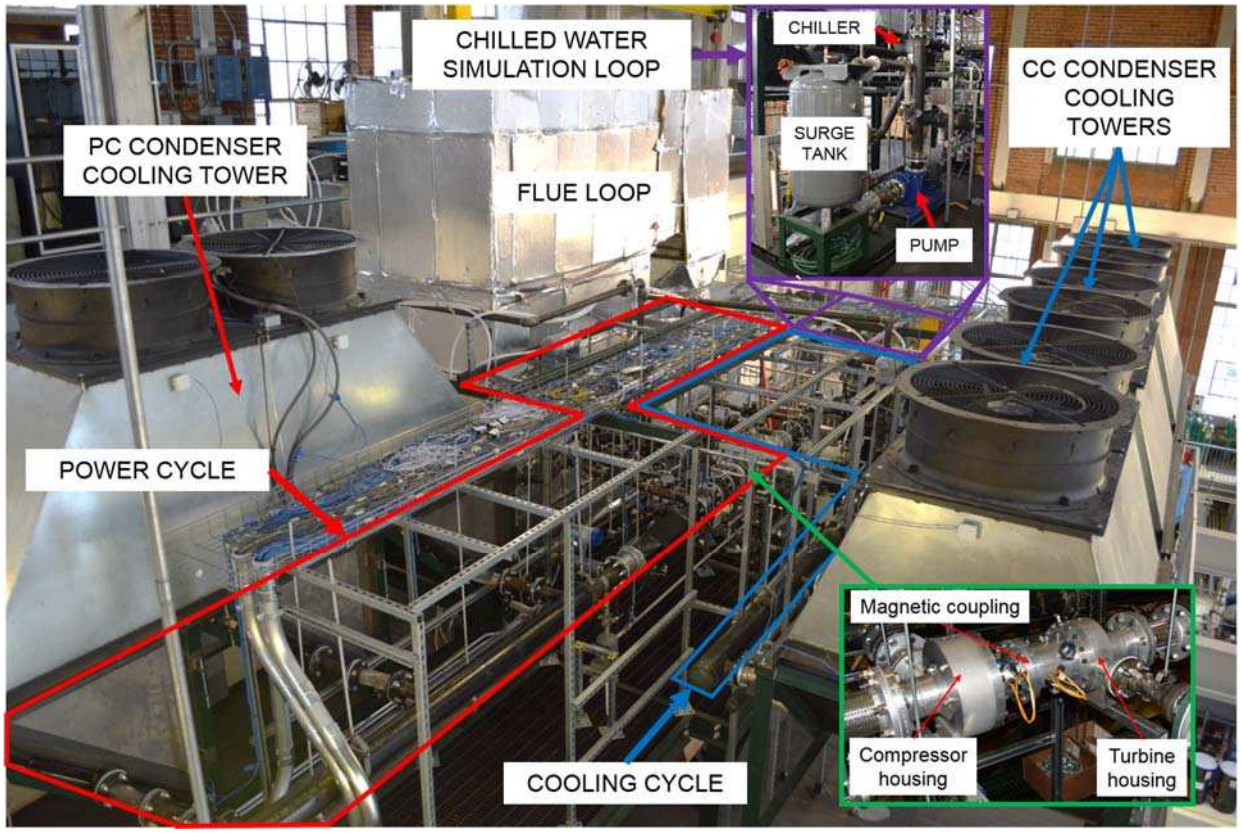

Figure 4-1. Overview of the TCCS facility located at the Powerhouse Energy Campus.

condenser cooling towers, and one cooling water simulation loop. The power cycle is denoted by red lines in the P&ID and is a recuperative Rankine cycle operating with HFE-7000 as the working fluid. The cooling cycle is shown by blue lines in the P&ID and is a vapor-compression cycle operating with R134a as the working fluid. The flue gas exhaust simulation loop (denoted by purple lines in the PFD) circulates hot air across the PC boiler heat exchangers. One condenser cooling tower is located on the power cycle, while three are in the cooling cycle. The condenser cooling tower fans pull air through the condensers in their respective loops to cool the working fluids. The air side of the condenser cooling towers are shown as purple lines on the second page of the P&ID. The cooling water simulation loop working fluid is a 30:70 mixture of propylene-gylol:water and is shown as a green line in the P&ID. The cooling water loop interacts with the cooling cycle evaporators to provide a chilling load. The cooling water loop also has interaction with the Powerhouse high temperature coolant system (~75°C, and also 30:70 propylene-glycol:water mixture). These lines are shown as beige on the P&ID.

The following sections describe the test facility components in detail. First, the major system components are described including the turbo-compressor, power cycle, cooling cycle, exhaust simulation loop, cooling water simulation loop, and bearing lines. The second section is the miscellaneous components such as valves, piping, safety equipment, lifting equipment, and electrical. Third, the instrumentation and data acquisition systems are described. Finally, the test matrix and calculation of the primary system metrics is outlined and concludes with an uncertainty analysis. Although the components are described in detail in this section, complete component, valve, and instrument lists are shown in Appendices C, D, and E, respectively.

4.1. Major System Component Description

4.1.1. Turbo-Compressor

The BNTC-07-000 Magnetically-Coupled Turbo Compressor is a turbine driven compressor unit. The turbine and compressor sides were designed for fluids HFE-7000 and R152a, respectively. However, the cooling cycle fluid selected for this research was R134a due to its low flammability in comparison to R152a. The refrigerants are isolated from one another by a hermetic barrier can, which is plastic and allows a magnetic field to transmit across it and couple the assembly.

A schematic cut-away diagram is shown in Figure 4-2 and the actually installed device is shown in Figure 4-3. On the power cycle, the vapor from the boiler enters the turbine radially and exits axially, while on the cooling cycle, the vapor enters the compressor axially and exits radially. The turbine rotating assembly consists of a radial inflow turbine, shaft, and female magnetic coupling, all supported by two ball bearings. Similarly, the compressor rotating assembly consists of a centrifugal compressor, shaft, and male magnetic coupling, all supported by two ball bearings. Housings surround both shafts to serve as aligning mechanisms for the shafts, structural support,

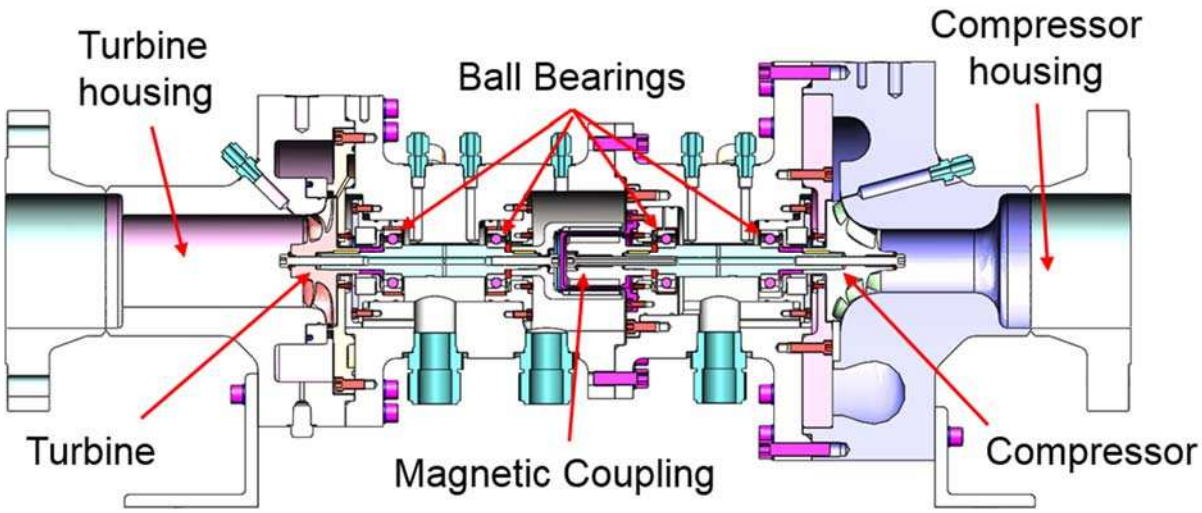

Figure 4-2. Schematic cut-away diagram of the turbo-machine.

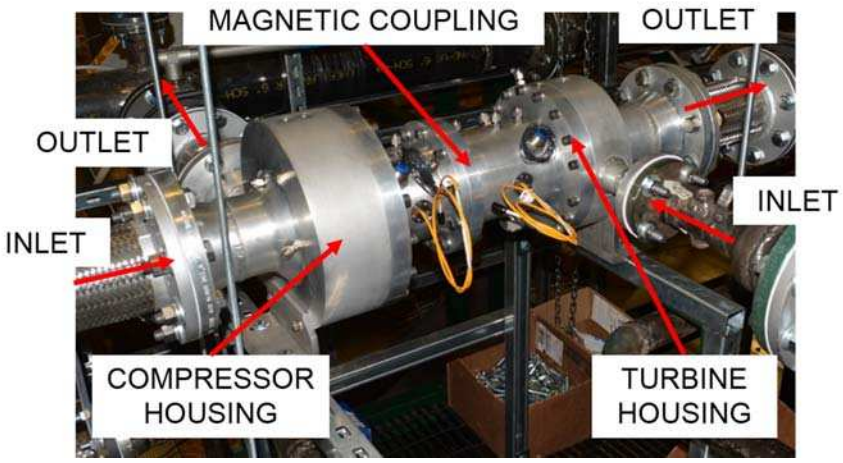

Figure 4-3. Turbo-compressor installed in facility.

and pressure containing devices. The maximum operating speed of the unit is 30,000 rpm. The magnetic coupling will provide the required torque to transmit approximately 12 kW of power through the coupling at the nominal speed. The baseline design case is labeled on the turbine and compressor performance maps shown in Figures 3-9 and 3-10. These maps can be used with the performance methodology provided in Chapter three to determine the turbo-machine efficiency and speed at any operating condition.

4.1.2. Power Cycle Components

The power cycle is an organic Rankine cycle operating with Novec 7000 Engineering Fluid (HFE-7000). HFE-7000's technical name and chemical formula are 1-methoxyheptafluoropropane and $C_3F_7OCH_3$, respectively, and it is manufactured by 3M Manufacturing Company. It is a non-flammable, non-corrosive, low global warming potential fluid that boils at 34°C at standard atmospheric pressure.

The HFE-7000 fluid starts as a liquid at the power cycle pump (Figure 4-4) where it is pumped to a high pressure. The pump is a Model H7F Heavy Duty Industrial Gear Pump manufactured by Liquiflo and has a maximum differential pressure of 225 psi, a maximum flow rate of 10.7 GPM, and a NPSH required of 5.2 ft. To avoid cavitation, the pump is located on the

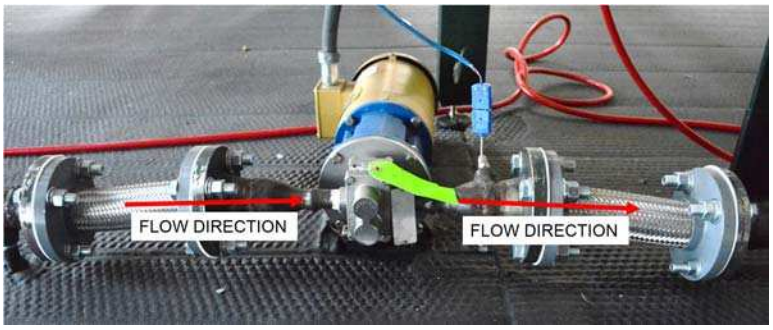

Figure 4-4. PC Pump

mezzanine floor to take advantage of added gravity head. The pump is driven by a magnetic-drive 1.5 HP Baldor Motor (Part #VEM3554) with a maximum spin speed of 1750 RPM. The motor is powered and controlled by an "Altivar 312" variable frequency drive (VFD) (Part# ATV312HU15M2) manufactured by Schneider Electric shown in Figure 4-5. The VFD operates on 480VAC 3-phase power and outputs frequencies between 0 and 60 Hz.

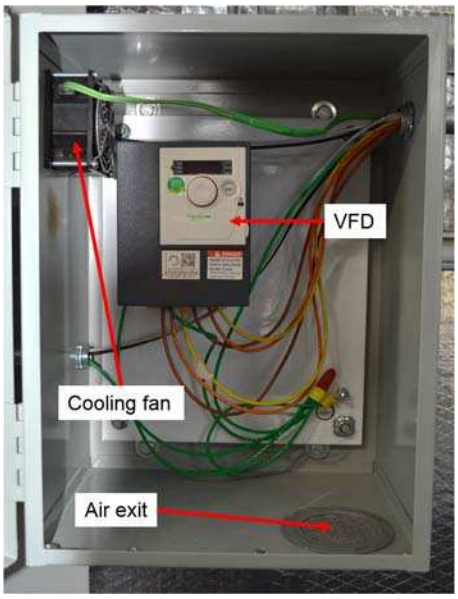

Figure 4-5. PC pump VFD containment box.

Immediately following the pump is a bladder type accumulator manufactured by Parker-Hannifin (Part #BA15B3T01P2) shown in Figure 4-6. The pressure rating is 3000 psi, the total volume is 15 gallons, and the bottom connection is a 1.5" NPT. The accumulator allows space for pump surge and helps regulate the high side pressure of the cycle. The power cycle accumulator

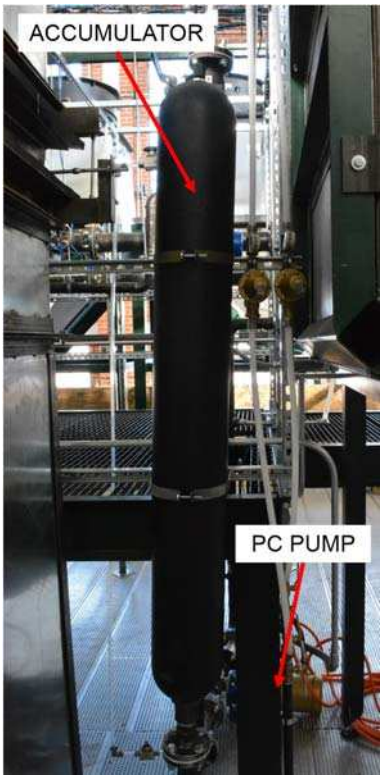

Figure 4-6. PC accumulator and pump.

was selected specifically because the bladder is made of an ethylene-propylene (EPR) compound, which does not degrade when in contact with HFE-7000. The accumulator is located directly after the pump at the lowest point of the loop.

The filter bypass loop is located directly after the accumulator. The bypass loop has three isolation valves and one replaceable core filter-drier manufactured by Parker Hannifin Corporation (Model #P9617-400716) as shown in Figure 4-7. The filters have a 2-1/8" ODF copper connection, which was welded to a NPT male threaded copper coupler. The copper welding was done by Distinctive Welding, Inc. located in Fort Collins. The filter-drier removes particulates in the flow (i.e. dust, dirt, weld slag, etc.) and any water vapor that may be present. The filter-drier has two replaceable cores (Parker Part #PFE-48BF 031858-00) that are suitable in bi-directional applications and have filtration capabilities down to 20 microns.

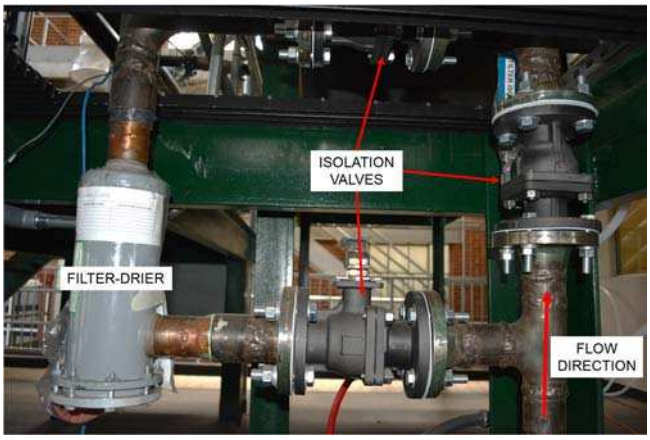

Figure 4-7. PC filter-drier loop

The high pressure HFE-7000 liquid now passes through a mass flow meter shown in Figure 4-8. The mass flow meter is a twin tube Coriolis meter (Optimass 1400 – S25) manufactured by Krohne. The S25 has a maximum flow rate of 27,000 kg/hr, minimal pressure drop, and a ±0.15% accuracy. The meter has a 2 inch flanged connection and is made of stainless steel. The meter comes equipped with MFC 400 signal converter also manufactured by Krohne. The device takes signals from the mass flow meter, converts them to a usable analog signal, and displays the flow rate on an LCD screen. The converters operate on 120 VAC power which is delivered from the south wall distribution panel as shown in Section 4.2.6.

The recuperator follows the mass flow meter and provides efficiency benefits for the Rankine cycle by using the hot vapor at the turbine outlet to preheat the liquid before it enters the

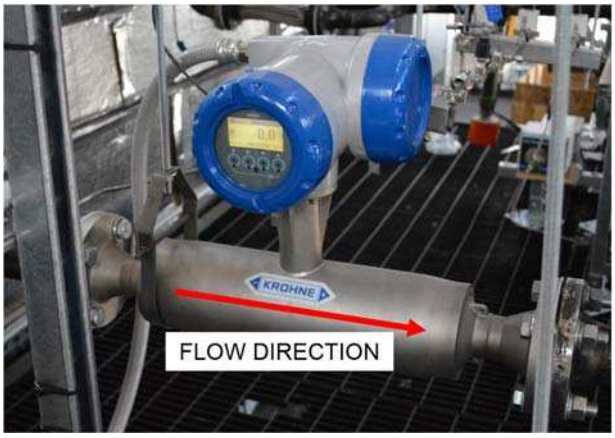

Figure 4-8. PC mass flow meter.

boiler, thus reducing the required boiler heat input. The heat exchanger was manufactured by Modine and is a brazed aluminum plate and fin type with a total heat duty of 26.5 kW in the baseline case. The design data for the heat exchanger is shown in Table 4-1 and a photo of the install shown in Figure 4-9. The heat exchanger has dimensions of 450 × 154 × 150 mm and weighs 22 kg. The hot vapor travels through the large ports and the cold fluid travels in a counter flow configuration with 25 liquid plates and 26 vapor plates.

Table 4-1. Power cycle recuperator predicted performance.

	Working fluid vapor: HFE 7000						Working fluid liquid: HFE 7000					
Q (kW)	m (kg/s)	P_{in} (kPa)	ΔP (kPa)	T_{in} (°C)	T_{out} (°C)	ΔT_{sat} (°C)	m (kg/s)	P_{in} (kPa)	ΔP (kPa)	T_{in} (°C)	T_{out} (°C)	ε (%)
26.5	0.61	89.2	4.7*	75.0	30.0	0	0.61	577	1.6*	23.5	58.3	87.4

Black indicates specification, blue indicates modeling result.

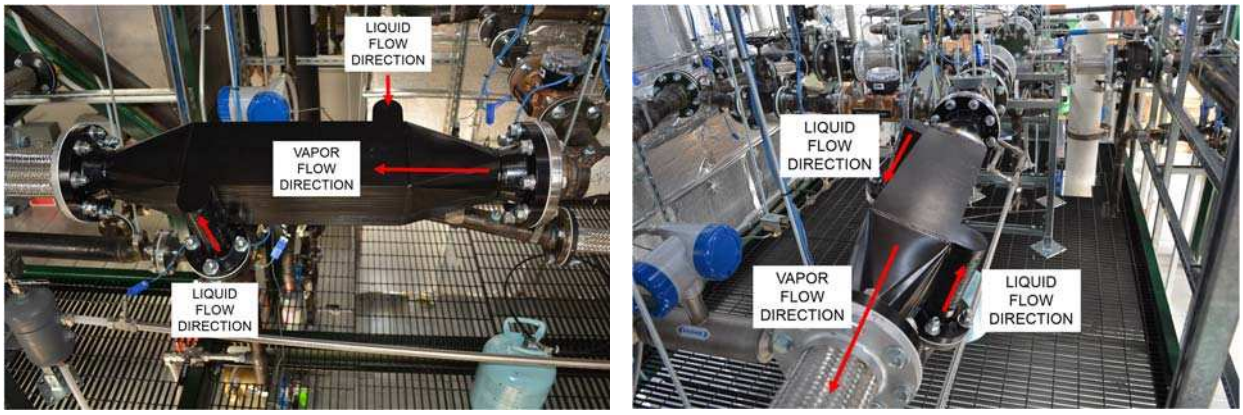

(a) **(b)**

Figure 4-9. Recuperator installed in the power cycle of the TCCS.

The next component in the power cycle is the boiler heat exchangers manufactured by Modine Manufacturing. The HFE-7000 fluid enters the boilers as a liquid and exits as a superheated vapor because heat is added from the exhaust simulation loop. There are two boilers on the power cycle. The heat exchangers are brazed aluminum tube fin construction with a total heat duty of 99.8 kW in the baseline design case. The design data for each heat exchanger is shown in Table 4-2 and photos of the install in Figures 4-10 and 4-11. Each of the two heat exchangers each have dimensions of 1500 × 1237 mm and weigh 120 kg. As noted in Section 3.1.5, the heat

Table 4-2. Power cycle waste heat boiler predicted performance (Single HEX).

Q (kW)	Working fluid: HFE 7000						Exhaust: Hot Air					ε (%)
	m (kg/s)	P_{in} (kPa)	ΔP (kPa)	T_{in} (°C)	T_{out} (°C)	ΔT_{sat} (°C)	V (m³/h)	P_{in} (kPa)	ΔP (kPa)	T_{in} (°C)	T_{out} (°C)	
49.9	0.30	573.5	1.6*	58.1	103.8	11.3	15682	85	0.21	106	91.5	98.6

Black indicates specification, blue indicates modeling result.

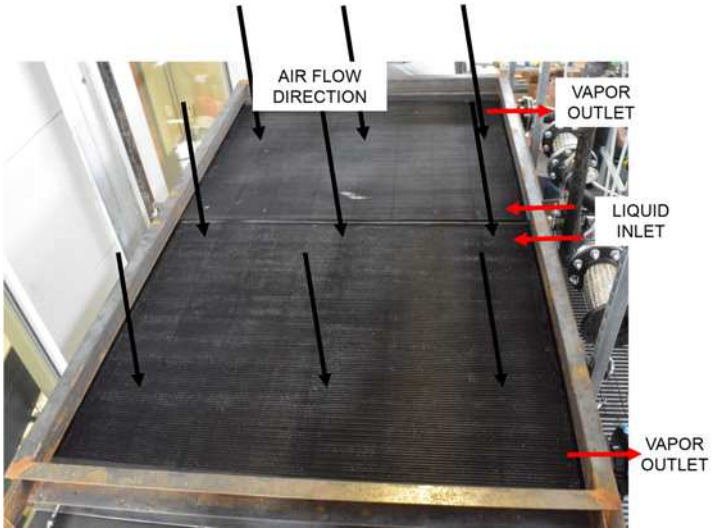

Figure 4-10. Both boilers in the test facility prior to flue loop completion.

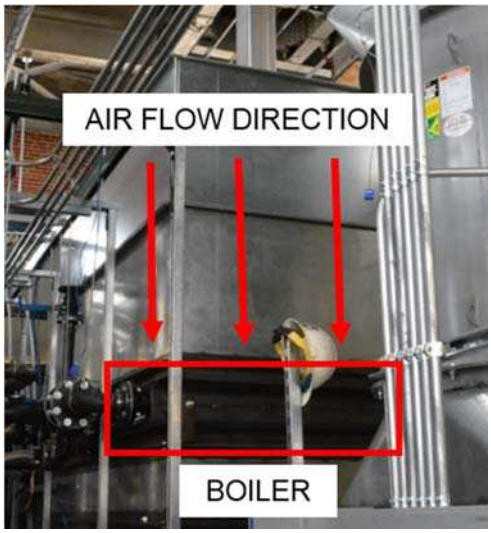

Figure 4-11. Side view of boilers with flue loop tops connected.

exchangers are fairly large because the secondary fluid is air, so a large surface area is required to transfer enough heat. The fluid travels in a 2-row, 2-pass, cross-counter flow arrangement with 130 tubes per row.

The HFE-7000 fluid exits the boilers as a superheated vapor and has three options for flow depending on valve condition: through the turbine, turbine bypass, or emergency blow-down safety valves as shown in Figure 4-12. The turbine is described in Section 4.1.1. The turbine bypass line is used during start-up and shutdown to avoid sending liquid droplets into the turbine. Lack of superheat at the boiler outlet is common during start-up and shutdown phases. The turbine bypass line has a globe style expansion valve (Valve 27 in the P&ID shown in Appendix B). The expansion valve is used to control the pressure ratio of the loop before the flow accesses the turbine. After the expansion valve is a XMTR model turbine wheel volumetric flow meter,

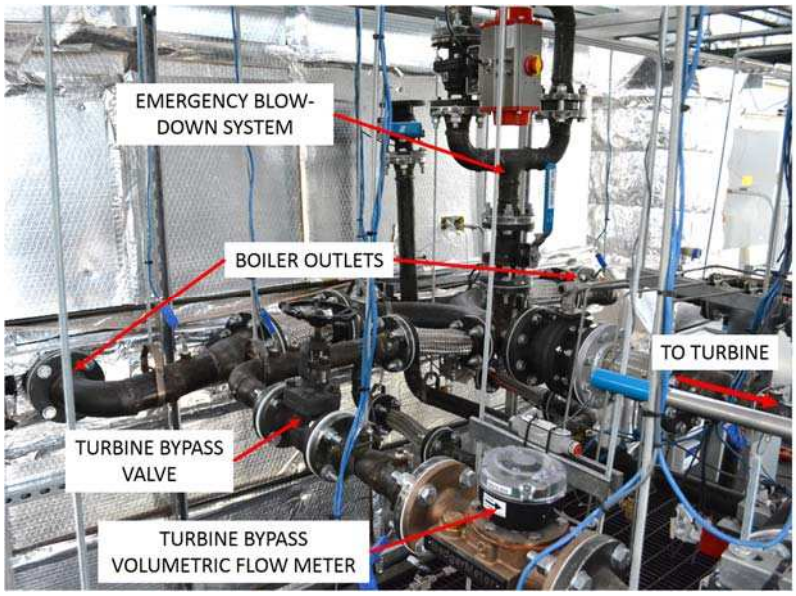

Figure 4-12. The fluid flows from the outlet of the boilers and has options to enter the emergency blow-down, the turbine bypass, or the turbine.

manufactured by Badger Meter, Inc (Part #PFTA20/2). The flow meter outputs 17.60 pulses per gallon to the built in signal converter, which converts the signal into a 4-20mA source. The flow meter is bronze, has two inch flange connections, and has temperature and pressure ratings of 121°C and 150 psi, respectively. The accuracy of the measurement for the flow range between 20 and 160 GPM is ±0.5%.

The emergency blow-down safety system for the power cycle includes a pneumatically actuated blow-down valve and a burst disk shown in Figure 4-13. More information regarding system safety is shown in Section F.1 and the emergency shut-down procedure in Section F.4.4.

The emergency blow-down valves are used to manually release the pressure in the power cycle when an over-pressurization situation occurs. The valve is a 2 inch pneumatically actuated Triac Series 90 (Part# 90C-F1-0200) valve. The valve is operated by an 80 psi pneumatic line tied into the main Powerhouse shop lines. The emergency valves fail to the open position, so when the 80 psi air lines are activated, the emergency valve will be in the closed position. An electrically activated solenoid valve (Grainger Part#24W658) determines if air pressure is being supplied to

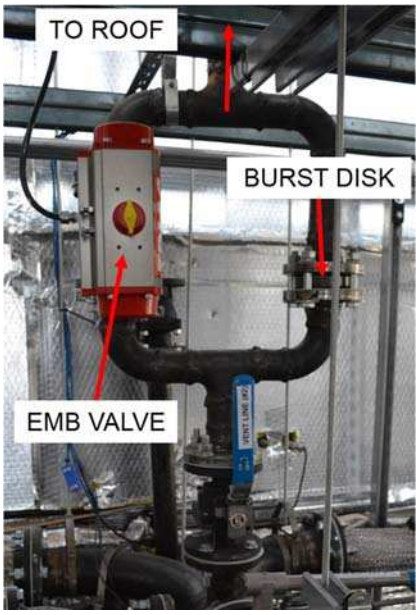

Figure 4-13. PC EMB system.

the emergency valve. The solenoid valve fails to the closed position, so when electricity is supplied, the valve is in the open position and pressure is supplied to the blow-down valve. The solenoid valves are powered by a 24 V power supply (Grainger Part # 21XP10), which itself is powered by a 2000VA/1200W uninterrupted power supply (UPS) (model #VP2000) manufactured by DirectUPS and shown in Figure 4-14. The UPS can supply a 120 VAC output voltage to the DC power supply for an estimated 12 hours if the electricity is lost in the building. In the case of lost pneumatic pressure from the main Powerhouse shop line, a 2 gallon air storage tank, manufactured by Amalga Composites (ACI2102-954), can supply air to the blow-down valves for a limited time.

The valve has two red switch-buttons, one inside the control room, and the other on the mezzanine. Figure 4-15 shows an example of the cage to protect the buttons. The switch-buttons stop electricity to the solenoid valves, thus dropping the pressure and opening the emergency blow-down valves. Only under emergency circumstances should the buttons be pressed while the system is charged.

Figure 4-14. The UPS maintains power to EMB systems in a power loss scenario.

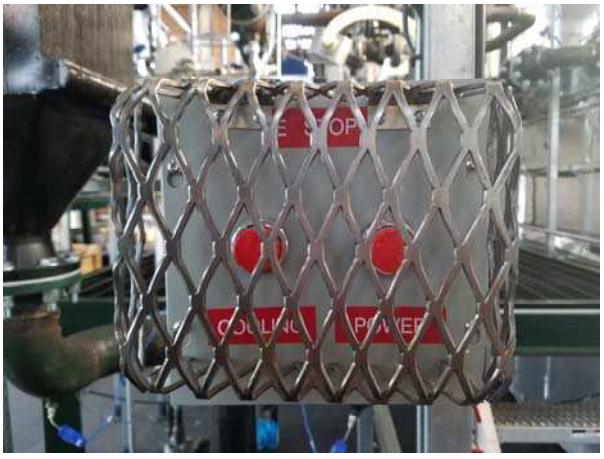

Figure 4-15. EMB buttons located on the mezzanine. An identical box is located in the control room.

The burst disk is the other method of limiting an over-pressurization situation in the power cycle. The burst disk is a Flange-Mounted Graphite Disc manufactured by Mersen and purchased through McMaster-Carr. The burst disk breaks at 175 psi (Part #4858K505) to be above the maximum allowable working pressure and the emergency blow down burst pressure. The disks have a temperature range of -20 to 300°F and have a burst accuracy of 5%. The gasket material is neoprene, so there is some potential for degradation of the gasket material on the power cycle. The gasket materials should be monitored carefully throughout the TCCS life.

The HFE-7000 fluid next travels from the turbine bypass or turbine to the vapor side of the recuperator. The properties of the recuperator are shown in Table 4-1. After exiting the recuperator, the vapor enters the condenser distribution manifold and into the three condensers manufactured by Modine. The superheated HFE-7000 vapor enters the heat exchangers and condenses to a sub-cooled liquid by transferring the heat to air passing through the secondary side of the heat exchanger. The heat exchangers are brazed aluminum tube and fin construction with a total heat duty of 91.8 kW in the baseline design case. The install photos are shown in Figure 4-16 and Figure 4-17 and the design data for each heat exchanger is shown in Table 4-3 and. Each heat exchanger

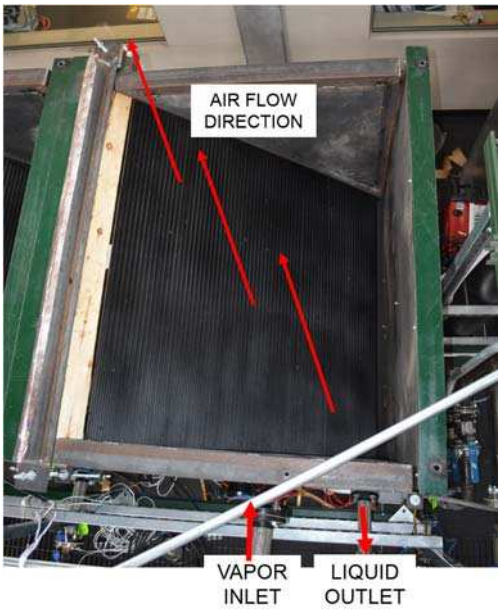

Figure 4-16. Top view of a PC condenser before installation.

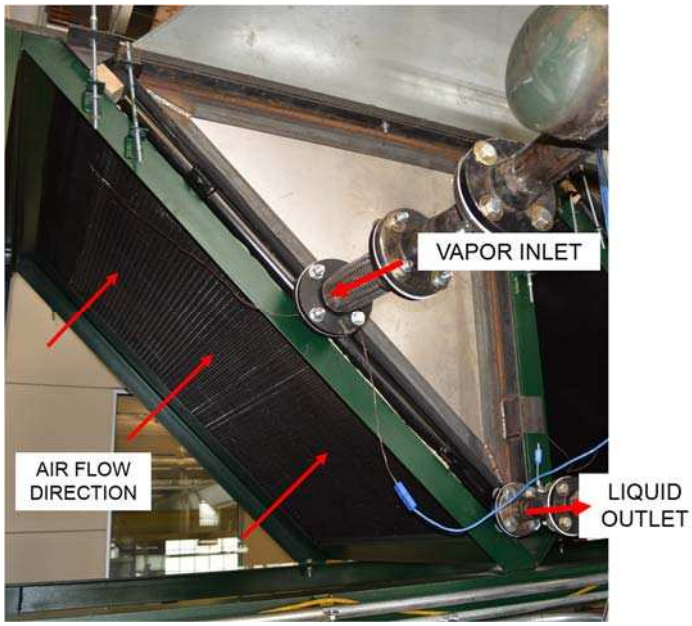

Figure 4-17. Side view of a PC condenser after installation

Table 4-3. Power cycle condenser predicted performance (Single HEX).

	Working fluid: HFE 7000						Air					
Q (kW)	m (kg/s)	P_{in} (kPa)	ΔP (kPa)	T_{in} (°C)	T_{out} (°C)	ΔT_{sat} (°C)	V (m^3/h)	P_{in} (kPa)	ΔP (kPa)	T_{in} (°C)	T_{out} (°C)	ε (%)
30.6	0.21	83.2	15.2*	29.4	19.8	-3.85	13000	85	0.045	15.0	23.2	96.2

Black indicates specification, blue indicates modeling result.

has dimensions of 1300 × 1384 mm and weighs 49 kg. The fluid travels in a 1 row, 2 pass, cross-flow arrangement with 145 total tubes. As noted in Section 3.1.5, the size of these heat exchangers is largely dependent on the heat exchanger *UA* and the secondary fluid flow.

The three power cycle condensers are supported by one cooling tower rack as shown in Figure 4-18. A sheet metal reducer is fixed above the condensers to funnel ambient air to the condenser fans. The two power cycle condenser fans are used to pull air through the condenser heat exchangers. Each fan is the same design (Part #ZN091-ZIQ.GL.V5P1) and was manufactured and purchased through Ziehl-Abegg. The fans are powered by an ECBlue motor running on a 3 phase 240VAC power source at 60 HZ. The power cycle baseline thermodynamic design condition is a total air flow volume of 39,000 m^3 hr^{-1} with a pressure drop of 45 Pa. The ECBlue motor has

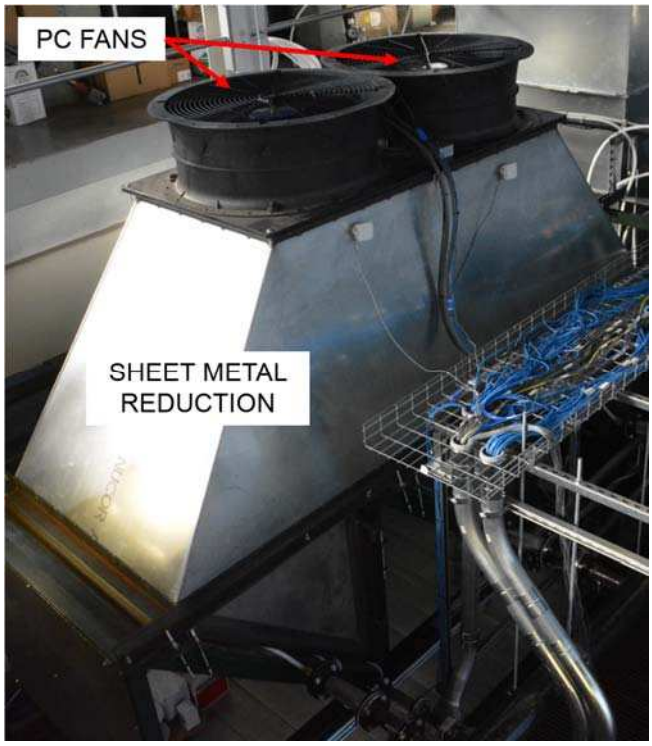

Figure 4-18. PC condenser cooling tower.

a total power intake of 2.46 kW at the design condition. The free delivery volumetric flow rate of each individual fan is approximately 33,200 m^3 hr^{-1} and the maximum static pressure is approximately 275 Pa.

The condenser fans are controlled by a UNIcon MODBUS Master Universal Control Module (Part #CXE/AV(E)) manufactured and purchased by Ziehl-Abegg and shown in Figure 4-19. The control module supplies a 0-10 VDC signal to the ECBlue motor to control the motor spin speed and thus volume flow. There is one control module for each set of two fans. One of the fans receives the master signal, while the other fan follows in a slave configuration. Finally, the sub-cooled HFE-7000 exits the condenser into the liquid collection manifold and is sent back to the pump to restart the cycle.

Figure 4-19. UNIcon Modbus master control unit for condenser fans.

4.1.3. Cooling Cycle Components

The cooling cycle is a vapor-compression cycle operating with fluid 1,1,1,2-Tetrafluoroethane (R134a). R134a was selected for testing in the cooling cycle due to its similar properties to R152a, commercial availability, and low flammability. The fluid was manufactured and purchased through Airgas, an Air Liquide Company. R134a has a chemical composition of $C_2H_2F_4$ and a CAS number 811-97-2. The fluid is compatible with all sealing surfaces and is a very common refrigerant.

The cooling cycle starts with a two-phase mixture exiting the expansion valves and entering the CC chiller as shown in Figure 4-20. The expansion valves are 1/2 inch globe style (Valves 28 and 29 in the P&ID in Appendix B). The expansion valves control the pressure ratio in the cooling

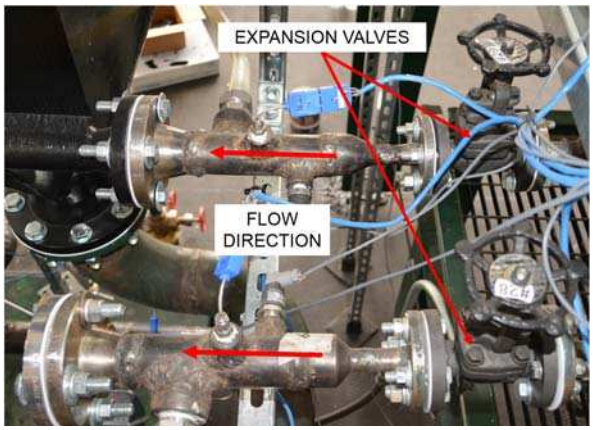

Figure 4-20. Cooling cycle expansion valves

cycle and are critical control mechanisms for the TCCS. The two-phase R134a enters the two chillers designed by Modine manufacturing. The two-phase refrigerant at the inlet becomes superheated vapor at outlet by transferring heat to the chilled water simulation loop (Section 4.1.5). The heat exchangers are a brazed aluminum plate and fin construction with a total heat duty of 251.8 kW in the baseline design case. The design data for each heat exchanger is shown in Table 4-4 and install photos are shown in Figure 4-21 and 4-22.

Table 4-4. Cooling cycle evaporator predicted performance. (Single HEX).

	Refrigerant: R152a						Coolant: 30% ethylene glycol 70% water (vol.)					
Q (kW)	m (kg/s)	P_{in} (kPa)	ΔP (kPa)	T_{in} (°C)	T_{out} (°C)	ΔT_{sat} (°C)	V (GPM)	P_{in} (kPa)	ΔP (kPa)	T_{in} (°C)	T_{out} (°C)	ε (%)
125.9	0.46	443	18.8	15.3	16.1	2.6	428.5	150	27.2	17.15	16	99.6

Black indicates specification, blue indicates modeling result.

Figure 4-21. Chillers installed in facility.

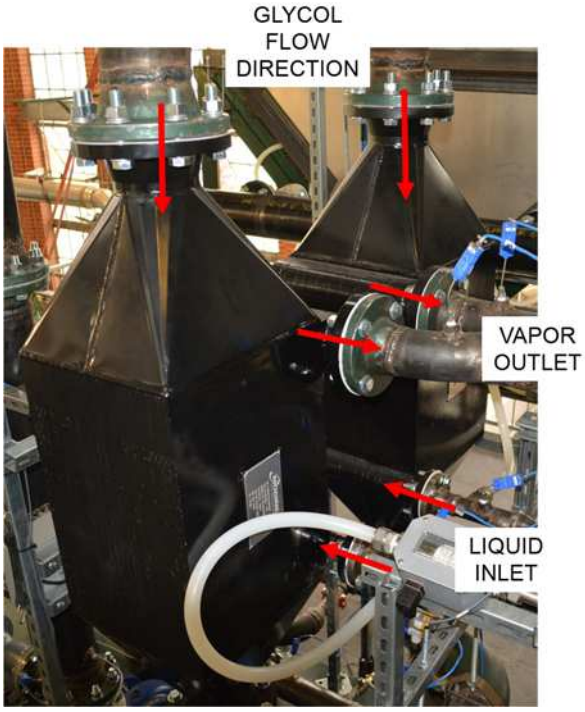

Figure 4-22. Chillers installed in facility.

Each heat exchanger has dimensions of 366 × 395 × 555 mm and weighs 93 kg. The fluid travels in an 8-pass cross-counter flow arrangement with 51 refrigerant layers and 52 coolant layers. One of the chillers developed a cross leak between the refrigerant and glycol sides, so it

was removed. For this reason, the research for this thesis included testing for only one chiller as shown in Figure 4-23.

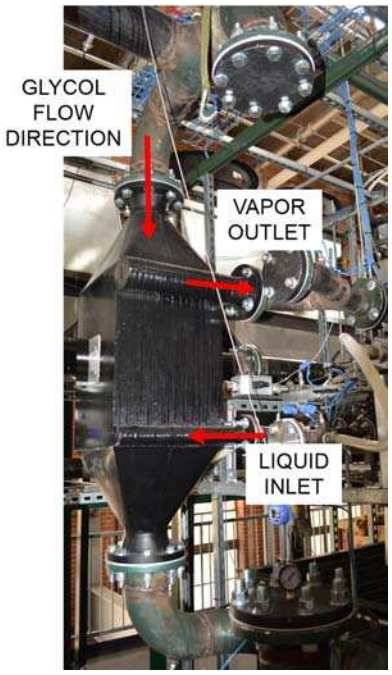

Figure 4-23. Single chiller installed in facility.

The superheated R134a vapor from the outlet of the chiller can either flow to the liquid-vapor separator bypass or directly to the compressor as shown in Figure 4-24. The compressor information is shown in Section 4.1.1. The liquid-vapor bypass line protects the compressor during scenarios in which liquid slugs could enter the compressor and damage the blades. The liquid vapor-separator bypass line has three isolation valves to open or close the lines during start-up and shut-down operations.

The TCCS liquid vapor separator is a Wright-Austin Type T Fabricated Liquid-Gas Separator (Model 2T150C) manufactured by Eaton. The separator is able to remove 99% of all liquid and solid entrainment particles 10 microns in size or larger. The pressure rating is 150 psi and the separator includes flanged connections and a drain port. The drain port contains a level

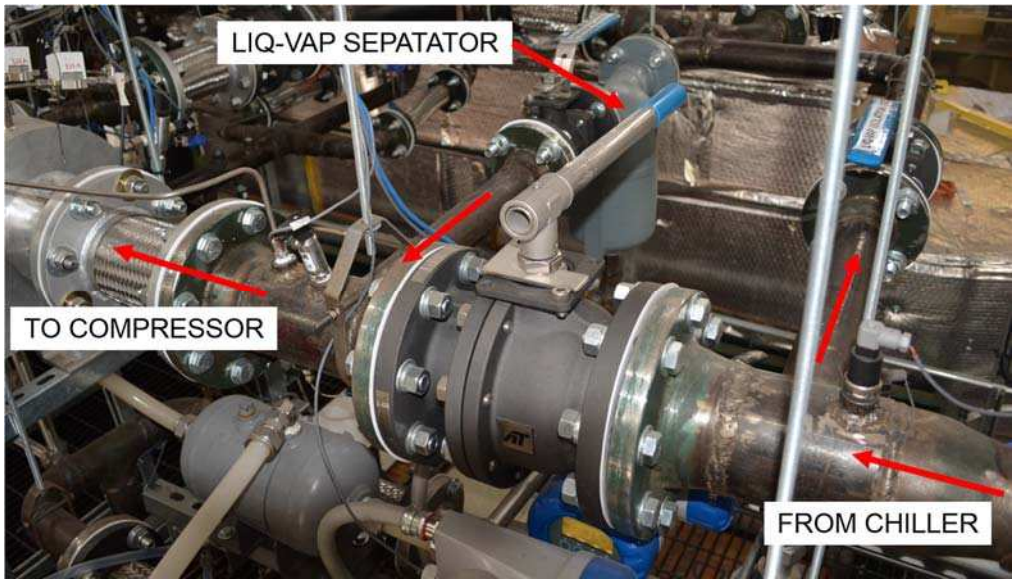

Figure 4-24. Liquid vapor separator bypass loop between the chiller and compressor.

switch and immersion heater so if the liquid level rises too high, the switch will engage the heater, thus boiling off the excess liquid.

The liquid vapor separator heater is a Screw-Plug Immersion Heater manufactured by Tempco Electric Heater Corporation (Part # TSP02794) and shown in Figure 4-25. The heater has a 1-1/4 NPT male threaded connector attached to the piping exiting the drain of the liquid-vapor separator. The heater is 316 stainless steel, has a temperature control knob, and has a heating element length of 9-1/4". The heater is able to supply 2000 Watts of power from a 120 VAC source and draws a 16.7 Amp current.

The heater is wired directly to the Horizontal-Mount Liquid-Level Float Switch manufactured by W.E. Anderson, a division of Dwyer Instruments, and purchased through McMaster-Carr (McMaster-Carr part # 48255K31). The float switch has a 1 inch NPT threaded connection attached to the piping just below the liquid-vapor separator drain. The material is 303/304 stainless steel and activates when the liquid refrigerant level reaches the sensor. The sensor is connected to the electrical relay, so when the switch activates, the relay powers the heater.

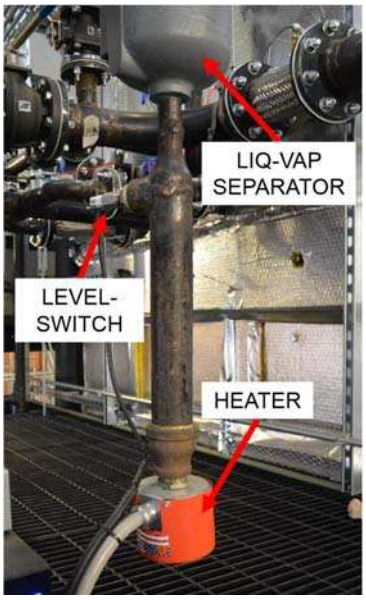

Figure 4-25. Liquid-vapor separator heater element.

The vapor exiting the liquid-vapor separator travels to the entrance of the compressor where the fluid is compressed to the high side pressure. The high pressure fluid is connected to the pressure relief safety lines as shown in Figure 4-26. The emergency blow-down safety system for the cooling cycle includes a pneumatically actuated blow-down valve and two burst disks. More information regarding system safety is shown in Section F.1 and the emergency shut-down procedure in Section F.4.4.

The emergency blow-down valve is used to manually release the pressure in cooling cycle when an over-pressurization situation occurs. The valve is a 2 inch pneumatically actuated Triac Series 90 (Part# 90C-F1-0200). The valves are operated by separate 80 psi pneumatic lines tied into the main Powerhouse shop lines. The emergency valve fails to the open position, so when the 80 psi air lines are activated, the emergency valve will be in the closed position. An electrically activated solenoid valve (Grainger Part#24W658) determines if air pressure is being supplied to

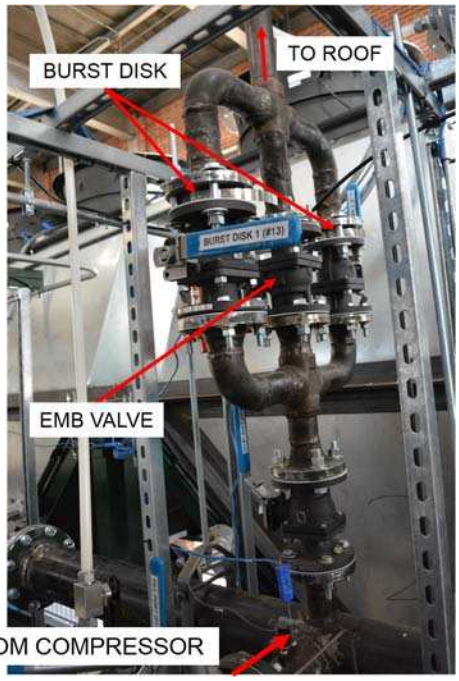

Figure 4-26. Cooling cycle emergency blow-down system.

the emergency valve. The solenoid valve fails to the closed position, so when electricity is supplied, the valve is in the open position and pressure is supplied to the blow-down valve. The solenoid valves are powered by a 24 V power supply (Grainger Part # 21XP10), which itself is powered by a 2000VA/1200W uninterrupted power supply (UPS) (model #VP2000) manufactured by DirectUPS. The UPS can supply a 120 VAC output voltage to the DC power supply for an estimated 12 hours if the electricity is lost in the building. In the case of lost pneumatic pressure from the main Powerhouse shop line, a 2 gallon air storage tank, manufactured by Amalga Composites (ACI2102-954), can supply air to the blowdown valves for a limited amount of time.

The valve has two red switch-buttons, one inside the control room, and the other on the mezzanine. The switch-buttons stop electricity to the solenoid valves, thus dropping the pressure and opening the emergency blow-down valves. A picture of the emergency blow-down buttons is shown in Figure 4-15. Only under emergency circumstances should the buttons be pressed while the system is full of charge.

The burst disks are the other method of limiting an over-pressurization situation in the power cycle. There are two burst disks in the cooling cycle and each is a Flange-Mounted Graphite Disk manufactured by Mersen and purchased through McMaster-Carr. The burst disks break at 175 psi (Part #4858K505) and 200 psi (Part #4858K506) depending on the operating conditions of the cooling cycle. The disks have a temperature range of -20 to 300°F and a 5% burst accuracy.

The R134a vapor then enters the distribution manifold so the cooling cycle condensers receive equal fluid distribution. There are six cooling cycle condensers mounted in the cooling tower racks. The heat exchangers take in superheated vapor from the distribution manifolds and condense the fluid to a sub-cooled liquid by transferring the heat to ambient air passing through the secondary side. The heat exchangers are brazed aluminum tube and fin construction with a total heat duty of 268.8 kW. The design data for each heat exchanger is shown in Table 4-5 and install photos in Figure 4-27 and Figure 4-28. Each of the heat exchangers has dimensions of 1650 × 1433 mm and weighs 68 kg. The fluid travels in a 1 row, 2 pass cross-flow arrangement with 145 total tubes. As noted in Section 3.1.5, the heat exchanger *UA* and secondary air side flow rate sets the large size required for these heat exchangers.

The cooling cycle has three heat exchanger racks with two heat exchangers per rack and two fans per rack (six total fans). A sheet metal reducer is fixed above the condensers to funnel ambient air up to the condenser fans as shown in Figure 4-29. Each fan is the same design (Part #ZN091-ZIQ.GL.V5P1) and was manufactured and purchased through Ziehl-Abegg. The fans are powered by an ECBlue motor running on a 3 phase 240VAC power source at 60 HZ. The cooling

Table 4-5. Cooling cycle condenser predicted performance. (Single HEX).

	Refrigerant: R152a						Air					
Q (kW)	m (kg/s)	P_{in} (kPa)	ΔP (kPa)	T_{in} (°C)	T_{out} (°C)	ΔT_{sat} (°C)	V (m^3/h)	P_{in} (kPa)	ΔP (kPa)	T_{in} (°C)	T_{out} (°C)	ε (%)
44.8	0.15	569.8	3.7*	31.3	21.7	-1.3	22500	85	0.1	15.0	21.9	96.1

Figure 4-27. Cooling cycle condensers in one rack prior to complete installation.

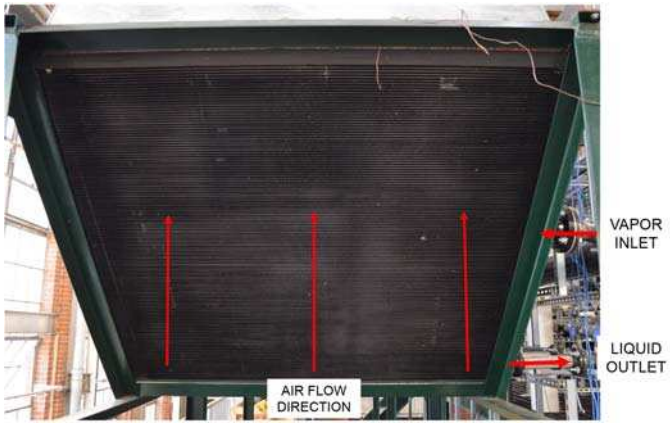

Figure 4-28. Cooling cycle condenser after installation.

cycle design condition is a total air flow volume of 135,000 m^3 hr^{-1} with a pressure drop of 89 Pa. The ECBlue motor has a total power intake of 11.34 kW at the design condition.

The condenser fans are controlled by a UNIcon MODBUS Master Universal Control Module (Part#CXE/AV(E)) manufactured and purchased by Ziehl-Abegg. The control module supplies a 0-10 VDC signal to the ECBlue motor to control the motor spin speed and thus volume flow. There is one control module for each set of two fans. One of the fans receives the master signal, while the other fan follows in a slave configuration.

Figure 4-29. Cooling cycle condenser fans on top of the sheet metal reductions

At the CC condenser outlet, the fluid enters an accumulator that helps regulate the CC pressure and protect against fluid surges. Figure 4-30 shows the accumulator installed in the facility. The accumulator is a bladder type manufactured by Accumulators, Inc. (Part #A15TR3100WS). The pressure rating is 3000 psi, the volume 15 gallons, and the connection port is a 1.25" NPT. The bladder material for the accumulator is made of Buna-Nitril.

Figure 4-30. Cooling cycle accumulator.

After the accumulator, the liquid refrigerant can enter the filter-drier bypass loop or continue to the expansion valves as shown in Figure 4-31. The bypass loop has three isolation valves and one replaceable core filter-drier manufactured by Parker Hannifin Corporation (Model #P9617-400716). The filters have a 2-1/8" ODF copper connection which was welded to a NPT male threaded copper coupler. The copper welding was done by Distinctive Welding, Inc. located in Fort Collins. The filter-drier removes particulates in the flow (i.e. dust, dirt, weld slag, etc.) and any water vapor that may be present. The filter-drier has two replaceable cores (Parker Part # PFE-

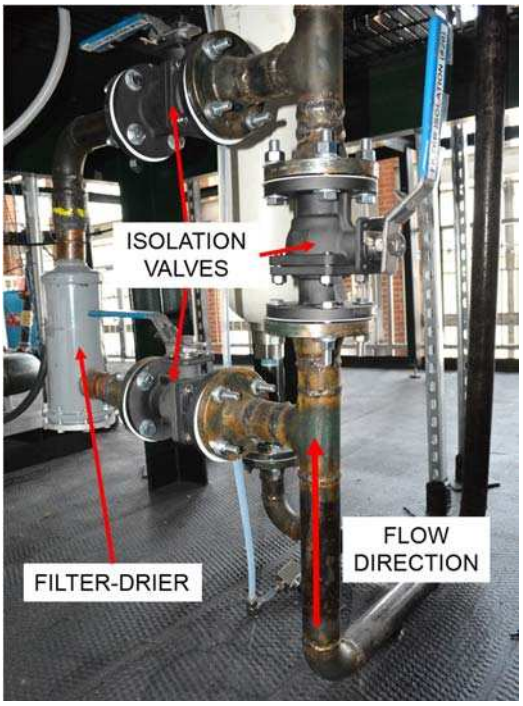

Figure 4-31. Cooling cycle filer bypass line.

48BF 031858-00) that are suitable in bi-directional applications and have filtration capabilities down to 20 microns.

After the filter-driers, the fluid splits into two sections to enter the two CC expansion valves separately. However, before the expansion valves, the fluid passes through mass flow meters shown in Figure 4-32. The mass flow meters are twin tube Coriolis meters (Optimass 1400 – S25) manufactured by Krohne. The S25 have a maximum flow rate of 27,000 kg hr^{-1}, minimal pressure drop, and a ±0.15% accuracy. The meters have a 2 inch flanged connection and are made of stainless steel. Each meter is equipped with MFC 400 signal converter also manufactured by Krohne. The device takes signals from the mass flow meter, converts them to a usable analog signal, and displays the flow rate on an LCD screen. The converters operate on 120 VAC power, which is delivered from the South wall distribution panel as shown in Section 4.2.6. Immediately following the mass flow meters are the cooling cycle expansion valves, where the cooling cycle restarts.

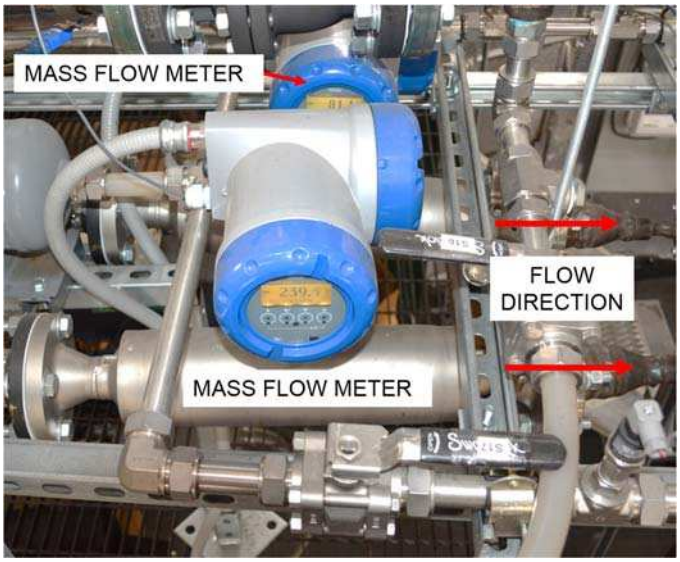

Figure 4-32. Cooling cycle mass flow meters.

4.1.4. Exhaust Simulation Loop Components

The waste heat simulation loop consists of three major components: the boiler heat exchangers, the air heater, and the circulation fan. Figure 4-33 shows the solid model of the loop. The boiler heat exchangers are described in Section 4.1.2. The sheet metal for the loop was constructed by Horizon Mechanical Solutions located in Fort Collins. The entire loop is covered in insulation to eliminate heat losses and provide safety to the TCCS operators.

The air heater simulates the exhaust gases by increasing the air temperature to 106°C at the boiler inlet. The unit is a Model RP-W coil resistance heater manufactured by Warren Technology (Serial #26184-001). Figure 4-34 shows the electric heater location in the facility. The heater has a maximum power rating of 120 kW and operates with 480VAC 3-phase power. The heater has a heating element panel located in the vertical position and a control panel (Figure 4-35) located on the third floor of the Powerhouse. The control panel is operated from the control room via LabVIEW software.

The flue gas circulation fan provides the air flow rate over the boiler heat exchangers as shown in Figure 4-36. The fan is an Aerovent Vaneaxial fan model VWBD 43W7. The fan has 7

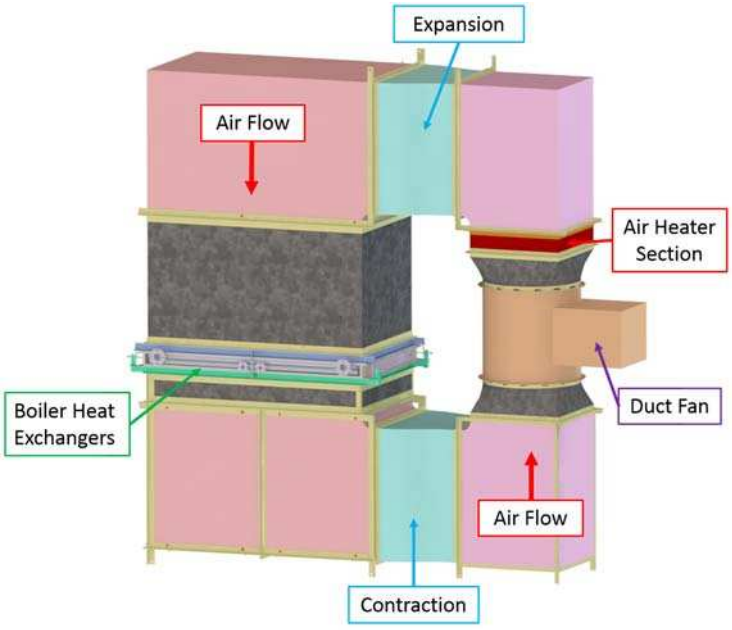

Figure 4-33. Flue loop model.

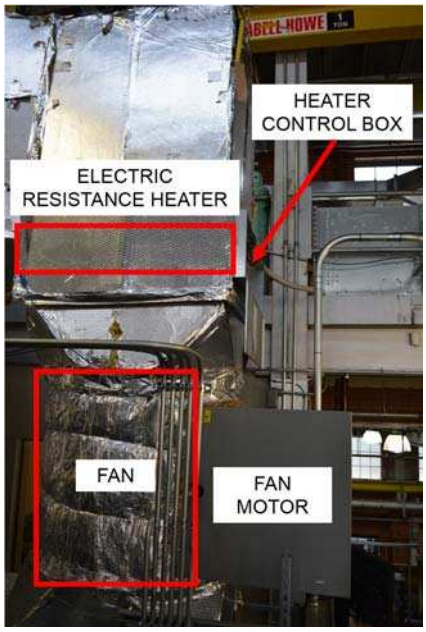

Figure 4-34. Heater and fan installed in flue loop.

blades, a 43" diameter, and a 15HP fixed speed V-belt drive motor set to operate at 1800 RPM with an operating frequency of 60 Hz. The fan was selected to deliver a maximum flow rate of 35,859 CFM at a pressure drop of 1" SP. The actual design point of the system is 18,459.6 CFM which equates to 31,362 m^3 hr^{-1} and meets the scaled power plant design condition as mentioned in Section 3.1.1.

Figure 4-35. Heater control panel with inputs from Labview program.

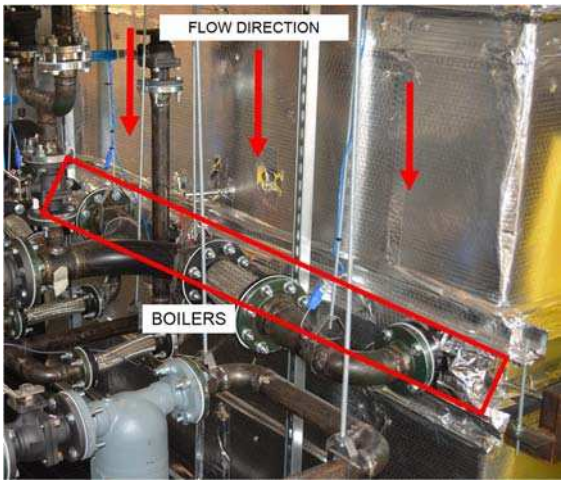

Figure 4-36. Boiler heat exchangers within the exhaust simulation loop.

The circulation fan is powered and controlled by an "Altivar 212" VFD (Part# ATV212HD11N4) manufactured by Schneider Electric and purchased through Grainger (Grainger # 6MVC5). The VFD, shown in Figure 4-37, has a maximum horsepower range of 15 HP and operates on 480VAC 3-phase power. It can output a frequency between 0 and 200 Hz and has a programmable control box with either local or remote control options.

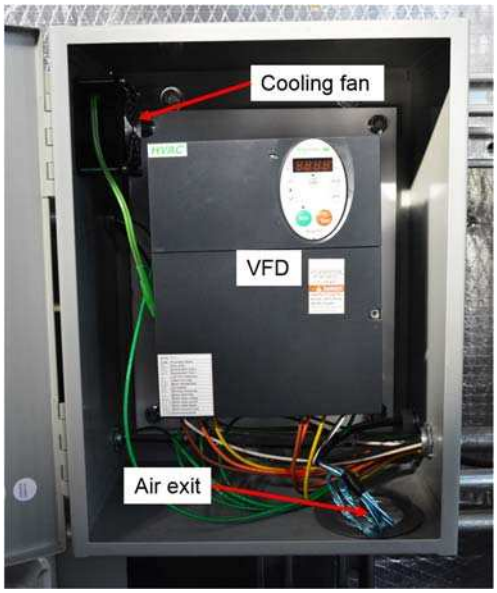

Figure 4-37. Tunnel circulation fan variable frequency drive.

4.1.5. Cooling Water Simulation Components

The cooling water simulation loop is used to provide a cooling load for the TCCS. Figure 4-38 and Figure 4-39 show two angles for the cooling simulation loop. The loops pump circulates a 30:70 mixture of propylene-glycol:water through the cooling cycle evaporators, the glycol heat exchanger, and the surge tank. The design point for the loop was to deliver 250 kW_{th} of heat over a 17.2°C to 16°C temperature drop at 850 GPM of cooling fluid flow rate. Due to design changes in construction, the system was unable to meet the design requirements.

A propylene-glycol:water mixture is used for the chilled water simulator to prevent corrosion and reduce the possibility of freezing. Dowfrost Heat Transfer Fluid manufactured by the Dow Chemical Company and purchased through Chempoint was used for the glycol loop. The mixture is 30% propylene-glycol and 70% water.

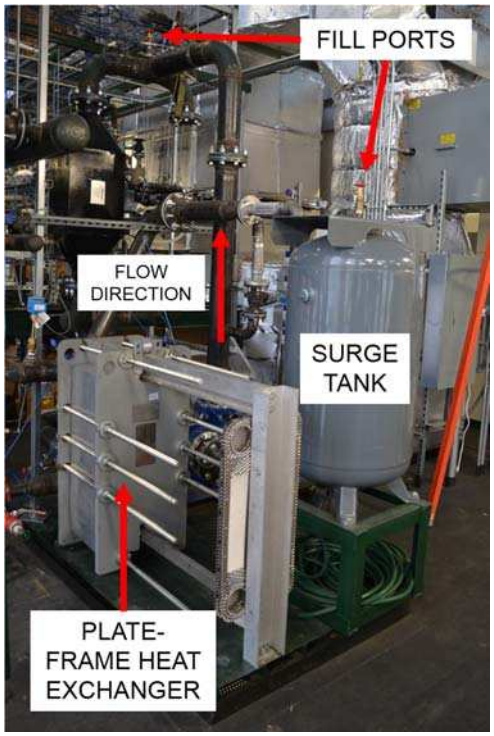

Figure 4-38. Cooling water circulation loop from East.

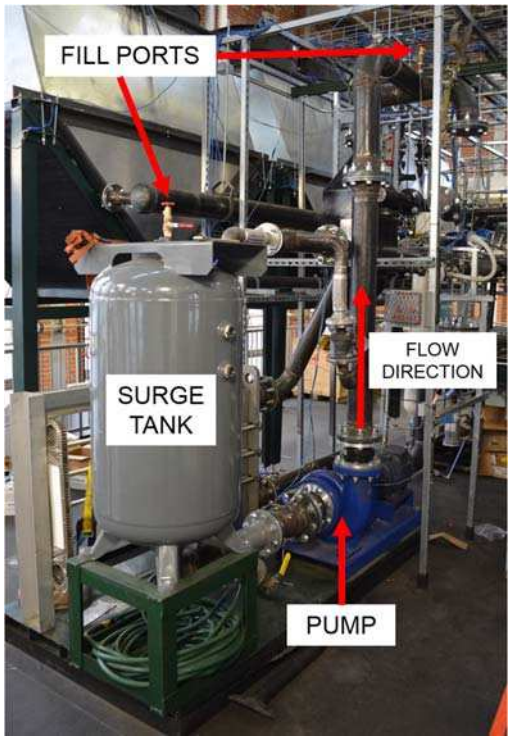

Figure 4-39. Cooling water circulation loop from West.

The glycol pump (Figure 4-40) circulates the 30:70 glycol:water mixture through the loop. The pump is a base mounted suction pump Model #3804 manufactured by Goulds Pumps and purchased through Water Technology Group. The pump is stainless steel fitted, oil lubricated, and is sealed mechanically. The pump is driven with a 15 HP, 1750 RPM premium efficient motor, manufactured by Marathon Motors (Part #254TTDCA6026) and can deliver 850 GPM of 30:70 propylene-glycol:water mixture at a pressure head of 40 ft. As will be noted later, the system pressure head is significanty higher than 40 ft which causes a decrease in flow rate.

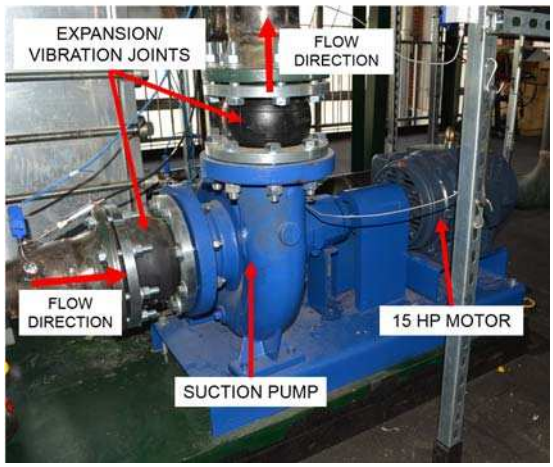

Figure 4-40. Glycol pump.

The glycol loop tank ensures complete fill of the glycol loop and provides surge protection for the pump. The tank was purchased through McMaster (Part #4376K12). The tank has a maximum capacity of 80 gallons and a maximum pressure of 200 psi. It has a 2 inch inlet port at the side of the tank and a 4 inch outlet port at the bottom of the tank. The bottom outlet port was installed by welding a 4 inch threaded outlet.

The plate-frame heat exchanger shown in Figure 4-38 provides the reheating required for the glycol fluid. The heat exchanger is a similar design to a plate and frame HEX manufactured by Alfa Laval (Model #M10M-FG). The heat exchanger is constructed with alloy 304 stainless steel, has NBRB Clip-on gaskets, and a 150 psi pressure rating. One side of the heat exchanger has the

cooled (~15°C) glycol fluid from the evaporator heat exchanger, while the other side contains hot (~70°C) glycol from the power house basement loop. The hot glycol supplies the reheat energy to increase the glycol loop temperature back to the desired inlet temperature.

The wye strainer on the glycol loop (Figure 4-41) is used to clean the fluid of debris before the pump. The strainer is a 5 inch flanged cast steel wye strainer (Model #77F-CSI) manufactured by Watts Water. The strainer has a maximum working pressure of 150 psi and has a self-aligning 304 stainless steel screen. At the bottom of the strainer is a valve with a hose, providing a drain port for the glycol loop. An additional drain port is located near the secondary basement plate frame heat exchanger.

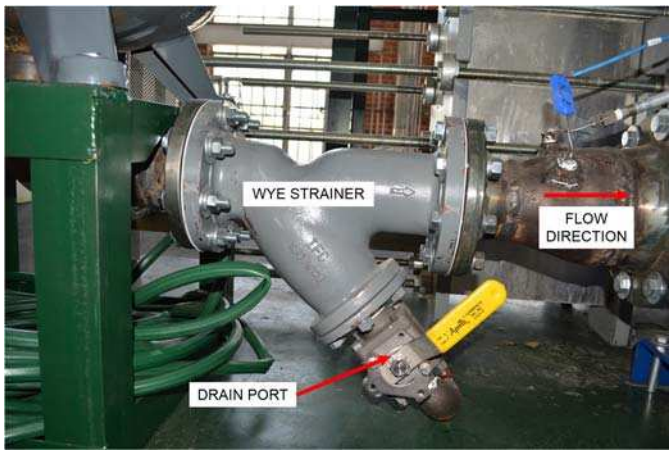

Figure 4-41. Glycol loop wye strainer.

4.1.6. Bearing Lines

The turbo-compressor bearing lines play a critical role in the operation of the turbo-machine because they provide coolant and lubrication. The turbo-compressor is an oil free device, but still requires lubrication, so some fluid flow is diverted from the primary loops and fed into the bearing housings. The effect of the fluid flow is to lubricate the ceramic bearings. The fluid entering the turbo-machine requires a pathway to exit, so both the turbine and compressor have large outlet ports (1 inch) to allow fluid to exit and dump back into the primary loop. The

components used for the power and cooling cycle bearing inlet lines are shown in Table 4-6 and Table 4-7.

Table 4-6. Power cycle bearing line component list.

Inlet Section	Components
Inlet	Filter (7 Micron) Ball Valve (S-4) Thermocouple (T57) Pressure Port (P20)
Bearing Inlet	Metering Valve (S-3) Volume Flow Meter (V109)
Bearing Inlet	Metering Valve (S-2) Volume Flow Meter (V108)
Magnetic Coupling Inlet	Ball Valve (S-5) Metering Valve (S-1) Volume Flow Meter (V107)

Table 4-7. Cooling cycle bearing line component list.

Inlet Section	Components
Inlet	Ball Valve (S-11) Filter (7 Micron)
Pump bypass	Ball Valve (S-10) Gear Pump Ball Valve (S-12) Thermocouple (T87) Pressure Port (P27)
Bearing Inlet	Metering Valve (S-13) Volume Flow Meter (V113)
Bearing Inlet	Metering Valve (S-14) Volume Flow Meter (V112)
Magnetic Coupling Inlet	Ball Valve (S-21) Metering Valve (S-15) Volume Flow Meter (V114)

The power cycle bearing inlet lines shown in Figure 4-42 are fed from a single liquid line connected after the power cycle pump. The inlet line passes through a filter, a thermocouple, and a pressure transducer then splits into the three inlet ports shown in Figure 4-43. Two cooling cycle bearing inlets are fed from liquid exiting the condensers, while the third inlet returns refrigerant vapor from the outlet of the compressor back to the magnetic coupling. The cooling cycle bearing

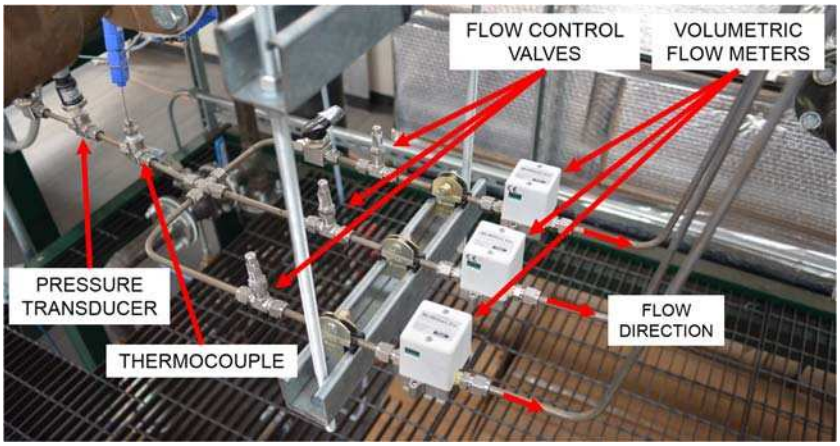

Figure 4-42. Power cycle bearing inlet lines.

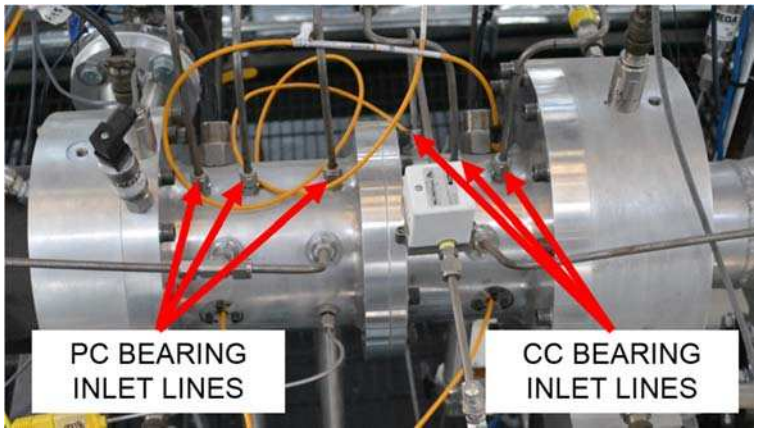

Figure 4-43. Bearing inlet lines for the turbo-compresssor.

pump is used to supply bearing flow to the two inlet ports if the compressor is not fully active or if a boost in bearing cooling is required. The 7 micron particulate polishing filters are manufactured by Swagelok (Part #SS-4TF-7) and have a replaceable filter core.

Because the compressor is being lubricated with refrigerant, a bearing pump is required during the initial stages of operation before the compressor has spun up completely. The bearing pump specifications are located in Table 4-8 and Figure 4-44 shows the pump installed. To achieve these requirements, a gear pump "Series GB" manufactured by Micropump (Part #GB-P35.JVS.A-B1) was purchased through the online retailer TESCO pumps. The pump has a maximum flow rate of 6.4 L/min (1.70 gpm) and a maximum rated pressure of 21 bar (300 psi). The pump has an A-mount style magnetic drive coupled with a variable frequency console drive motor built by Cole

Table 4-8. Bearing-line pump specifications.

Parameter	Specification
Pumping Fluid	R152a or R134a
Flow Rate	1.21 L/min (0.3 GPM)
Head Required	18.6 kPa (2.7 psi or 6.2 feet)
Viscosity, Dynamic and Kinematic	0.000167 Pa-s (0.17 cp) and 0.185 cSt
Inlet Temperature and Pressure	22.7°C and 566 kPa (82 psi)
Density	905 kg/m^3
Pressure Rating	150 psi

Parmer (Part # EW-75211-10). By using the two volumetric flow meter readings (V112 and V113 in the P&ID in Appendix B), the bearing metering valves (S13 and S14 in the P&ID), and the VFD motor drive, the flow rate into the bearing lines is controlled precisely.

The bearing drain and vent lines provide a means for liquid or vapor to exit the turbo-compressor. The lines are critically important to reducing windage in the turbo-machine, because

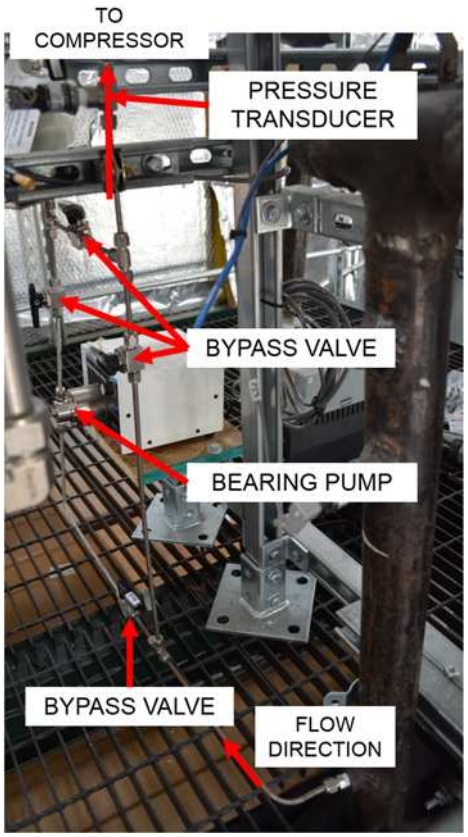

Figure 4-44. Cooling cycle bearing inlet lines.

excess fluid in the magnetic coupling cavity causes significant drag on the rotating shaft. Both the vapor vent and the liquid drain lines have outlets connected to the low pressure sections of the loop to provide an adequate drain path. There is one vent port from the cooling cycle magnetic coupling which outlets into a piping section just before the compressor. The vent line is a quarter inch stainless steel tube and the connections are made with Swagelok port connections. There is one cooling cycle drain port, which allows liquid to exit. The drain line is a 1 inch tube with some plastic and some stainless steel sections. Figure 4-45 shows the bearing drain line components. The plastic sections provide flexibility when connecting rigid piping. All of the connections are 1 inch Swagelok port connections. The drain port first passes through a 1 gallon tank (McMaster Part #9888K9) where liquid and vapor separate. A vent exits the top of the tank and passes through a valve and sight glass (McMaster Part #1079K44) before reentering the main loop just before the liquid-vapor separator bypass. The liquid exit of the tank splits into two lines that mirror each other. Each line contains a pressure transducer, thermocouple, and flow meter. The drain lines exit after the expansion valves but before the evaporators.

There are two vent ports from the power cycle magnetic coupling, which combine into a single line and then exit downstream of the turbine and before the recuperator. The vent lines are 1/4" stainless steel tube and the connections are made with Swagelok port connections. There are

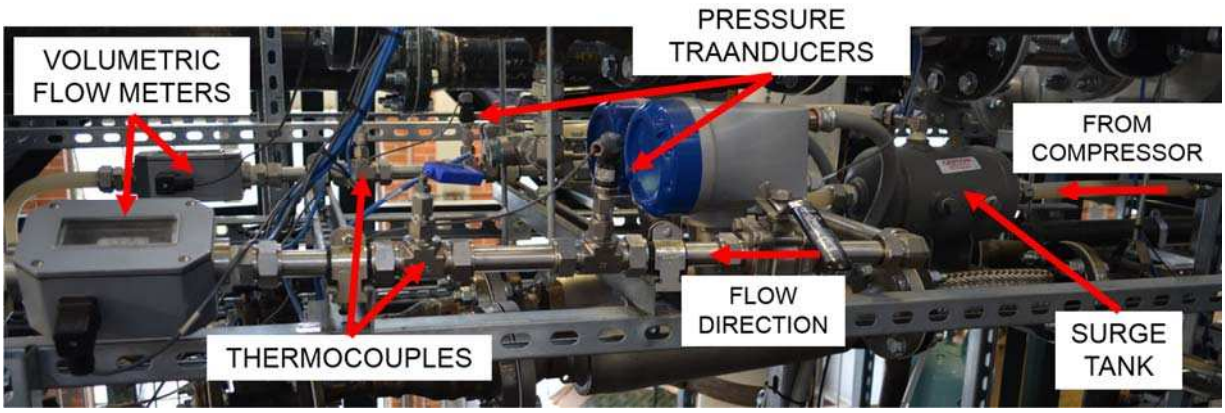

Figure 4-45. Cooling cycle condenser bearing drain lines.

two power cycle drain ports on the bottom of the turbo-compressor which allow liquid to exit shown in Figure 4-46. The drain lines are 1 inch tube size with some plastic and some stainless steel sections. Figure 4-47 shows the drain components. The plastic sections provide flexibility when connecting rigid tubing. All of the connections are made with 1 inch Swagelok port connectors. The two drain port lines combine into one single tube which leads to a thermocouple, then into a 1 gallon surge tank (McMaster Part #9888K9) where liquid and vapor separate. The vapor exits at the top of the tank where it passes through a valve and sight glass (McMaster Part #1079K44) before entering the main power cycle flow just before the large vapor manifold. The

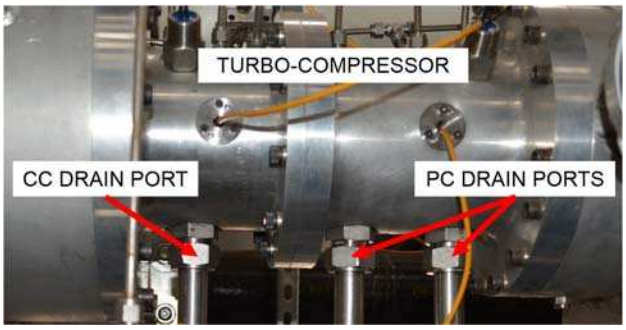

Figure 4-46. Drain ports from the bottom of the turbo-compressor.

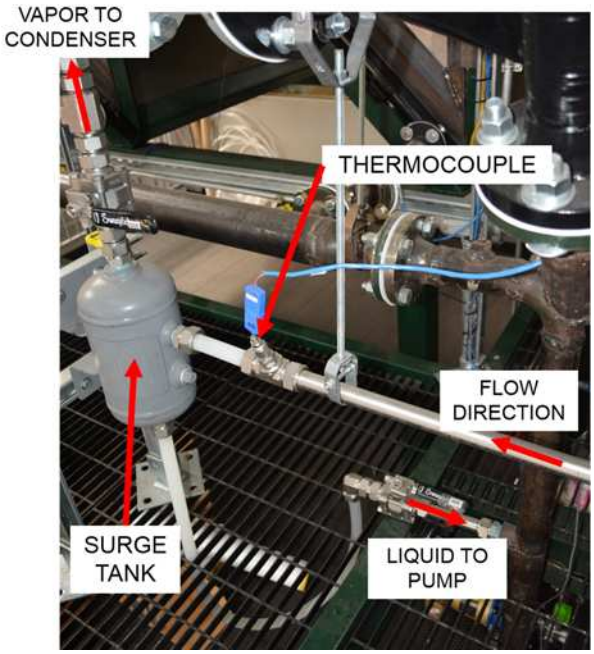

Figure 4-47. Power cycle drain components.

liquid exits at the bottom of the tank and connects to the main flow after the liquid manifold but before the pump inlet.

4.2. Miscellaneous System Components

Some of the notable general system components include pipe, tubing, fittings, valves, the refrigerant leak detectors, permanent lifting equipment, fill and drain equipment, and electrical. Each of these components are described in detail in the following several sections.

4.2.1. Piping, Tubing, and Fittings

The system components listed in the sections above were all oriented in a manner to reduce elbows, constrictions, and length in the connection piping. By orienting the facility with simple connection paths, the pressure drop between components was minimized, which improves the overall efficiency of the system. Once the length between components was determined, the pipe diameter of each section required calculation. The pipe diameter plays a significant role in the connection line pressure drop. Several equations were used to properly size the components for minimal pressure loss. The target for connection line pressure loss was less than 2 kPa. The inputs for the pressure drop model were the final state points and flow rates found in the basic thermodynamic state point modeling. The first step to calculate the pressure drop in the lines was to find the Reynolds number using the inlet conditions of the piping section in question and by guessing an initial inner piping diameter.

$$\mathrm{Re} = \frac{4\dot{m}}{\mu \pi D} \tag{4.1}$$

The Reynolds number was used to find the friction factor in the pipe with the Churchill Friction factor. The roughness of the pipe was neglected.

$$f_{\text{church}} = 8\left(\left(\frac{8}{Re}\right)^{12} + \frac{1}{(A+B)^{1.5}}\right)^{1/12} \tag{4.2}$$

The values of A and B are given by the equations shown below:

$$A = \left(2.457 \ln\left(\frac{1}{\left(\frac{7}{Re}\right)^{0.9} + 0.27eD}\right)\right)^{16} \tag{4.3}$$

$$B = \left(\frac{37530}{Re}\right)^{16} \tag{4.4}$$

Now that the friction factor is determined, the pressure drop in the lines, in Pascals, can be found with the following equation.

$$\Delta P_{\text{line}} = \frac{8\dot{m}^2}{\pi^2 D^4 \rho}\left(f_{\text{church}}\frac{L}{D} + No_{\text{bend}}K_{\text{bend}}\right) \tag{4.5}$$

In equation (4.5), the number of bends (No_{bend}) was input from the solid modeling and the bend pressure loss factor (K_{bend}) was assumed to be 0.3 [97]. The calculated value for pressure drop (ΔP_{line}) was compared with the desired 2 kPa value. If the pressure drop was less than this amount, then a smaller diameter piping was selected; if it was greater, a larger pipe was selected to decrease the pressure drop through the lines. Table 4-9 shows the pipe diameters and predicted pressure drop at the baseline condition for each section in the TCCS. All piping in the TCCS is rated to withstand the maximum allowable working pressure (MAWP) of either cycle. All metal piping, flanges, or reducers are Class 150 black carbon steel. All of the pipe to pipe connections were welded and pressure checked to withstand leak up to 150 psi.

The stainless steel and plastic tubing used in the TCCS is rated to at least 150 psi. The stainless steel tubing is used for the bearing inlet and drain lines and is either 1/8", 1/4" or 1". The plastic tubing is semi-hard and is used to connect rigid sections of tubing. There are several sizes

Table 4-9. Pipe diameters and predicted pressure drop through lines.

Line Location	Length [m]	Pipe Diameter [in]	Pressure Drop Estimate [kPa]
Power Cycle			
Boiler to Turbine	4.66	4	0.11
Turbine to Recuperator	0.79	4	0.04
Recuperator to Condenser	9.35	4	0.44
Condenser to Pump	15.3	2	0.20
Pump to Recuperator	7.03	2	0.12
Recuperator to Boiler	6.55	2	0.19
Cooling Cycle			
Compressor to Condenser	11.1	4	1.22
Condenser to Expansion Valve	18.2	2	0.93
Expansion Valve to Chiller	1.1	1.5	0.04
Chiller to Compressor	4.65	4	1.31

of plastic tubing, including 1/2", 7/8", and 1". Pressure drop calculations were not performed for this stage of the facility design.

There are four fitting styles in the TCCS including flanged, grooved, threaded, and Swaged (compression fitting). The flanged connections (Figure 4-48) are used to connect pipe runs or to connect to various components of the TCCS. Each flange has a PTFE (Teflon) gasket providing a non-degradable leak free seal. Larger flanges were torqued with 5/8" hex head bolts to 120 ft-lbs, while smaller flanges were torqued with 1/2" hex head bolts to 100 ft-lbs (aluminum flanges torqued to 60 ft-lbs). Grooved pipe connections (Figure 4-49) were used for the lines to the basement glycol loop. The pipe connections were manufactured by Gruv-Lok and purchased through Grainger. The threaded connections (Figure 4-50) are all male to female NPT fittings and include instrument ports, filter lines, Swagelok connections, refrigerant vent lines, and glycol loop piping. Before threading the connections, PTFE tape and PTFE putty was applied to the male

threads to stop leaks through the threads. In some cases (filter lines and some Swagelok fittings), the PTFE tape and PTFE putty combination did not stop the leak and hardening epoxy was applied to completely seal the threads. Stainless steel Swagelok fittings (Figure 4-51) were used in the system to provide compression seals for tube connections and instruments. All fittings were tightened to the specification, but, in some cases, leaks occurred. In those cases, additional torque was applied to stop the leak. Several of the Swagelok fittings leaked from the backside of the swage nut. To solve this problem, PTFE tape and PTFE putty was applied to the internal Swagelok threads.

4.2.2. Valves

A complete valve list is shown in Appendix D. The valves in the TCCS are all rated to at least 150 psig pressure. There are both threaded and flanged valves with most on the primary loop being flanged. The valve sizes include 1/2", 1.5", 2", and 4" and are manufactured by Triac,

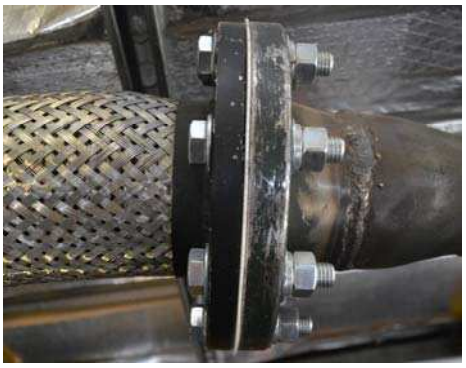

Figure 4-48. Flanged connection.

Figure 4-49. Grooved connection.

Figure 4-50. Threaded connection.

Figure 4-51. Swagelok fitting.

Williams Valve Co., Milwaukee Valve, and KF Hale. The types of valves include ball for shut-off (Figure 4-52) or general purpose and globe valves for precision flow control through throttle locations. All of the valves are manually actuated except for the emergency blow-down valves, which have a pneumatic actuator controlled by a solenoid valve.

Figure 4-52. Example two inch ball valve.

There are also Swagelok valves on the bearing drain and vent lines with sizes of 1/4", 1/2", and 1". The Swagelok valves include metering valves for precise flow control and ball valves for general purpose locations. All of the valves are manually actuated.

4.2.3. Refrigerant Leak Detectors

The refrigerant leak detectors are in place to prevent asphyxiation from refrigerant inhalation and explosion from flammable refrigerant R152a. There are two Polytron 5000 Stationary Gas Detectors (Part #4544221) manufactured by Drager and purchased through Frontier Controls Corporation. The detectors also come with a status indicator (Part #6811625). One sensor is located below the mezzanine (Figure 4-53) and the other is located above. The sensors can measure many types of refrigerants and will send an alarm signal if gas is detected.

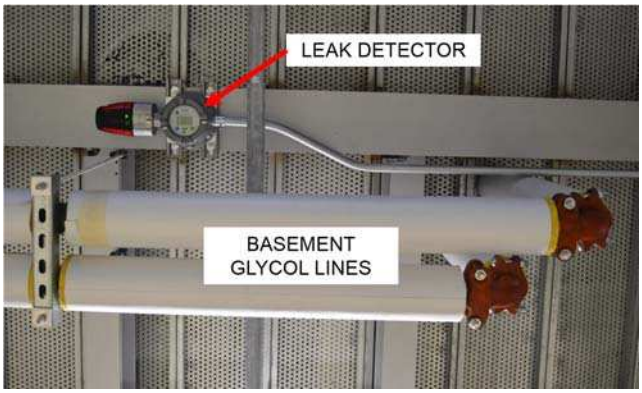

Figure 4-53. Leak detector location below the mezzanine.

4.2.4. Lifting Equipment

The crane, trolley, and hoist were vital components to the construction of the TCCS because they assisted in lifting the heavy components during construction. An Abell-Howe's (Part #J-906-FCT-1F1A) wall bracket mount jib crane is bolted to the center beam on the West wall of the mezzanine as shown in Figure 4-54. The crane has a capacity of 2000 lbs (1 ton) and a 20 foot span. The crane is mounted so it is approximately 20 ft above the mezzanine. The trolley used on the crane has a capacity of 2200 lbs and is manufactured by Dayton (Part #3MB60). The trolley is set on rollers so it can slide along the crane, enabling lifts along the entire span of the crane. The chain hoist is attached to the trolley and is manually operated in the up or down directions by

Figure 4-54. Crane installation prior to facility construction.

pulling the chains associated with up or down movement. The hoist was manufactured by Dayton (Part #1VW57). The hoist has a maximum length of 20 ft and a latching hook attached to the end.

4.2.5. Fill and Drain Equipment

The fill and drain equipment includes the components required to fill the power cycle, cooling cycle, and cooling water simulation loop with appropriate fluids. The power cycle has two fill ports, one located just before the boiler and one located just after the pump (Figure 4-55 and Figure 4-56). The drain ports are located at low height or trapped locations of the piping including the pipe connecting the recuperator to the boiler, and the pipe just before the pump. The cooing cycle has one fill port (Figure 4-57 located near the liquid distribution manifold after the condenser and one drain port located next to the accumulator. The drain ports through the mezzanine floor are shown in Figure 4-58. The cooling water simulation loop has two fill ports and two drain ports; the fill ports are located on the top of the piping entering the chillers and on top of the surge tank, while the drain ports are located on the wye strainer and before the plate frame heat exchanger. The basement glycol lines have a fill port at the exit of the plate-frame heat exchanger, and the drain port at the inlet. The components used for filling and draining the loops include the vacuum

Figure 4-55. Power cycle fill port 2.

Figure 4-56. Power cycle fill port 1.

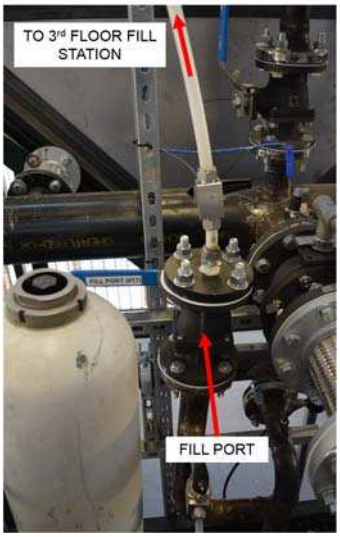

Figure 4-57. Cooling cycle fill port.

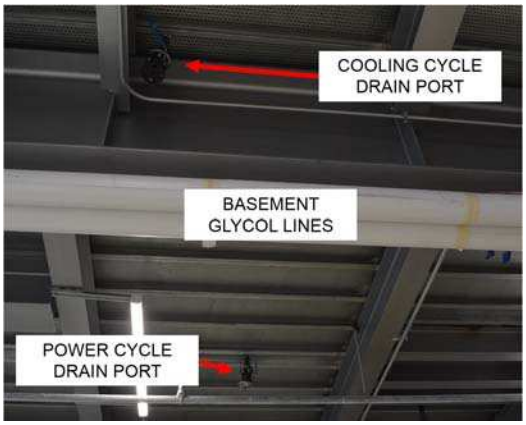

Figure 4-58. Drain lines that extend through the mezzanine.

pump, liquid gear pump, refrigerant pump, mass scale, and refrigerant recovery device. Each of these are described here.

The vacuum pump is used to remove the air from the power and cooling cycles prior to filling. Having excess air in the cycles hinders performance because it restricts heat transfer and fluid flow. The vacuum pump is a Platinum Series Vacuum Pump (Model #DV-85N) manufactured by JB Industries Inc and shown in Figure 4-59. The pump has a free air displacement of 3 CFM (82 LPM) and is powered by a standard 120 VAC electrical connection. The pump is lubricated by Edwards Ultra Grade 19 oil (Part #H11025013) – ensure enough oil is lubricating the pump at all times during operation.

Figure 4-59. Vacuum pump.

The Fill-Rite gear pump is used to fill both the power cycle and cooling water simulation loop with their respective fluids (Figure 4-60). The pump is a rotary vane, model FR610G, manufactured by Fill-Rite and purchased through Grainger (Part #4RP94). The pump has a telescoping inlet port that threads into the top of either the HFE-7000 of propelyne-glycol:water drums. The telescoping port can extend to the bottom of the drum to ensure only liquid enters the loop. The pump is capable of delivering 15 GPM of flow and is powered by a 1/4 HP motor through a standard 115 VAC electrical connection.

Figure 4-60. Fill-rite gear pump.

The refrigerant pump is used to fill the cooling cycle with liquid (Figure 4-61). The pump is a "Series GB" model gear pump manufactured by Micropump (Part #GB-P35.JVS.A-B1). The pump is driven by an A-mount configuration magnetic drive coupled to a variable frequency console drive motor manufactured by Cole Parmer (Part #EW-75211-10). The console drive allows for rotation speeds up to 5000 rpm which corresponds to a maximum flow rate of 6.4 L/min (1.70 gpm).

The mass scale is used to measure the amount of fluid during charging and draining. The scale is a "GFK Floor Checkweighing Scale" (Part #GFK 330aH) manufactured by Adams (Figure

Figure 4-61. Refrigerant pump.

4-62). The scale has a capacity of 330 lbs (150 kg) and has a readability of 0.005 lbs (2 g). The unit is powered with a 12 VDC 800 mA adaptor, but also contains an internal rechargeable battery.

The refrigerant recovery compressor system is used to remove refrigerant from the cooling cycle during the drain process and is shown in Figure 4-63. The system is a CMEP-OL Butane Recovery Pump (Reciprocating Piston) manufactured by CM refrigeration, a subsidiary of Nanjing Wonfulay Precision Machinery Co, Ltd. The system is equipped with a 1 HP stainless steel oil-

Figure 4-62. Scale used for fill and drain procedures.

Figure 4-63. CMEP-OL refrigerant recovery device.

less twin-cylinder compressor with a gas displacement of 1.25 CFM. The system can recover 15-22 lbs of refrigerant per hour.

4.2.6. Electrical

The TCCS has many electrically powered components with sources of 480V 3-phase, 240V 3-phase, and 120 V single phase. The final electrical one line drawing that will help guide the description of this section is shown in Figure 4-64. The primary components in the electrical system are the switchboard, the main distribution breaker panel, the step-down transformer, the heater disconnect switch, the current transformers, and the low-voltage devices. Table 4-10 shows the power feed list for every electrical component in the facility.

The switchboard takes the high amperage 480V 3-phase feeds from the electrical grid and converts them to the appropriate power sources for the TCCS. The switchboard is located on the first floor of the Powerhouse and shown in Figure 4-65 The model installed is a Cutler-Hammer (Eaton, Inc) Pow-R-Line C low voltage switchboard (600 VAC Max). The switchboard can deliver a maximum current supply of 800 amps at a frequency of 60 Hz. One 200 amp feed powers the air heat disconnect and one 250 amp feed powers the distribution box for the rest of the components.

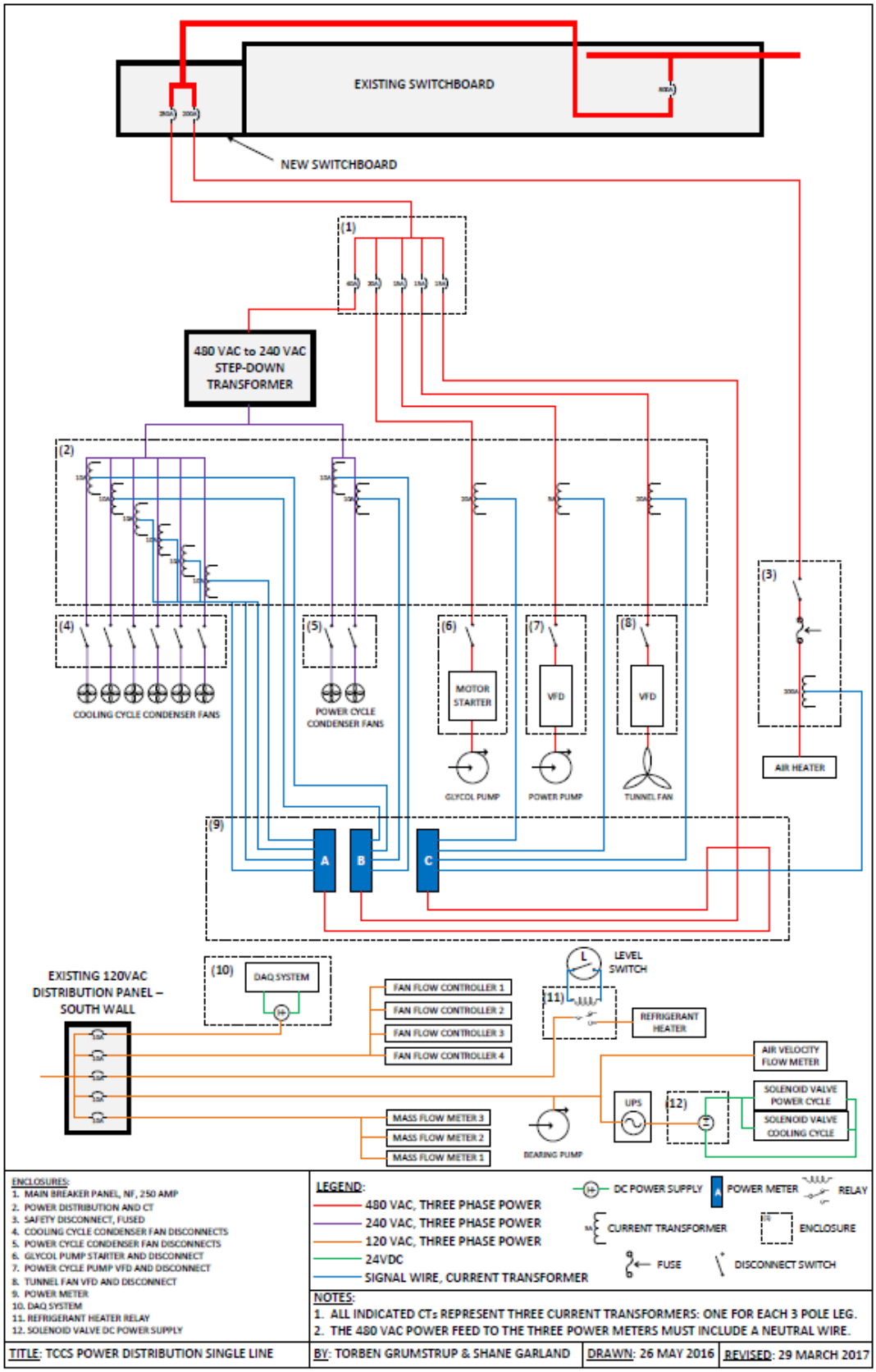

Figure 4-64. Electrical single line drawing.

Table 4-10. Power feed list for electrical components in the TCCS.

Feed From	Feed To	Power Feed
Powerhouse Switchboard	TCCS Switchboard	480 VAC 3-Phase, 800 Amp Breaker
TCCS Switchboard	Air Heater Disconnect	480 VAC 3-Phase, 200 Amp Breaker
TCCS Switchboard	Main Breaker Panel	480 VAC 3-Phase, 250 Amp Breaker
Main Breaker Panel	Step-Down Transformer	480 VAC 3-Phase, 40 Amp Breaker
Main Breaker Panel	Glycol Pump	480 VAC 3-Phase, 60 Amp Breaker
Main Breaker Panel	Power Cycle Pump	480 VAC 3-Phase, 15 Amp Breaker
Main Breaker Panel	Flue Loop Fan	480 VAC 3-Phase, 15 Amp Breaker
Main Breaker Panel	Power Meters	480 VAC 3-Phase, 15 Amp Breaker
Step-Down Transformer	Six Condenser Fans	240 VAC 3-Phase
Step-Down Transformer	Two Condenser Fans	240 VAC 3-Phase
Distribution Panel	DAQ System	120 VAC, 10 Amp Breaker
Distribution Panel	Four Fan Controllers	120 VAC, 10 Amp Breaker
Distribution Panel	Three Mass Flow Meters	120 VAC, 10 Amp Breaker
Distribution Panel	Bearing Line Pump Air Velocity Sensor UPS to Solenoid Valves	120 VAC, 10 Amp Breaker
Distribution Panel	Refrigerant Heater	120 VAC, 10 Amp Breaker

Figure 4-65. Switchboard for the TCCS.

The main distribution panel (Figure 4-66) takes a 250 amp 480 VAC 3-phase power feed from the switchboard and routes it through the circuit breakers that distribute power to the various

components of the TCCS. There are five operational (six total) circuit breakers in the main panel all manufactured by Square D and purchased through CED. One 40 amp breaker (Part #EDB34040) powers the transformer through the transformer disconnect switch (Figure 4-67). One 60 amp breaker (Part #EDB34020) feeds the glycol motor starter. Three 15 amp breakers (Part #EDB34015) power the current transformer measurement boxes (power meters), the tunnel fan, and the power pump. There is one extra 15 amp circuit breaker for additional power requirements in the future.

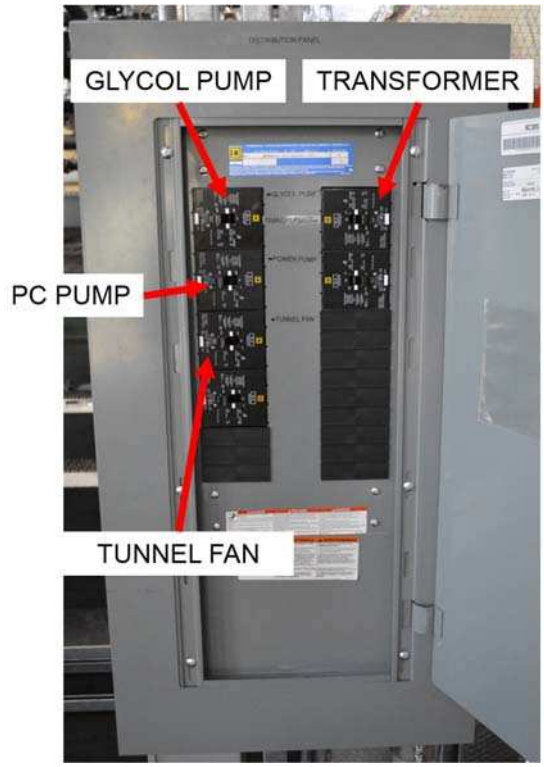

Figure 4-66. Main distribution panel.

The step-down transformer (Figure 4-68) is used to convert 480VAC 3-Phase power into 240VAC 3-Phase power. The transformer is a Square D General Purpose Transformer Model #EX15T6HCT and was purchased through Grainger (Item #45NZ29). The transformer is fed from the 40 amp breaker in the main distribution panel which routes through the transformer disconnect switch. The transformer takes power from the disconnect switch and outputs 240VAC 3-phase

Figure 4-67. Transformer disconnect switch.

Figure 4-68. Transformer located beneath the mezzanine.

power to the eight condenser cooling fans. The transformer has a maximum VA and frequency rating of 15 kVA and 60 Hz, respectively.

The heater disconnect switch, shown in Figure 4-69, is used to start/stop the power supply for the electrical heater in the flue gas loop. The heater disconnect is a Square D model H364 and was purchased through the Powerhouse. The heater disconnect takes in a 480 VAC 3-phase power

Figure 4-69. Air heater disconnect switch.

source at 200 amps directly from the switchgear. The switch is installed with three Bussmann Fusetron fuses (Model # FRS-R-200) with a current rating of 200 amps and a voltage rating of 600 VAC, purchased through CED. The fuses are designed to protect the switchgear from any over current which may occur in the system. There is also a 200 amp current transformer located around each power lead in the heater disconnect box to measure the total power draw of the heater. The heater disconnect is activated by pushing the handle switch into the "ON" configuration.

The current transformers are used to measure the power output of the electrical components. The current transformers were manufactured and purchased from eGauge Systems LLC. Since the components are three-phase powered, one CT is required for each electrical lead, or three total CTs per component. Table 4-11 shows the voltage source and CT size for each components. The CT's are located at the power source and the signal wires are routed to the CT electrical box. The CT electrical box contains three eGauge EG3000 wiring boxes which take current signals and transmit the data to the DAQ.

The components that require 120 VAC power include the National Instruments DAQ system, the condenser fan controllers, the mass flow meters, the liquid-vapor separator heater, the uninterrupted power supply (for vent line solenoid valves), the cooling cycle bearing inlet pump, and the anemomaster velocity flow meter (flue gas loop). The power for all of those components

Table 4-11. Current transformer size based on component type and voltage source.

Component	Voltage Source [VAC]	CT Size [Amps]
Air Heater	480	200
Tunnel Fan	480	20
Power Cycle Pump	480	5
Glycol Loop Pump	480	20
Power Cycle Condenser Fans	240	10
Cooling Cycle Condenser Fans	240	10

is routed from the Powerhouse distribution panel located on the second floor landing on the South side stairwell and shown in Figure 4-70. Each breaker in the South wall distribution panel has a 10 amp limit, but each of the components does not have its own circuit. Table 4-12 shows each of the breakers and the components which they power.

Table 4-12. 120 VAC components and locations in the distribution panel.

Panel Breaker #	Landing Location	Components Powered
6	NI DAQ Panel	NI PS-15 24V Power Supply BelPower -24V Power Supply
14	Condenser Fan Controllers	4 Ziehl-Abegg Controllers
16	Mezzanine Deck Outlet	Uninterrupted Power Supply CC Bearing Inlet Pump Anemomaster Velocity Meter
18	Mass Flow Meters	2 CC Optimass Mass Flow Meters 1 PC Optimass Mass Flow Meter
20	Liquid-Vapor Separator Heater	Liquid-Vapor Separator Heater

Figure 4-70. 120VAC powerhouse distribution panel.

4.3. Instrumentation and Data Acquisition

The TCCS DAQ system includes instrumentation, wiring, and data measurement devices. The instrumentation list is shown in Appendix E. This section first describes the instrumentation and then details the design and functionality of the National Instruments DAQ hardware.

4.3.1. Instrumentation

There are many instruments used in the TCCS that provide data to calculate state points, diagnose problems, or ensure good system operation. The instrument types include pressure transducers, differential pressure transducers, thermocouples, RTD temperature sensors, speed and proximity sensors, load cells, accelerometers, power meters, mass flow meters (already described in Sections 4.1.2 and 4.1.3), velocity flow meters, and volumetric flow meters. This section provides some information on each of these instruments.

There are numerous absolute pressure transducers with varying ranges including 26-32 in Hg., 0-15 psi, 0-100 psi, 0-200 psi, and 0-300 psi. Figure 4-71 is an example of an absolute pressure transducer installed in the loop. Many transducers are used to calculate the thermodynamic properties of the system during the data analysis phase while others are used for system operation

Figure 4-71. Absolute pressure transducer installed in pipe.

and monitoring. The transducers are all loop powered through the NI 9205 analog input channel and have a 4-20mA output signal. The transducers have 1/4 inch threaded NPT connections for each installation into the facility. The accuracy of the instruments vary from ±0.25 – 1.5% of the span.

There are several differential pressure transducers to measure the pressure drop across various components. Figure 4-72 is an example of a differential pressure transducer. The measurement is used in the calculation of state points and for system operation and monitoring. The differential pressure transducers have a high side and low side pressure connection made through a swagelok connector to a 1/8 inch tube. The ranges of the transducers include 0-4 inches of water, 0-10 inches of water, 0-20 inches of water, 0-40 inches of water, 0-200 inches of water, 0-400 inches of water, 0-75 psi, and 0-100 psi. The pressure transducers are all loop powered through the NI 9205 analog input channel and output a 4-20mA signal. The accuracy of all the transducers is ±0.5% of full scale value.

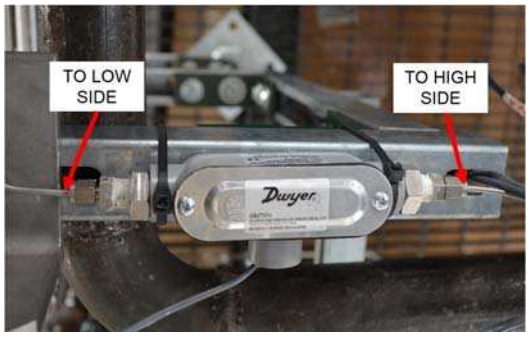

Figure 4-72. Differential pressure transducer.

There are four types of thermocouples used to measure the temperature at various locations: K-type probes, T-type probes, T-type wire, and T-type high temperature wires. The temperature measurements are primarily used to determine the thermodynamic state points in the system but are also used during system operation and monitoring. Each thermocouple connects to a quick disconnect standard connector and then to the DAQ module NI 9213. There is one ungrounded K-

Type thermocouple (Omega KQSS-18U-12) located in the magnetic coupling bearing cavity. The K-type thermocouple can handle temperature ranges from -270°C to 1372°C and is a Chromega®-Alomega® metal combination with a 304 SS Sheath. The tolerance range of the thermocouple is 2.2°C or 0.75%.

There are many ungrounded T-type thermocouples probes (Omega TQSS series) in the facility depending on the pipe or tube size. One example is shown in Figure 4-73. Each probe is a Copper-Constantan metal combination with a 304 SS sheath that can handle a temperature range between -270°C and 400°C. The tolerance value is 1.0°C or 0.75%. The most common probe thickness is 1/8 inch, but the bearing drain lines are 1/16 inch. The lengths of the probes vary as well with general lengths of 3, 4 or 6 inches.

Figure 4-73. Thermocouple in pipe.

There are several T-type bare wire thermocouples (Omega PP-T-24) used to measure the ambient air temperature before and after the cooling cycle condenser towers. One sample is shown in Figure 4-74. The wires are a Copper-Constantan metal combination and are duplex insulated with a polyvinyl coating. The two leads were flash welded together using a capacitor. The wires have a temperature range up to 105°C.

Finally, the thermocouples used in the flue gas loop are rated to higher temperatures. These thermocouples are bare wire T-type (Omega TT-T-24) that are a Copper-Constantan metal

Figure 4-74. Bare wire thermocouple.

combination. The two leads were flash welded together using a capacitor. The wires are insulated with high performance Neoflon PFA and can withstand a maximum temperature of 200°C.

There are a number of instruments located on the turbo-compressor as shown in Figure 4-75. There are two RTD sensors in the turbo-compressor used to measure the bearing cavity temperatures. Both sensors are thin film Platinum RTDs (HEL-705) manufactured by Honeywell. The sensors are a 1000Ω half Wheatstone bridge interface with a 28 ga. TFE Teflon mounting

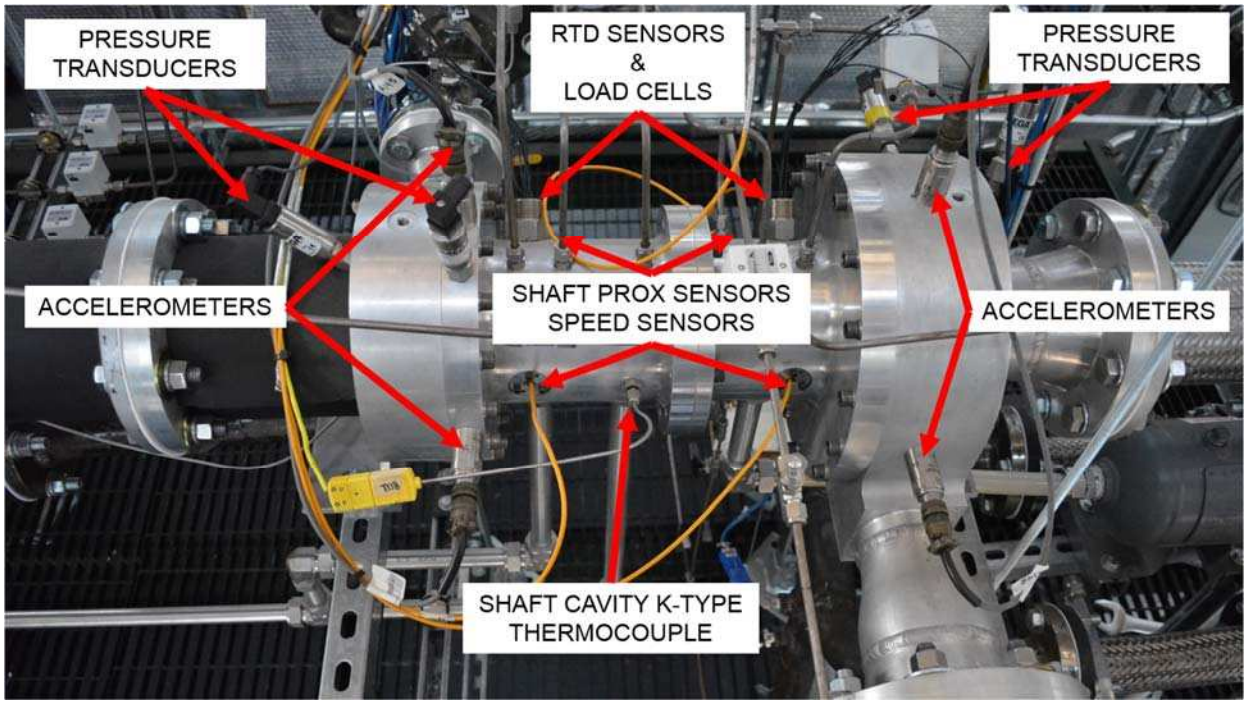

Figure 4-75. Turbo-compressor instrumentation.

wire. They have a maximum temperature range between -200°C and 260°C, but are set between 0°C and 200°C. The RTD sensors are connected to signal conditioners that output a 0-5 V signal to the NI 9205 analog input module.

The speed and proximity sensors are located in the turbo-compressor to measure the rotation speed and displacement of the shaft. The probes are High Pressure Proximity Probes (Part #10026-925-10-02) manufactured and purchased through Metrix Instrument Co. The probes are made of Ryton and are a 1 meter reverse mount design with a series 300 stainless steel case and coaxial cable. The speed and proximity sensors connect via a coaxial cable to the Metrix proximity drivers (MX2033 and MX2034). The MX2033 driver outputs a negative pulse signal, and is used for proximity and speed measurements with an oscilloscope or Bentley Nevada processor. For standard measurements by the data acquisition system, driver MX2034 is used because it outputs a 4-20mA signal corresponding to the speed. Each driver has a coaxial connection cable and a screw terminal output connection. There is a 4 meter extension cable for a total length of 5 meters from proximity probe to driver.

Two load cells are located within the turbo-compressor to characterize the bearing thrust load. The load cells are Compact Through Hole Load Cells (Part #LC8200-1.00-500) manufactured and purchased through Omega. They have a 2 inch outer diameter, and can handle a force range between 0 and 500 lbf. The instruments are a full Wheatstone bridge so they require a separate DC power source. The Puls power supply (Part #ML15.121) provides as 12 VDC power source which excites the cell and outputs a 2 mV/V nominal voltage. The output signal wires are measured by the NI 9205 module set in differential mode.

There are four accelerometers located on the turbo-compressor. The accelerometers thread into the top and sides of the turbine and compressor to measure the acceleration in two directions.

The devices are OMEGAROMETER series (Part #ACC793) purchased from Omega. They have an output of 100 mV/g and have a peak acceleration of 80 g. The devices have a top mount 2-pin MIL cable which runs to a power supply/signal conditioner also purchased through Omega (ACC-PS2). The output channel of the ACC-PS2 is used to connect an output voltage signal to the DAQ through the NI 9230 vibration input module.

The power meters (current transformers) in the TCCS are used to measure the electrical current passing through the three phase powered electrical components. A sample, unused current transformer is shown in Figure 4-76. The current transformers are all manufactured and supplied by E-Gauge and include several different sizes including 200 amp, 20 amp, 10 amp, and 5 amp. Because the electrically powered devices operate on 3-phase power, there are three current transformers for each device. The output of the signals is routed to the collection adaptors (EG3000) also manufactured by E-Gauge. An ethernet connection interfaces to the DAQ system.

Figure 4-76. Current transformer.

There are two velocity flow meter styles used to measure air speed in the flue gas loop and condenser fans. The air speed of the flue gas loop is measured using a Middle/High Temperature Anemomaster with a 5 meter temperature extension probe (Part #6162-0204-04) that was manufactured by Kanomax but purchased through Instrumart. The unit has an air temperature

measurement range up to 500°C with air velocity ranges between 0.2 and 50 m s^{-1} depending on temperature. The measurement accuracy is typically ±3% of the full scale reading. The Anemomaster measurements are not connected to the data acquisition system, and are read on a separate LCD display as shown in Figure 4-77.

Figure 4-77. Kanomax anemomaster control module and LCD display.

The condenser fan velocity sensors are model MAL 10 (Part #384052) manufactured and supplied by Ziehl-Abegg. There is one sensor located before each fan as shown in Figure 4-78. The sensors have a measuring range of 0-20 m s^{-1}, a voltage supply of 24 VDC, and an output signal of 4-20 mA. The accuracy of the instruments are ±0.2 m s^{-1} of the measuring value.

There are four different volumetric flow meters in the TCCS: turbine bypass line, cooling cycle drain line, bearing inlet lines, and the glycol loop. The turbine bypass flow meter is described in Section 4.1.2. The cooling cycle bearing drain volumetric flow meters are In-Line Liquid Flow

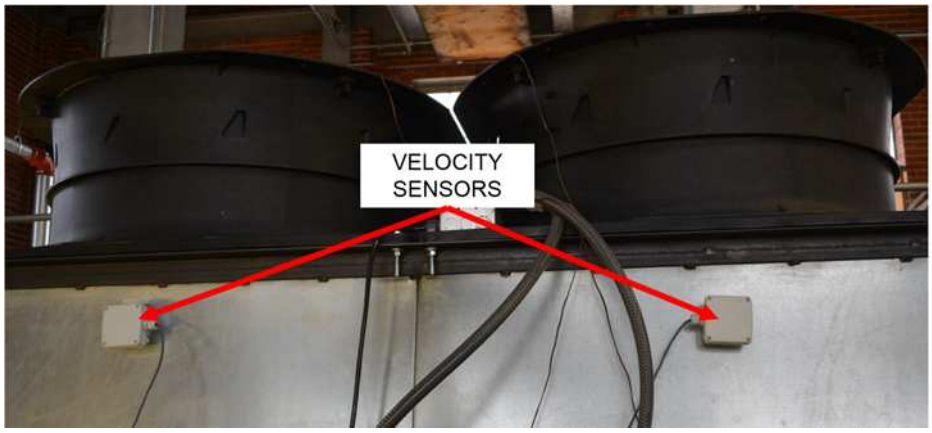

Figure 4-78. Condenser velocity sensors sit just below the fans.

Meters (Part# FLMH-1002SS-MA) manufactured and purchased through Omega and shown in Figure 4-79. The meters have 1 inch NPT connections and the wetted components are made of stainless steel for corrosion resistance and high pressure rating. The flow meters have a measuring

Figure 4-79. Bearing drain line volumetric flow meter.

range between 0.4 and 550 LPM with an accuracy of ±2.5% FS and output a 4-20mA signal. The volumetric flow for the six bearing inlet lines (3 cooling cycle, 3 power cycle) is monitored by a Microturbine Liquid Flo-Sensor (Model 107) manufactured by McMillan Company, but purchased through Cole-Parmer. Figure 4-80 shows the sensor installed on a bearing line. The sensor has a flow rate range between 50 and 500 mL/min with an accuracy of ±1% of the full scale value. The meter is made of 316 L stainless steel with swage style inlet ports and a 500 psig pressure rating. The sensors are loop powered by a 24 VDC source and output a 4-20mA signal. There is one

Figure 4-80. Bearing inlet volumetric flow meter.

volumetric flow meter for the glycol loop and one for the basement glycol lines. Figure 4-81 shows the flow meter installed in the loop. The instruments are SDI series insertion style flow sensors (Part #SDI1D1N10-0200) manufactured by Badger Meter. The sensors have a brass body and a PVDF rotor with a flow measurement range between 0.15 and 6.1 m s^{-1}, a maximum pressure rating of 200 psi, temperature rating of 93°C. The fitting size is a 1" NPT connection threaded into the five inch pipe downstream of the chillers. The sensor has its own built in signal processor, powered by a 24 VDC source, outputting a 4-20mA current signal.

Figure 4-81. Glycol loop insertion style flow meter.

4.3.2. Instrument Calibration

Each instrument used in the TCCS has its own calibration curve which takes the input voltage and converts it to the appropriate units. The thermocouples and pressure transducers were calibrated in house, while the flow meters, RTDs, proximity/speed probes, accelerometers, and power meters all used the factory calibration. The thermocouples and pressure transducers were calibrated with the actual length of wiring to account for any resistance through the wires.

The thermocouples were calibrated with an oil bath model One 29 manufactured by Memmert. The following section presents the calibration method. Figure 4-82 and Figure 4-83 show the thermocouples in the oil bath during calibration. An insertion style reference thermometer, manufactured by Digi-Sense and purchased through Cole Parmer (Part #EW-37804-04) was used to measure the temperature of the bath and the thermocouple measurement was

Figure 4-82. Thermocouple oil bath front view.

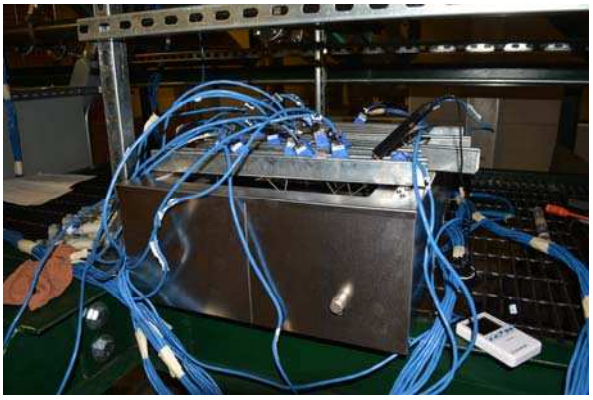

Figure 4-83. Thermocouple oil bath side view.

recorded for comparison. Oil, DC 210H (Part #01894CL01), manufactured by Boss Products was poured into the oil bath and then heated to five set temperatures. The thermocouple temperature was recorded as well as the reference thermometer temperature, so that empirical calibration correlations could be derived based on the differences.

Two methods were used to calibrate the pressure transducers depending on the pressure range of the transducer: a compressed air system and a dead weight scale system. The compressed air method was used for low range pressure up to 15 psi, while the dead weight scale system was used for higher measurement scales up to 300 psi. In both cases five set pressures were applied by either adjusting an air valve or by placing the weights. The voltage was recorded at each set pressure so the calibration curve could be created.

The uncertainty of the instrument measurements is based on the accuracy of each individual instrument as specified in their datasheets. While processing data the instrument uncertainty is input into EES to determine the uncertainty of the COP calculation based on the propagation through the measurements. The uncertainty calculation is shown in Section 4.4.3.

4.3.3. Data Acquisition Hardware

The DAQ system monitors and records the instrumentation. The DAQ consists of several components including the data acquisition containment cabinet, power supplies, National Instruments data acquisition hardware, and data reading software through the LabVIEW program.

The data acquisition equipment is located in the large DAQ cabinet on the South end of the test facility as shown in Figure 4-84. The 120VAC power for the DC power supplies is routed from to the South stairs breaker panel to the conduit at the bottom of the DAQ box. A separate conduit exits the bottom of the cabinet in which a Gigabit Ethernet cable is routed into the Powerhouse local area network connection. There are three conduit pipes exiting the top of the cabinet for the instrumentation wires to enter the DAQ cabinet. The conduit pipes go to the instrument wire cage above the facility. The wires travel along the wire cage and descend to the appropriate measurement locations in the TCCS.

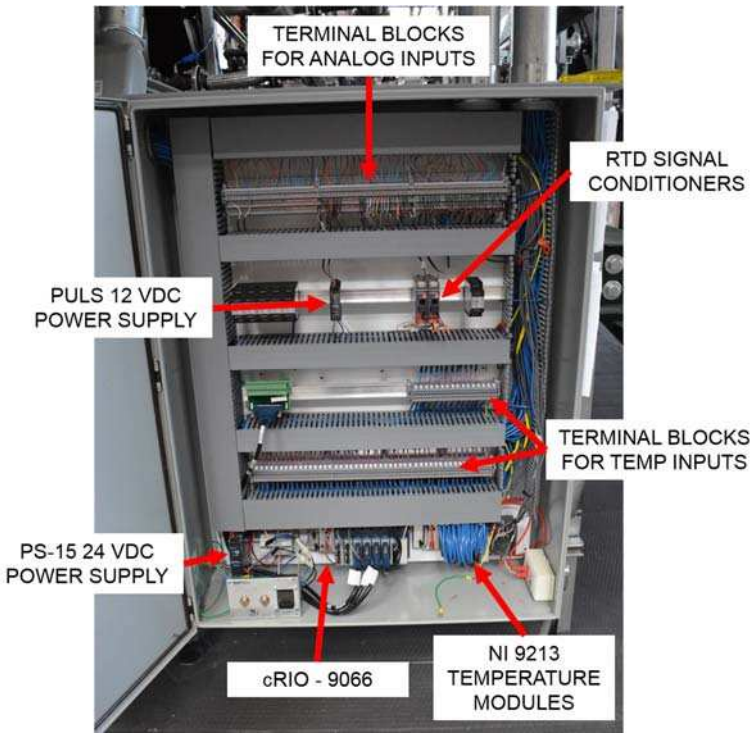

Figure 4-84. Data acquisition cabinet.

The data acquisition hardware used to measure and record the instrument data was purchased through National Instruments. The acquisition system is centered on a CompactRio Controller with 8-slots for variable inputs. Table 4-13 shows a list of the hardware components, while Figure 4-85 shows a diagram of the hardware connections.

Table 4-13. Data acquisition system component list.

QTY	PART	PART NUMBER	SUPPLIER
1	Compact Rio	cRIO-9066	National Instruments
1	cRIO 8-Slot Additional Chassis	NI 9149	National Instruments
4	16 Ch. Temperature Input Module	NI 9213	National Instruments
3	32 Ch. Analog Input Module	NI 9205	National Instruments
2	Vibration Input Module	NI 9230	National Instruments
1	±10VDC Signal Supply	NI 9263	National Instruments
2	RTD Signal Conditioners	iDRX	Omega
4	Accelerometer Power Supply	ACC-PS2	Omega
2	Proximity Driver, 4-20mA Output	MX2034	Metrix
1	24 VDC Power Supply	NI PS-15	National Instruments
1	12 VDC Power Supply	ML15.121	Puls
3	37-Pin DSUB Screw Terminal Block	778673-01	National Instruments
2	Proximity Driver, Neg. Pulse Output	MX2033	Metrix
1	BelPower -24VDC Power Supply	179-2319-ND	Digikey

The CompactRio (cRIO-9066) is the main embedded controller allowing instrument monitoring and control. The system has 8-Slots for various modules, contains a 667 MHz Dual–Core CPU with a Zynq-7020 FPGA and a real-time processor running the NI Linux Real-Time OS. There is also a cRIO 8-Slot expansion chassis (NI 9149), allowing for additional control or monitoring modules.

There are four types of modules to measure or control the various aspects of the TCCS. Four NI 9213 modules (16 Channel C-Series Temperature Inputs) provide measurement for thermocouples. The three NI 9205 modules each have 32 channels available to measure general analog inputs. Two vibration input modules (NI 9230) are used to measure data from the four accelerometers located on the turbo-compressor. Finally, there is one ±10VDC Signal Supply (NI

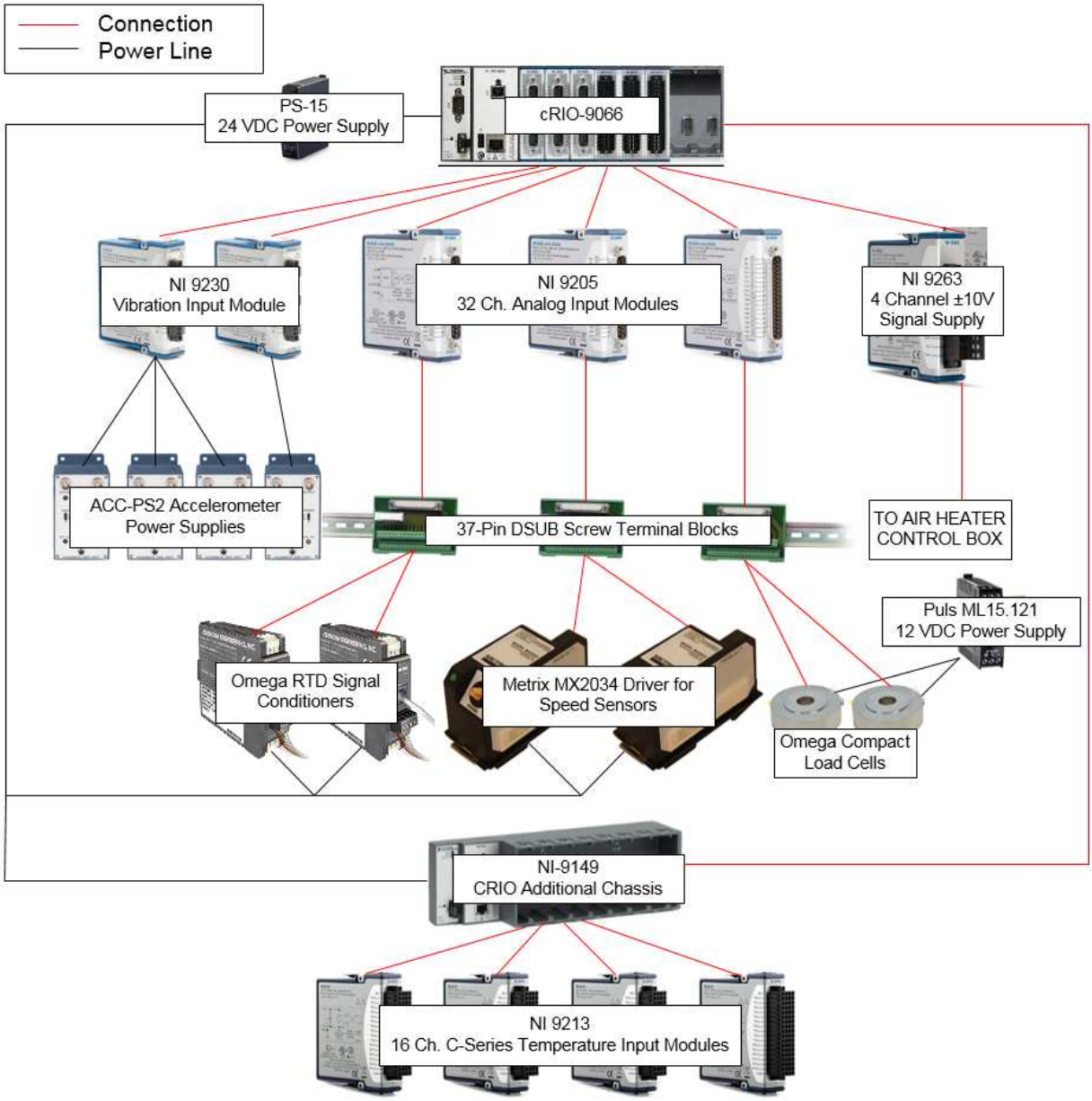

Figure 4-85. Data acquisition hardware components and connections. Instrument connections are not shown.

9263) providing a control output for the flue loop heater. The instruments are either directly connected to a specified module or are routed through a screw terminal block allowing for organization and easier wiring.

Each component in the DAQ box requires some form of DC power, and there are three different types of DC power supplies. One 24 VDC power supply (NI PS-15) with a maximum 5

amp output is used to power the instruments and control modules within the DAQ. The power supply is fed with a standard 120 VAC power from the South breaker panel. The output DC power is routed through 2 amp fuses before heading to the required equipment. One 12 VDC power supply, manufactured by Puls (ML15.121), but purchased through Grainger (Part #45ET71) provides the power to operate the two full bridge load cells located in the turbo-compressor. This 12 VDC supply is also powered by the same 120VAC power source from the South breaker panel. The final power supplies from Omega (ACC-PS2) are a supply and signal conditioner combination that deliver 24VDC through a BNC/MIL cable directly to the accelerometers.

Finally, there are two types of signal conditioners. The RTD signal conditioners (iDRX) from Omega take in the measurements from the half bridge temperature measurements in the turbo-compressor and output a 0-5 V signal. The two Metrix Proximity Drivers (Part #MX2034) are powered by 24 VDC loop power, take in speed pulse measurements, and output 4-20mA signals. Each signal conditioner is connected to the standard NI 9205 Analog Modules.

When measuring the proximity or speed with a counter module, the oscilloscope, or a Bentley Nevada processor, use the Metrix Driver with a pulse output (MX2033). The driver is powered by a -24VDC source supplied by a BelPower power supply (Part #179-2319-ND) purchased through Digikey. The output signal from the driver is connected to a BNC cable read by the oscilloscope or Bentley Nevada processor. The other option is to use the Metric 2034 driver, outputting a 4-20mA signal, to connect directly with the NI 9205 module. This style allows measurements of the speed through the Labview NI interface.

There two types of analog signal inputs depending on the instrument type. The analog signal input module is set to intake voltage signal ranges 0-10V, 0-5V, 0-1V or 0-200mV. By using the LabVIEW program, the input voltage range can be changed to one of those four preset ranges

depending on the input signal source. Additionally, the input configuration can be changed from single ended to differential. The input signal source for each instrument and the wiring list are shown in Appendix E.

The 2-wire voltage signal inputs (Figure 4-86) are the most basic configuration with the ground to ground and the power to signal. The instruments with a 3-wire voltage signal are wired with the signal wire connected to the signal input connection, the ground connected to the ground connection, and the power connected to the power connection (Figure 4-87). The instruments with 2-wire 4-20mA current signals (Figure 4-88 are wired with the power connected to the power connection, the ground connected to the signal connection, and a 250Ω resistor connected from the signal to the ground. By wiring a 4-20mA signal with a resistor, the signal is transferred to a 1-5V signal read by the DAQ module. The instruments with a 3-wire 4-20 mA current signal (Figure 4-89) are wired with the power connected to power, ground to ground, signal to signal,

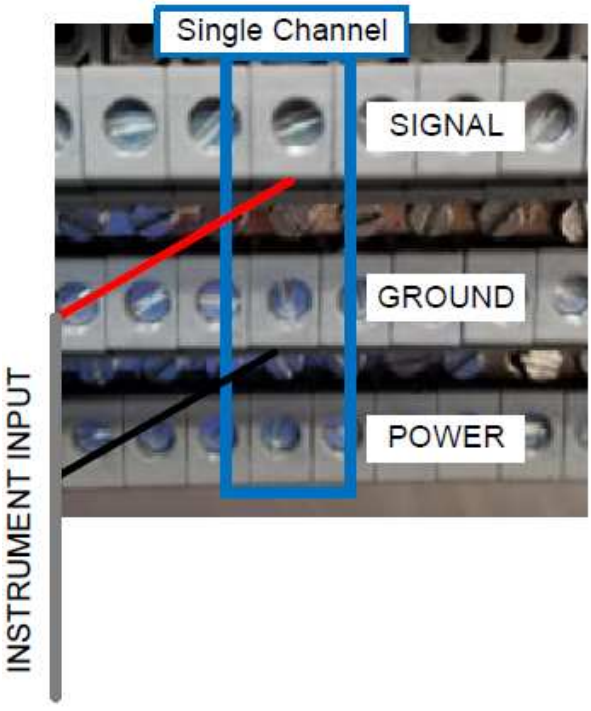

Figure 4-86. Wiring diagram for a 2-wire voltage input signal.

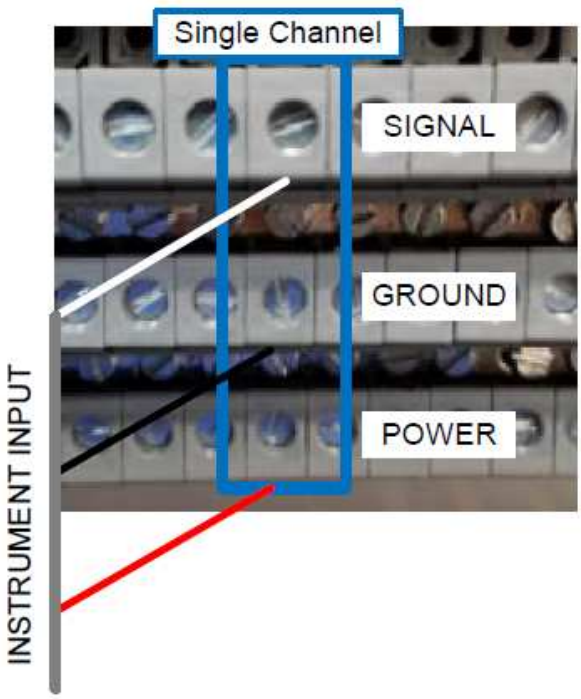

Figure 4-87. Wiring diagram for a 3-wire voltage input signal.

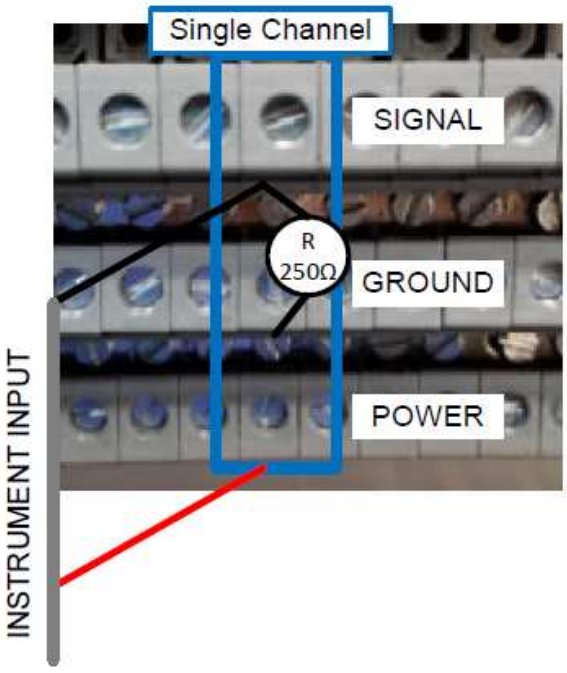

Figure 4-88. Wiring diagram for a 2-wire 4-20mA current signal.

and a 250Ω resistor connected from the signal to the ground. The instruments with a 4-wire voltage signal (Figure 4-90) are wired in differential mode by connecting the green cable with any input AI0-7 as long as the white cable connects to the corresponding AI8-15 input (wires should be 8 spaces apart).

4.4. Test Matrix and Calculation Method for Primary System Metrics

Successful test facility operation was critical to make accurate comparisons between the two modeling approaches and the experimental data. The full facility operation procedure is shown in Appendix F. One primary difference between the testing presented in this research and the actual baseline modeling approach is fluid used for the cooling cycle. The baseline modeling fluid, R152a, was chosen based on its favorable properties as described in Section 3.1.4. However, due to R152a's high flammability, R134a was selected as the cooling cycle fluid for this research. Due to the different fluid, the system would not operate at as high of a COP and the state points would

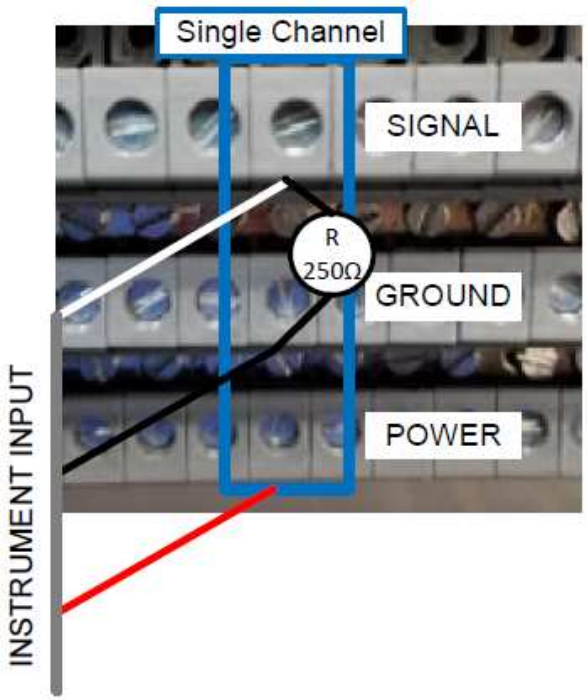

Figure 4-89. Wiring diagram for a 3-wire 4-20mA current signal.

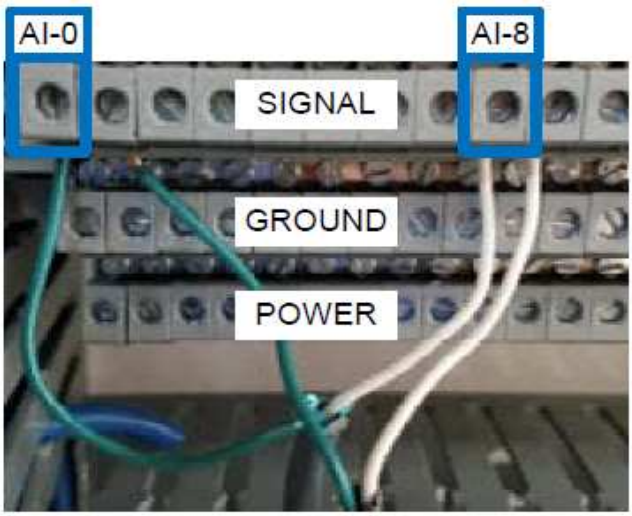

Figure 4-90. Wiring diagram for a 4-wire differential voltage signal – two power wires not shown here.

be slightly different than in the original baseline case. However, the off-design modeling approach can accommodate the change in fluid due to the fluid factor in the *UA* scaling approach shown in equation (3.49).

4.4.1. Test Matrix

To obtain operational points across a full range of conditions, a test matrix was developed based on the two main control parameters for the system: power cycle mass flow and cooling cycle expansion valve position. The power cycle mass flow rate is controlled by a VFD that varies motor operational speed. By changing the speed the power cycle mass flow and pressure rise were controlled. The cooling cycle expansion valve has a maximum of four turns. By adjusting the valve, the cooling cycle mass flow rate and pressure ratio in the cycle are set. Each point in the test matrix is achieved by adjusting the pump frequency and valve position accordingly. Each block in the matrix has a position to record the time, speed of the turbo-machine, and cooling cycle

mass flow rate. Each data point was held for at least two minutes to ensure steady state operation conditions. The test matrix is shown in Figure 4-91. By completing the test matrix enough data points were available to create a COP map as will be described in the next section.

4.4.2. Calculation of Primary System Metrics

The TCCS test facility was operated over multiple test days by using the test matrix presented in Figure 4-91 at an ambient temperature of 27.5°C. As noted above, the fluids used for the testing were HFE-7000 and R134a for the power and cooling cycles, respectively. During the tests, several conditions were held constant to allow for comparison between tests across multiple days. The exhaust mass flow rate was held at 6.9 kg s^{-1}, the exhaust temperature at 106°C, and the power and cooling cycle air side mass flow rates were held at 23.2 kg s^{-1} and 51.6 kg s^{-1}, respectively. As noted in the test matrix, the two driving variables for the tests were the power and cooling cycle mass flow rates which are controlled by the VFD and expansion valve position, respectively. Varying the power and cooling cycle mass flow rates allowed for a wide range of operating conditions at 27.5°C ambient. The performance across all operating conditions was found by using data collected from instrumentation listed in Appendix E.

Test data is saved in an excel data file at a 2 Hz rate. Each instrument has as a separate column in the spreadsheet, so the data can be easily plotted over the entire time range. By separating the data based on time, the COP or other interesting parameters can be analyzed. The parameter calculations follow similar steps as the basic thermodynamic modeling, but the temperatures, pressures, and flow are taken directly from the experimental data. The heat exchanger heat duties are calculated by using inlet and outlet pressures and temperature to calculate the enthalpy change. The turbine and compressor power are calculated in a similar manner.

START TIME:_____ TEST NAME:_____ ENDING TIME:_____

START OUTDOOR TEMP:_____ OPERATORS:_____ ENDING OUTDOOR TEMP: _____

DATE:		Expansion Valve Position						
		1 Turn	1.25 Turn	1.5 Turn	1.75 Turn	2.25 Turn	3 Turn	4 Turn
PC MASS FLOW [kg/s]	0.25	T: N: m:	T: N: m:	T: N: m:	T: N: m:	T: N: m:	T: N: m:	T: N: m:
	0.3	T: N: m:	T: N: m:	T: N: m:	T: N: m:	T: N: m:	T: N: m:	T: N: m:
	0.35	T: N: m:	T: N: m:	T: N: m:	T: N: m:	T: N: m:	T: N: m:	T: N: m:
	0.4	T: N: m:	T: N: m:	T: N: m:	T: N: m:	T: N: m:	T: N: m:	T: N: m:
	0.45	T: N: m:	T: N: m:	T: N: m:	T: N: m:	T: N: m:	T: N: m:	T: N: m:
	0.5	T: N: m:	T: N: m:	T: N: m:	T: N: m:	T: N: m:	T: N: m:	T: N: m:
	0.55	T: N: m:	T: N: m:	T: N: m:	T: N: m:	T: N: m:	T: N: m:	T: N: m:
	0.6	T: N: m:	T: N: m:	T: N: m:	T: N: m:	T: N: m:	T: N: m:	T: N: m:
	0.65	T: N: m:	T: N: m:	T: N: m:	T: N: m:	T: N: m:	T: N: m:	T: N: m:

NOTE: Record the time (T), turbo-machine speed (N) and CC mass flow (m) in the box corresponding to the data point. Hold on each point for 2 min to ensure steady state operating conditions. Record any abnormal behavior in separate log book.

Figure 4-91. Sample test matrix for the TCCS. The PC mass flow and CC expansion valve position are the primary control mechanisms for the system. All tests should be done in full operating mode as listed in Section F.7.

4.4.3. Uncertainty Analysis

The uncertainty analysis associated with evaluating the test data is important to determining the relevance of that value. In all cases, the uncertainty is directly related to the accuracy of the instrumentation used for a given measurment. Table 4-14 shows the accuracy of the important instruments used to calculate the primary thermodynamic properties. EES has a built-in uncertainty function that propagates measurement error throughout the calculation to determine the final uncertainty. The uncertainty function in EES uses the standard method of error propagation equation to produce an uncertainty for each calculation [98]:

$$u_c(y) = \sqrt{\sum_{i=1}^{N} \left(\frac{\partial f}{\partial x_i} \right)^2 u^2(x_i)} \tag{4.6}$$

The uncertainty propagation equation is used by taking the sum of the partial derivatives of all of the measurement terms used for a calculation. In the case of calculating the work done by the compressor, there are five specific measurements required: inlet pressure, outlet pressure, inlet temperature, outlet temperature, and mass flow rate. Each of these measurements has an uncertainty used in equation (4.6) to find the uncertainty. The data from Table 4-14 was input to find the uncertainty of the more important calculated parameters. The results of the uncertainty calculation are shown in Table 4-15.

The heat duty calculations are fairly accurate, with low uncertainties on the order of 1%. This low uncertainty is explained by the large enthalpy change across the heat exchangers because they include a phase change. In contrast, the turbine and compressor work and efficiencies have high relative uncertainties because their change in enthalpy is small. For example, the inlet and out enthalpies for the cooling cycle evaporator are 237.5 kJ kg^{-1} and 434.9 kJ kg^{-1}, respectively, while

for the compressor they are 434.9 kJ kg^{-1} and 439.8 kJ kg^{-1}, respectively. Because the difference is much smaller for the compressor case, the inaccuracy of the instruments exerts a large effect on

Table 4-14. Uncertainty for instruments required in uncertainty analysis.

Instrument Type	Range	Uncertainty
Thermocouple	All	1°C
Diff. Pressure Transducer	All	0.5% FS
Pressure Transducer	0-15 PSI	1.5% FS
Pressure Transducer	0-15 PSI 0-200 PSI, 0-300 PSI	1% FS
Pressure Transducer, 85°C to 125°C	0-200 PSI	1.5% FS
Pressure Transducer, Omega	0-300 PSI	0.25% FS
Velocity Flow Meter, Flue Loop	0-50 m s^{-1}	3% FS
Velocity Flow Meter, Condenser Cooling Towers	0-20 m s^{-1}	0.2 + 9% MV
Volumetric Flow Meter, Cooling Water	0-6.1 m s^{-1}	1% FS
Mass Flow Meter	0-7.5 kg s^{-1}	0.15% MV
Power Meter	All	1% MV

Table 4-15. Results and uncertainty for power and cooling cycle flow rates of 0.4 kg s^{-1} and 0.74 kg s^{-1}, respectively.

Parameter	Result and Uncertainty
COP	1.80 ± 0.02
$\dot{Q}_{p,b}$	63.1 ± 0.61 kW
$\dot{Q}_{p,cond}$	59.8 ± 0.49 kW
$\dot{Q}_{p,recup}$	17 ± 0.41 kW
$\dot{Q}_{c,e}$	145.3 ± 1.3 kW
$\dot{Q}_{c,cond}$	148.7 ± 0.56 kW
$\dot{W}_{p,t}$	3.38 ± 0.58 kW
$\dot{W}_{c,comp}$	3.59 ± 1.11 kW
$\eta_{p,t}$	0.66 ± 0.11
$\eta_{c,cond}$	0.79 ± 0.30

the measurement. The thermocouples in particular create a large uncertainty because over small enthalpy change ranges because minor deviations in temperature can have a prominent effect on the enthalpy. The uncertainty in the thermocouple measurements is ±1°C and those measurements are used to calculate the enthalpy which is used to calculate the compressor work. In one representative case, the compressor work was 3.59 ± 1.11 kW. A large majority of the uncertainty is related to the partial derivatives from the inlet and outlet temperatures which accounted for 45.5% and 48.0% of the uncertainty. One solution to the high turbo-machine uncertainties is to operate the system over larger power levels. The full design condition operation point is roughly 12 kW, and it is estimated the uncertainty will be a significantly smaller fraction of the calculations at these conditions. The overall system COP has a low uncertainty because the calculation is based on heat exchanger heat duties and auxiliary power loads. The heat exchanger heat duty uncertainties are low due to their large enthalpy change and the auxiliary power loads have minimal error due to the high accuracy of current transformer instrumentation. Having a low uncertainty in COP provides trust in the results.

CHAPTER 5. DATA ANALYSIS AND DISCUSSION OF RESULTS

The previous two chapters outlined the thermodynamic modeling approach and the test facility designs. This chapter will present the results obtained from the modeling efforts and the experiments. First, the baseline thermodynamic modeling results will be presented because they provide the initial design conditions and key inputs to calculate system performance during off-design modeling. Heat exchanger *UA* calculations are also shown to define the baseline conditions for the off-design modeling. Next, a test matrix used during the experiments is shown followed by the test results over multiple days of operation at a 27.5°C ambient temperature. A COP map is generated for the test results which shows contours of COP for a range of power and cooling cycle mass flow rates. The final results of the off-design performance modeling is given, and a similar COP plot is generated to make direct comparisons with the experimental data. Next, the results are discussed in detail, including descriptive comparisons between the prediction methodology and experimental results. Finally, an uncertainty analysis is performed which provides some context to the accuracy of the experimental calculations.

5.1. Results of Baseline Modeling with HFE-7000 and R152a

The following section shows the results of the basic thermodynamic modeling, Cordier analysis, and heat exchanger calculations as presented in Section 3.1. The basic thermodynamic model was evaluated using high, medium, and low temperatures of 106°C, 16°C, and 15°C, assumptions listed in Table 3-3, and the inputs listed in Table 3-4. T-s diagrams for the power and cooling cycles, using fluids HFE-7000 and R152a, respectively, are shown in Figure 5-1 while a summary of the basic results is listed in Table 5-1.

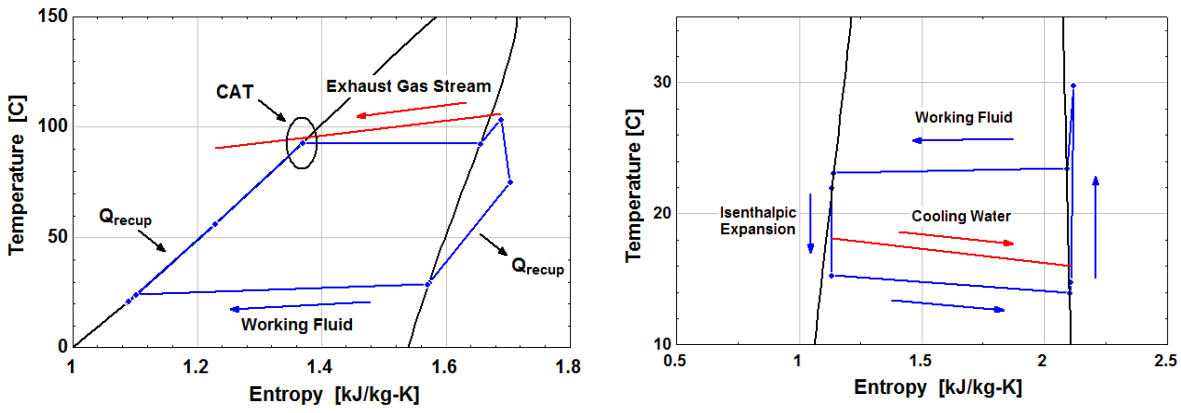

Figure 5-1. Temperature-entropy diagrams for the Rankine TCCS powered by a waste heat source while providing chilled water at 16°C and an ambient temperature of 15°C: **(a)** Power fluid HFE7000 **(b)** Cooling fluid R152a.

Table 5-1. Final system design point with fluids HFE-7000 and R152a for the power and cooling cycle, respectively.

System Parameters	Value	
COP	2.10	
Shaft Speed	30000	RPM
HFE-7000 Flow Rate	0.61	kg/s
R152a Flow Rate	0.92	kg/s
Pressure Ratio Compressor	1.36	
Pressure Ratio Turbine	6.30	
Shaft Efficiency	93.4%	
Compressor Efficiency	80%	
Turbine Efficiency	80%	
Pump Efficiency	50%	
Recuperator Effectiveness	89%	
Specific Speed Compressor	107.1	
Specific Speed Turbine	62.1	
Specific Diameter Compressor	1.57	
Specific Diameter Turbine	1.79	
Diameter Compressor	3.90	in
Diameter Turbine	4.09	in

System Parameters	Value	
Total Turbine Work	12.4	kW
Total Compressor Work	11.6	kW
Pump Power	0.45	kW
Heat Duty Cooling Cycle Evaporator	250.8	kW
Heat Duty Power Cycle Condenser	89.4	kW
Heat Duty Cooling Cycle Condenser	267.5	kW
Heat Duty Boiler	99.5	kW
Heat Duty Recuperator	26.4	kW
ΔP Cooling Cycle Condenser	15.5	kPa
ΔP Cooling Cycle Evaporator	20.1	kPa
ΔP Power Cycle Condenser	3.46	kPa
ΔP Power Cycle Recuperator – Liquid	1.4	kPa
ΔP Power Cycle Recuperator – Vapor	4.7	kPa
ΔP Power Cycle Boiler	1.6	kPa
Air Flow Rate Cooling Condenser	135000	m^3/hr
Air Flow Rate Power Condenser	39000	m^3/hr
Air Flow Rate Power Boiler	31363	m^3/hr

The T-s diagrams follow typical patterns for Rankine and vapor-compression cycles. The inlet and outlet state point for each component is shown as well as each heat exchanger regime. The pressure drop through the condensing and evaporating heat exchangers is seen plainly in the

diagrams because the path through the vapor dome is not horizontal. In an ideal heat exchanger, the pressure drop would be zero, and the temperature would not change in the vapor dome. For instance, in the condensing region of the cooling cycle, the fluid enters the vapor dome (quality of 1) at 23.45°C but exits (quality of 0) at 23.25°C. The non-zero slope of the line through the vapor dome represents realistic performance because these heat exchangers are modeled with realistic pressure drops.

In both T-s diagrams, the important secondary side temperature changes for the boiler and the chiller are shown. For the power cycle, the exhaust gas stream is plotted above the boiler heat exchange regions, and, for the cooling cycle, the cooling water temperature is plotted above the chiller regions. The temperature glides provide heat exchanger performance insight and help explain the COP calculation. The closest approach temperature (CAT) for a sub-critical Rankine cycle occurs either at the heat exchanger inlet or the fluid saturated liquid point. In the baseline modeling with HFE-7000 the CAT was 2.9°C which occurred at the fluid saturated liquid point. The CAT is a proxy for the effectiveness of the heat exchanger: a smaller number increases the required heat exchanger effectiveness. The CAT in the baseline case is fairly low, which is manifested in the high effectiveness and large size of the boiler heat exchangers. The cooling cycle evaporator has an even closer CAT of 1.2°C, occurring at the evaporator fluid outlet. There is very minimal superheat at the chiller outlet, so the saturation temperature is still very close to the chilling load. Since the outlet temperature and the saturation temperature are close to the cooling water temperature, the evaporator has a very high *UA* value of 212 kW K^{-1}, three times more than the next closest heat exchanger. As shown in Table 3-9, the chiller *UA* is dominated by the two-phase region with a value of 209.3 kW K^{-1}. This large two-phase *UA* is attributed to the high amount of heat duty required in the two-phase region and the closeness of the temperatures.

Although the chiller *UA* is the largest, the size and mass is small compared with the other heat exchangers because the secondary fluid is water. Water has a significantly higher heat transfer coefficient than air, so the chiller can be much smaller than the other heat exchangers even with a higher *UA*. As mentioned in Table 3-9, the total mass of the chiller is 154.8 kg as compared to the cooling cycle condenser which has a total mass of 405 kg. The performance of the evaporator changes for different temperature lift requirements, and the CAT temperature will be examined during the evaluation of those cases.

Another interesting point regarding the T-s diagrams is the difference in vapor dome shape for the power cycle versus cooling cycle. The power cycle fluid, HFE-7000, has a positively sloped saturated vapor line, which provides more room for turbine expansion and recuperation. In contrast, the cooling cycle fluid, R152a, has nearly vertical saturated liquid and vapor lines, which allows for more evaporative heat transfer and a less chance of forming liquid droplets in the compressor. These differences give context to the fluid selection techniques provided in Section 3.1.4. If a fluid with a positively sloped vapor dome (i.e., HFE-7000) were used in a vapor compression cycle, there would be a good chance liquid droplets would form in the compressor for high efficiency compressors. For example, in a HFE-7000 vapor-compression system with a pressure ratio of 2.5, the maximum efficiency of the compressor would be 39.5% before vapor droplets begin to form. In contrast, a R152a system has no efficiency limit for a similar configuration. In addition, a fraction of the evaporator heat duty would be lost through the expansion valve because the quality at the evaporator inlet would be higher for a positively sloped dome. For example, if both cycles started at the saturated liquid line (quality of 0) with a pressure of 500 kPa and had a pressure ratio of 2.5, the outlet quality for R152a as compared with HFE-7000 would be 0.15 and 0.35, respectively. The difference between the two qualities represents

lost heat duty in the evaporator. Similarly, if a refrigerant, such as R152a, were implemented in a Rankine cycle, the power from the turbine and recuperation ability would be limited due to the vertical slope of the dome. For instance, if two similar turbines (η = 60%) with pressure ratios of 2.5 were used, the recuperation capability for R152a compared with HFE-7000 would be 0.56 kJ kg^{-1} and 19.9 kJ kg^{-1}, respectively. HFE-7000 clearly has much more space to add a recuperative heat exchanger. These differences point to optimal power cycle fluids having large positive slopes and cooling cycle fluids having near vertical slopes. If additional fluids are considered in future tests, the slope of the vapor dome could be a reasonable predictor of performance.

Table 5-1 shows some important system parameters for the baseline design case with a 250 kW_{th} cooling load at the evaporator. The results of the Cordier analysis are also shown and the specific speed and diameter meet the required targets for 80% efficiency. This result validates the original efficiency targets for the baseline model. The turbine and compressor diameters, at 4.09 inches and 3.90 inches, are fairly small for rotation machinery with high efficiency due to the small relative size between the tips of the blades and housing. However, design calculations by Barber-Nichols confirm the ability to achieve the 80% efficiency. BNI also have confirmed the shaft efficiency estimates. There are several shaft efficiency losses, but the most prevalent loss is the windage due to fluid sheering within the shaft housing cavity. As the shaft spins within the turbo-machine, some fluid is entrained around the shaft and creates friction that causes a loss in power transfer. Meeting the turbo-machine efficiency targets will be one challenge to system performance.

The heat exchanger pressure drop inputs were developed by working closely with the Modine Manufacturing team to input realistic conditions into the modeling approach. The final heat exchanger pressure drops shown in the table are for the core areas only and do not include the

headers. These header pressure drops were included in the connection line pressure drop calculations (<2 kPa).

5.2. Comparison between R152a and R134a Cooling Cycles

As mentioned in Section 4.4, although R152a was selected as the cooling cycle design fluid, R134a was used during tests due to its low flammability characteristics. Due to the change in fluids, the performance of the system would decrease under all operating conditions due to the difference in fluid properties. Table 5-2 shows the difference in some key system parameters for an R134a system compared to R152a system when operating with similar thermodynamic state points. The results provided in Table 5-2 were tabulated using the off-design modeling approach under the same operating temperatures as the baseline R152a design case. The chiller *UA* and turbo-machine size were held constant to simulate the actual system components.

The first item is the COP and it is clear that the R134a system will not meet the required COP of 2.1. The lower COP is primarily driven by the lower chiller heat duty produced when operating with R134a. One explanation for the difference could be the difference in the vapor

Table 5-2. Full cycle comparison for baseline thermodynamic conditions comparing R152a and R134a cooling cycles.

Parameter	R152a	R134a
COP	2.1	2.0
CC mass flow rate [kg s^{-1}]	0.91	1.31
Chiller heat duty [kW]	250	244
Chiller *UA* [kW K^{-1}]	212	212
Compressor efficiency [%]	80	80
Turbine efficiency [%]	80	77
Turbo-machine speed [RPM]	30,000	24,233

dome. R152a has a slightly more vertically sloped dome, so the quality at the chiller inlet is 0.03. In contrast, for the same saturation conditions, the inlet quality for an R134a chiller is 0.09. This minor deviation could contribute to the differences shown in the heat duty. The mass flow rate is another note when considering Table 5-2. The mass flow rate of R134a is 1.31 kg s^{-1} while for R152a it is 0.91 kg s^{-1}. As was noted in Section 3.2.2, the difference in mass flow rate is attributed to the much larger enthalpy of vaporization for R152a. Figure 3-14 clearly shows the smaller enthalpy of vaporization for R134a. Due to the smaller enthalpy of vaporization, and similar chiller heat duty requirements, the mass flow rate for the R134a system must be larger than R152a to compensate. The difference in mass flow and the properties also has a significant effect on the turbo-machine performance. The efficiencies are computed by utilizing the turbo-machine maps, and are reliant on the mass flow rate, speed, and enthalpy rise. Although the mass flow rate is lower for R134a, the densities at the compressor inlet are very different (i.e., 13 kg m^{-3} compared to 22.7 kg m^{-3} for R152a and R134a, respectively). The difference in density drives the compressor inlet volumetric flow rates to be 2.38 ft^3 s^{-1} and 2.04 ft^3 s^{-1} for R152a and R134a, respectively. This volumetric flow rate difference is the likely reason for the drop in turbo-machine speed even though the mass flow rate of R134a is higher.

Based on the differences noted above, it is clear that a R134a cooling cycle has an entirely different performance as compared with R152a. These differences are accounted for by the UA scaling methodology because a fluid factor is employed in equation (3.49). This fluid factor allows the modeling approach to scale the *UA* based on any fluid combination. Future studies will consider incorporating multiple fluid combinations with the same heat exchangers to gain a broader understanding of system performance.

5.3. Test Facility Data Analysis

The testing done with the fluids HFE-7000 and R134a followed the general test matrix shown in Figure 4-91. The results of the testing are presented in the section below. The heat duties for the heat exchangers were generally consistent, but the turbine and compressor work were not—in some cases they were extremely high while in other cases they were close to zero. These errors are manifested in Figure 5-2, which shows the calculated turbine and compressor work over the entire test range on a given test day at roughly 27.5°C ambient. The first 1500 seconds of the test are during facility warm-up in which the turbine and compressor are not spinning. At approximately the 2000 second mark, the data becomes more consistent and the test matrix is filled. The sharp increases in compressor work (shown around the 2500, 4500, 5000, 7000, 10200, and 11200 second marks) are caused by a complete lack of superheating at the compressor inlet. As the fluid enters the vapor dome, temperature and pressure are no longer independent properties. Thus, small errors in either the pressure or temperature measurement sometimes cause the predicted thermodynamic state to

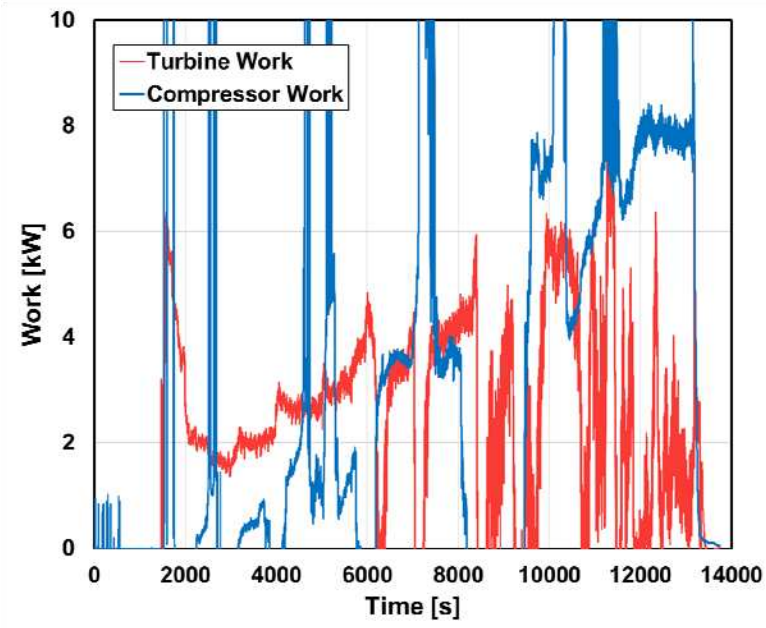

Figure 5-2. Turbine and compressor work plotted as a function of time for one test day.

erroneously be liquid instead of a vapor. Figure 5-3 shows the compressor inlet temperature and the saturation temperature at the inlet pressure. The points where the inlet temperature drops to the saturated line indicate a loss of superheated vapor entering the compressor. The change in superheat is rapid because the amount of heat duty required to maintain a superheating temperature is miniscule compared to the amount required for the two-phase region. For example, at a saturation temperature of 30°C, the heat duty for the two-phase region is 129 kW, while for the superheated region it is 14.2 kW. If the glycol loop was not monitored closely, the heat in the loop could suddenly drop below the heat duty required for the two-phase region, and cause a rapid loss of superheating.

When the compressor work decreases to zero (shown at 1800, 3000, 4000, 6000, and 8200 seconds) the compressor is stalling because the mass flow rate of the cooling cycle is too low. The low mass flow rate is caused by the high restriction by the expansion valve in these conditions. During these conditions there is still a pressure rise across the compressor, but the cooling cycle mass flow rate has decreased. The pressure rise across the compressor is therefore not a strong indicator of compressor stall and another metric is required. One indicator that can be used is the temperature rise

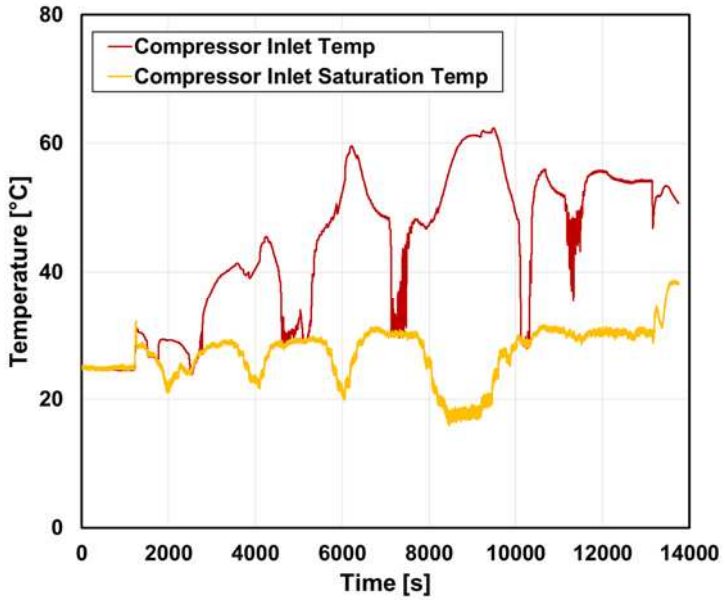

Figure 5-3. Compressor inlet temperature and saturation temperature to show loss of superheating.

across the compressor. During a compression process, a rise in temperature always accompanies a pressure rise. Therefore, during test runs, a good proxy for compressor stall was if a temperature rise existed across the compressor. This observation is exemplified by Figure 5-4 which shows the compressor inlet and outlet temperatures. The points at which the outlet temperature drops below the inlet occur at similar points as when zero compression occurs in Figure 5-2.

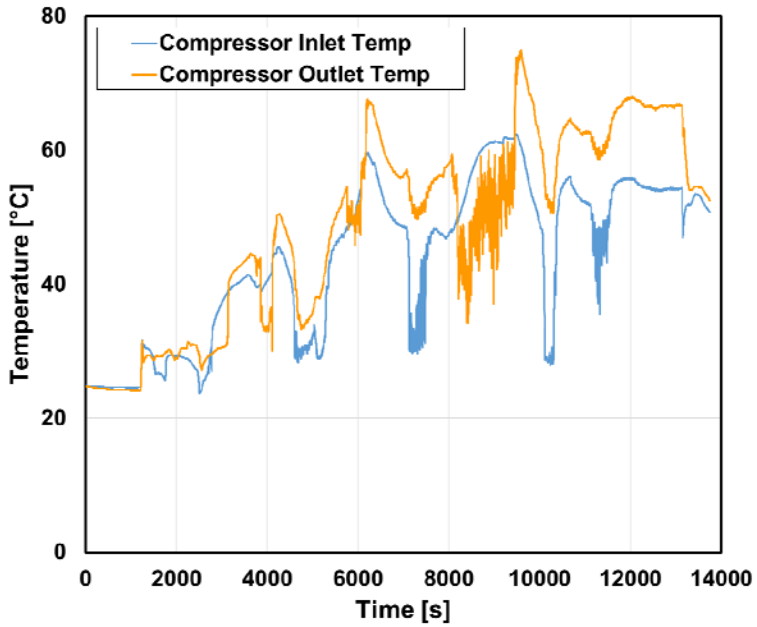

Figure 5-4. Compressor inlet and outlet temperatures.

The turbine work shown in Figure 5-2 is fairly consistent at each incremental power level for the opening 6000 seconds, but then experiences periods of high variability, and in some cases drops to zero. The variability in the calculations is caused by a loss of superheating at the turbine inlet. Similar to the compressor, the enthalpy at the turbine inlet cannot be calculated for points within the vapor dome because only pressure and temperature are measured and two independent properties are required. Figure 5-5 shows the turbine inlet temperature and the saturation temperature calculated at the inlet pressure. Towards the end of the testing, the turbine work calculation becomes erratic which is indicated by the low amount of superheat at the turbine inlet. During the tests, the boiler was slightly limited by the lack of heater power, but primarily from maldistribution of flow in the duct work. The

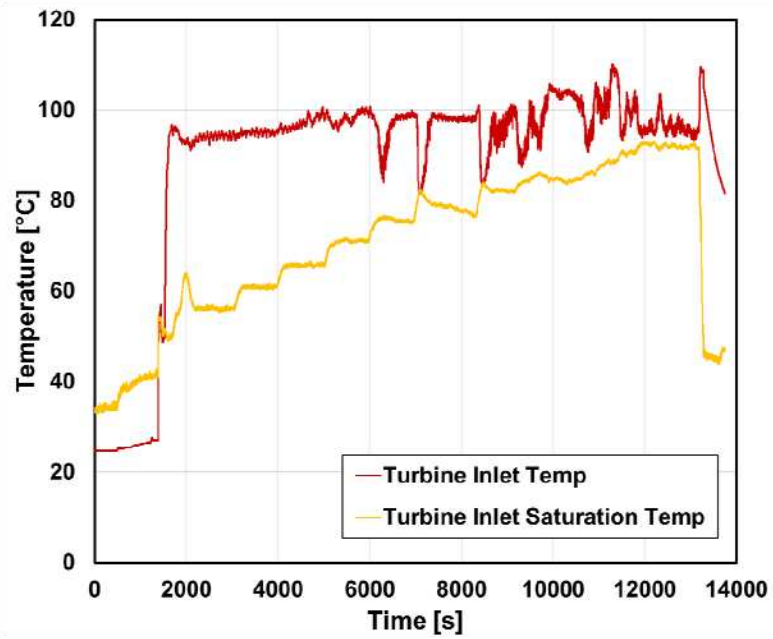

Figure 5-5. Turbine inlet and saturation temperatures.

outlet temperatures of the left and right boilers were significantly different during the testing, with one boiler having on average a 10°C higher temperature than the other. This indicates that the higher temperature boiler is receiving more mass flow, a higher temperature flow, or both. Figure 5-6 shows the differences between the two boilers as well as the turbine inlet temperature. The maldistribution is caused by a large area expansion in the flue gas loop and by the lack of mixing elements in the duct. Future testing will address this issue by characterizing the flow in the duct work and implementing mixing elements above the boilers if necessary. In addition, Figure 5-6 shows the turbine inlet temperature as sometimes being significantly less than the average of the two outlet temperatures. In one case, at the 5000 second mark, the average temperature from the two boilers is 104°C but the turbine inlet temperature is only 99°C. This temperature drop from the boilers to the turbine inlet could be caused by ambient heat loss from the lack of pipe insulation. One representative heat transfer calculation found that over the 1.2 m distance between the boilers and the turbine inlet, 2.3°C was lost due to natural convection. During future tests, insulation is recommended to limit efficiency losses for the system.

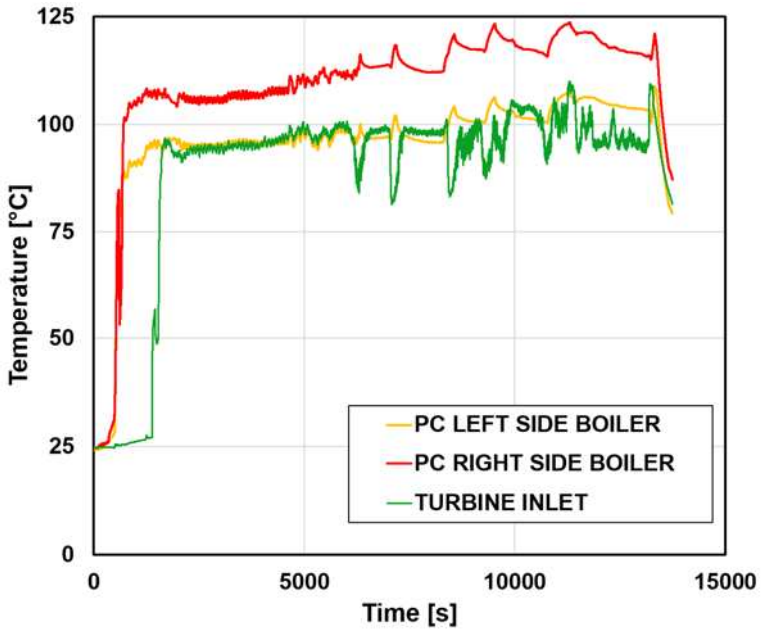

Figure 5-6. Boiler outlet temperature differences.

The increase in turbine saturation temperature throughout the tests as shown in Figure 5-2 is due to the increasing pressure ratio in the power cycle. During the test day, the power cycle mass flow was increased while following the test matrix plan. This mass flow increase is accompanied by a turbine inlet pressure increased caused by the pump moving along its system pressure curve. The turbine inlet saturation temperature then follows the pressure increase which reduces the superheating at higher pressure ratios. In general, the increase in mass flow rate also increases the turbine and compressor work as shown in Figure 5-2. Figure 5-7 shows the mass flow rates of the cooling cycle and power cycle for the same test day. The movement through the test matrix is clearly shown by the variation in power and cooling cycle mass flow. Each point was held for approximately two minutes to ensure steady state operating conditions. Since the time scale is fairly large, the pauses in cooling cycle flow rate appear to be small. For the first 7,000 seconds of testing the power cycle mass flow rate is fairly consistent at each power level, but then significant variation occurs, with dramatic variance at high flow rates after the 12,000 second mark. The variability is caused by a combination of low power cycle condenser pressure and high mass flow rate. These two factors cause the actual

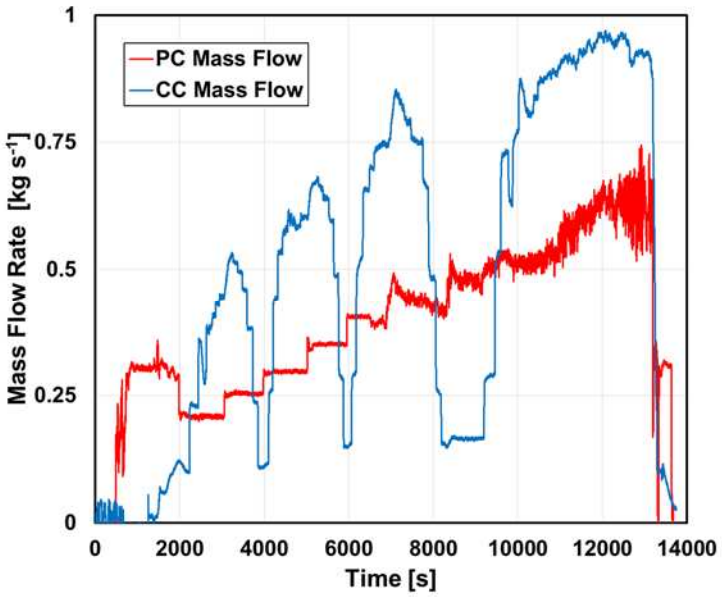

Figure 5-7. Power cycle and cooling cycle mass flow rates.

Net Positive Suction Head (NPSH) for the system to decrease below the required NPSH for consistent pump operation. The NPSH is the suction head that is required for the pump to operate without vapor bubbles forming in the pump. If vapor bubbles form, the pump will operate poorly and the blades could be damaged. One primary cause of pump cavitation is pump operation at high shaft speeds increases the pressure ratio which can cause a decrease of pressure at the inlet and incite vaporization within the pump. The NPSH for a pump is defined by the following equation [99]:

$$NPSH_a = H_A \pm H_Z - H_F + H_V - H_{VP} \tag{4.7}$$

where each of the terms on the right hand side of the equation relate to calculating the head entering the pump: H_A represents the absolute head of the fluid entering the pump, H_Z is the vertical distance between the surface of the supply and the pump, H_F is the friction losses in the piping, H_V is the head velocity at the pump suction port, and H_{VP} is the vapor pressure of the liquid. Many of these terms were omitted during the calculations by making some assumptions. The primary assumption used to eliminate the terms is that the pressure measurement is just before the pump inlet, so gravitational and

frictional losses can be neglected. Furthermore, the velocity head is neglected because it is small in comparison to the absolute head. After eliminating those three variables, a simple equation is left:

$$NPSH_a = H_A - H_{VP} \tag{4.8}$$

The vapor pressure is calculated by using a property relationship from the temperature measured at the pump inlet and the NPSH available to the pump is resolved. The power cycle pump is rated to operate at a NPSH of 5.2 ft when operating with a 1 cP fluid. Figure 5-8 suggests cavitation at NPSH levels of nearly 16 ft, significantly higher than the rating. One explanation could be that HFE-7000 has a significantly lower viscosity than 1 cP. The pump does not have specifications for low viscosity fluids such as HFE-7000 (i.e., viscosity of 0.3 cP). Thus, at these low pressure and high flow conditions, the pump cavitates and is unable to deliver a consistent flow. The data at high mass flow rates is generally unusable due to the high variance in flow. Figure 5-8 shows a NPSH estimation due to the low viscosity fluid. The black "required NPSH" line seems to match closely with the actual NPSH available and could explain the large variation in power cycle mass flow rate at higher pump

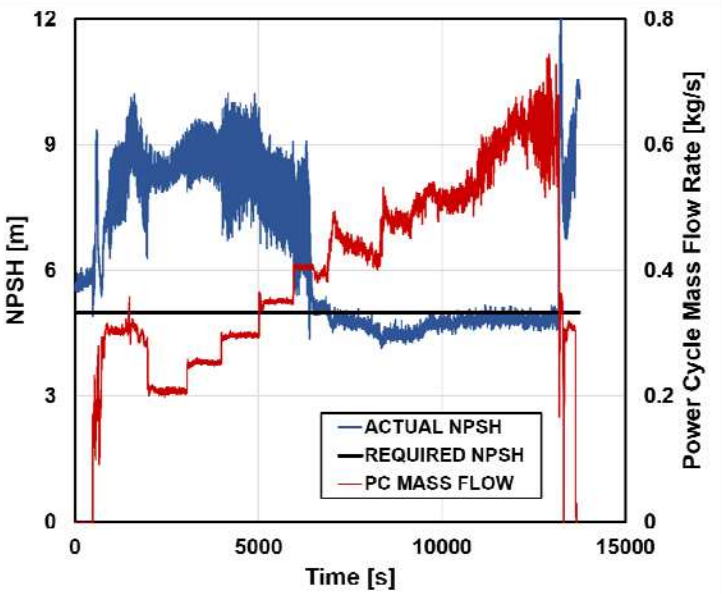

Figure 5-8. Comparison between actual and required NPSH and the effect on power cycle mass flow rate. Note, the required NPSH is an estimation based on experimental

speeds. It is clear that after 6000s the actual NPSH drops below the estimated required NPSH, causing cavitation.

Further evidence for pump cavitation is shown in Figure 5-9. The figure shows the power cycle mass flow rate and the condenser inlet pressure. For the first 3750 seconds, the pressure is low (~105 kPa) and mass flow rate has a large variance. Next, one of the power cycle condenser fans is powered off, thus decreasing the heat transfer across the condenser and increasing the saturation pressure. This increase in pressure, shown at 3800 seconds, is accompanied by the power cycle mass flow rate becoming steady (not shown in figure). One issue with pump cavitation is that for low ambient conditions, the pump will cavitate at lower mass flow rates, so achieving steady state conditions is challenging. Some possible solutions for the cavitation are to purchase a new pump with a lower NPSH requirement, to add a booster pump to increase the pressure of the flow, to operate two pumps in parallel to reduce the flow rate of each, or to move the pump to a lower elevation to take advantage of gravitational head. Each option requires a system redesign and extensive calculation.

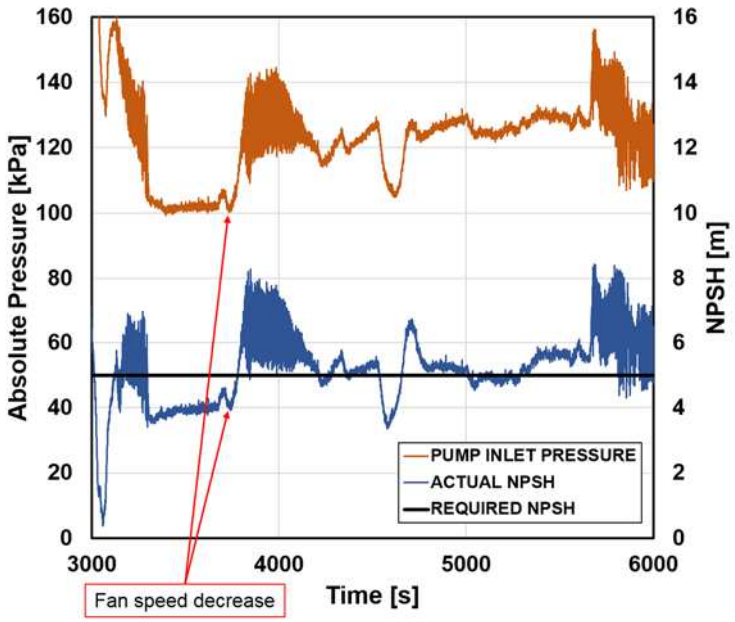

Figure 5-9. Power cycle pump NPSH changes at varying fan speeds for a steady state mass flow rate. Note, the required NPSH is an estimation based on experimental data.

One other option to continue testing in the current configuration is to artificially increase the condenser pressure by operating the fans at a lower power or operating at high ambient conditions. By operating the fans at low flow rates, the pressure will reduce because the heat exchangers will become less effective and will not be able to provide as much cooling. The risk to this method is that the condensation will reduce and a two-phase mixture will be sent to the pump. Operating at higher ambient conditions is not a particularly promising option either because the entire system will perform sub-optimally.

Other effects of the low condensation pressure are the recuperator and condenser performance. The saturation conditions in the condensers are primarily a function of the ambient air temperature. Since the saturation temperature must remain above the ambient temperature, higher ambients will produce higher condensing temperatures and, therefore, saturation pressures. As the power cycle mass flow rate increases, the heat duty for the recuperator increases, and, for mass flow rates above 0.45 kg s^{-1} during this particular test day, the vapor entering the recuperator condenses before it reaches the condenser. This is shown in Figure 5-10, where the recuperator outlet temperature is plotted against the saturation temperature at that condition. At about the 7,000 second mark, the outlet temperature drops to the saturation temperature, thus indicating condensation. This condensation means the recuperator is operating at a higher performance than expected, and that the heat duty of the condenser decreases. These two factors make it challenging to predict the heat exchanger performance with a theoretical approach because the inlet temperature and pressure are no longer independent properties (i.e. the inlet point is in the vapor dome). Further discussion will be provided on this phenomenon in Section 5.4.

Further analysis of Figure 5-2 shows that the turbine and compressor work do not always align with the efficiency estimates. For cases less than 6000 seconds, the shaft efficiency is significantly

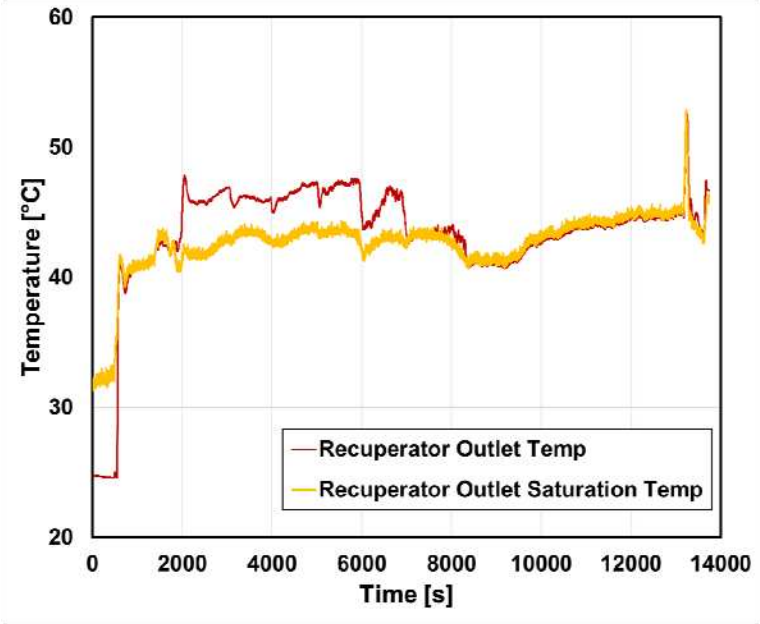

Figure 5-10. Recuperator outlet and saturation temperatures.

less than 93% with one sample at 5,600 seconds having a shaft efficiency of only 38%. It should be noted, however, that the uncertainty of the instrumentation can cause a large error the shaft efficiency. In the case noted above the uncertainty in the measurement is ±39% which makes it challenging to validate the results. There are two possibilities for this low shaft efficiency: that the cooling cycle is not at full capacity and that the design and test case are significantly different. Some of the cases have low shaft efficiency because there is a wide range of cooling cycle conditions for each turbine power output due to the mass flow rate control from the cooling cycle expansion valve. The power cycle will always output a similar power at a given mass flow rate, but the cooling cycle mass flow can be adjusted so the compressor does not always use the maximum work available, causing the shaft efficiency to be low. The other explanation for the error is that the turbine and compressor work are very low as compared with the full design case. The full design case has a turbine work of 12.4 kW, and in those cases the turbine is outputting only 3 kW. Barber-Nichols has not made efficiency predictions at these low conditions, so additional data at higher turbine powers will be collected to validate the shaft efficiency. In several of the cases, especially after the 8,000 second mark, the

compressor work is higher than the turbine work, which is impossible since the turbine drives the compressor. This sort of error is attributed to the aforementioned calculation errors such as lack of superheating for the turbo-machine and pump cavitation.

Due to the limitations outlined in the paragraphs above, an appropriate data range was selected to calculate the COP. The power cycle mass flow rate range selected was 0.35 – 0.5 kg s^{-1} while the cooling cycle mass flow rate range was 0.5 – 0.85 kg s^{-1}. Lower power and cooling cycle mass flows than the ranges caused stall conditions in the compressor, while higher power cycle mass flow rates showed high variance in power cycle mass flow. These differences are further exemplified by plotting the test data on the turbine and compressor maps. Figure 5-11 shows the cooling cycle data plotted on the compressor map while Figure 5-12 shows the power cycle data on the turbine map. The data points on the turbine map stay within the bounds of the map which indicates it will be easy to predict performance with the modeling approaches. It is clear, however, that many of the operating points were in the stall region of the compressor, which presents a modeling challenge. Many of the points outside the stall line did not present any unusual operating conditions or lack of compression. In fact,

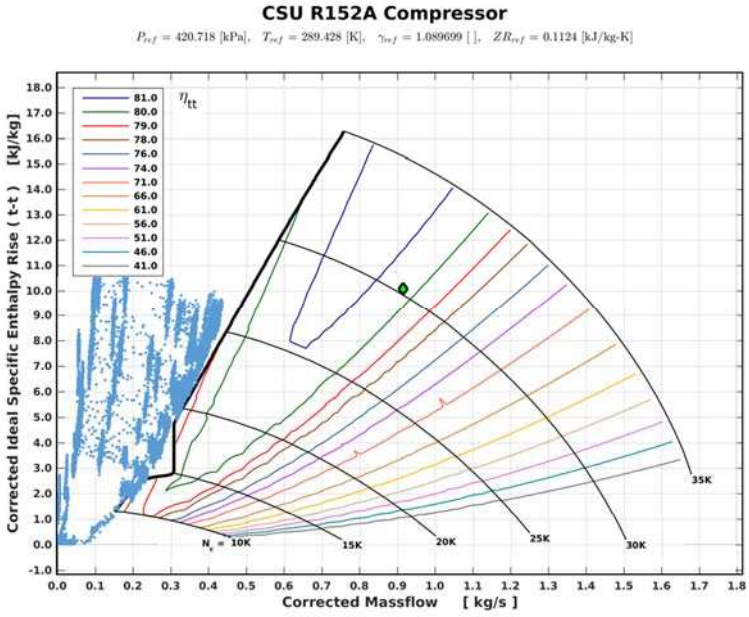

Figure 5-11. Data points plotted on compressor efficiency map.

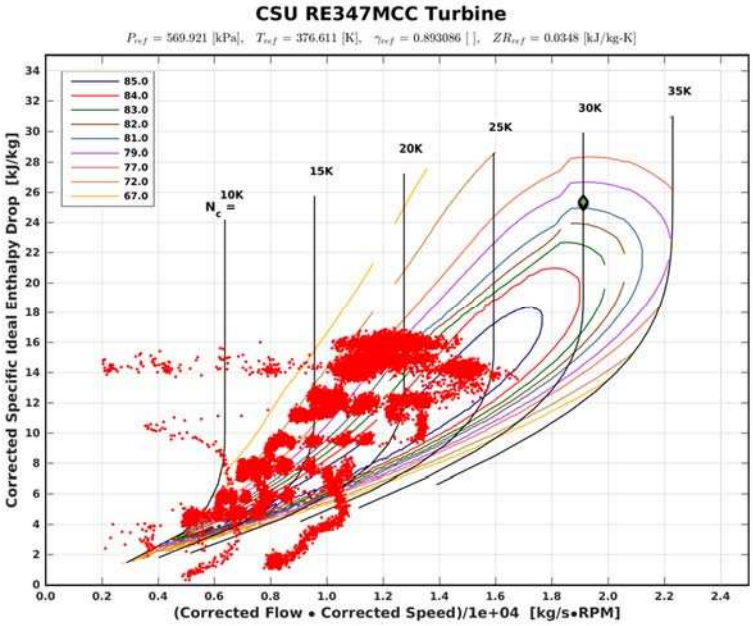

Figure 5-12. Data points plotted on turbine efficiency map.

if the points of very low cooling cycle mass flow are removed (those lower than 0.28 kg s^{-1}) where there was an observed compression loss (shown in Figure 5-2), there are still many operating points beyond the projected stall line as shown in Figure 5-13. This result suggests that the compressor stall condition actually occurs at lower cooling cycle mass flow rates than projected. The compressor stall condition may be a conservative approximation by Barber-Nichols, and future work will focus on determining the actual compressor stall line. It is expected that at lower ambient temperatures, the enthalpy rise and mass flow will reach higher values which will shift the data points from the stall region and onto the actual map.

One of the important results from the uncertainty calculations presented in Section 4.4.3 was that the uncertainty in the COP calculation is low. In the case noted in Table 4-15, the COP is 1.80 ± 0.02 which indicates the calculation can be trusted. The uncertainty is so low because the COP calculation is determined from large heat duties which can be found with a high degrees of certainty. The boiler and chiller have minimal uncertainty because they are phase change heat exchangers with a large difference in enthalpy between the inlet and outlet (i.e., chiller enthalpy rise of 196 kJ kg^{-1})

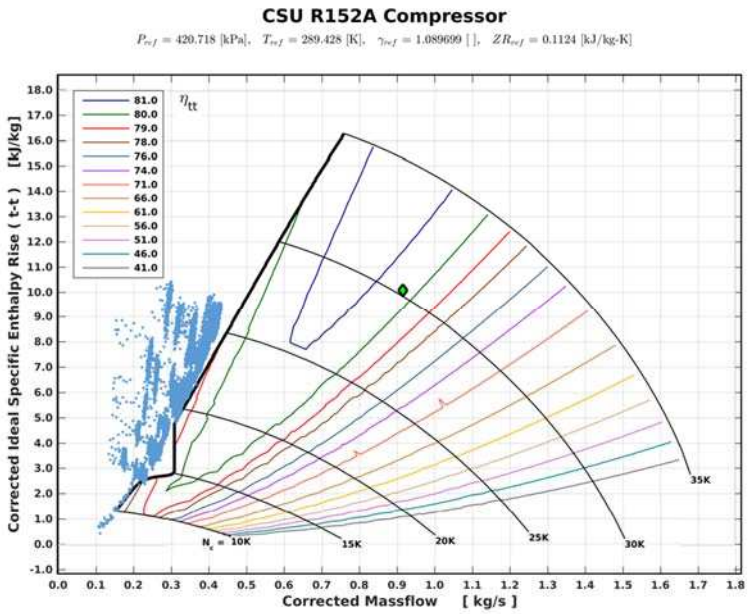

Figure 5-13. Data points plotted on efficiency map when removing those points below 0.28 kg s^{-1}, where no compression occurred.

that allows the temperature and pressure uncertainty to have small effects. For instance, the chiller and boiler heat duties are 145.3 ± 1.3 kW and 63.1 ± 0.61 kW, respectively. By employing the data recorded during the test days, the COP was plotted as a function of power and cooling cycle mass flow rate. The resulting plot, shown in Figure 5-14, is a COP map for 27.5°C ambient conditions. Each colored region on the map represents the COP range listed in the specified contour. In the case below, the lowest range reported is 1.3-1.4 in the bottom right corner, and the highest range is 1.8-1.9 in the center near a power cycle mass flow of 0.4 kg s^{-1}. The maximum COP recorded during these tests was 1.8 with power and cooling cycle flows of 0.4 kg s^{-1} and 0.74 kg s^{-1}, respectively. As mentioned above, the cooling cycle mass flow rate is set based on the power cycle flow rate and the cooling cycle expansion valve position. Because the turbine directly drives the compressor at the same speed, the power transferred through the turbine affects the compressor work and, therefore, cooling

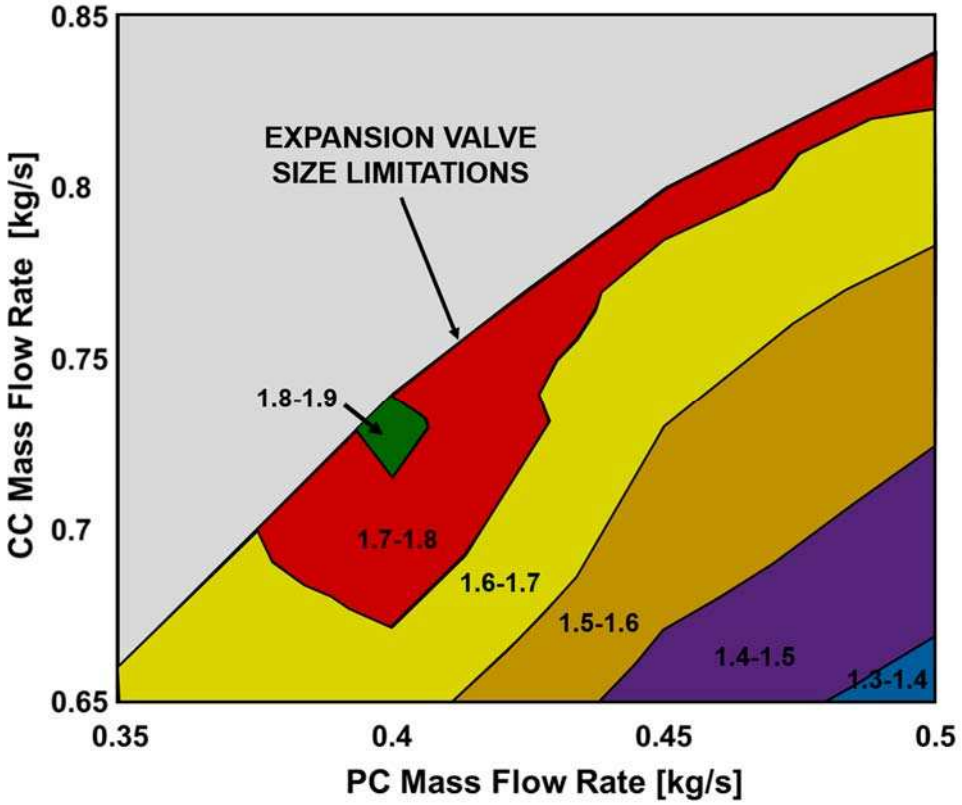

Figure 5-14. Measured system COP islands for various power and cooling cycle mass flow rates and at a 27.5°C ambient condition.

cycle mass flow. For each power cycle flow rate, there is a range of cooling cycle flow rates available depending on the expansion valve position. A fully closed valve will produce a mass flow rate of zero while a fully open valve will produce the maximum flow rate available. The gray region represents the cooling cycle mass flow rate limitation due to expansion valve. The line at the start of the gray region is when the expansion valve is fully open, thus generating the maximum possible cooling cycle mass flow. By increasing the diameter of the expansion valve, it may be possible to achieve higher cooling cycle mass flow rates and, therefore, COPs, for a given power cycle mass flow.

Increasing the cooling cycle mass flow rate by increasing the expansion valve size may be critical to achieving a high COP under any ambient condition. As shown in Figure 5-14, the COP of the system increases up to 1.8 around 0.4 kg s^{-1}, but then stagnates or even decreases back to 1.7 at higher flow rates. The primary driver behind the gradually increasing COPs as the power cycle mass

flow increases is that, during testing, the auxiliary power loads remain constant while the cooling duties increase. The auxiliary power loads, such as the condenser fans (10.6 kW), boiler fan (6.81 kW), and cooling water pump (0.18 kW), remain constant because the air and water flow rates remain the same across all tests. The COP calculation (equation (3.15)) includes the auxiliary power consumption in the denominator and the evaporator heat duty in the numerator, so as the evaporator heat duty increases, the auxiliary power load becomes a smaller percentage of the cooling duty, thus increasing the COP. For example, three different power cycle mass flow rate cases can be evaluated (i.e., 0.35 kg s^{-1}, 0.4 kg s^{-1}, and 0.45 kg s^{-1}) while operating at the maximum cooling cycle load. The auxiliary power load remains constant in all of these cases at approximately 17.6 kW, but both the heat duty (55.7 kW, 63.1 kW, and 72.4 kW) and the cooling duty (125 kW, 145 kW, and 158 kW) increase. One item to notice is that the cooling duties do not increase linearly or at the same rate as the boiler heat duty increases. The cooling duty is primarily a function of the cooling cycle mass flow, which can help explain the non-linear increase. For the test cases after 0.4 kg s^{-1}, the cooling cycle mass flow rate does not increase as rapidly as below 0.4 kg s^{-1}, which causes the boiler and auxiliary power loads to consume a larger fraction of the evaporator heat duty and lower the COP. An example of this effect is shown by the constantly decreasing ratio of mass flow rates as shown in Table 5-3.

Table 5-3. Mass flow rate ratio shows the steady decrease in mass flow rate ratio.

PC Mass Flow [kg s^{-1}]	Maximum CC Mass Flow [kg s^{-1}]	CC to PC Mass Flow Ratio
0.3	0.59	1.97
0.35	0.66	1.89
0.4	0.74	1.85
0.45	0.8	1.78
0.5	0.84	1.68

For an R134a system, the mass flow rates required for full operation are 0.61 kg s^{-1} and 1.4 kg s^{-1} for the power and cooling cycles, respectively. The ratio between those two flows is 2.3, and it can be noted that there is not a single case in Table 5-3 in which the cooling cycle to power cycle mass flow rate ratio meets the requirement. The explanation for the decreasing ratio is the expansion valve size. The cooling cycle expansion valve has a 0.5 inch diameter which is clearly undersized for an R134a application. This expansion valve issue will be explored in further detail with comparisons to the theoretical modeling approaches in the next section.

Another explanation behind the COP decrease is the effect caused by the changing exhaust and cooling water inlet temperatures. The exhaust and cooling water inlet temperatures have a direct influence on boiler and chiller heat duties. If the conditions vary from state point to state point, the performance of the system could be effected. Both temperatures were adjusted throughout the tests to maintain appropriate amounts of superheated vapor were entering the turbo-compressor. If the degrees of superheating decreased dramatically, liquid slugs could have entered the turbo-compressor, causing damage to the blades. Figure 5-15 and Figure 5-16 show the inlet temperatures of the exhaust gas and cooling water streams. It is clear that the temperatures vary between tests, and that the exhaust

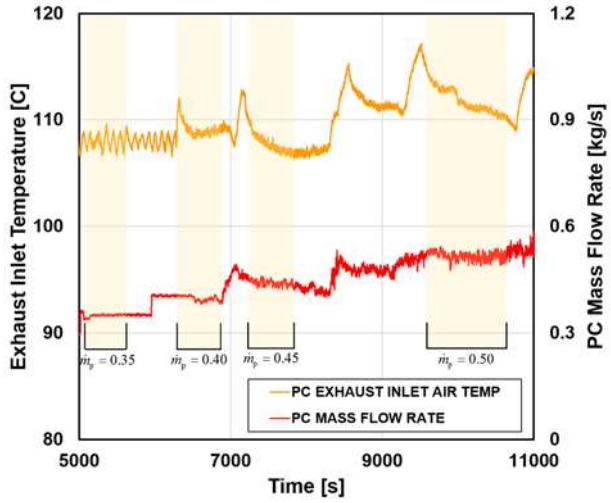

Figure 5-15. Variance in exhaust inlet air temperature for mass flow rates used to predict the system COP.

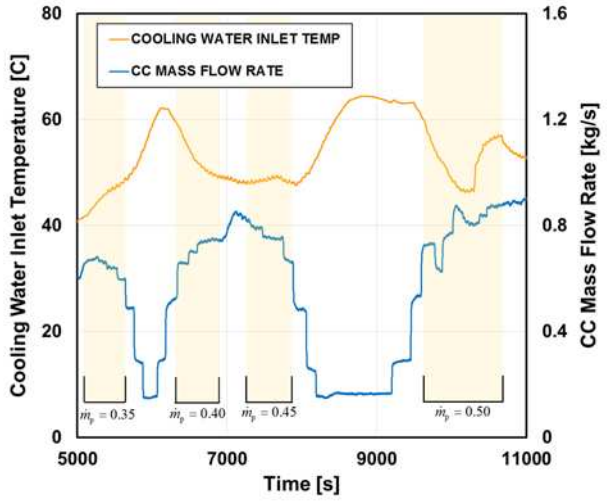

Figure 5-16. Variance in cooling water inlet temperature for mass flow rates used to predict the system COP.

gas temperature increases for higher flow rates. For example, at a PC mass flow of 0.4 kg s^{-1} the average exhaust temperature is 108°C, but for a mass flow of 0.5 kg s^{-1} the average is 111°C. This increase causes the boiler heat duty to increase, and, since the chiller has minimal temperature change, the COP decreases at higher flow rates.

The cooling water loop flow rate was another factor in the COP calculations. Figure 5-17 shows the volumetric flow rate for a test day. As can be seen in the figure, the volumetric flow rate varied dramatically and was much lower than the original design point prediction. The expected flow rate for the full design condition is 193 m^3 hr^{-1} (850 GPM), but the actual flow rate from Figure 5-17 is approximately 40 m^3 hr^{-1}. The large decrease is attributed to two factors: the pressure losses are higher than expected in the circulation loop and the pump lacks enough NPSH for full operation. To solve the NPSH issue, a surge tank should be added at a higher elevation to provide a gravity effect on the pump inlet. The high pressure losses can be solved by replacing the smaller pipe diameter sections with larger diameters, thus reducing the velocity through the piping and, therefore, pressure drop.

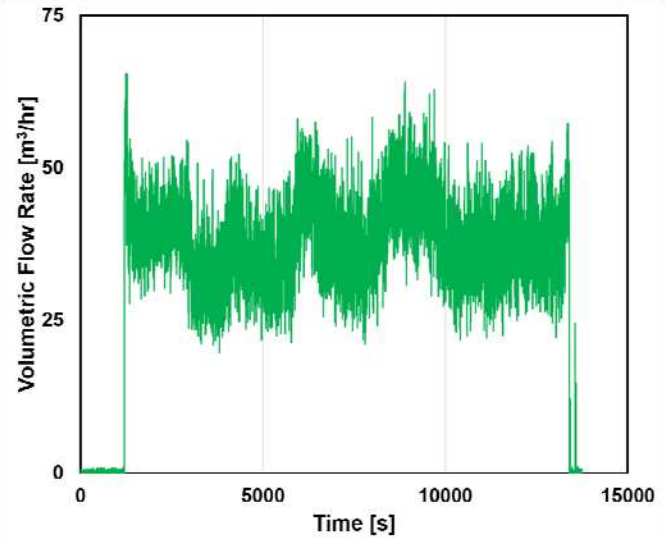

Figure 5-17. Cooling water volumetric flow rate variation during testing.

5.4. Comparison to Modeling Approach

In the previous section, the experimental results were presented for a range of test conditions at a 27.5°C ambient temperature. This section will present the theoretical modeling results for the method described in Chapter 3. The modeling approach was evaluated over power and cooling cycle ranges of 0.35 – 0.5 kg s^{-1} and 0.65 – 0.85 kg s^{-1}, respectively, so the COP map could be directly compared to the experimental results. The expansion valve size limitation, exhaust inlet temperature, and cooling water inlet temperature were all included in the theoretical modeling. For the exhaust air and cooling water inlet temperatures, Figure 5-15 and Figure 5-16 were used to find the actual flow temperatures. Since the test data is categorized on a time basis, the temperatures from Figure 5-15 and 5-16 were matched with the appropriate steady state operating condition to find the actual flow temperatures for the modeling. Table 5-4 shows a comparison of four representative data points for varying power cycle mass flow and generally a fully open expansion valve (i.e. maximum cooling cycle mass flow and COP). The cooling cycle evaporator and power cycle boiler

Table 5-4. Experimental data and modeling comparisons for TCCS performance at T_{amb} = 27.5°C.

	COP	Evap. heat duty [kW]	Boiler heat duty [kW]	Aux. Power [kW]	Chiller sat. temp [°C]	CC Condenser sat. temp [°C]	Boiler sat. temp [°C]	PC Condenser sat. temp [°C]
PC Mass Flow: 0.35, CC Mass Flow: 0.67								
Test	1.74	127	55.7	17.2	33.0	37.3	72.9	45.4
Model	1.26	123	78.0	19.5	32.1	37.3	75.2	41.9
Mod. Model	1.77	125	52.8	17.5	32.2	36.8	68.4	40.6
PC Mass Flow: 0.40, CC Mass Flow: 0.74								
Test	1.80	145	63.1	17.5	31.8	36.9	76.7	43.1
Model	1.37	143	84.9	19.5	28.3	36.7	79.4	39.8
Mod. Model	1.82	143	60.6	17.6	30.1	36.3	73.3	38.0
PC Mass Flow: 0.43, CC Mass Flow: 0.74								
Test	1.68	146	69.1	17.8	30.9	37.1	79.8	43.2
Model	1.35	143	86.4	19.4	27.5	37.3	80.9	39.7
Mod. Model	1.70	142	65.6	17.7	29.1	36.7	75.9	37.7
PC Mass Flow: 0.52, CC Mass Flow: 0.87								
Test	1.76	175	81.7	17.9	32.3	39.2	85.9	43.8
Model	1.49	171	100	19.3	27.9	38.3	87.3	42.0
Mod. Model	1.76	172	79.1	17.9	28.6	37.6	83.2	38

are included because they have a direct influence on the system COP. The saturation conditions of each phase change heat exchanger are included because they provide a context for the *UA* scaling method accuracy. The points were also selected due to their relative accuracy in terms of turbine and compressor power levels. In three of the four test cases, the compressor work was less than the turbine work with a fairly good shaft efficiency. The only case where the compressor work was erroneously above the turbine work is with power and cooling cycle mass flow rates of 0.4 kg s^{-1} and 0.74 kg s^{-1}. For this case the compressor work was 3.6 kW and the turbine 3.4 kW. As was documented in detail in Section 4.4.3, the uncertainties for these two values are very high due to the inaccuracy of the instrumentation. The uncertainties for the compressor and turbine work during this case were ± 0.58 kW and ± 1.1 kW, respectively. Since the two uncertainties are within the difference in the calculated values, the error is attributed to that uncertainty calculation. Increasing the turbine and compressor work in future tests by operating at lower ambient temperatures and higher mass flow rates will result in a lower uncertainty.

As shown in Table 5-4, the COP predictions are not very close to the experimental data. Further examination reveals that the cooling cycle evaporator heat duty and auxiliary power loads are fairly consistent in each case, but the power cycle boiler heat duty is dramatically higher causing a COP decrease. The reason for the boiler heat duty difference is from the maldistribution of flow in the exhaust simulation loop. Figure 5-6 shows that the outlet temperature of the superheated vapor from the two boiler heat exchangers are not consistent, and, in some cases, are different by up to 15°C. Due to lack of flow mixers, the air flow, air temperature, or both could be maldistributed in the loop causing the boiler temperature difference. The distribution causes the model to over-predict the boiler heat duty because the model assumes the full flow rate is utilized, when in reality a large portion of the flow is wasted. Thus, a corrected volumetric flow was calculated to account for the

maldistribution (Figure 5-18). By inspecting the data, it was clear that a linear relationship between the corrected volumetric flow and the power cycle mass flow rate was sufficient, and is as follows:

$$\dot{V}_{\text{p,b,a}} = 27124\dot{m}_{\text{p}} + 12972 \tag{4.9}$$

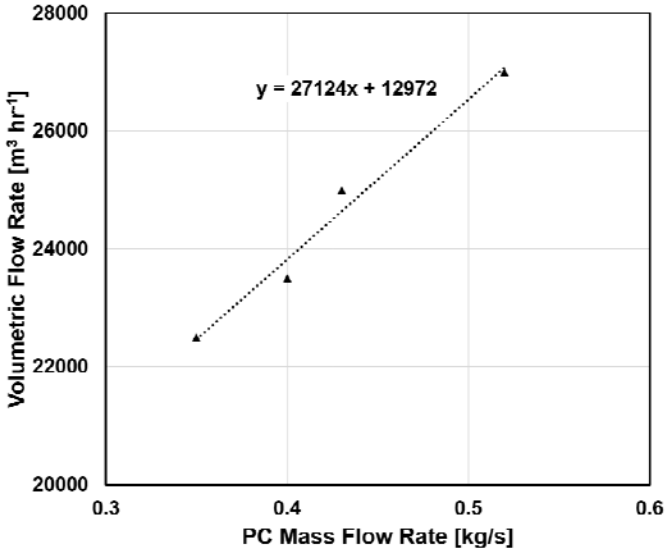

Figure 5-18. Plot of volumetric flow rate as a function of power cycle mass flow rate that is required to meet the boiler heat duty requirements.

One note about the above equation is that the percentage of wasted flow changes as the mass flow rate increases. Table 5-5 shows the percent difference in percentage between the required and baseline flow rates. For high power cycle mass flow rates, there is less wasted flow as compared to the lower flow limits. This fact explains the need for a linear best fit equation as opposed to a simple factor.

Table 5-5. Percentage of actual flow rate (32,500 m^3 hr^{-1}) for the range of mass flows examined.

Power cycle mass flow rate [kg s^{-1}]	Required volumetric flow rate [m^3 hr^{-1}]	Percentage of actual flow rate
0.35	22500	69.1
0.4	23500	73.3
0.43	25000	75.8
0.52	27000	83.3

Equation (4.9) was applied to the modeling approach and the four state points was recalculated as shown in Table 5-4. By analyzing the new data, it is clear that there is a dramatic accuracy improvement for boiler heat duty and COP. The maximum difference in COP for the experimental case as compared with modeling was 2.0%. This result provides validity for the model at the 27.5°C ambient condition. The modeling approach can be used to generate a COP map similar to Figure 5-14 for a detailed comparison of results. The predicted COP map (Figure 5-19) shows similar trends to the experimental modeling approach. This lends more credibility to the approach and provides a basis for extrapolation to future design conditions.

Figure 5-14 with Figures 5-19 generally follow similar trends, but there are some differences. The region of highest COP for the two maps is slightly different, with the experiment being a small

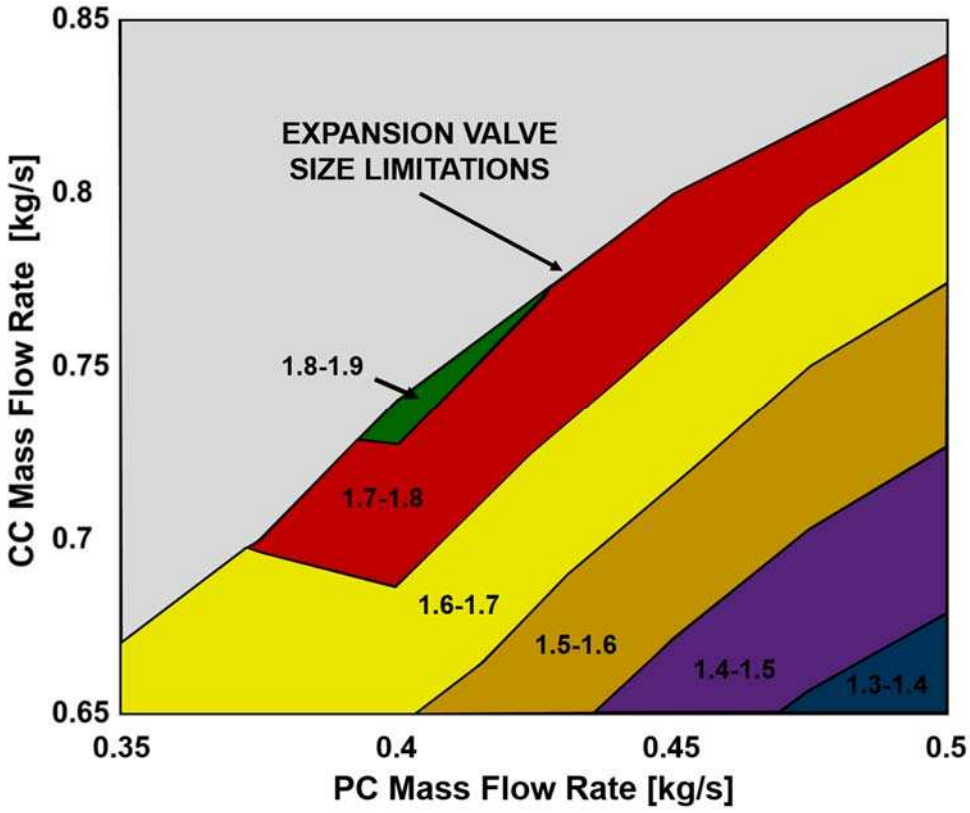

Figure 5-19. Predicted system COP islands for various power and cooling cycle mass flow rates at a 27.5°C ambient condition.

region isolated around power cycle mass flow of 0.4 kg s^{-1}, and the modeling results show an extended region of maximum COP for a power cycle mass flow between 0.4 kg s^{-1} and 0.44 kg s^{-1}. For the modeling approach, the COP increases in a smooth, linear fashion when the power cycle flow increases beyond 0.45 kg s^{-1}, while the experimental data follows a similar trend the path but not nearly as smooth.

Although the COPs aligned well between the two cases, the saturation temperatures of the heat exchangers did not always agree. The cooling cycle temperatures were fairly close throughout the initial three tests with differences less than 1.8°C, but there were some larger differences during the highest flow rate case, with maximum saturation temperature differences for the chiller and condenser of 3.7°C and 1.6°C, respectively. The power cycle saturation temperatures were predicted less accurately, which indicates the power cycle heat exchanger scaling was less accurate (i.e., maximum temperature differences of 4.5°C and 5.8°C for the boiler and condenser, respectively). These low differences help to explain the closeness between the heat duties.

One factor that drives the difference in power cycle condenser temperatures is the recuperator performance as mentioned in Section 5.4. Since the recuperator is a counter-flow heat exchanger, the area calculation approach is the same for the both the modeling and test cases. In the case above 0.43 kg s^{-1}, the recuperator partially condenses the vapor before it reaches the condenser. The recuperator *UA* calculation becomes erroneous because a two-phase section exists in the recuperator which is not accounted for in the experimental calculation or modeling approach. The *UA* calculations for the experiment and modeling are 4.0 kW K^{-1} and 2.27 kW K^{-1}, respectively. This effect also manifests itself as a difference in saturation conditions for the power cycle condenser at high flow rates. The superheated vapor region does not exist at these conditions, and the modeling approach does not account for these changes. Future modeling efforts will focus on analyzing a phase change within the

recuperator and removal of the power cycle condenser superheated region to make better system predictions.

Another of the major differences between the test and modeling are the turbo-machine efficiencies. Similar to the turbine and compressor work mentioned in Section 5.3, there is a high uncertainty associated with the efficiency calculations. A complete uncertainty calculation is shown in Section 4.4.3. In one example, with a power cycle flow of 0.52 kg s^{-1} and cooling cycle flow of 0.87 kg s^{-1}, the compressor efficiency is 107%, well above theoretical possibility. This error is attributed to inaccurate instrumentation over low enthalpy change ranges. A representative uncertainty calculation, gives an uncertainty for turbine and compressor efficiency of 66 ± 11.4% and 79 ± 29.5%, respectively. In contrast, the modeling approach predicts efficiencies within a small range. The range of efficiencies for the compressor is between 78% and 79% while the turbine has a slightly larger range between 74% and 80%. The reason the compressor has minimal prediction change is that the data points are located very close to the stall line of the compressor map. Figure 5-20 shows some representative results of the modeling effort plotted on the off-design compressor prediction map. At the far left of the map there is minimal efficiency change. This result shows that points very close to the stall line will almost always be predicted around 78% or 79%. Several of the points lie just outside of the noted stall region, and the model is at the edge of making predictions. These modeling points show some similarities to Figure 5-12, where most of the points are near or to the left of the stall line. In contrast, the data points plotted on the turbine efficiency map lie in the center or slightly left of center such that there are more available efficiencies. Figure 5-21 shows some representative results of the modeling effort plotted on the off-design turbine prediction map. The representative modeling points are consistent with those shown in Figure 5-13 where most of the points span across the center of the plot. As the power

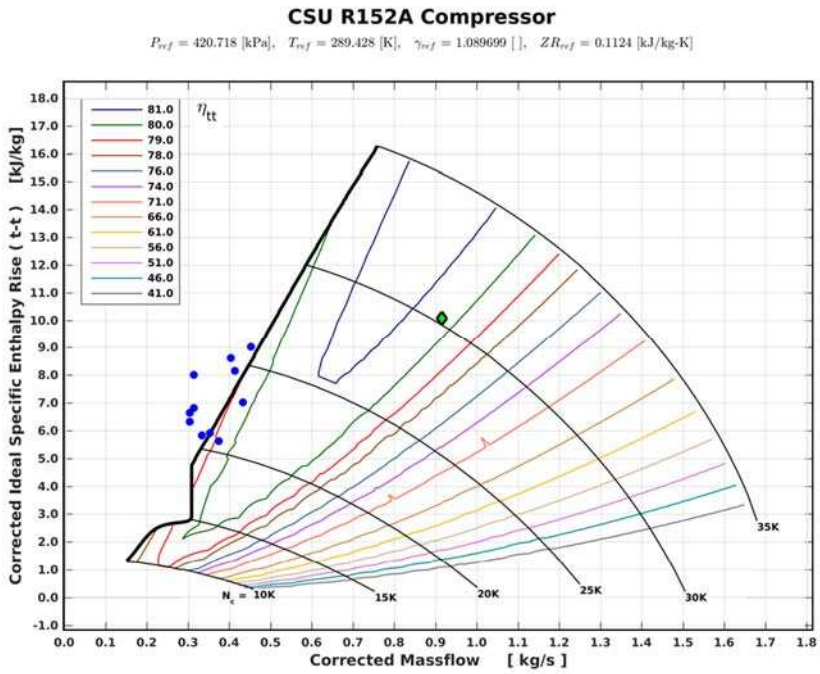

Figure 5-20. Representative modeling points plotted on the compressor map that show prediction along the stall line.

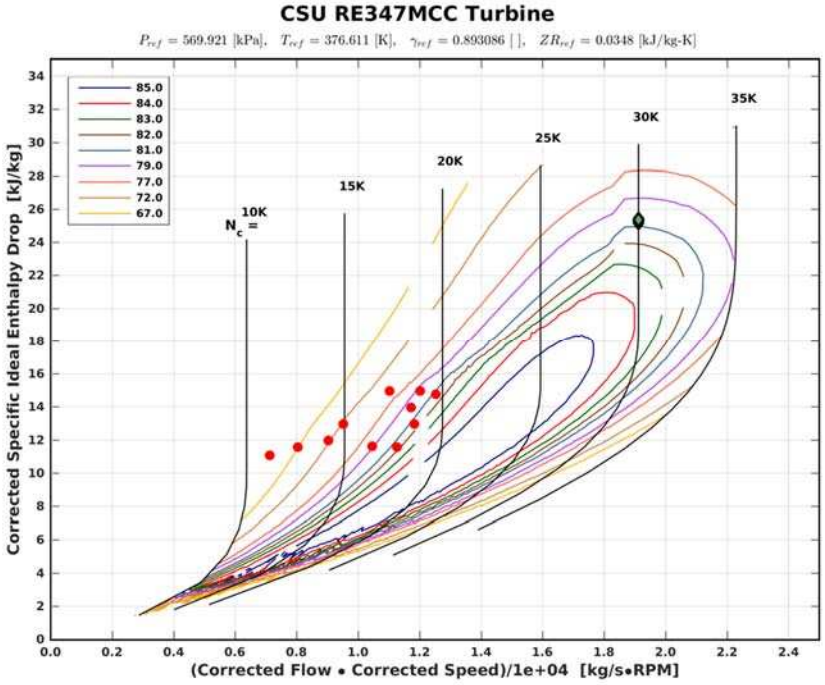

Figure 5-21. Representative modeling points plotted on the turbine map that show prediction in the center of the map region.

cycle mass flow rate and turbine work are increased, higher efficiencies could be realized. In addition, by increasing the turbine and compressor work in future tests, the uncertainties would decrease, leading to more realistic efficiencies.

Although the work and efficiency for the turbo-machine have a high uncertainty, the COP calculations have minimal uncertainty, because the heat exchanger heat duties are large. At the best COP point, the results including uncertainties for the COP, evaporator heat duty, and boiler heat duty were 1.8 ± 0.02, 145 ± 1.3 kW, and 63 ± 1.3 kW, respectively. These uncertainties are so low because the fluid undergoes a phase change in the boiler and chiller, dramatically increasing the outlet enthalpy compared to the inlet. This large enthalpy rise negates the inaccuracy of the thermocouple measurements, which were the largest contributors to the high turbine and compressor uncertainties. In the case of the chiller, the uncertainty in thermocouple measurements is still ±1°C, and the inlet and outlet temperatures account for 62% and 31% of the uncertainty, but the difference in enthalpy between the inlet and outlet of the phase change heat exchanger is 196 kJ kg^{-1}. The ±1°C thermocouples then only have a small effect over such a large enthalpy rise.

5.5. Comparison to State-of-the-Art Heat Activated Cooling

The predicted and test efficiencies are fairly high as compared with other heat activated cooling systems because of the high chilled water temperature. As was described in the Chapter 3, the TCCS was designed for a power plant application, in which the cooling water temperature is slightly above the ambient condition [6]. In these applications, the heat from the power plants cooling water can be rejected directly to the chiller two-phase fluid, while the TCCS condenser temperature is on average higher than the circulating water in the cooling tower. Although previous studies have shown that the total heat exchanger *UA* can be reduced with low temperature lift, future studies with higher temperature lifts are planned. These future tests would require a turbo-compressor with a

different blade design that could accommodate a higher pressure ratio and temperature lift. However, the current study operated under low temperature lift conditions and a cooling water temperature that was above the ambient, similar to another ORVC study performed by Wang et al. [21]. A representative evaporator saturation condition during testing was 32°C which, although significantly less than the waste heat temperature, is high when making direct comparisons to other state-of-the-art heat activated cooling systems. For instance, the maximum theoretical (Carnot) COP for the three reservoir TCCS system was 4.02 with the low, medium, and high temperatures of 27.5°C, 40°C, and 106°C, respectively. In comparison, a representative single effect absorption system had a maximum theoretical COP of 2.35 with low, medium, and high temperatures of 7°C, 29.4°C, and 100.6°C, respectively [55]. The results from the TCCS can be further compared to other state of the art heat activated cooling systems by plotting the experimental data similar to Figure 2-2.

Figure 5-22 shows the maximum COP vs the COP fraction for the four TCCS data points as compared with other ORVCs as well as typical single effect and double effect absorption systems. The data points for the TCCS are high because their COP fraction is close to the maximum theoretical COP. As was noted in Section 2.1, a system with points upwards and to the right is a more efficient system. Based on the data points provided, the TCCS has better performance than single effect absorption systems and could rival double effect systems. However, additional data points with higher theoretical COPs will be required to fully validate this claim. The four data points for the TCCS are all collected within a small range of max theoretical COPs (2.62 to 2.97) and COP fractions (0.59 to 0.69) because most of the data fell within similar temperature ranges. The temperature ranges for the boiler, condensers, and chiller during the four data points are 73-86°C, 43-44°C, and 31-33°C, respectively. Since the temperature ranges do not have a broad range, most of the data points fall fairly close to each other. In contrast, due to the wide range of literature studies compiled for the plot,

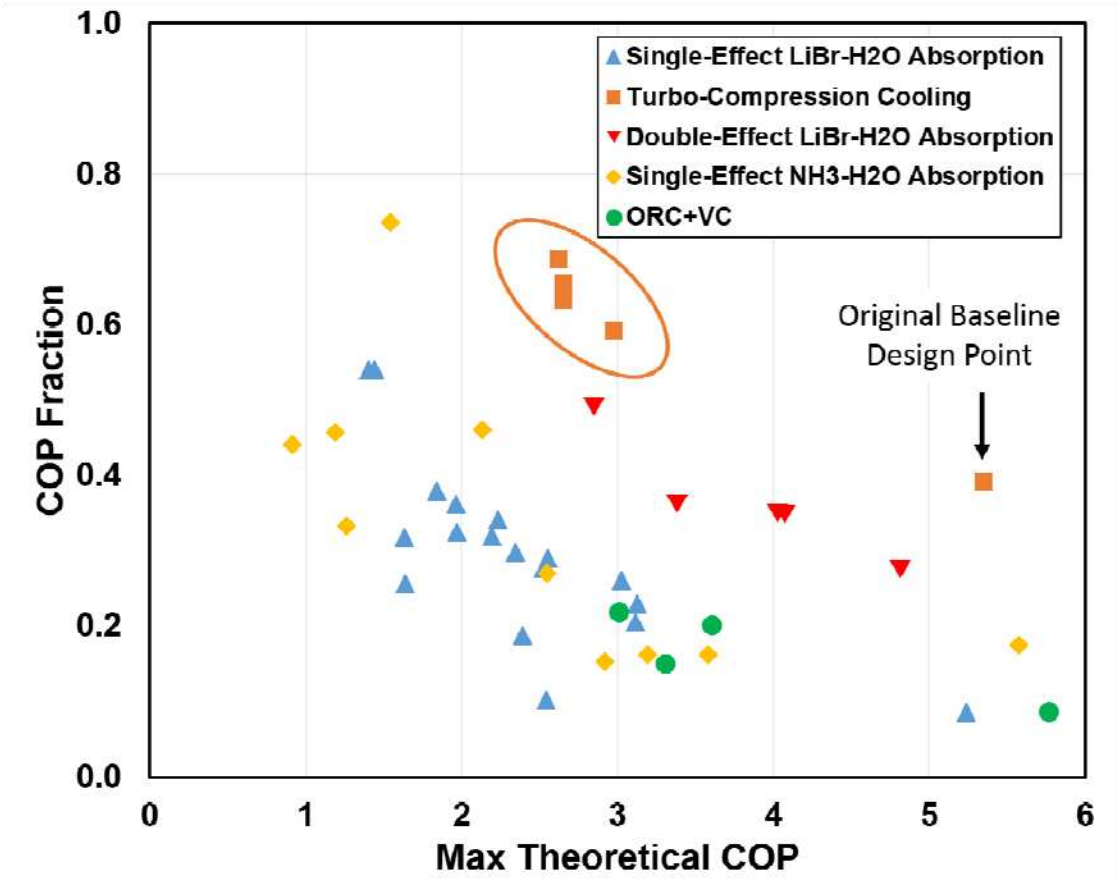

Figure 5-22. Comparison between the max theoretical and COP fraction for absorption and ORVC systems vs. the TCCS.

the other systems have a much larger range on the plot. It should be noted, however, that there are a variety of factors that can cause a high maximum theoretical COP. For instance, the single-effect lithium bromide-water absorption point with a max theoretical COP of 5.24 has high, medium and low temperatures of 85°C, 27°C, and 18°C, respectively [36]. The values that create the high max theoretical COP are the high evaporator temperature and low condenser temperature. In contrast, the single-effect ammonia-water system (max theoretical 5.58) has high, medium, and low temperatures of 150°C, 25°C, and 10°C, respectively, so the high boiler temperature creates the high max theoretical COP [13, 30]. These differences in the calculation show the need for Figure 5-22 because the two systems have radically different temperature ranges, and yet fall within a similar region in the figure.

Some direct comparisons can be made for systems with similar max theoretical COPs as the TCCS data points to gain a better understanding of the performance benefits. The high, medium, and low temperatures for a sample TCCS data point are 86°C, 44°C, and 32°C and the COP is 1.76 with a maximum theoretical COP of 2.97. A sample single-effect lithium bromide absorption chiller has a max theoretical COP of 2.35 with high, medium, and low temperatures of 100°C, 29.4°C, and 7°C, respectively [9]. Since the COP for this chiller is only 0.7, it is very clear that the TCCS is outperforming the single-effect chiller. A sample double-effect lithium bromide absorption chiller has a maximum theoretical COP of 2.85 with high, medium, and low temperatures of 170°C, 42°C, and 13°C, respectively [49]. The actual COP for this chiller is 1.4, so the COP fraction aligns closely to the TCCS. There are many examples shown in Figure 5-22, and it is fairly clear that the TCCS is outperforming the other heat activated cooling technologies. However, more TCCS data points should be plotted to further validate the test facility.

One final note regarding the comparisons between experimental testing and the modeling approach was the limitations which occurred in the modeling. The modeling approach has limitations below the presently reported modeling range due to the complex iterative techniques required. The modeling approach fails to converge on a solution when either the calculated turbine and compressor work or the heat exchanger *UAs* become too small compared to the original design point. It is expected that for higher mass flow rates than tested for this study, that the modeling approaches will have less calculation limitations. Future modeling approaches will focus on expanding the calculation range for the modeling approach and making applications to real system applications.

5.6. Power Plant Cooling Predictions

One application for the modeling approach is to make predictions for TCCS performance when operating under power plant conditions as noted in Section 3.1.1. The present experimental results are for similar waste heat temperatures, but significantly different cooling temperatures. Insights can therefore be found by using the off-design performance methodology to predict system performance under the current experimental restrictions. The two major differences between the original design case and the current configuration are the smaller chiller size (half of design point) and the use of R134a as the cooling cycle fluid. The analysis will provide useful information on how the system will perform if the lower temperature conditions were achieved and provide ideas on potential modifications to achieve the final design target. As mentioned in Section 3.1.1, the original performance targets of the system were to achieve a COP of 2.1 with high, medium, and low heat reservoir temperatures of 106°C, 16°C, and 15°C. By adjusting the temperature and mass flow rate inputs in the model, the COP of the R134a system is 2.0 with a chiller *UA* of 212 kW K^{-1}. One method to increase the COP is to increase the chiller size, since the currently configured system uses only one of the two original design chillers. Figure 5-23 shows the COP as a function of cooling cycle chiller *UA* while the system operates at the design temperature for two different fluid cycle options: R134a and R152a. For these simulations, the chiller *UA* increased manually while the rest of the *UA*s were calculated with the scaling methodology. The flow rates for the condensers (60,000 m^3 hr^{-1} and 190,000 m^3 hr^{-1} for the power and cooling cycles, respectively) and boiler (31,363 m^3 hr^{-1}) were fixed to simulate the power plant design conditions, but the chilled water flow rate could vary as the chiller *UA* increased. During the simulations the chilled water temperature met the design target of 17.2°C to 16°C and the chiller saturation conditions were allowed to vary depending on the chiller *UA* value. For example, at chiller *UA*s of 155 kW K^{-1} and 255 kW K^{-1}, the chiller saturation

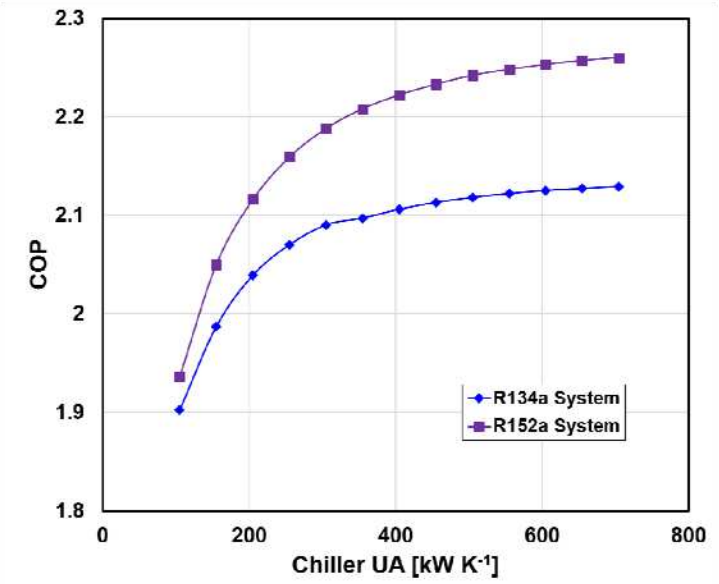

Figure 5-23. System performance as a function of chiller *UA* for the power plant application heat reservoir temperatures.

condition for R134a changed from 13.78°C to 14.3°C, respectively. For the same *UA*s on the R152a cycle, the chiller saturation conditions were 13.43°C and 13.48°C. The difference in saturation temperature between the two fluids provides some explanation for why R152a requires less *UA*: the saturation temperature for R152a is farther from the chilled water temperature, so the effectiveness can be smaller, thus driving a lower *UA*.

The first points at the left of the figure represent the system operating with the currently sized chiller (*UA* = 105 kW K^{-1}). As the chiller *UA* is increased, the performance of the both systems increases because more heat exchanger area is available. However, there is a diminishing effect to the increase because the effectiveness of the heat exchangers is maximized, which limits the heat duty. As is shown in the figure, R152a has consistently higher performance than R134a: the maximum COP for R134a is 2.12, while for R152a it is 2.27. This result relates back to the original fluid selection process (Section 3.1.4) in that the best cooling cycle fluid was R152a, and none of the other fluids met the design targets. For R134a to meet a COP of 2.1, the *UA* requirement would be approximately

390 kW K^{-1} or four of the current heat exchangers. If several other fluid options were compared in a similar manner, it is expected that R152a would have the lowest *UA* requirement. As noted briefly above, R152a will have a low *UA* partially due to its low chiller saturation temperature and pressure compared to other refrigerants. For instance, at the design condition, the chiller saturation temperatures for R152a and R134a were 13.8°C and 14.3°C, respectively. Since R152a has a lower saturation temperature, the effectiveness is lower, and the heat exchanger *UA* is not as high for R134a, which allows better system performance for a smaller heat exchanger. Future experimental studies should focus on increasing the chiller size and changing the cooling cycle fluid to R152a, allowing the system to meet the final power plant performance target.

CHAPTER 6. CONLUSIONS AND RECOMMENDATIONS

The previous chapters have focused on the modeling, design, and testing of a waste heat driven cooling system. Chapter three presented the basic modeling approach including the thermodynamic equations, fluid selection process, and heat exchanger *UA* calculations. The off-design performance methodology was then described by defining a *UA* scaling method and presenting the turbo-machinery efficiency maps. These two factors were used to describe an off-design performance methodology to predict system COP at any condition. Chapter four presented the design and construction of the TCCS test facility. The facility can provide a cooling load of 250 kW_{th}, but was not operated at the maximum potential due to a few design limitations. Future efforts will correct these design limitations to achieve the final design condition. Chapter five is focused on modeling and experimental results. First, the thermodynamic and heat exchanger *UA* calculations for the baseline case were presented to provide a context for the rest of the chapter. The experimental results were shown for test days in which the ambient design condition was approximately 27.5°C. The system design limitations were also explained in these sections with supporting arguments for modifications that would produce optimal performance in future tests. Next, the test data and modeling analysis were compared and the results showed poor correlation due to the differences in boiler heat duty. A boiler flow rate maldistribution factor was derived that could correct the poor correlation. When applying the new boiler flow rate factor, the largest error in COP between the modeling approach and the experimental data was only 2.0% which suggests strong correlation between the model and experiment. However, it is important to note that the modeling approach is only validated over the power and cooling cycle mass flow ranges of 0.35 – 0.5 kg s^{-1} and 0.65 – 0.85 kg s^{-1} with an ambient temperature of approximately 27.5°C. Further

testing will be required at a variety of temperatures and mass flow conditions to fully validate the model and provide complete confidence in the validity at all conditions.

The experimental COPs are fairly high as compared with traditional heat activated cooling systems because the medium and low reservoir temperatures are close to the high temperature reservoir. The application for this research was to provide a cooling load for power plants at a fairly high temperature of 17°C. The current testing results did not replicate the final design condition and, as a result, the chilled water temperature was much higher than the design case (approximately 35°C). These high temperatures increase the maximum theoretical COP and, therefore, the actual COP that can be achieved. By plotting the maximum theoretical COP and the COP fraction for the TCCS test points along with current state-of-the-art heat activated cooling technologies, the performances can be compared graphically. Figure 5-22 shows a sample of several single effect and double effect absorption systems as compared with traditional ORVC and the TCCS. The figure shows that experimental TCCS data lies upward and to the right of single effect systems and is very similar to double effect absorption. The major disadvantage of double effect absorption systems is that they are more complex and have many large heat exchangers which can drive capital costs upward. The TCCS, by comparison, can operate over a range of conditions without requiring any capital cost increase. Furthermore, TCCS operation is simple compared to other heat activated cooling systems, which could lead to easier adoption in the future. Although these results present a potentially disruptive technology, future tests will collect data for a wider range of operating conditions to improve the comparison between the TCCS and other heat activated cooling systems.

The experimentally validated model was used to project system performance for power plant design conditions. If the currently configured system (R134a cooling cycle with a chiller *UA*

= 105 kW K^{-1}) was used under the power plant conditions it is projected the COP would be 2.0. Increasing the size of the chiller would be beneficial to the COP, and a *UA* of 390 kW K^{-1} would be required to reach a 2.1 COP. The best solution is to implement a larger chiller with the original design fluid R152a. If the chiller *UA* is increased to 190 kW K^{-1} then a COP of 2.1 can be achieved.

Although the modeling approach does make good predictions of the results within the data range and for the original design condition, further work may be required for the model to operate over the entire range of possible conditions. One limitation is that the modeling approach is cannot make predictions at low mass flow rates due to heat exchanger scaling limitations. As the mass flow decreases, the heat exchanger *UA*s become small relative to the original baseline point. The decrease in *UA* drives the NTU and effectiveness of the condensing heat exchangers to very low levels which makes the model calculation difficult. Similarly, if the temperatures or volumetric flow conditions go out of range for a given mass flow conditions, the heat exchanger NTUs and effectivenesses can increase to their respective limits. One example of this is the boiler exhaust gas volumetric flow rate. In many modeling cases, the effectiveness of the two-phase and vapor regions of the boiler are between 0.95 and 0.99 because the volumetric flow rate of the air includes the maldistribution factor, which decreases the flow rate available to the boiler and causes it to be extremely effective. Another issue with the scaling methodology occurs when making predictions at *UA* levels above the baseline point. For instance, the baseline chiller *UA* is 105 kW K^{-1}, and the model can solve up to approximately 130 kW K^{-1}, but then has difficulty. The main reason for the difficulty is that the heat exchangers in the baseline case have a high effectiveness already, and increasing the *UA* above the baseline case imparts a higher effectiveness requirement, thus making it impossible to remain below the theoretical limit. Therefore, the *UA* scaling methodology cannot be applied well for making predictions at mass flow rates above the baseline design conditions.

Another difficult aspect to the off-design modeling approach is the heat exchanger scaling equations. The most challenging heat exchanger to predict is the power cycle boiler. The boiler is a cross-flow heat exchanger, but has two passes which also makes it similar to a counter-flow heat exchanger. The present modeling approach attempts to join these two heat exchanger types by calculating the area as a cross-flow heat exchanger (without two passes), but calculating effectiveness and NTUs (required for *UA*) by assuming a counter-flow heat exchanger. The boiler heat duty results could, therefore, be erroneous, and yield incorrect COPs for conditions outside of those examined in this study. In addition, the counter-flow evaporator does not include any area scaling because it is challenging to determine the flow area without detailed heat transfer calculations. Future modeling approaches could focus on deriving a counter-flow heat exchanger *UA* scaling methodology that could apply to the chiller. This area scaling methodology could also extend to the counter-flow recuperator which, in some test conditions, began condensing the vapor before the fluid reached the condenser. The power cycle condenser *UA* scaling could also be modified to follow similar considerations because in some test cases the superheated region was non-existent, which was not accounted for by the modeling.

There were several test facility limitations that will require correction prior to full system operation at the optimal design condition. The problems identified in Section 5.3 are the lack of superheating at the turbine inlet, the power cycle pump cavitation, the low cooling water flow rate, the expansion valve size, and the chiller size. As noted in Table 5-5 the turbine superheating is a problem for high mass flow conditions. There are two possible solutions to the inability to produce superheated vapor at the turbine inlet: pipe insulation and flue loop maldistribution. The pipe insulation between the boiler outlets and the turbine inlet will reduce the ambient temperature loss in the connection lines and prevent the lack of superheating. The other solution is to characterize

the flow in the flue loop and create a flow mixing device to evenly distribute the flow. The evenly distributed flow will allow more boiler heat exchange, thus increasing the amount of superheated vapor available.

The second major issue with the power cycle is pump cavitation. Figure 5-8 shows that for high flow rates and low ambient temperatures the power cycle pump will cavitate, causing a large fluctuation in flow and loss of power. The solution to the cavitation issue is to increase the actual NPSH at the pump inlet. There are a few options, but the most recommended option is to add a booster pump in series with the main pump to increase the pressure. The booster pump would require a lower NPSH than the current pump and also be able to handle HFE-7000, a low viscosity fluid. By increasing the pressure before the pump it will be possible to operate at higher power cycle mass flows.

The chiller replacement and cooling water simulation are very similar issues because the both involve the ability to simulate the full scale cooling load required for the design condition. Unfortunately, only one of the two chillers was used for this research, so the total *UA* is half the design condition. The *UA* drives the ability to provide 250 kW_{th} of cooling for a low temperature change (1.15°C). The current chiller could most likely provide the requisite chilling, but with a larger temperature change on the order of several degrees. To rectify this problem, a second chiller with similar *UA* should be installed to replace the missing chiller. The chilled water flow rate is also critical to achieve the full design condition because the chilled water loop flow rate also affects the chiller temperature difference. The current flow rate is only 40 $m^3\ hr^{-1}$ and the requirement is 193 $m^3\ hr^{-1}$, so a dramatic increase in flow rate is required. Some potential solutions include increasing the NPSH before the pump to decrease cavitation or increasing the line sizes in the

piping to decrease friction losses. If these two options do not solve the problem, a new pump is necessary.

The final facility issue is the expansion valve size. Since only one chiller was used, the expansion valve is too small to allow enough mass flow through the system. Figure 5-7 shows that for low power cycle mass flows, the cooling cycle mass flow rate is nearly two times the power cycle mass flow, but at high power cycle mass flows, the cooling cycle mass flow rate is much less than double. For example, at a power cycle mass flow of 0.5 kg s^{-1} the maximum possible cooling cycle mass flow was 0.92 kg s^{-1}, which is only a factor of 1.5 times larger. The final design condition has mass flow rates for the power and cooling cycles of 0.61 kg s^{-1} and 1.4 kg s^{-1}, respectively. The mass flow rates for both cycles are a major factor behind the chiller and boiler heat duties, and, therefore, COP. The solution to the expansion valve size issue is to implement a larger expansion valve to provide more mass flow in the cooling cycle.

Although the currently configured system has not met the final power plant design targets, the results of this study are still positive. The TCCS performs with similar COPs as current state-of-the-art heat activated cooling technologies and has several operational advantages. With further development, it is possible that these features could lead to the TCCS becoming a disruptive technology in the market for heat activated cooling.

6.1. Recommendations for Future Research

The current study has validated an experimental off-design approach for a TCCS operating at 27.5°C ambient conditions at power and cooling cycle mass flow ranges between 0.35 kg s^{-1} to 0.5 kg s^{-1} and 0.65 kg s^{-1} to 0.85 kg s^{-1}, respectively. Continuation of this research could include:

- The current modeling approach is only validated over a limited range of test conditions. Future tests should be performed at various ambient conditions and mass flow rate ranges

that include the final design point. The experimental data can be directly compared with the modeling, and can also be plotted on the system comparisons chart (similar to Figure 5-22). To achieve the broader range of experimental test conditions, several facility modifications will be required. The current issues with the test facility include lack of superheating at the turbine inlet, power cycle pump cavitation, cooling water flow rate, expansion valve size, and the chiller size. There are several solutions outlined above that include correcting the flue loop flow maldistribution, installing an additional power cycle booster pump, installing a new glycol loop pump, increasing the expansion valve size, and increasing the chiller *UA*.

- The theoretical modeling could be modified to make more accurate predictions for a wide range of operating conditions. Although the modeling does have a strong correlation to the data in the current research, there are improvements to be made with the *UA* scaling methodology that can improve modeling accuracy over a more broad range of system predictions.
- Finally, the heat activated cooling system performance chart could be expanded to include an economic factor. Currently, the system comparison chart is purely performance based and does not include system size or cost. In one example, the TCCS data found in this study matches well with double-effect LiBr-Water absorption systems, but it is commonly known that double-effect absorption systems have high capital costs. One modeling attempt could be to create a set of techno-economic equations comparing multiple heat activated cooling systems on a cost and performance basis to determine the most optimal system for a given application.

REFERENCES

[1] (2015). *Resources*. Available: https://www.barber-nichols.com/resources

[2] L. L. N. Laboratory, "Estimated U.S. Energy Consumption in 2016: 97.3 Quads," March 2017.

[3] B. Incorporated, "Waste Heat Recovery: Technology and Opportunities in U.S. Industry," U.S. Department of Energy2008.

[4] "Trane Classic Absorption Series," Trane2005.

[5] C. Borgnakke and R. E. Sonntag, *Fundamentals of Thermodynamics*, 8th ed. New Jersey: John Wiley & Sons, 2013.

[6] T. M. Bandhauer and S. D. Garland, "Dry Air Turbo-Compression Cooling," presented at the ASME Power and Energy Conference, Charlotte, North Carolina, 2016.

[7] D. Prigmore and R. Barber, "Cooling with the sun's heat Design considerations and test data for a Rankine Cycle prototype," *Solar Energy,* vol. 17, pp. 185-192, 1975/07/01 1975.

[8] S. Aphornratana, S. Chungpaibulpatana, and P. Srikhirin, "Experimental investigation of an ejector refrigerator: Effect of mixing chamber geometry on system performance," *International Journal of Energy Research,* vol. 25, pp. 397-411, 2001.

[9] "16LJ Single Effect, Low Temperature Hot Water Hermetic Absorption Liquid Chiller," Carrier Corporation2005.

[10] K. Chunnanond and S. Aphornratana, "Ejectors: applications in refrigeration technology," *Renewable and Sustainable Energy Reviews,* vol. 8, pp. 129-155, 2004/04/01/ 2004.

[11] S. Z. Xu, L. W. Wang, and R. Z. Wang, "Thermodynamic analysis of single-stage and multi-stage adsorption refrigeration cycles with activated carbon–ammonia working pair," *Energy Conversion and Management,* vol. 117, pp. 31-42, 6/1/ 2016.

[12] H. Li, X. Bu, L. Wang, Z. Long, and Y. Lian, "Hydrocarbon working fluids for a Rankine cycle powered vapor compression refrigeration system using low-grade thermal energy," *Energy and Buildings,* vol. 65, pp. 167-172, 10// 2013.

[13] C. P. Jawahar, B. Raja, and R. Saravanan, "Thermodynamic studies on NH3–H2O absorption cooling system using pinch point approach," *International Journal of Refrigeration,* vol. 33, pp. 1377-1385, 11// 2010.

[14] R. Yapıcı and C. C. Yetişen, "Experimental study on ejector refrigeration system powered by low grade heat," *Energy Conversion and Management,* vol. 48, pp. 1560-1568, 5// 2007.

[15] A. B. Little and S. Garimella, "Comparative assessment of alternative cycles for waste heat recovery and upgrade," *Energy,* vol. 36, pp. 4492-4504, 7// 2011.

[16] S. Aphornratana and T. Sriveerakul, "Analysis of a combined Rankine–vapour–compression refrigeration cycle," *Energy Conversion and Management,* vol. 51, pp. 2557-2564, 12// 2010.

[17] R. Gomri, "Investigation of the potential of application of single effect and multiple effect absorption cooling systems," *Energy Conversion and Management,* vol. 51, pp. 1629-1636, 8// 2010.

[18] D.-W. Sun, "Comparative study of the performance of an ejector refrigeration cycle operating with various refrigerants," *Energy Conversion and Management,* vol. 40, pp. 873-884, 1999/05/01/ 1999.

[19] (2017). *Water Fired Single Effect Chillers*. Available: http://www.yazakienergy.com/waterfiredspecifications.htm
[20] H. Wang, R. Peterson, and T. Herron, "Design study of configurations on system COP for a combined ORC (organic Rankine cycle) and VCC (vapor compression cycle)," *Energy,* vol. 36, pp. 4809-4820, 8// 2011.
[21] H. Wang, R. Peterson, K. Harada, E. Miller, R. Ingram-Goble, L. Fisher*, et al.*, "Performance of a combined organic Rankine cycle and vapor compression cycle for heat activated cooling," *Energy,* vol. 36, pp. 447-458, 1// 2011.
[22] Y. Teng, R. Z. Wang, and J. Y. Wu, "Study of the fundamentals of adsorption systems," *Applied Thermal Engineering,* vol. 17, pp. 327-338, 1997/04/01 1997.
[23] Z. Tamainot-Telto and R. E. Critoph, "Adsorption refrigerator using monolithic carbon-ammonia pair," *International Journal of Refrigeration,* vol. 20, pp. 146-155, 1997/03/01/ 1997.
[24] L. Z. Zhang, "Design and testing of an automobile waste heat adsorption cooling system," *Applied Thermal Engineering,* vol. 20, pp. 103-114, 2000/01/01/ 2000.
[25] F. Poyelle, J.-J. Guilleminot, and F. Meunier, "Experimental Tests and Predictive Model of an Adsorptive Air Conditioning Unit," *Industrial & Engineering Chemistry Research,* vol. 38, pp. 298-309, 1999/01/01 1999.
[26] K. C. A. Alam, B. B. Saha, Y. T. Kang, A. Akisawa, and T. Kashiwagi, "Heat exchanger design effect on the system performance of silica gel adsorption refrigeration systems," *International Journal of Heat and Mass Transfer,* vol. 43, pp. 4419-4431, 2000/12/15/ 2000.
[27] G. Najeh, G. Slimane, M. Souad, B. Riad, and E. G. Mohammed, "Performance of silica gel-water solar adsorption cooling system," *Case Studies in Thermal Engineering,* vol. 8, pp. 337-345, 2016/09/01/ 2016.
[28] W. Han, Q. Chen, L. Sun, S. Ma, T. Zhao, D. Zheng*, et al.*, "Experimental studies on a combined refrigeration/power generation system activated by low-grade heat," *Energy,* vol. 74, pp. 59-66, 9/1/ 2014.
[29] H. T. Chua, H. K. Toh, and K. C. Ng, "Thermodynamic modeling of an ammonia–water absorption chiller," *International Journal of Refrigeration,* vol. 25, pp. 896-906, 11// 2002.
[30] A. A. Manzela, S. M. Hanriot, L. Cabezas-Gómez, and J. R. Sodré, "Using engine exhaust gas as energy source for an absorption refrigeration system," *Applied Energy,* vol. 87, pp. 1141-1148, 4// 2010.
[31] B. Kim and J. Park, "Dynamic simulation of a single-effect ammonia–water absorption chiller," *International Journal of Refrigeration,* vol. 30, pp. 535-545, 5// 2007.
[32] B. Le Lostec, N. Galanis, and J. Millette, "Simulation of an ammonia–water absorption chiller," *Renewable Energy,* vol. 60, pp. 269-283, 12// 2013.
[33] S. A. M. Said, K. Spindler, M. A. El-Shaarawi, M. U. Siddiqui, F. Schmid, B. Bierling*, et al.*, "Design, construction and operation of a solar powered ammonia–water absorption refrigeration system in Saudi Arabia," *International Journal of Refrigeration,* vol. 62, pp. 222-231, 2// 2016.
[34] A. S. Mehr, V. Zare, and S. M. S. Mahmoudi, "Standard GAX versus hybrid GAX absorption refrigeration cycle: From the view point of thermoeconomics," *Energy Conversion and Management,* vol. 76, pp. 68-82, 12// 2013.

[35] A. Iranmanesh and M. A. Mehrabian, "Dynamic simulation of a single-effect LiBr–H2O absorption refrigeration cycle considering the effects of thermal masses," *Energy & Buildings,* vol. 60, pp. 47-59, 2013.
[36] P. Kohlenbach and F. Ziegler, "A dynamic simulation model for transient absorption chiller performance. Part II: Numerical results and experimental verification," *International Journal of Refrigeration,* vol. 31, pp. 226-233, 3// 2008.
[37] G. Evola, N. Le Pierrès, F. Boudehenn, and P. Papillon, "Proposal and validation of a model for the dynamic simulation of a solar-assisted single-stage LiBr/water absorption chiller," *International Journal of Refrigeration,* vol. 36, pp. 1015-1028, 5// 2013.
[38] M. Zinet, R. Rulliere, and P. Haberschill, "A numerical model for the dynamic simulation of a recirculation single-effect absorption chiller," *Energy Conversion and Management,* vol. 62, pp. 51-63, 10// 2012.
[39] R. Lizarte, M. Izquierdo, J. D. Marcos, and E. Palacios, "An innovative solar-driven directly air-cooled LiBr–H2O absorption chiller prototype for residential use," *Energy and Buildings,* vol. 47, pp. 1-11, 4// 2012.
[40] Y. L. Yin, Z. P. Song, Y. Li, R. Z. Wang, and X. Q. Zhai, "Experimental investigation of a mini-type solar absorption cooling system under different cooling modes," *Energy and Buildings,* vol. 47, pp. 131-138, 4// 2012.
[41] M. Izquierdo, R. Lizarte, J. D. Marcos, and G. Gutiérrez, "Air conditioning using an air-cooled single effect lithium bromide absorption chiller: Results of a trial conducted in Madrid in August 2005," *Applied Thermal Engineering,* vol. 28, pp. 1074-1081, 6// 2008.
[42] K. A. Joudi and A. H. Lafta, "Simulation of a simple absorption refrigeration system," *Energy Conversion and Management,* vol. 42, pp. 1575-1605, 9// 2001.
[43] W. Salmi, J. Vanttola, M. Elg, M. Kuosa, and R. Lahdelma, "Using waste heat of ship as energy source for an absorption refrigeration system," *Applied Thermal Engineering,* vol. 115, pp. 501-516, 3/25/ 2017.
[44] S. Disawas and S. Wongwises, "Experimental investigation on the performance of the refrigeration cycle using a two-phase ejector as an expansion device," *International Journal of Refrigeration,* vol. 27, pp. 587-594, 9// 2004.
[45] I. W. Eames, S. Aphornratana, and H. Haider, "A theoretical and experimental study of a small-scale steam jet refrigerator," *International Journal of Refrigeration,* vol. 18, pp. 378-386, 1995/07/01 1995.
[46] K. Cizungu, A. Mani, and M. Groll, "Performance comparison of vapour jet refrigeration system with environment friendly working fluids," *Applied Thermal Engineering,* vol. 21, pp. 585-598, 2001/04/01/ 2001.
[47] B.-J. Huang, B. Jiang, and F. L. Hu, *Ejector Performance Characteristics and Design Analysis of Jet Refrigeration System* vol. 107, 1985.
[48] B. J. Huang, J. M. Chang, V. A. Petrenko, and K. B. Zhuk, "A SOLAR EJECTOR COOLING SYSTEM USING REFRIGERANT R141b," *Solar Energy,* vol. 64, pp. 223-226, 1998/12/01/ 1998.
[49] L. Jiang, Z. Gu, X. Feng, and Y. Li, "Thermo-economical analysis between new absorption–ejector hybrid refrigeration system and small double-effect absorption system," *Applied Thermal Engineering,* vol. 22, pp. 1027-1036, 6// 2002.
[50] G. P. Xu, Y. Q. Dai, K. W. Tou, and C. P. Tso, "Theoretical analysis and optimization of a double-effect series-flow-type absorption chiller," *Applied Thermal Engineering,* vol. 16, pp. 975-987, 1996/12/01 1996.

[51] A. Iranmanesh and M. Mehrabian, "Thermodynamic modelling of a double-effect LiBr-H 2 O absorption refrigeration cycle," *Heat Mass Transfer,* vol. 48, pp. 2113-2123, 2012.
[52] "ProChill B4k: Steam Fired Vapor Absorption Chiller," Thermax2008.
[53] J. Jeong and Y. T. Kang, "Analysis of a refrigeration cycle driven by refrigerant steam turbine," *International Journal of Refrigeration,* vol. 27, pp. 33-41, 1// 2004.
[54] "Broad X Absorption Chiller: Model Selection & Design Manual," Broad Air Conditioning2008.
[55] "16TJ Single-Effect, Steam Hermetic Absorption Liquid Chiller," C. Corporation, Ed., ed. Syracuse, New York, 2005.
[56] I. E. Agency, "India Outlook Energy," 2015.
[57] M. M. Kostic, "Sadi Carnot's Ingenious Reasoning of Ideal Heat Engine Reversible Cycles," presented at the Energy, Environment, Ecosystems and Sustainable Development, Algarve, Portugal, 2008.
[58] EPRI, "Water Use for Electricity Generation and Other Sectors: Recent Changes (1985-2005) and Future Projections (2005-2030)," Electric Power Research Institute2011.
[59] M. A. Maupin, Kenny, J.F., Hutson, S.S., Lovelace, J.K., Barber, N.L., and Linsey, K.S., "Estimated use of water in the United States in 2010: U.S. Geological Survey Circular 1405," 2014.
[60] DOE, "The Water-Energy Nexus: Challenges and Opportunities," Department of Energy2014.
[61] S. Shukla, M. Safeeq, A. AghaKouchak, K. Guan, and C. Funk, "Temperature impacts on the water year 2014 drought in California," *Geophysical Research Letters,* vol. 42, pp. 4384-4393, 2015.
[62] DOE/NETL, "Estimating Freshwater Needs to Meet Future Thermoelectric Generation Requirements - 2011 Update," Department of Energy, National Energy Technology Laboratory2011.
[63] R. E. Putman and D. Jaresch, "The cleaning of air cooled condensers to improve performance," in *Proceedings of the IJPGC 2002 International Joint Power Generation Conference, June 24, 2002 - June 26, 2002*, Scottsdale, AZ, United states, 2002, pp. 139-146.
[64] DOE/NETL, "Cost and Performance Baseline for Fossil Energy Plants, Volume 1: Bituminous Coal and Natural Gas to Electricity," 2013.
[65] P. Srikhirin, S. Aphornratana, and S. Chungpaibulpatana, "A review of absorption refrigeration technologies," *Renewable and Sustainable Energy Reviews,* vol. 5, pp. 343-372, 2001/12/01/ 2001.
[66] A. Shirazi, R. A. Taylor, S. D. White, and G. L. Morrison, "Multi-effect Absorption Chillers Powered by the Sun: Reality or Reverie," *Energy Procedia,* vol. 91, pp. 844-856, 2016/06/01/ 2016.
[67] S. I.-u.-H. Gilani and M. S. M. S. Ahmed, "Solution Crystallization Detection for Double-effect LiBr-H2O Steam Absorption Chiller," *Energy Procedia,* vol. 75, pp. 1522-1528, 2015/08/01/ 2015.
[68] L. Garousi Farshi, S. M. Seyed Mahmoudi, M. A. Rosen, and M. Yari, "A comparative study of the performance characteristics of double-effect absorption refrigeration systems," *International Journal of Energy Research,* vol. 36, pp. 182-192, 2012.
[69] "Absorption Chiller," LG2016.

[70] A. W. Raymond, "Invesitgation of Microparticle to System Level Phenomena in Thermally Activated Adsorption Heat Pumps," Masters of Science, George W. Woodruff School of Mechanical Engineering, Georgia Institute of Technology, 2010.
[71] D. C. Wang, Y. H. Li, D. Li, Y. Z. Xia, and J. P. Zhang, "A review on adsorption refrigeration technology and adsorption deterioration in physical adsorption systems," *Renewable and Sustainable Energy Reviews,* vol. 14, pp. 344-353, 2010/01/01/ 2010.
[72] O. M. M. Eltom and A. A. M. Sayigh, "A simple method to enhance thermal conductivity of charcoal using some additives," *Renewable Energy,* vol. 4, pp. 113-118, 1994/02/01/ 1994.
[73] J. J. Guilleminot, A. Choisier, J. B. Chalfen, S. Nicolas, and J. L. Reymoney, "Heat transfer intensification in fixed bed adsorbers," *Heat Recovery Systems and CHP,* vol. 13, pp. 297-300, 1993/07/01/ 1993.
[74] G. Cacciola, G. Restuccia, and L. Mercadante, "Composites of activated carbon for refrigeration adsorption machines," *Carbon,* vol. 33, pp. 1205-1210, 1995/01/01/ 1995.
[75] R. Z. Wang, J. P. Jia, Y. H. Zhu, Y. Teng, J. Y. Wu, J. Cheng*, et al.*, "Study on a New Solid Absorption Refrigeration Pair: Active Carbon Fiber—Methanol," *Journal of Solar Energy Engineering,* vol. 119, pp. 214-218, 1997.
[76] S.-H. Cho and J.-N. Kim, "Modeling of a silica gel/water adsorption-cooling system," *Energy,* vol. 17, pp. 829-839, 1992/09/01/ 1992.
[77] D. S. Kim and C. A. Infante Ferreira, "Solar refrigeration options – a state-of-the-art review," *International Journal of Refrigeration,* vol. 31, pp. 3-15, 2008/01/01/ 2008.
[78] M. Dubey, S. P. S. Rajput, P. K. Nag, and R. D. Misra, "Energy analysis of a coupled power-refrigeration cycle," *Journal of Power and Energy,* vol. 224, pp. 749-759, 2010.
[79] V. M. Nguyen, S. B. Riffat, and P. S. Doherty, "Development of a solar-powered passive ejector cooling system," *Applied Thermal Engineering,* vol. 21, pp. 157-168, 2001/01/01/ 2001.
[80] A. Arbel, A. Shklyar, D. Hershgal, M. Barak, and M. Sokolov, "Ejector Irreversibility Characteristics," *Journal of Fluids Engineering,* vol. 125, pp. 121-129, 2003.
[81] C. J. Korres, A. T. Papaioannou, V. Lygerou, and N. G. Koumoutsos, "Solar cooling by thermal compression: The dependence of the jet thermal compressor efficiency on the compression ratio," *Energy,* vol. 27, pp. 795-805, 2002/08/01/ 2002.
[82] D.-W. Sun, "Variable geometry ejectors and their applications in ejector refrigeration systems," *Energy,* vol. 21, pp. 919-929, 1996/10/01/ 1996.
[83] I. W. Eames, "A new prescription for the design of supersonic jet-pumps: the constant rate of momentum change method," *Applied Thermal Engineering,* vol. 22, pp. 121-131, 2002/02/01/ 2002.
[84] S. Wantanawanavet, "Optimization of a high-efficiency jet ejector by computational fluid dynamic software," Texas A&M University, 2006.
[85] W. Holton, "Effect of moleciular weight of entrained fluid on the performance of steam-jet ejector," in *ASME Trans*, 1951.
[86] N. M. Khattab and M. H. Barakat, "Modeling the design and performance characteristics of solar steam-jet cooling for comfort air conditioning," *Solar Energy,* vol. 73, pp. 257-267, 2002/10/01/ 2002.
[87] H. L. Wang and R. B. Peterson, "Performance enhancement of a thermally activated cooling system using microchannel heat exchangers," *Applied Thermal Engineering,* vol. 31, pp. 2951-2962, Oct 2011.

[88] P. A. Domanski and M. O. McLinden, "A simplified cycle simulation model for the performance rating of refrigerants and refrigerant mixtures," *International Journal of Refrigeration,* vol. 15, pp. 81-88, 1992/01/01/ 1992.
[89] F. P. Incropera, and DeWitt, D.P., *Fundamentals of Heat and Mass Transfer*. New York: Wiley, 1996.
[90] S. L. a. H. Dixon, C.A. , *Fluid Mechanics and Thermodynamics of Turbomachinery*. MA: Elsevier Inc., 2014.
[91] Y.-J. Chang and C.-C. Wang, "A generalized heat transfer correlation for louver fin geometry," *International Journal of Heat and Mass Transfer,* vol. 40, pp. 533-544, 1997/02/01/ 1997.
[92] F. W. Dittus and L. M. K. Boelter, "Heat transfer in automobile radiators of the tubular type," *University of California at Berkley,* pp. 443-461, 1985/01/01/ 1930.
[93] M.-H. Kim, B. Youn, and C. W. Bullard, "Effect of inclination on the air-side performance of a brazed aluminum heat exchanger under dry and wet conditions," *International Journal of Heat and Mass Transfer,* vol. 44, pp. 4613-4623, 2001/12/01/ 2001.
[94] M. K. Dobson and J. C. Chato, "Condensation in Smooth Horizontal Tubes," *Journal of Heat Transfer,* vol. 120, pp. 193-213, 1998.
[95] M. M. Shahs, "Evaluation of General Correlations for Heat Transfer During Boiling of Saturated Liquids in Tubes and Annuli," *HVAC&R Research,* vol. 12, pp. 1047-1063, 2006/10/01 2006.
[96] K. E. Gungor and R. H. S. Winterton, "Simplified General Correlation for Saturated Flow Boiling and Comparisons of Correlations With Data," *The Canadian Journal of Chemical Engineering,* vol. 65, pp. 148-156, 1987.
[97] B. R. Munson, D. F. Young, T. H. Okiishi, and W. W. Huebsch, *Fundamentals of Fluid Mechanics*, Sixth Edition ed. Hoboken, NJ: John Wiley and Sons, Inc., 2009.
[98] JGCM. (2008). *Evaluation of measurment data--guide to the expression of uncertainty in measurement (First ed.)*.
[99] T. Wright and P. M. Gerhart, *Fluid Machinery: Application, Selection, and Design*. Florida: CRC Press, 2010.

APPENDIX A. SAMPLE CALCULATIONS

The following appendix shows sample hand calculations to validate the EES evaluation of the basic thermodynamic calculations, the heat transfer calculations, and the experimental data. The state point format for the equations is displayed in Figure A-1 and in Table A-1 and Table A-2.

A.1. Basic Thermodynamic Calculations

The basic thermodynamic calculation is a hand calculation used to validate the EES code. The calculation was performed with the input parameters given in Table A-3 and the fluids for the power and cooling cycles of HFE7000 and R152a, respectively. The saturation temperatures specified in Table A-3 were used to find the saturation pressures for the heat exchangers through property calculations that are not shown. The pressures at each state point were determined by using the specified saturation pressures and adding or subtracting the relevant pressure drops. For

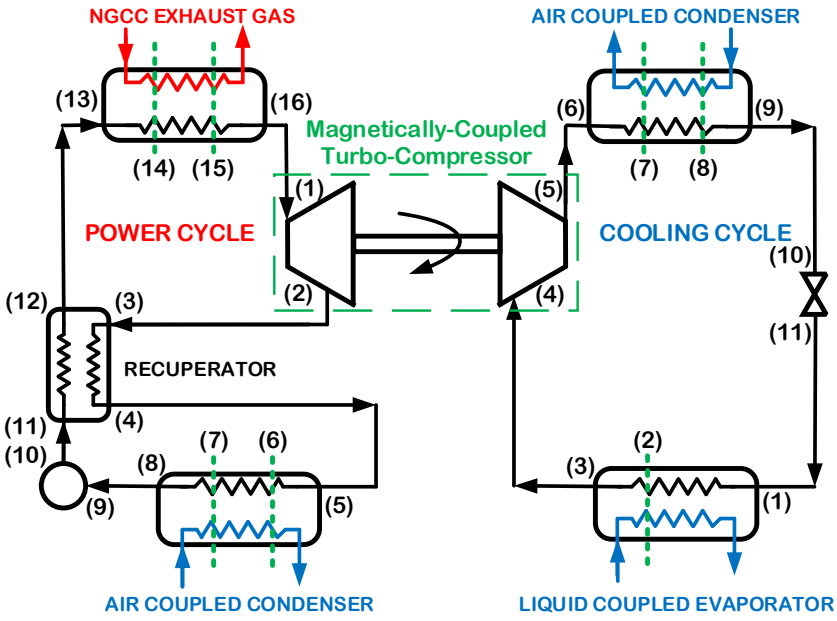

Figure A-1. PFD showing the cycle state points used for sample calculations.

Table A-1. Power cycle state points.

State Point	Location
	Turbine Inlet
2	Turbine Outlet
3	Recuperator Inlet
4	Recuperator Outlet
5	Condenser Inlet
6	Condenser Saturated Vapor
7	Condenser Saturated Liquid
8	Condenser Outlet
9	Pump Inlet
10	Pump Outlet
11	Recuperator Inlet
12	Recuperator Outlet
13	Boiler Inlet
14	Boiler Saturated Liquid
15	Boiler Saturated Vapor
16	Boiler Outlet

Table A-2. Cooling cycle state points.

State Point	Location
1	Evaporator Inlet
2	Evaporator Saturated Vapor
3	Evaporator Outlet
4	Compressor Inlet
5	Compressor Outlet
6	Condenser Inlet
7	Condenser Saturated Vapor
8	Condenser Saturated Liquid
9	Condenser Outlet
10	Expansion Valve Inlet
11	Expansion Valve Outlet

example, the saturated liquid condition of the PC boiler is specified (Point 14), so the pressure at Point 13 is found by adding the pressure drop through the sub-cooled section of the PC boiler heat exchanger to the pressure at Point 14. The pressure at Point 15 is found by subtracting the pressure drop through the two-phase section from the pressure at Point 14. Since all of the pressure drops are specified from Modine or line estimates, the pressure at any point in the cycle can be determined in a similar fashion. The enthalpies in the hand calculations are determined through property tables (REFPROP) with reference to the pressure and either the temperature or entropy at each state point. All of the enthalpies and entropies at each point are used to thermodynamically solve the system as shown in Table A-4.

A.2. Heat Exchanger UA Calculations

The heat exchanger UA calculations can be made after the general thermodynamic calculations are complete as shown in Section A.1. The inputs for the heat exchanger calculations are the outputs from the thermodynamic state point modeling. The correlation used for the heat

exchangers is determined depending on the type and phase of the heat exchanger. A sample UA calculation is shown in Table A-5.

A.3. Off-Design Compressor and Turbine Map Calculation

The performance of the turbo-machine in off design conditions is described in Section 3.2. The calculations for the modeling approach were calculated with the input parameters given in Table A-6. The fluids for the power and cooling cycles are HFE7000 and R134a, respectively. R134a was selected as the cooling cycle fluid to make direct comparisons with the experimental data. The model includes pressure drops through both components and connection piping. The model operates by scaling the heat exchanger *UAs* from the basic thermodynamic modeling approach. By scaling the heat exchanger *UAs,* the performance of the system can be found with varying ambient temperature and cooling cycle evaporator heat duties. For the off-design performance modeling, the first step is to calculate the *UA* scaling factors. These calculations are shown in Table A-7. The model also operates by iterating with the turbo-machine efficiency maps. The hand calculations shown in Table A-8 are evaluated with turbine and compressor efficiencies that have already been iterated.

A.4. Test Data Parameter Reduction and Analysis.

The test facility data, including pressures, temperatures, and flow rates, are used to calculate the parameters for the facility analysis. Each of the instrument values for the representative data point are listed in Table A-9 and are used to determine the enthalpies and entropies at each state point in the cycle. Those property calculations are not shown in this appendix. However, the thermodynamic calculations are provided in Table A-10 to validate the EES model.

Table A-3. Input parameters for evaluation of basic thermodynamic and heat exchanger UA equations using EES and hand calculations.

Parameter	Value	Units
Compressor efficiency (η_{comp})	80	%
Turbine efficiency (η_{t})	80	%
Pump efficiency (η_{pump})	50	%
Shaft efficiency (η_{shaft})	93	%
PC Exhaust fan efficiency ($\eta_{p,bf}$)	70	%
CC Glycol pump efficiency ($\eta_{c,gp}$)	50	%
CC Condenser fan number ($N_{c,cf}$)	6	fans
PC Condenser fan number ($N_{p,cf}$)	2	fans
Exhaust air inlet temperature (T_{exh})	106	°C
Exhaust air flow rate ($\dot{V}_{exh}$)	8.61	$m^3\ s^{-1}$
Exhaust air specific heat (Cp_{exh})	1.012	$kJ\ kg^{-1}\ K^{-1}$
Exhaust air density (ρ_{exh})	0.7809	$kg\ m^3$
Specific heat of 30:70 Propylene Glycol: Water mixture (Cp_g)	3.86	$kJ\ kg^{-1}\ K^{-1}$
Density of 30:70 Propylene Glycol: Water mixture (ρ_g)	1019	$kg\ m^3$
PC Boiler saturation temperature ($T_{p,sat}$)	92.4	°C
PC Condenser liquid saturation temperature ($T_{p,7}$)	24.9	°C
CC Condenser liquid saturation temperature ($T_{c,9}$)	23.6	°C
CC Evaporator vapor saturation temperature ($T_{c,7}$)	15.3	°C
Degrees of superheating at the PC boiler outlet ($\Delta T_{p,b,sh}$)	11.2	°C

Parameter	Value	Units
Degrees of superheating at the PC condenser inlet ($\Delta T_{p,cond,sh}$)	2.7	°C
Degrees of sub-cooling at the PC condenser outlet ($\Delta T_{p,cond,sc}$)	0.5	°C
Degrees of superheating at the CC evaporator outlet ($\Delta T_{c,evap,sh}$)	0.5	°C
Degrees of sub-cooling at the CC condenser outlet ($\Delta T_{c,cond,sc}$)	0.5	°C
Ambient air temperature (T_{amb})	15	°C
Ambient air pressure (P_{amb})	85	kPa
Ambient air density (ρ_{amb})	1.028	kg m^3
Ambient air specific heat (Cp_{amb})	1.006	kJ kg^{-1} K^{-1}
Line pressure drops (ΔP_{line})	2	kPa
PC Recuperator vapor side pressure drop ($\Delta P_{p,recup,vap}$)	4.74	kPa
PC Recuperator liquid side pressure drop ($\Delta P_{p,recup,liq}$)	1.45	kPa
PC Boiler sub-cooled pressure drop ($\Delta P_{p,b,sc}$)	0.2	kPa
PC Boiler two-phase pressure drop ($\Delta P_{p,b,tp}$)	1.2	kPa
PC Boiler superheated pressure drop ($\Delta P_{p,b,sh}$)	0.2	kPa
PC Condenser sub-cooled pressure drop ($\Delta P_{p,cond,sc}$)	1	kPa
PC Condenser two-phase pressure drop ($\Delta P_{p,cond,tp}$)	8.8	kPa
PC Condenser superheated pressure drop ($\Delta P_{p,cond,sh}$)	1	kPa
CC Condenser sub-cooled pressure drop ($\Delta P_{c,cond,sc}$)	0.2	kPa
CC Condenser two-phase pressure drop ($\Delta P_{c,cond,tp}$)	1.71	kPa
CC Condenser superheated pressure drop ($\Delta P_{c,cond,sh}$)	0.2	kPa

Parameter	Value	Units
CC Evaporator two-phase pressure drop ($\Delta P_{c,evap,tp}$)	19	kPa
CC Evaporator superheated pressure drop ($\Delta P_{c,evap,sh}$)	1	kPa
PC Boiler air side pressure drop ($\Delta P_{p,b,a}$)	0.2	kPa
CC Evaporator glycol side pressure drop ($\Delta P_{c,g}$)	30.2	kPa
PC Condenser air flow rate ($\dot{V}_{p,cond,a}$)	10.8	$m^3\ s^{-1}$
CC Condenser air flow rate ($\dot{V}_{c,cond,a}$)	37.5	$m^3\ s^{-1}$
CC Evaporator glycol flow rate ($\dot{V}_{c,g}$)	0.053	$m^3\ s^{-1}$
Turbo-compressor speed (N)	30,000	RPM
PC Condenser sub-cooled baseline area fraction ($A_{per,p,cond,sc,base}$)	7	%
PC Condenser two-phase baseline area fraction ($A_{per,p,cond,tp,base}$)	91	%
PC Condenser superheated baseline area fraction ($A_{per,p,cond,sh,base}$)	2	%
PC Boiler sub-cooled baseline area fraction ($A_{per,p,b,sc,base}$)	15	%
PC Boiler two-phase baseline area fraction ($A_{per,p,b,tp,base}$)	49	%
PC Boiler superheated baseline area fraction ($A_{per,p,b,sh,base}$)	36	%
CC Condenser sub-cooled baseline area fraction ($A_{per,c,cond,sc,base}$)	10.6	%
CC Condenser two-phase baseline area fraction ($A_{per,c,cond,tp,base}$)	87	%
CC Condenser superheated baseline area fraction ($A_{per,c,cond,sh,base}$)	2.4	%

Table A-4. Hand calculations to support EES evaluation of the basic thermodynamic model.

Parameter	Equation	Evaluated	EES Calc. Value	Hand Calc. Value	Units
CC mass flow rate	$\dot{Q}_{c,evap} = \dot{m}_c \left(h_{c,3} - h_{c,1}\right)$	$250.8 = \dot{m}_c \left(516.9 - 240.3\right)$	0.906	0.907	kW
CC evaporator TP heat duty	$\dot{Q}_{c,evap,tp} = \dot{m}_c \left(h_{c,2} - h_{c,1}\right)$	$\dot{Q}_{c,evap,tp} = 0.907\left(516.3 - 240.3\right)$	250.2	250.3	kW
CC evaporator SH heat duty	$\dot{Q}_{c,evap,sc} = \dot{m}_c \left(h_{c,3} - h_{c,2}\right)$	$\dot{Q}_{c,evap,sc} = 0.907\left(516.9 - 516.3\right)$	0.57	0.54	kW
CC evaporator glycol mass flow	$\dot{m}_{c,g} = \dot{V}_{c,g}\rho_g$	$\dot{m}_{c,g} = 0.053 \times 1025$	54.3	54.3	kg s^{-1}
Compressor outlet enthalpy	$\eta_{c,comp} = \dfrac{\left(h_{c,s,5} - h_{c,4}\right)}{\left(h_{c,5} - h_{c,4}\right)}$	$0.8 = \dfrac{\left(527.2 - 516.9\right)}{\left(h_{c,5} - 516.9\right)}$	529.7	529.8	kJ kg^{-1}
Compressor work	$\dot{W}_{c,comp} = \dot{m}_c \left(h_{c,5} - h_{c,4}\right)$	$\dot{W}_{c,comp} = 0.907\left(529.7 - 516.9\right)$	11.56	11.61	kg s^{-1}
CC condenser heat duty	$\dot{Q}_{c,cond} = \dot{m}_c \left(h_{c,6} - h_{c,9}\right)$	$\dot{Q}_{c,cond} = 0.907\left(529.7 - 240.3\right)$	262.4	262.5	kW
CC condenser SC heat duty	$\dot{Q}_{c,cond,sc} = \dot{m}_c \left(h_{c,8} - h_{c,9}\right)$	$\dot{Q}_{c,cond,sc} = 0.907\left(241.2 - 240.3\right)$	0.83	0.82	kW
CC condenser TP heat duty	$\dot{Q}_{c,cond,tp} = \dot{m}_c \left(h_{c,7} - h_{c,8}\right)$	$\dot{Q}_{c,cond,tp} = 0.907\left(522.3 - 241.2\right)$	254.8	255.0	kW
CC condenser SH heat duty	$\dot{Q}_{c,cond,sh} = \dot{m}_c \left(h_{c,6} - h_{c,7}\right)$	$\dot{Q}_{c,cond,sh} = 0.907\left(529.7 - 522.3\right)$	6.7	6.7	kW
CC condenser air mass flow rate	$\dot{m}_{c,cond,a} = \dot{V}_{c,cond,a}\rho_{amb}$	$\dot{m}_{c,cond,a} = 37.5 \times 1.028$	38.6	38.6	kg s^{-1}
Turbine work	$\dot{W}_c = \dot{W}_t \eta_{shaft}$	$11.61 = \dot{W}_t \times 0.93$	12.36	12.48	kW

Parameter	Equation	Evaluated	EES Calc. Value	Hand Calc. Value	Units
Turbine outlet enthalpy	$\eta_t = \frac{(h_{p,1} - h_{p,2})}{(h_{p,1} - h_{p,s,2})}$	$0.8 = \frac{(435.1 - h_{p,2})}{(435.1 - 409.8)}$	414.8	414.9	kJ kg^{-1}
Power cycle mass flow rate	$\dot{W}_t = \dot{m}_p (h_{p,1} - h_{p,2})$	$12.48 = \dot{m}_p (435.1 - 414.8)$	0.61	0.61	kW
Recuperator heat duty	$\dot{Q}_{p,recup} = \dot{m}_p (h_{p,3} - h_{p,4})$	$\dot{Q}_{p,recup} = 0.61(414.8 - 372.5)$	25.9	25.8	kW
PC condenser heat duty	$\dot{Q}_{p,cond} = \dot{m}_p (h_{p,5} - h_{p,8})$	$\dot{Q}_{p,cond} = 0.61(372.5 - 229.3)$	87.5	87.4	kW
PC condenser SC heat duty	$\dot{Q}_{p,cond,sc} = \dot{m}_p (h_{p,7} - h_{p,8})$	$\dot{Q}_{p,cond,sc} = 0.61(229.9 - 229.3)$	0.37	0.37	kW
PC condenser TP heat duty	$\dot{Q}_{p,cond,tp} = \dot{m}_p (h_{p,6} - h_{p,7})$	$\dot{Q}_{p,cond,tp} = 0.61(370.1 - 229.9)$	85.6	85.5	kW
PC condenser SH heat duty	$\dot{Q}_{p,cond,sh} = \dot{m}_p (h_{p,5} - h_{p,6})$	$\dot{Q}_{p,cond,sh} = 0.61(372.5 - 370.1)$	1.47	1.46	kW
PC condenser air mass flow rate	$\dot{m}_{p,cond,a} = \dot{V}_{p,cond,a} \rho_{amb}$	$\dot{m}_{p,cond,a} = 10.83 \times 1.028$	11.1	11.1	kg s^{-1}
PC boiler heat duty	$\dot{Q}_{p,b} = \dot{m}_p (h_{p,16} - h_{p,13})$	$\dot{Q}_{p,b} = 0.61(435.1 - 272.4)$	99.4	99.2	kW
PC boiler SC heat duty	$\dot{Q}_{p,b,sc} = \dot{m}_p (h_{p,14} - h_{p,13})$	$\dot{Q}_{p,b,sc} = 0.61(317.1 - 272.4)$	27.35	27.3	kW
PC boiler TP heat duty	$\dot{Q}_{p,b,tp} = \dot{m}_p (h_{p,15} - h_{p,14})$	$\dot{Q}_{p,b,tp} = 0.61(422.5 - 317.1)$	64.37	64.3	kW
PC boiler SH heat duty	$\dot{Q}_{p,b,sh} = \dot{m}_p (h_{p,16} - h_{p,15})$	$\dot{Q}_{p,b,sh} = 0.61(435.1 - 422.5)$	7.68	7.69	kW
Recuperator inlet enthalpy	$\dot{Q}_{p,recup} = \dot{m}_p (h_{p,12} - h_{p,11})$	$25.8 = 0.61(272.4 - h_{p,11})$	230	230.1	kJ kg^{-1}
Pump work	$\dot{W}_{p,pump} = \dot{m}_p (h_{p,10} - h_{p,9})$	$\dot{W}_{p,pump} = 0.61(230 - 229.3)$	0.44	0.43	*kW*

Parameter	Equation	Evaluated	EES Calc. Value	Hand Calc. Value	Units
PC boiler TP+SH heat duty	$\dot{Q}_{\text{p,tp+sh}} = \dot{Q}_{\text{p,tp}} + \dot{Q}_{\text{p,sh}}$	$\dot{Q}_{\text{p,tp+sh}} = 64.37 + 7.68$	72.05	72.05	kW
Exhaust mass flow rate	$\dot{m}_{\text{exh}} = \dot{V}_{\text{exh}} \rho_{\text{exh}}$	$\dot{m}_{\text{exh}} = 8.61 \times 0.78$	6.73	6.72	kg s^{-1}
Air temperature at point 14	$\dot{Q}_{\text{p,tp+sh}} = \dot{m}_{\text{exh}} Cp_{\text{exh}} \left(T_{\text{p,a,16}} - T_{\text{p,a,14}}\right)$	$72.05 = 6.73 \times 1.01 \left(106 - T_{p,a,14}\right)$	95.41	95.4	°C
CAT	$T_{\text{p,a,14}} = T_{\text{p,sat}} + CAT_{\text{exh}}$	$95.4 = 92.4 + CAT_{\text{exh}}$	3.06	3.0	°C
PC boiler fan power	$\dot{W}_{\text{p,bf}} = \frac{\dot{V}_{\text{exh}} \Delta P_{\text{p,bf}}}{\eta_{\text{p,bf}}}$	$\dot{W}_{\text{p,bf}} = \frac{8.61 \times 0.2}{0.7}$	2.46	2.46	kW
PC condenser fan power	$\dot{W}_{\text{p,cf}} = N_{\text{p,cf}} \times 1.23[\text{kW}]$	$\dot{W}_{\text{p,cf}} = 2 \times 1.23[\text{kW}]$	2.46	2.46	kW
CC condenser fan power	$\dot{W}_{\text{c,cf}} = N_{\text{p,cf}} \times 1.89[\text{kW}]$	$\dot{W}_{\text{c,cf}} = 6 \times 1.89[\text{kW}]$	11.34	11.34	kW
Glycol pump power	$\dot{W}_{\text{c,gp}} = \frac{\dot{V}_{\text{c,gp}} \Delta P_{\text{c,gp}}}{\eta_{\text{c,gp}}}$	$\dot{W}_{\text{c,gp}} = \frac{0.05 \times 30.2}{0.5}$	3.02	3.02	kW
Auxiliary power consumption	$\dot{W}_{\text{aux}} = \dot{W}_{\text{p,bf}} + \dot{W}_{\text{p,cf}} + \dot{W}_{\text{c,cf}} + \dot{W}_{\text{c,gp}}$	$\dot{W}_{\text{aux}} = 2.5 + 2.5 + 11.3 + 3.0$	19.3	19.3	kW
COP	$COP = \frac{\dot{Q}_{\text{c,evap}}}{\dot{Q}_{\text{p,b}} + \dot{W}_{\text{p,pump}} + \dot{W}_{\text{aux}}}$	$COP = \frac{250.8}{99.4 + 0.44 + 19.28}$	2.10	2.11	-
Volumetric flow at turbine outlet	$\dot{V}_{\text{p,2}} = \frac{\dot{m}_{\text{p}}}{\rho_{\text{p,2}}}$	$\dot{V}_{\text{p,2}} = \frac{0.61}{6.37} \frac{35.3[\text{ft}^3\,\text{s}^{-1}]}{[\text{m}^3\,\text{s}^{-1}]}$	3.39	3.38	$ft^3\ s^{-1}$
Ideal turbine head	$H_{\text{t}} = \left(h_{\text{p,1}} - h_{\text{p,s,2}}\right)$	$H_{\text{t}} = \left(435.1 - 409.8\right) \frac{334.6[\text{ft lbf}]}{[\text{kJ kg}^{-1}]}$	8460	8465	ft lbf
Turbine specific speed	$Ns_{\text{t}} = \frac{N\sqrt{\dot{V}_{\text{p,2}}}}{H_{\text{t}}^{3/4}}$	$Ns_{\text{t}} = \frac{30000\sqrt{3.39}}{8460^{3/4}}$	62.6	62.6	$ft^{3/4}$ $lbm^{3/4}$ min^{-1} $s^{-1/2}$

Parameter	Equation	Evaluated	EES Calc. Value	Hand Calc. Value	Units
Turbine specific diameter	$Ds_t = 2\left(\frac{Ns_t}{50}\right)^{-0.515}$	$Ds_t = 2\left(\frac{62.6}{50}\right)^{-0.515}$	1.78	1.78	$lbf^{1/4}\ s^{1/2}\ lbm^{-1/4}\ ft^{-1/4}$
Turbine diameter	$Ds_t = \frac{D_t H_t^{1/4}}{\sqrt{\dot{V}_t}}$	$1.78 = \frac{D_t 8460^{1/4}}{\sqrt{3.38}}$	0.34	0.34	ft
Volumetric flow at compressor inlet	$\dot{V}_{c,4} = \frac{\dot{m}_c}{\rho_{c,4}}$	$\dot{V}_{c,4} = \frac{0.907}{13.1}\frac{35.3[ft^3\ s^{-1}]}{[m^3\ s^{-1}]}$	2.45	2.44	$ft^3\ s^{-1}$
Ideal compressor head	$H_c = \left(h_{c,s,5} - h_{c,4}\right)$	$H_c = (527.2 - 516.9)\frac{334.6[ft\ lbf]}{[kJ\ kg^{-1}]}$	3412	3446	$ft^2\ s^2$
Compressor specific speed	$Ns_c = \frac{N\sqrt{\dot{V}_{c,4}}}{H_c^{3/4}}$	$Ns_c = \frac{30000\sqrt{2.44}}{3446^{3/4}}$	105.2	104.2	$ft^{3/4}\ lbm^{3/4}\ min^{-1}\ s^{-1/2}$
Compressor specific diameter	$Ds_c = 1.75\left(\frac{Ns_c}{80}\right)^{-0.38}$	$Ds_c = 1.75\left(\frac{104.2}{80}\right)^{-0.38}$	1.58	1.58	$lbf^{1/4}\ s^{1/2}\ lbm^{-1/4}\ ft^{-1/4}$
Compressor diameter	$Ds_c = \frac{D_c H_c^{1/4}}{\sqrt{\dot{V}_c}}$	$1.58 = \frac{D_c 3446^{1/4}}{\sqrt{2.44}}$	0.32	0.32	ft

Table A-5. Hand calculations to support EES evaluation of the heat exchanger *UA* calculations.

Parameter	Equation	Evaluated	EES Calc. Value	Hand Calc. Value	Units
PC Condenser – Superheated Section, Cross-flow Heat Exchanger					
Air mass flow	$\dot{m}_{p,cond,a,sh} = \dot{m}_{p,cond,a} A_{per,p,cond,sh,base}$	$\dot{m}_{p,cond,a,sh} = 11.1 \times 0.025$	0.28	0.28	kg s^{-1}
Air heat capacity rate	$C_{p,cond,a,sh} = \dot{m}_{p,cond,a,sh} Cp_{amb}$	$C_{p,cond,a,sh} = 0.28 \times 1.006$	0.28	0.28	kW K^{-1}
Fluid heat capacity rate	$C_{p,cond,f,sh} = \dfrac{\dot{Q}_{p,cond,sh}}{\left(T_{p,5} - T_{p,6}\right)}$	$C_{p,cond,f,sh} = \dfrac{0.44}{\left(29.4 - 28.6\right)}$	0.58	0.55	kW K^{-1}
Heat capacity rate ratio	$Cr_{p,cond,sh} = \dfrac{C_{min,p,cond,sh}}{C_{max,p,cond,sh}} = \dfrac{C_{p,cond,a,sh}}{C_{p,cond,f,sh}}$	$Cr_{p,cond,sh} = \dfrac{C_{min,p,cond,sh}}{C_{max,p,cond,sh}} = \dfrac{0.28}{0.55}$	0.48	0.51	-
Effectiveness	$\varepsilon_{p,cond,sh} = \dfrac{\dot{Q}_{p,cond,sh}}{C_{min,p,cond,sh}\left(T_{p,5} - T_{amb}\right)}$	$\varepsilon_{p,cond,sh} = \dfrac{0.44}{0.28\left(29.4 - 15\right)}$	0.11	0.11	-
NTU	$\varepsilon_{p,cond,sh} = 1 - e^{1/Cr} NTU^{0.22}\left(e^{-CrNTU^{0.78}} - 1\right)$	$0.11 = 1 - e^{1/0.51} NTU^{0.22}\left(e^{-0.51NTU^{0.78}} - 1\right)$	0.12	0.12	-
UA	$UA_{p,cond,sh} = NTU_{p,cond,sh} C_{min,p,cond,sh}$	$UA_{p,cond,sh} = 0.12 \times 0.28$	0.03	0.03	kW K^{-1}
PC Condenser - Two-Phase Section, Cross-flow Heat Exchanger					
Air mass flow	$\dot{m}_{p,cond,a,tp} = \dot{m}_{p,cond,a,total} A_{per,p,cond,tp,base}$	$\dot{m}_{p,cond,a,tp} = 11.1 \times 0.91$	10.08	10.1	kg s^{-1}
Air heat capacity rate	$C_{p,cond,a,tp} = \dot{m}_{p,cond,a,tp} Cp_{amb}$	$C_{p,cond,a,tp} = 10.1 \times 1.006$	10.12	10.16	kW K^{-1}
Effectiveness	$\varepsilon_{p,cond,tp} = \dfrac{\dot{Q}_{p,cond,tp}}{C_{min,p,cond,tp}\left(T_{p,6} - T_{amb}\right)}$	$\varepsilon_{p,cond,tp} = \dfrac{86.5}{10.16\left(28.6 - 15\right)}$	0.63	0.63	-
NTU	$NTU_{p,cond,tp} = -\ln\left(1 - \varepsilon_{p,cond,tp}\right)$	$NTU_{p,cond,tp} = -\ln\left(1 - 0.63\right)$	0.99	0.99	-

Parameter	Equation	Evaluated	EES Calc. Value	Hand Calc. Value	Units
UA	$UA_{p,cond,tp} = NTU_{p,cond,tp} C_{min,p,cond,tp}$	$UA_{p,cond,tp} = 0.99 \times 10.16$	10.05	10.06	kW K^{-1}
PC Condenser – Sub-cooled Section, Cross-flow Heat Exchanger					
Air mass flow	$\dot{m}_{p,cond,a,sc} = \dot{m}_{p,cond,a,total} A_{per,p,cond,sc,base}$	$\dot{m}_{p,cond,a,sc} = 11.1 \times 0.07$	0.78	0.78	kg s^{-1}
Air heat capacity rate	$C_{p,cond,a,sc} = \dot{m}_{p,cond,a,sc} Cp_{amb}$	$C_{p,cond,a,sc} = 0.78 \times 1.006$	0.78	0.78	kW K^{-1}
Fluid heat capacity rate	$C_{p,cond,f,sc} = \frac{\dot{Q}_{p,cond,sc}}{\left(T_{p,7} - T_{p,8}\right)}$	$C_{p,cond,f,sc} = \frac{0.65}{\left(23.9 - 23.1\right)}$	0.75	0.81	kW K^{-1}
Heat capacity rate ratio	$Cr_{p,cond,sc} = \frac{C_{min,p,cond,sc}}{C_{max,p,cond,sc}} = \frac{C_{p,cond,a,sc}}{C_{p,cond,f,sc}}$	$Cr_{p,cond,sc} = \frac{C_{min,p,cond,sc}}{C_{max,p,cond,sc}} = \frac{0.78}{0.81}$	0.95	0.96	-
Effectiveness	$\varepsilon_{p,cond,sc} = \frac{\dot{Q}_{p,cond,sc}}{C_{min,p,cond,sc}\left(T_{p,7} - T_{amb}\right)}$	$\varepsilon_{p,cond,sc} = \frac{0.65}{0.78\left(23.9 - 15\right)}$	0.097	0.094	-
NTU	$\varepsilon_{p,cond,sc} = 1 - e^{1/Cr} NTU^{0.22} \left(e^{-CrNTU^{0.78}} - 1\right)$	$0.094 = 1 - e^{1/0.96} NTU^{0.22} \left(e^{-0.96 NTU^{0.78}} - 1\right)$	0.11	0.11	-
UA	$UA_{p,cond,sc} = NTU_{p,cond,sc} C_{min,p,cond,sc}$	$UA_{p,cond,sc} = 0.11 \times 0.78$	0.083	0.086	kW K^{-1}
PC Boiler – Sub-cooled Section, Counter-flow Heat Exchanger					
Air heat capacity rate	$C_{p,b,a,sc} = \dot{m}_{exh,base} Cp_{exh} A_{per,p,b,sc,base}$	$C_{p,b,a,sc} = 6.8 \times 1.012 \times 0.15$	1.03	1.03	kW K^{-1}
Fluid heat capacity rate	$C_{p,b,f,sc} = \frac{\dot{Q}_{p,b,sc}}{\left(T_{p,14} - T_{p,13}\right)}$	$C_{p,b,f,sc} = \frac{27.94}{\left(92.7 - 58.1\right)}$	0.76	0.81	kW K^{-1}
Heat capacity rate ratio	$Cr_{p,b,sc} = \frac{C_{min,p,b,sc}}{C_{max,p,b,sc}} = \frac{C_{p,b,f,sc}}{C_{p,b,a,sc}}$	$Cr_{p,b,sc} = \frac{C_{min,p,b,sc}}{C_{max,p,b,sc}} = \frac{0.81}{1.03}$	0.74	0.79	-
Effectiveness	$\varepsilon_{p,b,sc} = \frac{\dot{Q}_{p,b,sc}}{C_{min,p,b,sc}\left(T_{p,a,14} - T_{p,13}\right)}$	$\varepsilon_{p,b,sc} = \frac{27.94}{0.81\left(95.6 - 58.1\right)}$	0.92	0.92	-

Parameter	Equation	Evaluated	EES Calc. Value	Hand Calc. Value	Units
NTU	$NTU_{p,b,sc} = \frac{1}{(Cr-1)} \ln\left(\frac{\varepsilon_{p,b,sc}-1}{\varepsilon_{p,b,sc} Cr - 1}\right)$	$NTU_{p,b,sc} = \frac{1}{(0.79-1)} \ln\left(\frac{0.92-1}{0.92 \times 0.79 - 1}\right)$	5.42	5.86	-
UA	$UA_{p,b,sc} = NTU_{p,b,sc} C_{min,p,b,sc}$	$UA_{p,b,sc} = 5.86 \times 0.81$	4.14	4.74	kW K^{-1}
PC Boiler – Two-Phase Section, Counter-flow Heat Exchanger					
Exhaust heat capacity rate	$C_{p,b,a,tp} = \dot{m}_{exh,base} Cp_{exh} A_{per,p,b,tp,base}$	$C_{p,b,a,tp} = 6.8 \times 1.012 \times 0.49$	3.37	3.37	kW K^{-1}
Effectiveness	$\varepsilon_{p,b,tp} = \frac{T_{a,15} - T_{a,14}}{T_{a,15} - T_{p,14}}$	$\varepsilon_{p,b,tp} = \frac{104.9 - 95.6}{104.9 - 92.7}$	0.76	0.76	-
NTU	$NTU_{p,b,tp} = -\ln\left(1 - \varepsilon_{p,b,tp}\right)$	$NTU_{p,b,tp} = -\ln\left(1 - \varepsilon_{p,b,tp}\right)$	1.44	1.43	-
UA	$UA_{p,b,tp} = NTU_{p,b,tp} C_{min,p,b,tp}$	$UA_{p,b,tp} = 1.43 \times 3.37$	4.79	4.81	kW K^{-1}
PC Boiler – Superheated Section, Counter-flow Heat Exchanger					
Air heat capacity rate	$C_{p,b,a,sh} = \dot{m}_{exh,base} Cp_{exh} A_{per,p,b,sh,base}$	$C_{p,b,a,sh} = 6.8 \times 1.012 \times 0.36$	2.5	2.48	kW K^{-1}
Fluid heat capacity rate	$C_{p,b,f,sh} = \frac{\dot{Q}_{p,b,sh}}{\left(T_{p,16} - T_{p,15}\right)}$	$C_{p,b,f,sh} = \frac{7.42}{(103.5 - 92.6)}$	0.58	0.68	kW K^{-1}
Heat capacity rate ratio	$Cr_{p,b,sh} = \frac{C_{min,p,b,sh}}{C_{max,p,b,sh}} = \frac{C_{p,b,f,sh}}{C_{p,b,a,sh}}$	$Cr_{p,b,sh} = \frac{C_{min,p,b,sh}}{C_{max,p,b,sh}} = \frac{0.68}{2.48}$	0.23	0.27	-
Effectiveness	$\varepsilon_{p,b,sh} = \frac{T_{p,16} - T_{p,15}}{T_{a,16} - T_{p,15}}$	$\varepsilon_{p,b,sh} = \frac{103.5 - 92.6}{106 - 92.6}$	0.81	0.81	-
NTU	$NTU_{p,b,sh} = \frac{1}{(Cr-1)} \ln\left(\frac{\varepsilon_{p,b,sh}-1}{\varepsilon_{p,b,sh} Cr - 1}\right)$	$NTU_{p,b,sh} = \frac{1}{(0.27-1)} \ln\left(\frac{0.81-1}{0.81 \times 0.27 - 1}\right)$	1.91	1.93	-
UA	$UA_{p,b,sh} = NTU_{p,b,sh} C_{min,p,b,sh}$	$UA_{p,b,sh} = 1.93 \times 0.68$	1.1	1.31	kW K^{-1}

Parameter	Equation	Evaluated	EES Calc. Value	Hand Calc. Value	Units
PC Recuperator – Counter-flow Heat Exchanger					
Vapor heat capacity rate	$C_{\text{p,recup,vap}} = \frac{\dot{Q}_{\text{p,recup}}}{\left(T_{\text{p,3}} - T_{\text{p,4}}\right)}$	$C_{\text{p,recup,vap}} = \frac{26.35}{\left(74.95 - 29.4\right)}$	0.58	0.58	kW K^{-1}
Liquid heat capacity rate	$C_{\text{p,recup}} = \frac{\dot{Q}_{\text{p,recup}}}{\left(T_{\text{p,12}} - T_{\text{p,11}}\right)}$	$C_{\text{p,recup}} = \frac{26.35}{\left(58.1 - 23.5\right)}$	0.76	0.76	kW K^{-1}
Heat capacity rate ratio	$Cr_{\text{p,recup}} = \frac{C_{\text{min,p,recup}}}{C_{\text{max,p,recup}}} = \frac{C_{\text{p,recup,vap}}}{C_{\text{p,recup,liq}}}$	$Cr_{\text{p,recup}} = \frac{C_{\text{min,p,recup}}}{C_{\text{max,p,recup}}} = \frac{0.58}{0.76}$	0.76	0.76	-
Effectiveness	$\varepsilon_{\text{p,recup}} = \frac{\left(T_{\text{p,3}} - T_{\text{p,4}}\right)}{\left(T_{\text{p,3}} - T_{\text{p,11}}\right)}$	$\varepsilon_{\text{p,recup}} = \frac{\left(74.95 - 29.4\right)}{\left(74.95 - 23.5\right)}$	0.886	0.885	-
NTU	$NTU_{\text{p,recup}} = \frac{1}{\left(Cr - 1\right)} \ln\left(\frac{\varepsilon_{\text{p,recup}} - 1}{\varepsilon_{\text{p,recup}} Cr - 1}\right)$	$NTU_{\text{p,recup}} = \frac{1}{\left(0.76 - 1\right)} \ln\left(\frac{0.885 - 1}{0.885 \times 0.76 - 1}\right)$	4.37	4.35	-
UA	$UA_{\text{p,recup}} = NTU_{\text{p,recup}} C_{\text{min,p,recup}}$	$UA_{\text{p,recup}} = 4.35 \times 0.58$	2.53	2.52	kW K^{-1}
CC Evaporator - Two-Phase Section, Counter-flow Heat Exchanger					
Glycol heat capacity rate	$C_{\text{c,evap,g,tp}} = \dot{m}_{\text{c,g}} Cp_{\text{g}}$	$C_{\text{c,evap,g,tp}} = 56.2 \times 3.71$	218.2	208	kW K^{-1}
Effectiveness	$\varepsilon_{\text{c,evap}} = \frac{\dot{Q}_{\text{c,e,tp}}}{C_{\text{min,e,tp}}\left(T_{\text{g,2}} - T_{\text{c,1}}\right)}$	$\varepsilon_{\text{c,evap}} = \frac{248.2}{218.2\left(17.1 - 15.3\right)}$	0.62	0.63	-
NTU	$NTU_{\text{c,evap,tp}} = -\ln\left(1 - \varepsilon_{\text{c,evap,tp}}\right)$	$NTU_{\text{c,evap,tp}} = -\ln\left(1 - 0.63\right)$	0.97	0.99	-
UA	$UA_{\text{c,evap,tp}} = NTU_{\text{c,evap,tp}} C_{\text{min,c,evap,tp}}$	$UA_{\text{c,evap,tp}} = 0.99 \times 208$	210.6	206	kW K^{-1}
CC Evaporator - Superheated Section, Counter-flow Heat Exchanger					
Glycol heat capacity rate	$C_{\text{c,evap,g,sh}} = \dot{m}_{\text{c,g}} Cp_{\text{g}}$	$C_{\text{c,evap,g,sh}} = \dot{m}_{\text{c,g}} Cp_{\text{g}}$	208.4	208	kW K^{-1}

Parameter	Equation	Evaluated	EES Calc. Value	Hand Calc. Value	Units
Fluid heat capacity rate	$C_{c,evap,f,sh} = \frac{\dot{Q}_{c,evap,sh}}{\left(T_{c,3} - T_{c,2}\right)}$	$C_{c,evap,f,sh} = \frac{2.65}{\left(16.3 - 13.9\right)}$	1.09	1.1	kW K^{-1}
Heat capacity rate ratio	$Cr_{c,evap,sh} = \frac{C_{min,c,evap,sh}}{C_{max,c,evap,sh}} = \frac{C_{c,evap,f,sh}}{C_{c,evap,g,sh}}$	$Cr_{c,evap,sh} = \frac{C_{min,c,evap,sh}}{C_{max,c,evap,sh}} = \frac{1.1}{208}$	0.005	0.005	-
Effectiveness	$\varepsilon_{c,evap,sh} = \frac{\dot{Q}_{c,evap,sh}}{C_{min,c,evap,sh}\left(T_{c,g,3} - T_{c,2}\right)}$	$\varepsilon_{c,evap,sh} = \frac{2.65}{1.1\left(17.15 - 13.9\right)}$	0.75	0.74	-
NTU	$NTU_{c,evap,sh} = \frac{1}{\left(Cr - 1\right)} \ln\left(\frac{\varepsilon_{c,evap,sh} - 1}{\varepsilon_{c,evap,sh} Cr - 1}\right)$	$NTU_{c,evap,sh} = \frac{1}{\left(0.005 - 1\right)} \ln\left(\frac{0.74 - 1}{0.74 \times 0.005 - 1}\right)$	1.4	1.35	-
UA	$UA_{c,evap,sh} = NTU_{c,evap,sh} C_{min,c,evap,sh}$	$UA_{c,evap,sh} = 1.35 \times 1.1$	1.52	1.49	kW K^{-1}
CC Condenser - Superheated Section, Cross-flow Heat Exchanger					
Air mass flow	$\dot{m}_{c,cond,a,sh} = \dot{m}_{c,cond,a,total} A_{per,c,cond,sh,base}$	$\dot{m}_{c,cond,a,sh} = 38.54 \times 0.024$	0.92	0.92	kg s^{-1}
Air heat capacity rate	$C_{c,cond,a,sh} = \dot{m}_{c,cond,a,sh} Cp_{amb}$	$C_{c,cond,a,sh} = 0.92 \times 1.006$	0.93	0.93	kW K^{-1}
Fluid heat capacity rate	$C_{c,cond,f,sh} = \frac{\dot{Q}_{c,cond,sh}}{\left(T_{c,6} - T_{c,7}\right)}$	$C_{c,cond,f,sh} = \frac{8.83}{\left(31.3 - 23.5\right)}$	1.13	1.13	kW K^{-1}
Heat capacity rate ratio	$Cr_{c,cond,sh} = \frac{C_{min,c,cond,sh}}{C_{max,c,cond,sh}} = \frac{C_{c,cond,a,sh}}{C_{c,cond,f,sh}}$	$Cr_{c,cond,sh} = \frac{C_{min,c,cond,sh}}{C_{max,c,cond,sh}} = \frac{0.93}{1.13}$	0.82	0.82	-
Effectiveness	$\varepsilon_{c,cond,sh} = \frac{\dot{Q}_{c,cond,sh}}{C_{min,c,cond,sh}\left(T_{c,6} - T_{amb}\right)}$	$\varepsilon_{c,cond,sh} = \frac{8.83}{0.93\left(31.3 - 15\right)}$	0.59	0.58	-
NTU	$\varepsilon_{c,cond,sh} = 1 - e^{1/Cr} NTU^{0.22} \left(e^{-CrNTU^{0.78}} - 1\right)$	$0.58 = 1 - e^{1/0.82} NTU^{0.22} \left(e^{-0.82 NTU^{0.78}} - 1\right)$	1.45	1.45	-
UA	$UA_{c,cond,sh} = NTU_{c,cond,sh} C_{min,c,cond,sh}$	$UA_{c,cond,sh} = 1.45 \times 0.93$	1.34	1.35	kW K^{-1}

Parameter	Equation	Evaluated	EES Calc. Value	Hand Calc. Value	Units
CC Condenser - Two-Phase Section, Cross-flow Heat Exchanger					
Air mass flow	$\dot{m}_{c,cond,a,tp} = \dot{m}_{c,cond,a,total} A_{per,c,cond,tp,base}$	$\dot{m}_{c,cond,a,tp} = 38.54 \times 0.87$	33.53	33.53	kg s^{-1}
Air heat capacity rate	$C_{c,cond,a,tp} = \dot{m}_{c,cond,a,tp} Cp_{amb}$	$C_{c,cond,a,tp} = 33.53 \times 1.006$	33.67	33.7	kW K^{-1}
Effectiveness	$\varepsilon_{c,cond,tp} = \frac{\dot{Q}_{c,cond,tp}}{C_{min,c,cond,tp}\left(T_{c,7} - T_{amb}\right)}$	$\varepsilon_{c,cond,tp} = \frac{257.8}{33.7\left(23.5 - 15\right)}$	0.91	0.90	-
NTU	$NTU_{c,cond,tp} = -\ln\left(1 - \varepsilon_{c,cond,tp}\right)$	$NTU_{c,cond,tp} = -\ln\left(1 - 0.9\right)$	2.36	2.30	-
UA	$UA_{c,cond,tp} = NTU_{c,cond,tp} C_{min,c,cond,tp}$	$UA_{c,cond,tp} = 2.30 \times 33.7$	79.4	77.5	kW K^{-1}
CC Condenser - Sub-cooled Section, Cross-flow Heat Exchanger					
Air mass flow	$\dot{m}_{c,cond,a,sc} = \dot{m}_{c,cond,a,total} A_{per,c,cond,sc,base}$	$\dot{m}_{c,cond,a,sc} = 38.54 \times 0.106$	4.09	4.09	kg s^{-1}
Air heat capacity rate	$C_{c,cond,a,sc} = \dot{m}_{c,cond,a,sc} Cp_{amb}$	$C_{c,cond,a,sc} = 4.09 \times 1.006$	4.11	4.11	kW K^{-1}
Fluid heat capacity rate	$C_{c,cond,f,sc} = \frac{\dot{Q}_{c,cond,sc}}{\left(T_{c,8} - T_{c,9}\right)}$	$C_{c,cond,f,sc} = \frac{0.84}{\left(23.3 - 22.7\right)}$	1.64	1.4	kW K^{-1}
Heat capacity rate ratio	$Cr_{c,cond,sc} = \frac{C_{min,c,cond,sc}}{C_{max,c,cond,sc}} = \frac{C_{c,cond,f,sc}}{C_{c,cond,a,sc}}$	$Cr_{c,cond,sc} = \frac{C_{min,c,cond,sc}}{C_{max,c,cond,sc}} = \frac{1.4}{4.11}$	0.40	0.34	-
Effectiveness	$\varepsilon_{c,cond,sc} = \frac{\dot{Q}_{c,cond,sc}}{C_{min,c,cond,sc}\left(T_{c,8} - T_{amb}\right)}$	$\varepsilon_{c,cond,sc} = \frac{0.84}{1.4\left(23.3 - 15\right)}$	0.062	0.07	-
NTU	$\varepsilon_{c,cond,sc} = 1 - e^{1/Cr} NTU^{0.22}\left(e^{-CrNTU^{0.78}} - 1\right)$	$0.07 = 1 - e^{1/0.34} NTU^{0.34}\left(e^{-0.34\,NTU^{0.78}} - 1\right)$	0.066	0.064	-
UA	$UA_{c,cond,sc} = NTU_{c,cond,sc} C_{min,c,cond,sc}$	$UA_{c,cond,sc} = 0.064 \times 1.4$	0.11	0.09	kW K^{-1}
Summation of UA's					
PC Condenser	$UA_{p,cond} = UA_{p,cond,sc} + UA_{p,cond,tp} + UA_{p,cond,sh}$	$UA_{p,cond} = 0.086 + 10.06 + 0.03$	10.2	10.18	kW K^{-1}

Parameter	Equation	Evaluated	EES Calc. Value	Hand Calc. Value	Units
PC Boiler	$UA_{p,b} = UA_{p,b,sc} + UA_{p,b,tp} + UA_{p,b,sh}$	$UA_{p,b} = 1.31 + 4.81 + 4.74$	10.0	10.9	kW K^{-1}
CC Condenser	$UA_{c,cond} = UA_{c,cond,sc} + UA_{c,cond,tp} + UA_{c,cond,sh}$	$UA_{c,cond} = 0.09 + 77.5 + 1.35$	80.9	78.9	kW K^{-1}
CC Evaporator	$UA_{c,evap} = UA_{c,evap,tp} + UA_{c,evap,sh}$	$UA_{c,evap} = 206 + 1.49$	212	207.5	kW K^{-1}

Table A-6. Model input parameters for the off-design performance hand calculation. Some parameters are results of baseline modeling.

Parameter	Value	Units
Compressor efficiency guess (η_{comp})	78.3	%
Turbine efficiency guess (η_{t})	78.7	%
Pump efficiency (η_{pump})	32	%
Shaft efficiency (η_{shaft})	93	%
PC Exhaust fan efficiency ($\eta_{p,bf}$)	45	%
CC Glycol pump efficiency ($\eta_{c,gp}$)	45	%
CC Condenser fan number ($N_{c,cf}$)	6	fans
PC Condenser fan number ($N_{p,cf}$)	2	fans
Exhaust air inlet temperature (T_{exh})	106	°C
Exhaust air flow rate ($\dot{V}_{exh}$)	32500	$m^3\ hr^{-1}$
Exhaust air specific heat (Cp_{exh})	1.012	$kJ\ kg^{-1}\ K^{-1}$
Exhaust air density (ρ_{exh})	0.7809	$kg\ m^{-3}$
Specific heat of 30:70 Propylene Glycol: Water mixture (Cp_{g})	3.86	$kJ\ kg^{-1}\ K^{-1}$
PC Condenser UA for two-phase and superheated sections ($UA_{p,cond,tp+sh}$)	9.1	$kW\ K^{-1}$
PC Condenser UA for sub-cooled section ($UA_{p,cond,sc}$)	0.4	$kW\ K^{-1}$
PC Boiler UA for two-phase and sub-cooled sections ($UA_{p,b,tp+sc}$)	11.56	$kW\ K^{-1}$
PC Boiler UA for superheated section ($UA_{p,cond,sh}$)	1.44	$kW\ K^{-1}$
PC Recuperator UA ($UA_{p,recup}$)	2.53	$kW\ K^{-1}$
CC Condenser UA for two-phase and superheated sections ($UA_{c,cond,tp+sh}$)	63	$kW\ K^{-1}$
CC Condenser UA for sub-cooled section ($UA_{c,cond,sc}$)	2	$kW\ K^{-1}$

Parameter	Value	Units
CC Evaporator UA for two-phase section ($UA_{c,evap,tp}$)	211	kW K^{-1}
CC Evaporator UA for superheated section ($UA_{c,cond,sh}$)	1	kW K^{-1}
Ambient air temperature (T_{amb})	27.5	°C
Ambient air pressure (P_{amb})	85	kPa
Ambient air density (ρ_{amb})	1.028	kg m^{-3}
Ambient air specific heat (Cp_{amb})	1.006	kJ kg^{-1} K^{-1}
Line pressure drops (ΔP_{line})	1	kPa
PC Recuperator vapor side pressure drop ($\Delta P_{p,recup,vap}$)	4.74	kPa
PC Recuperator liquid side pressure drop ($\Delta P_{p,recup,liq}$)	1.45	kPa
PC Boiler sub-cooled pressure drop ($\Delta P_{p,b,sc}$)	0.2	kPa
PC Boiler two-phase pressure drop ($\Delta P_{p,b,tp}$)	1.2	kPa
PC Boiler superheated pressure drop ($\Delta P_{p,b,sh}$)	0.2	kPa
PC Condenser sub-cooled pressure drop ($\Delta P_{p,cond,sc}$)	1	kPa
PC Condenser sub-cooled pressure drop ($\Delta P_{p,cond,sc}$)	8.8	kPa
PC Condenser two-phase pressure drop ($\Delta P_{p,cond,tp}$)	1	kPa
PC Condenser superheated pressure drop ($\Delta P_{p,cond,sh}$)	0.2	kPa
CC Condenser sub-cooled pressure drop ($\Delta P_{c,cond,sc}$)	1.71	kPa
CC Condenser two-phase pressure drop ($\Delta P_{c,cond,tp}$)	0.2	kPa
CC Evaporator two-phase pressure drop ($\Delta P_{c,evap,tp}$)	19	kPa
CC Evaporator superheated pressure drop ($\Delta P_{c,evap,sh}$)	1	kPa
PC Boiler air side pressure drop ($\Delta P_{p,b,a}$)	0.2	kPa

Parameter	Value	Units
CC Evaporator glycol side pressure drop ($\Delta P_{c,g}$)	30.2	kPa
PC Condenser air flow rate ($\dot{V}_{p,cond,a}$)	56,000	$m^3\ hr^{-1}$
CC Condenser air flow rate ($\dot{V}_{c,cond,a}$)	168,000	$m^3\ hr^{-1}$
Universal gas constant (R_{univ})	8.314	kJ $kmol^{-1}$ K^{-1}
Gravitational constant (g_c)	9.81	m s^{-2}
Turbine reference temperature ($T_{t,ref}$)	376.611	°K
Turbine reference pressure ($P_{t,ref}$)	569.921	kPa
Turbine reference specific heat ratio ($\gamma_{t,ref}$)	0.893086	-
Turbine reference ZR value ($ZR_{t,ref}$)	0.0348	kJ kg^{-1} K^{-1}
Compressor reference temperature ($T_{comp,ref}$)	289.428	°K
Compressor reference pressure ($P_{comp,ref}$)	420.718	kPa
Compressor reference specific heat ratio ($\gamma_{comp,ref}$)	1.089699	-
Compressor reference ZR value ($ZR_{comp,ref}$)	0.1124	kJ kg^{-1} K^{-1}
PC Recuperator baseline heat duty ($\dot{Q}_{recup}$)	25.9	kW
PC Boiler sub-cooled baseline heat duty ($\dot{Q}_{p,b,sc}$)	27.35	kW
PC Boiler two-phase baseline heat duty ($\dot{Q}_{p,b.tp}$)	64.3	kW
PC Boiler superheated baseline heat duty ($\dot{Q}_{p,b,sh}$)	7.68	kW
PC Condenser sub-cooled baseline heat duty ($\dot{Q}_{p,cond,sc}$)	0.37	kW
PC Condenser two-phase baseline heat duty ($\dot{Q}_{p,cond,tp}$)	85.6	kW
PC Condenser superheated baseline heat duty ($\dot{Q}_{p,cond,sh}$)	1.47	kW
CC Condenser sub-cooled baseline heat duty ($\dot{Q}_{c,cond,sc}$)	0.82	kW

Parameter	Value	Units
CC Condenser two-phase baseline heat duty ($\dot{Q}_{c,cond,tp}$)	254.8	kW
CC Condenser superheated baseline heat duty ($\dot{Q}_{c,cond,sh}$)	6.7	kW
CC Evaporator two-phase baseline heat duty ($\dot{Q}_{c,evap,tp}$)	250.2	kW
CC Evaporator superheated baseline heat duty ($\dot{Q}_{c,e,sh}$)	0.57	kW
PC Condenser sub-cooled baseline area fraction ($A_{per,p,cond,sc,base}$)	2	%
PC Condenser two-phase baseline area fraction ($A_{per,p,cond,tp,base}$)	91	%
PC Condenser superheated baseline area fraction ($A_{per,p,cond,sh,base}$)	7	%
PC Boiler sub-cooled baseline area fraction ($A_{per,p,b,sc,base}$)	15	%
PC Boiler two-phase baseline area fraction ($A_{per,p,b,tp,base}$)	49	%
PC Boiler superheated baseline area fraction ($A_{per,p,b,sh,base}$)	36	%
CC Condenser sub-cooled baseline area fraction ($A_{per,c,cond,sc,base}$)	2	%
CC Condenser two-phase baseline area fraction ($A_{per,c,cond,tp,base}$)	87	%
CC Condenser superheated baseline area fraction ($A_{per,c,cond,sh,base}$)	11	%
Baseline PC mass flow rate ($\dot{m}_{p,base}$)	0.61	kg s^{-1}
Baseline CC mass flow rate ($\dot{m}_{c,base}$)	0.92	kg s^{-1}
Baseline CC mass flow rate R134a ($\dot{m}_{c,base,r134a}$)	1.4	kg s^{-1}
Baseline exhaust air temperature ($T_{exh,base}$)	106	°C
Baseline ambient air temperature ($T_{amb,base}$)	15	°C
Baseline exhaust air pressure ($P_{exh,base}$)	85	kPa
Baseline PC condenser air mass flow rate ($\dot{m}_{p,cond,a,base}$)	11.1	kg s^{-1}

Parameter	Value	Units
Baseline CC condenser air mass flow rate ($\dot{m}_{c,cond,a,base}$)	38.54	kg s^{-1}
Baseline PC exhaust air mass flow rate ($\dot{m}_{exh,base}$)	6.9	kg s^{-1}
Baseline Glycol mass flow rate ($\dot{m}_{g,base}$)	52.1	kg s^{-1}
Baseline PC Boiler inlet temperature ($T_{p,13,base}$)	58.1	°C
Baseline PC Boiler outlet temperature ($T_{p,16,base}$)	103.5	°C
Baseline PC Boiler pressure ($P_{p,13,base}$)	573.5	kPa
Baseline PC Condenser inlet temperature ($T_{p,5,base}$)	29.4	°C
Baseline PC Condenser outlet temperature ($T_{p,8,base}$)	23	°C
Baseline PC Condenser pressure ($P_{p,5,base}$)	83.2	kPa
Baseline PC Recuperator vapor inlet temperature ($T_{p,3,base}$)	75	°C
Baseline PC Recuperator vapor outlet temperature ($T_{p,4,base}$)	29.4	°C
Baseline PC Recuperator pressure ($P_{p,3,base}$)	89.2	kPa
Baseline PC Recuperator liquid inlet temperature ($T_{p,11,base}$)	23.54	°C
Baseline PC Recuperator liquid outlet temperature ($T_{p,12,base}$)	58.1	°C
Baseline PC Recuperator pressure ($P_{p,11,base}$)	577	kPa
Baseline CC Condenser inlet temperature ($T_{c,6,base}$)	31.3	°C
Baseline CC Condenser outlet temperature ($T_{c,9,base}$)	22.7	°C
Baseline CC Condenser pressure ($P_{c,6,base}$)	569.8	kPa
Baseline CC Evaporator inlet temperature ($T_{c,1,base}$)	15	°C
Baseline CC Evaporator outlet temperature ($T_{c,3,base}$)	16.3	°C
Baseline CC Evaporator pressure ($P_{c,1,base}$)	442.8	kPa

Table A-7. Hand calculations to support EES evaluation of *UA* scaling methodology.

Parameter	Equation	Evaluated	EES Calc. Value	Hand Calc. Value	Units
PC Boiler - Air Side Heat Transfer Scaling Factor (Subscripts "p,b" omitted)					
Geometric C1 factor	$C_1 = \left(\frac{\theta}{90}\right)^{0.27}\left(\frac{F_p}{L_p}\right)^{-0.14}\left(\frac{F_l}{L_p}\right)^{-0.29}\left(\frac{T_d}{L_p}\right)^{-0.23}\left(\frac{L_l}{L_p}\right)^{0.68}\left(\frac{T_p}{L_p}\right)^{-0.28}\left(\frac{\delta_f}{L_p}\right)^{-0.05}$	Values omitted due to confidentiality	0.31	0.31	-
Baseline mass flux	$G_{base} = \frac{\dot{m}_{a,base}}{A_{face}}$	$G_{base} = \frac{6.9}{3.71}$	1.86	1.86	kg m^{-2} s^{-1}
Baseline louver pitch Reynolds	$Re_{base} = \frac{G_{base} L_p}{\mu_{exh,base}}$	$Re_{base} = \frac{1.86 \times L_p}{0.000022}$	117.5	118.4	-
Baseline Colburn Factor	$j_{base} = C_1 Re_{base}^{-0.49}$	$j_{base} = 0.31 \times 118.4^{-0.49}$	0.030	0.03	-
Baseline heat transfer coefficient	$h_{a,base} = \frac{j_{base} Cp_{exh,base} G_{base}}{Pr_{exh,base}^{2/3}}$	$h_{a,base} = \frac{0.03 \times 1.012 \times 1.86}{0.70^{2/3}}$	0.072	0.072	W m^{-2} K^{-1}
Off-design mass flux	$G_{off} = \frac{\dot{m}_{a,off}}{A_{face}}$	$G_{off} = \frac{5.03}{3.71}$	1.36	1.36	kg m^{-2} s^{-1}
Off-design louver pitch Reynolds	$Re_{off} = \frac{G_{off} L_p}{\mu_{exh,off}}$	$Re_{off} = \frac{1.36 \times L_p}{0.000022}$	85.3	86.5	-
Off-design Colburn Factor	$j_{off} = C_1 Re_{off}^{-0.49}$	$j_{off} = 0.31 \times 86.5^{-0.49}$	0.035	0.035	-
Off-design heat transfer coefficient	$h_{a,off} = \frac{j_{off} Cp_{exh,off} G_{off}}{Pr_{exh,off}^{2/3}}$	$h_{a,off} = \frac{0.035 \times 1.012 \times 1.36}{0.70^{2/3}}$	0.062	0.061	W m^{-2} K^{-1}
Heat transfer factor	$f_{h,a} = \frac{h_{a,off}}{h_{a,base}}$	$f_{h,a} = \frac{0.061}{0.072}$	0.85	0.85	-

Parameter	Equation	Evaluated	EES Calc. Value	Hand Calc. Value	Units
PC Boiler – Superheated Section Scaled *UA* (Subscripts "p,b" omitted)					
Air side resistance	$R_{sh,a} = h_{a,base} A_a A_{per,sh,base}$	$R_{sh,a} = 0.072 \times 689.5 \times 0.3644$	18.2	18.1	kW K^{-1}
Fluid side resistance	$UA_{sh,base} = \left(\frac{1}{R_{sh,f}} + \frac{1}{R_{sh,a}} \right)^{-1}$	$1.107 = \left(\frac{1}{R_{sh,f}} + \frac{1}{18.1} \right)^{-1}$	1.18	1.18	kW K^{-1}
Heat transfer factor	$f_{h,sh} = \left(\frac{\frac{\dot{m}_{p,off}}{\mu_{vap,off}}}{\frac{\dot{m}_{p,base}}{\mu_{vap,base}}} \right)^{0.8} \left(\frac{Pr_{vap,off}}{Pr_{vap,base}} \right)^{0.3}$	$f_{h,sh} = \left(\frac{\frac{0.4}{0.0000138}}{\frac{0.61}{0.0000138}} \right)^{0.8} \left(\frac{0.909}{0.933} \right)^{0.3}$	0.71	0.71	-
Area factor	$f_{A,sh} = \left(\frac{\frac{\dot{Q}_{sh,off}}{\dot{Q}_{total,off}}}{\frac{\dot{Q}_{sh,base}}{\dot{Q}_{total,base}}} \right) f_{h,sh}$	$f_{A,sh} = \left(\frac{\frac{9.58}{57.97}}{\frac{7.42}{99.52}} \right) 0.71$	1.57	1.57	-
UA	$UA_{sh,off} = \left(\frac{1}{R_{sh,f} f_{h,sh} f_{A,sh}} + \frac{1}{R_{sh,a} f_{h,a} f_{A,sh}} \right)^{-1}$	$UA_{sh,off} = \left(\frac{1}{1.18 \times 0.71 \times 1.57} + \frac{1}{18.1 \times 0.85 \times 1.57} \right)^{-1}$	1.25	1.25	kW K^{-1}
PC Boiler – Two-phase Section Scaled *UA* (Subscripts "p,b" omitted)					
Air side resistance	$R_{tp,a} = h_{a,base} A_a A_{per,tp,base}$	$R_{tp,a} = 0.072 \times 689.5 \times 0.4856$	24.22	24.1	kW K^{-1}
Fluid side resistance	$UA_{tp,base} = \left(\frac{1}{R_{tp,f}} + \frac{1}{R_{tp,a}} \right)^{-1}$	$4.799 = \left(\frac{1}{R_{tp,f}} + \frac{1}{24.1} \right)^{-1}$	5.99	5.99	kW K^{-1}
Baseline Froude number	$Fr_{base} = \frac{\dot{m}_{p,base}^2}{\rho_{liq,base} g}$	$Fr_{base} = \frac{0.61^2}{1311 \times 9.81}$	2.8E-5	2.9E-5	-

Parameter	Equation	Evaluated	EES Calc. Value	Hand Calc. Value	Units
Baseline Boiling number	$Bo_{\text{base}} = \frac{\dot{Q}_{\text{tp,base}}}{\dot{m}_{\text{p,base}} h_{\text{fg,base}}}$	$Bo_{\text{base}} = \frac{64.2}{0.61 \times 105.3}$	1.0	1.0	-
Baseline liquid heat transfer coefficient	$h_{\text{liq,base}} = \left(\frac{\dot{m}_{\text{p,base}}}{\mu_{\text{liq,base}}} \right)^{0.8} Pr_{\text{liq,base}}{}^{0.4} k_{\text{liq,base}}$	$h_{\text{liq,base}} = \left(\frac{0.61}{0.00031} \right)^{0.8} 6.20^{0.4} 0.065$	58.2	58.2	W m$^{-0.2}$ K^{-1}
Baseline H_1 factor	$H_{1,\text{base}} = 1 + 3000 Bo_{\text{base}}^{0.86} Fr_{\text{base}}^{(0.1-2Fr_{\text{base}})}$	$H_{1,\text{base}} = 1 + 3000 \times 1^{0.8} \left(2.9 \times 10^{-5}\right)^{\left(0.1-2\times 2.9\times 10^{-5}\right)}$	1056	1056	-
Baseline H_2 factor	$H_{2,\text{base}} = 1.12 Fr_{\text{base}}^{0.5} \left[\frac{x}{1-x} \right]^{0.75} \left[\frac{\rho_{\text{l,base}}}{\rho_{\text{g,base}}} \right]^{0.41}$	$H_{2,\text{base}} = 1.12 \left(2.9 \times 10^{-5}\right)^{0.5} \left[\frac{0.5}{1-0.5} \right]^{0.75} \left[\frac{1311}{43.8} \right]^{0.41}$	0.024	0.024	-
Baseline two-phase heat transfer coefficient	$h_{\text{TP,base}} = \left(H_{1,\text{base}} + H_{2,\text{base}} \right) h_{\text{liq,base}}$	$h_{\text{TP,base}} = \left(1056 + 0.024\right) 58.2$	61261	61461	W m$^{-0.2}$ K^{-1}
Off-design Froude number	$Fr_{\text{off}} = \frac{\dot{m}_{\text{p,off}}^2}{\rho_{\text{liq,off}} g}$	$Fr_{\text{off}} = \frac{0.4^2}{1273 \times 9.81}$	1.3E-5	1.3E-5	-
Off-design Boiling number	$Bo_{\text{off}} = \frac{\dot{Q}_{\text{tp,off}}}{\dot{m}_{\text{p,off}} h_{\text{fg,off}}}$	$Bo_{\text{off}} = \frac{46.24}{0.4 \times 115.6}$	1	1	-
Off-design liquid heat transfer coefficient	$h_{\text{liq,off}} = \left(\frac{\dot{m}_{\text{p,off}}}{\mu_{\text{liq,off}}} \right)^{0.8} Pr_{\text{liq,off}}{}^{0.4} k_{\text{liq,off}}$	$h_{\text{liq,off}} = \left(\frac{0.4}{0.00027} \right)^{0.8} 5.67^{0.4} 0.062$	0.992	0.98	W m$^{-0.2}$ K^{-1}
Off-design H_1 factor	$H_{1,\text{off}} = 1 + 3000 Bo_{\text{off}}^{0.86} Fr_{\text{off}}^{(0.1-2Fr_{\text{off}})}$	$H_{1,\text{off}} = 1 + 3000 \left(1\right)^{0.8} \left(1.3 \times 10^{-5}\right)^{\left(0.1-2\left(1.3\times 10^{-5}\right)\right)}$	974	975	-
Off-design H_2 factor	$H_{2,\text{off}} = 1.12 Fr_{\text{off}}^{0.5} \left[\frac{x}{1-x} \right]^{0.75} \left[\frac{\rho_{\text{l,off}}}{\rho_{\text{g,off}}} \right]^{0.41}$	$H_{2,\text{off}} = 1.12 \left(1.3 \times 10^{-5}\right)^{0.5} \left[\frac{0.5}{1-0.5} \right]^{0.75} \left[\frac{1273}{24.81} \right]^{0.41}$	0.020	0.02	-

Parameter	Equation	Evaluated	EES Calc. Value	Hand Calc. Value	Units
Off-design two-phase heat transfer coefficient	$h_{\mathrm{TP,off}} = \left(H_{1,\mathrm{off}} + H_{2,\mathrm{off}}\right) h_{\mathrm{liq,off}}$	$h_{\mathrm{TP,off}} = \left(975 + 0.020\right) 42.4$	40958	41340	W $m^{-0.2}$ K^{-1}
Heat transfer factor	$f_{\mathrm{h,tp}} = \dfrac{h_{\mathrm{TP,off}}}{h_{\mathrm{TP,base}}}$	$f_{\mathrm{h,tp}} = \dfrac{41340}{61461}$	0.69	0.67	-
Area factor	$f_{\mathrm{A,tp}} = \left(\dfrac{\dfrac{\dot{Q}_{\mathrm{tp,off}}}{\dot{Q}_{\mathrm{total,off}}}}{\dfrac{\dot{Q}_{\mathrm{tp,base}}}{\dot{Q}_{\mathrm{total,base}}}} \right) f_{\mathrm{h,tp}}$	$f_{\mathrm{A,tp}} = \left(\dfrac{\dfrac{46.2}{57.9}}{\dfrac{64.2}{99.52}} \right) 0.67$	0.83	0.83	-
UA	$UA_{\mathrm{tp,off}} = \left(\dfrac{1}{R_{\mathrm{tp,f}} f_{\mathrm{h,tp}} f_{\mathrm{A,tp}}} + \dfrac{1}{R_{\mathrm{tp,a}} f_{\mathrm{h,a}} f_{\mathrm{A,tp}}} \right)^{-1}$	$UA_{\mathrm{tp,off}} = \left(\dfrac{1}{5.99(0.67)0.83} + \dfrac{1}{24.1(0.85)0.83} \right)^{-1}$	2.90	2.79	kW K^{-1}
PC Boiler –Sub-cooled Section Scaled *UA* (Subscripts "p,b" omitted)					
Air side resistance	$R_{\mathrm{sc,a}} = h_{\mathrm{a,base}} A_{\mathrm{a}} A_{\mathrm{per,sc,base}}$	$R_{\mathrm{sc,a}} = 0.072 \times 689.5 \times 0.15$	7.48	7.45	kW K^{-1}
Fluid side resistance	$UA_{\mathrm{sc,base}} = \left(\dfrac{1}{R_{\mathrm{sc,f}}} + \dfrac{1}{R_{\mathrm{sc,a}}} \right)^{-1}$	$4.137 = \left(\dfrac{1}{R_{\mathrm{sc,f}}} + \dfrac{1}{7.45} \right)^{-1}$	9.26	9.35	kW K^{-1}
Heat transfer factor	$f_{\mathrm{h,sc}} = \left(\dfrac{\dfrac{\dot{m}_{\mathrm{p,off}}}{\mu_{\mathrm{liq,off}}}}{\dfrac{\dot{m}_{\mathrm{p,base}}}{\mu_{\mathrm{liq,base}}}} \right)^{0.8} \left(\dfrac{Pr_{\mathrm{liq,off}}}{Pr_{\mathrm{liq,base}}} \right)^{0.3}$	$f_{\mathrm{h,sc}} = \left(\dfrac{\dfrac{0.4}{0.00027}}{\dfrac{0.61}{0.000313}} \right)^{0.8} \left(\dfrac{5.67}{6.20} \right)^{0.3}$	0.79	0.78	-

Parameter	Equation	Evaluated	EES Calc. Value	Hand Calc. Value	Units
Area factor	$f_{A,sh} = \left(\frac{\frac{\dot{Q}_{sh,off}}{\dot{Q}_{total,off}}}{\frac{\dot{Q}_{sh,base}}{\dot{Q}_{total,base}}} \right) f_{h,sh}$	$f_{A,sh} = \left(\frac{\frac{2.15}{57.97}}{\frac{27.9}{99.52}} \right) 0.78$	0.105	0.103	-
UA	$UA_{sc,off} = \left(\frac{1}{R_{sc,f} f_{h,sc} f_{A,sc}} + \frac{1}{R_{sc,a} f_{h,a} f_{A,sc}} \right)^{-1}$	$UA_{sc,off} = \left(\frac{1}{9.35(0.78)0.1} + \frac{1}{7.45(0.85)0.1} \right)^{-1}$	0.36	0.34	kW K^{-1}
PC Condenser – Air Side Heat Transfer Scaling (Subscripts "p,cond" omitted)					
Geometric C1 factor	$C_1 = \left(\frac{\theta}{90}\right)^{0.27} \left(\frac{F_p}{L_p}\right)^{-0.14} \left(\frac{F_l}{L_p}\right)^{-0.29} \left(\frac{T_d}{L_p}\right)^{-0.23} \left(\frac{L_l}{L_p}\right)^{0.68} \left(\frac{T_p}{L_p}\right)^{-0.28} \left(\frac{\delta_f}{L_p}\right)^{-0.05}$	Values omitted due to confidentiality	0.33	0.33	-
Baseline mass flux	$G_{base} = \frac{\dot{m}_{a,base}}{A_{face}}$	$G_{base} = \frac{11.1}{5.4}$	2.06	2.06	kg m^{-2} s^{-1}
Baseline louver pitch Reynolds	$Re_{base} = \frac{G_{base} L_p}{\mu_{amb,base}}$	$Re_{base} = \frac{2.06 L_p}{0.000018}$	160.2	160.6	-
Baseline Colburn Factor	$j_{base} = C_1 Re_{base}^{-0.49}$	$j_{base} = 0.33 \times 160.6^{-0.49}$	0.027	0.027	-
Baseline heat transfer coefficient	$h_{a,base} = \frac{j_{base} Cp_{amb,base} G_{base}}{Pr_{amb,base}^{2/3}}$	$h_{a,base} = \frac{0.027(1.006)2.06}{(0.71)^{2/3}}$	0.072	0.072	W m^{-2} K^{-1}
Off-design mass flux	$G_{off} = \frac{\dot{m}_{a,off}}{A_{face}}$	$G_{off} = \frac{16.38}{5.4}$	3.03	3.03	kg m^{-2} s^{-1}
Off-design louver pitch Reynolds	$Re_{off} = \frac{G_{off} L_p}{\mu_{exh,off}}$	$Re_{off} = \frac{3.03 L_p}{0.0000186}$	228	228	-
Off-design Colburn Factor	$j_{off} = C_1 Re_{off}^{-0.49}$	$j_{off} = 0.33 \times 228^{-0.49}$	0.023	0.023	-

Parameter	Equation	Evaluated	EES Calc. Value	Hand Calc. Value	Units
Off-design heat transfer coefficient	$h_{a,off} = \frac{j_{off} Cp_{exh,off} G_{off}}{Pr_{exh,off}^{2/3}}$	$h_{a,off} = \frac{0.023(1.006)3.03}{0.71^{2/3}}$	0.089	0.088	W m^{-2} K^{-1}
Heat transfer scaling factor	$f_{h,a} = \frac{h_{a,off}}{h_{a,base}}$	$f_{h,a} = \frac{0.088}{0.070}$	1.24	1.25	-
PC Condenser – Superheated Section Scaled *UA* (Subscripts "p,cond" omitted)					
Air side resistance	$R_{sh,a} = h_{a,base} A_a A_{per,sh,base}$	$R_{sh,a} = 0.07(281.5)0.021$	0.43	0.41	kW K^{-1}
Fluid side resistance	$UA_{sh,base} = \left(\frac{1}{R_{sh,f}} + \frac{1}{R_{sh,a}} \right)^{-1}$	$0.034 = \left(\frac{1}{R_{sh,f}} + \frac{1}{0.41} \right)^{-1}$	0.037	0.037	kW K^{-1}
Heat transfer factor	$f_{h,sh} = \left(\frac{\frac{\dot{m}_{p,off}}{\mu_{vap,off}}}{\frac{\dot{m}_{p,base}}{\mu_{vap,base}}} \right)^{0.8} \left(\frac{Pr_{vap,off}}{Pr_{vap,base}} \right)^{0.3}$	$f_{h,sh} = \left(\frac{\frac{0.4}{1.2\times10^{-5}}}{\frac{0.61}{1.1\times10^{-5}}} \right)^{0.8} \left(\frac{0.91}{0.91} \right)^{0.3}$	0.68	0.67	-
Area factor	$f_{A,sh} = \left(\frac{\frac{\dot{Q}_{sh,off}}{\dot{Q}_{total,off}}}{\frac{\dot{Q}_{sh,base}}{\dot{Q}_{total,base}}} \right) f_{h,sh}$	$f_{A,sh} = \left(\frac{\frac{6.86}{56.5}}{\frac{0.44}{89.5}} \right) 0.67$	16.8	16.5	-
UA	$UA_{sh,off} = \left(\frac{1}{R_{sh,f} f_{h,sh} f_{A,sh}} + \frac{1}{R_{sh,a} f_{h,a} f_{A,sh}} \right)^{-1}$	$UA_{sh,off} = \left(\frac{1}{0.037(0.67)16.5} + \frac{1}{0.41(1.25)16.5} \right)^{-1}$	0.40	0.39	kW K^{-1}
PC Condenser – Two-Phase Section Scaled *UA* (Subscripts "p,cond" omitted)					
Air side resistance	$R_{tp,a} = h_{a,base} A_a A_{per,tp,base}$	$R_{tp,a} = 0.071(281.5)0.91$	18.3	18.2	kW K^{-1}

Parameter	Equation	Evaluated	EES Calc. Value	Hand Calc. Value	Units
Fluid side resistance	$UA_{\text{tp,base}} = \left(\frac{1}{R_{\text{tp,f}}} + \frac{1}{R_{\text{tp,a}}} \right)^{-1}$	$9.88 = \left(\frac{1}{R_{\text{tp,f}}} + \frac{1}{18.2} \right)^{-1}$	21.5	21.6	kW K^{-1}
Baseline Martenelli parameter	$X_{\text{tt,base}} = \left(\frac{\rho_{\text{vap,base}}}{\rho_{\text{liq,base}}} \right)^{0.5} \left(\frac{\mu_{\text{liq,base}}}{\mu_{\text{vap,base}}} \right)^{0.1} \left(\frac{1-x}{x} \right)^{0.9}$	$X_{\text{tt,base}} = \left(\frac{6.97}{1410} \right)^{0.5} \left(\frac{0.00043}{1.1\times10^{-5}} \right)^{0.1} \left(\frac{1-0.5}{0.5} \right)^{0.9}$	0.10	0.10	-
Baseline Nusselt number	$Nu_{\text{base}} = \left(\frac{\dot{m}_{\text{p,base}}}{\mu_{\text{liq,base}}} \right)^{0.8} Pr_{\text{liq,base}}^{0.4} \left(1 + \frac{2.22}{X_{\text{tt,base}}^{0.89}} \right)$	$Nu_{\text{base}} = \left(\frac{0.61}{0.00043} \right)^{0.8} 7.26^{0.4} \left(1 + \frac{2.22}{0.1^{0.89}} \right)$	13109	13371	m$^{0.8}$
Off-design Martenelli parameter	$X_{\text{tt,off}} = \left(\frac{\rho_{\text{vap,off}}}{\rho_{\text{liq,off}}} \right)^{0.5} \left(\frac{\mu_{\text{liq,off}}}{\mu_{\text{vap,off}}} \right)^{0.1} \left(\frac{1-x}{x} \right)^{0.9}$	$X_{\text{tt,off}} = \left(\frac{10.12}{1372} \right)^{0.5} \left(\frac{0.00041}{1.2\times10^{-5}} \right)^{0.1} \left(\frac{1-0.5}{0.5} \right)^{0.9}$	0.12	0.12	-
Off-design Nusselt number	$Nu_{\text{off}} = \left(\frac{\dot{m}_{\text{p,off}}}{\mu_{\text{liq,off}}} \right)^{0.8} Pr_{\text{liq,off}}^{0.4} \left(1 + \frac{2.22}{X_{\text{tt,off}}^{0.89}} \right)$	$Nu_{\text{off}} = \left(\frac{0.4}{0.00041} \right)^{0.8} 7.3^{0.4} \left(1 + \frac{2.22}{0.12^{0.89}} \right)$	8308.7	8537.9	m$^{0.8}$
Heat transfer factor	$f_{\text{h,tp}} = \frac{Nu_{\text{off}} k_{\text{vap,off}}}{Nu_{\text{base}} k_{\text{vap,base}}}$	$f_{\text{h,tp}} = \frac{8537.9(0.013)}{13371(0.012)}$	0.69	0.69	-
Area factor	$f_{\text{A,tp}} = \left(\frac{\frac{\dot{Q}_{\text{tp,off}}}{\dot{Q}_{\text{total,off}}}}{\frac{\dot{Q}_{\text{tp,base}}}{\dot{Q}_{\text{total,base}}}} \right) f_{\text{h,tp}}$	$f_{\text{A,tp}} = \left(\frac{\frac{49.02}{56.51}}{\frac{86.5}{89.5}} \right) 0.69$	0.62	0.62	-
UA	$UA_{\text{tp,off}} = \left(\frac{1}{R_{\text{tp,f}} f_{\text{h,tp}} f_{\text{A,tp}}} + \frac{1}{R_{\text{tp,a}} f_{\text{h,a}} f_{\text{A,tp}}} \right)^{-1}$	$UA_{\text{tp,off}} = \left(\frac{1}{21.6(0.69)0.62} + \frac{1}{18.2(1.25)0.62} \right)^{-1}$	5.58	5.59	kW K^{-1}
PC Condenser – Subcooled Section Scaled *UA* (Subscripts "p,cond" omitted)					
Baseline air side resistance	$R_{\text{sc,a}} = h_{\text{a,base}} A_{\text{a}} A_{\text{per,sc,base}}$	$R_{\text{sc,a}} = 0.07(281.5)0.07$	1.41	1.38	kW K^{-1}

Parameter	Equation	Evaluated	EES Calc. Value	Hand Calc. Value	Units
Fluid side resistance	$UA_{sc,base} = \left(\frac{1}{R_{sc,f}} + \frac{1}{R_{sc,a}} \right)^{-1}$	$0.08 = \left(\frac{1}{R_{sc,f}} + \frac{1}{1.38} \right)^{-1}$	0.089	0.085	kW K^{-1}
Heat transfer factor	$f_{h,sc} = \left(\frac{\frac{\dot{m}_{p,off}}{\mu_{liq,off}}}{\frac{\dot{m}_{p,base}}{\mu_{liq,base}}} \right)^{0.8} \left(\frac{Pr_{liq,off}}{Pr_{liq,base}} \right)^{0.3}$	$f_{h,sc} = \left(\frac{\frac{0.4}{0.00041}}{\frac{0.61}{0.00043}} \right)^{0.8} \left(\frac{7.3}{7.26} \right)^{0.3}$	0.74	0.74	-
Area factor	$f_{A,sc} = \left(\frac{\frac{\dot{Q}_{sc,off}}{\dot{Q}_{total,off}}}{\frac{\dot{Q}_{sc,base}}{\dot{Q}_{total,base}}} \right) f_{h,sc}$	$f_{A,sh} = \left(\frac{\frac{0.629}{56.51}}{\frac{0.65}{89.5}} \right) 0.74$	1.13	1.13	-
UA	$UA_{sc,off} = \left(\frac{1}{R_{sc,f} f_{h,sc} f_{A,sc}} + \frac{1}{R_{sc,a} f_{h,a} f_{A,sc}} \right)^{-1}$	$UA_{sc,off} = \left(\frac{1}{0.085(0.74)1.13} + \frac{1}{1.38(1.25)1.13} \right)^{-1}$	0.07	0.07	kW K^{-1}
PC Recuperator – Vapor Side Heat Transfer Scaling (Subscripts "p,recup" omitted)					
Hydraulic diameter	$D_{hyd} = \frac{4\left(2F_p - \delta_f\right)F_h}{\left(2F_h + 2\left(2F_p - \delta_f\right)\right)}$	Values omitted due to confidentiality	0.002	0.002	m
Reynolds number	$Re_{vap} = \frac{\dot{m}_{p,base}\left(\frac{D_{hyd}}{A_{cross}}\right)}{\mu_{vap,base}}$	$Re_{vap} = \frac{0.61\left(\frac{0.002}{0.023}\right)}{0.000013}$	4706	4131	-
Friction factor	$f = \left(0.79\ln\left(Re_{vap}\right) - 1.64\right)^{-2}$	$f = \left(0.79\ln\left(4131\right) - 1.64\right)^{-2}$	0.04	0.04	-

Parameter	Equation	Evaluated	EES Calc. Value	Hand Calc. Value	Units
Nusselt number	$Nu_{vap} = \frac{\left(\frac{f}{8}\left(Re_{vap} - 1000\right) Pr_{vap,base} 1000\right)}{\left(1 + 12.7\left(\frac{f}{8}\right)^{0.5}\left(Pr_{vap,base}^{2/3} - 1\right)\right)}$	$Nu_{vap} = \frac{\left(\frac{0.04}{8}(4131-1000)(0.00089)1000\right)}{\left(1 + 12.7\left(\frac{0.04}{8}\right)^{0.5}\left((0.00089)^{2/3} - 1\right)\right)}$	138	125	-
Vapor side heat transfer coefficient	$h_{vap} = \frac{Nu_{vap} k_{vap,base}}{D_{hyd}}$	$h_{vap} = \frac{125(0.014)}{0.002}$	0.87	0.87	kW m^{-2} K^{-1}
Vapor side resistance	$R_{vap,base} = h_{vap,base} A_{vap}$	$R_{vap,base} = 0.87(17.3)$	15.0	15.1	kW K^{-1}
Baseline resistances	$UA_{base} = \left(\frac{1}{R_{vap}} + \frac{1}{R_{liq}}\right)^{-1}$	$2.53 = \left(\frac{1}{15.1} + \frac{1}{R_{liq}}\right)^{-1}$	3.04	3.04	kW K^{-1}
Vapor side heat transfer factor	$f_{h,vap} = \left(\frac{\frac{\dot{m}_{p,off}}{\mu_{vap,off}}}{\frac{\dot{m}_{p,base}}{\mu_{vap,base}}}\right)^{0.8}\left(\frac{Pr_{vap,off}}{Pr_{vap,base}}\right)^{0.33}$	$f_{h,vap} = \left(\frac{\frac{0.4}{1.3\times10^{-5}}}{\frac{0.61}{1.3\times10^{-5}}}\right)^{0.8}\left(\frac{0.00089}{0.00089}\right)^{0.33}$	0.69	0.70	-
Liquid side heat transfer factor	$f_{h,liq} = \left(\frac{\frac{\dot{m}_{p,off}}{\mu_{liq,off}}}{\frac{\dot{m}_{p,base}}{\mu_{liq,base}}}\right)^{0.8}\left(\frac{Pr_{liq,off}}{Pr_{liq,base}}\right)^{0.33}$	$f_{h,liq} = \left(\frac{\frac{0.4}{0.00041}}{\frac{0.61}{0.00049}}\right)^{0.8}\left(\frac{0.0073}{0.0082}\right)^{0.33}$	0.80	0.79	-
Area factor	$f_A = \frac{\dot{Q}_{off}}{\dot{Q}_{base}}$	$f_A = \frac{16.48}{26.35}$	0.62	0.63	-
UA	$UA_{off} = \left(\frac{1}{R_{vap} f_{h,vap} f_A} + \frac{1}{R_{liq} f_{h,liq} f_A}\right)^{-1}$	$UA_{off} = \left(\frac{1}{15.1(0.70)0.63} + \frac{1}{3.04(0.79)0.63}\right)^{-1}$	1.23	1.23	kW K^{-1}

Parameter	Equation	Evaluated	EES Calc. Value	Hand Calc. Value	Units
CC Fluid Factor					
R134a factor	$f_{\text{r134a}} = \frac{\dot{m}_{\text{c,off}}}{\dot{m}_{\text{c,r134a,base}}}$	$f_{\text{r134a}} = \frac{0.74}{1.4}$	0.53	0.53	-
R152a factor	$f_{\text{r152a}} = \frac{\dot{m}_{\text{c,off}}}{\dot{m}_{\text{c,r152a,base}}}$	$f_{\text{r152a}} = \frac{0.74}{0.92}$	0.80	0.80	-
Fluid factor	$f_{\text{f}} = \frac{f_{\text{r134a}}}{f_{\text{r152a}}}$	$f_{\text{f}} = \frac{0.53}{0.80}$	0.66	0.66	-
CC Condenser – Air Side Heat Transfer Scaling (Subscripts "c,cond" omitted)					
Geometric C1 factor	$C_1 = \left(\frac{\theta}{90}\right)^{0.27}\left(\frac{F_{\text{p}}}{L_{\text{p}}}\right)^{-0.14}\left(\frac{F_{\text{l}}}{L_{\text{p}}}\right)^{-0.29}\left(\frac{T_{\text{d}}}{L_{\text{p}}}\right)^{-0.23}\left(\frac{L_{\text{l}}}{L_{\text{p}}}\right)^{0.68}\left(\frac{T_{\text{p}}}{L_{\text{p}}}\right)^{-0.28}\left(\frac{\delta_{\text{f}}}{L_{\text{p}}}\right)^{-0.05}$	Values omitted due to confidentiality	0.35	0.35	-
Baseline mass flux	$G_{\text{base}} = \frac{\dot{m}_{\text{a,base}}}{A_{\text{face}}}$	$G_{\text{base}} = \frac{38.54}{14.19}$	2.72	2.72	kg m^{-2} s^{-1}
Baseline louver pitch Reynolds	$Re_{\text{base}} = \frac{G_{\text{base}} L_{\text{p}}}{\mu_{\text{amb,base}}}$	$Re_{\text{base}} = \frac{2.72 L_{\text{p}}}{1.8\times10^{-5}}$	211.7	211.6	-
Baseline Colburn Factor	$j_{\text{base}} = C_1 \, \text{Re}_{\text{base}}^{-0.49}$	$j_{\text{base}} = 0.35\times211.6^{-0.49}$	0.025	0.025	-
Baseline heat transfer coefficient	$h_{\text{a,base}} = \frac{j_{\text{base}} Cp_{\text{amb,base}} G_{\text{base}}}{Pr_{\text{amb,base}}^{2/3}}$	$h_{\text{a,base}} = \frac{0.025(1.006)2.72}{0.71^{2/3}}$	0.086	0.086	W m^{-2} K^{-1}
Off-design mass flux	$G_{\text{off}} = \frac{\dot{m}_{\text{a,off}}}{A_{\text{face}}}$	$G_{\text{off}} = \frac{51.86}{14.19}$	3.66	3.65	kg m^{-2} s^{-1}
Off-design louver pitch Reynolds	$Re_{\text{off}} = \frac{G_{\text{off}} L_{\text{p}}}{\mu_{\text{exh,off}}}$	$Re_{\text{off}} = \frac{3.65 L_{\text{p}}}{1.9\times10^{-5}}$	275	269	-

Parameter	Equation	Evaluated	EES Calc. Value	Hand Calc. Value	Units
Off-design Colburn Factor	$j_{\text{off}} = C_1 \, \text{Re}_{\text{off}}^{-0.49}$	$j_{\text{off}} = 0.35 \times 269^{-0.49}$	0.022	0.023	-
Off-design heat transfer coefficient	$h_{\text{a,off}} = \frac{j_{\text{off}} Cp_{\text{exh,off}} G_{\text{off}}}{Pr_{\text{exh,off}}^{2/3}}$	$h_{\text{a,off}} = \frac{0.023(1.006)3.65}{0.71^{2/3}}$	0.10	0.10	W m^{-2} K^{-1}
Heat transfer scaling factor	$f_{\text{h,a}} = \frac{h_{\text{a,off}}}{h_{\text{a,base}}}$	$f_{\text{h,a}} = \frac{0.10}{0.086}$	1.19	1.16	-
CC Condenser – Superheated Section Scaled *UA* (Subscripts "c,cond" omitted)					
Air side resistance	$R_{\text{sh,a}} = h_{\text{a,base}} A_{\text{a}} A_{\text{per,sh,base}}$	$R_{\text{sh,a}} = 0.098(1215)0.024$	2.9	2.86	kW K^{-1}
Fluid side resistance	$UA_{\text{sh,base}} = \left(\frac{1}{R_{\text{sh,f}}} + \frac{1}{R_{\text{sh,a}}} \right)^{-1}$	$1.34 = \left(\frac{1}{R_{\text{sh,f}}} + \frac{1}{2.86} \right)^{-1}$	2.51	2.52	kW K^{-1}
Heat transfer factor	$f_{\text{h,sh}} = \left(\frac{\frac{\dot{m}_{\text{c,off}}}{\mu_{\text{vap,off}}}}{\frac{\dot{m}_{\text{c,base}}}{\mu_{\text{vap,base}}}} \right)^{0.8} \left(\frac{Pr_{\text{vap,off}}}{Pr_{\text{vap,base}}} \right)^{0.3}$	$f_{\text{h,sh}} = \left(\frac{0.74}{\frac{1.3 \times 10^{-5}}{1.1 \times 10^{-5}}} \right)^{0.8} \left(\frac{0.00087}{0.00092} \right)^{0.3}$	0.70	0.72	-
Area factor	$f_{\text{A,sh}} = \left(\frac{\dot{Q}_{\text{sh,off}}}{\frac{\dot{Q}_{\text{total,off}}}{\frac{\dot{Q}_{\text{sh,base}}}{\dot{Q}_{\text{total,base}}}}} \right) f_{\text{h,sh}}$	$f_{\text{A,sh}} = \left(\frac{15.98}{\frac{149.8}{\frac{8.83}{267.5}}} \right) 0.72$	2.26	2.32	-
UA	$UA_{\text{sh,off}} = \left(\frac{1}{R_{\text{sh,f}} f_{\text{h,sh}} f_{\text{A,sh}} f_{\text{f}}} + \frac{1}{R_{\text{sh,a}} f_{\text{h,a}} f_{\text{A,sh}} f_{\text{f}}} \right)^{-1}$	$UA_{\text{sh,off}} = \left(\frac{1}{2.9(0.72)2.32(0.66)} + \frac{1}{2.51(1.16)2.32(0.66)} \right)^{-1}$	1.88	1.86	kW K^{-1}

Parameter	Equation	Evaluated	EES Calc. Value	Hand Calc. Value	Units
CC Condenser – Two-Phase Section Scaled *UA* (Subscripts "c,cond" omitted)					
Air side resistance	$R_{tp,a} = h_{a,base} A_a A_{per,tp,base}$	$R_{tp,a} = 0.086(1215)0.87$	91.03	90.9	kW K^{-1}
Fluid side resistance	$UA_{tp,base} = \left(\frac{1}{R_{tp,f}} + \frac{1}{R_{tp,a}} \right)^{-1}$	$79.4 = \left(\frac{1}{R_{tp,f}} + \frac{1}{90.9} \right)^{-1}$	621.4	628.9	kW K^{-1}
Baseline Martenelli parameter	$X_{tt,base} = \left(\frac{\rho_{vap,base}}{\rho_{liq,base}} \right)^{0.5} \left(\frac{\mu_{liq,base}}{\mu_{vap,base}} \right)^{0.1} \left(\frac{1-x}{x} \right)^{0.9}$	$X_{tt,base} = \left(\frac{16.93}{904.8} \right)^{0.5} \left(\frac{0.00017}{1.1 \times 10^{-5}} \right)^{0.1} \left(\frac{1-0.5}{0.5} \right)^{0.9}$	0.18	0.18	-
Baseline Nusselt number	$Nu_{base} = \left(\frac{\dot{m}_{c,base}}{\mu_{liq,base}} \right)^{0.8} Pr_{liq,base}^{0.4} \left(1 + \frac{2.22}{X_{tt,base}^{0.89}} \right)$	$Nu_{base} = \left(\frac{0.92}{0.00017} \right)^{0.8} 2.96^{0.4} \left(1 + \frac{2.22}{0.18^{0.89}} \right)$	16930	16787	m$^{0.8}$
Off-design Martenelli parameter	$X_{tt,off} = \left(\frac{\rho_{vap,off}}{\rho_{liq,off}} \right)^{0.5} \left(\frac{\mu_{liq,off}}{\mu_{vap,off}} \right)^{0.1} \left(\frac{1-x}{x} \right)^{0.9}$	$X_{tt,off} = \left(\frac{40}{1191} \right)^{0.5} \left(\frac{0.00018}{1.3 \times 10^{-5}} \right)^{0.1} \left(\frac{1-0.5}{0.5} \right)^{0.9}$	0.24	0.24	-
Off-design Nusselt number	$Nu_{off} = \left(\frac{\dot{m}_{c,off}}{\mu_{liq,off}} \right)^{0.8} Pr_{liq,off}^{0.4} \left(1 + \frac{2.22}{X_{tt,off}^{0.89}} \right)$	$Nu_{off} = \left(\frac{0.74}{0.00018} \right)^{0.8} 3.27^{0.4} \left(1 + \frac{2.22}{0.24^{0.89}} \right)$	10965	11130	m$^{0.8}$
Heat transfer factor	$f_{h,tp} = \frac{Nu_{off}}{Nu_{base}}$	$f_{h,tp} = \frac{11130}{16787}$	0.69	0.66	-
Area factor	$f_{A,tp} = \left(\frac{\frac{\dot{Q}_{tp,off}}{\dot{Q}_{total,off}}}{\frac{\dot{Q}_{tp,base}}{\dot{Q}_{total,base}}} \right) f_{h,tp}$	$f_{A,tp} = \left(\frac{\frac{128.7}{149.8}}{\frac{257.8}{267.5}} \right) 0.66$	0.61	0.59	-
UA	$UA_{tp,off} = \left(\frac{1}{R_{tp,f} f_{h,tp} f_{A,tp} f_f} + \frac{1}{R_{tp,a} f_{h,a} f_{A,tp} f_f} \right)^{-1}$	$UA_{tp,off} = \left(\frac{1}{628.9(0.66)0.59(0.66)} + \frac{1}{90.9(1.16)0.59(0.66)} \right)^{-1}$	34.8	32.7	kW K^{-1}

Parameter	Equation	Evaluated	EES Calc. Value	Hand Calc. Value	Units
CC Condenser – Sub-cooled Section Scaled *UA* (Subscripts "c,cond" omitted)					
Baseline air side resistance	$R_{sc,a} = h_{a,base} A_a A_{per,sc,base}$	$R_{sc,a} = 0.098(1215)0.048$	5.02	5.6	kW K^{-1}
Fluid side resistance	$UA_{sc,base} = \left(\frac{1}{R_{sc,f}} + \frac{1}{R_{sc,a}} \right)^{-1}$	$0.11 = \left(\frac{1}{R_{sc,f}} + \frac{1}{5.6} \right)^{-1}$	0.11	0.11	kW K^{-1}
Heat transfer factor	$f_{h,sc} = \left(\frac{\frac{\dot{m}_{c,off}}{\mu_{liq,off}}}{\frac{\dot{m}_{c,base}}{\mu_{liq,base}}} \right)^{0.8} \left(\frac{Pr_{liq,off}}{Pr_{liq,base}} \right)^{0.3}$	$f_{h,sc} = \left(\frac{\frac{0.74}{0.000184}}{\frac{0.92}{0.00017}} \right)^{0.8} \left(\frac{3.27}{2.96} \right)^{0.3}$	0.80	0.81	-
Area factor	$f_{A,sc} = \left(\frac{\frac{\dot{Q}_{sc,off}}{\dot{Q}_{total,off}}}{\frac{\dot{Q}_{sc,base}}{\dot{Q}_{total,base}}} \right) f_{h,sc}$	$f_{A,sc} = \left(\frac{\frac{5.16}{149.8}}{\frac{0.84}{257.8}} \right) 0.81$	8.78	8.56	-
UA	$UA_{sc,off} = \left(\frac{1}{R_{sc,f} f_{h,sc} f_{A,sc} f_f} + \frac{1}{R_{sc,a} f_{h,a} f_{A,sc} f_f} \right)^{-1}$	$UA_{sc,off} = \left(\frac{1}{0.11(0.81)8.56(0.66)} + \frac{1}{5.6(1.16)8.56(0.66)} \right)^{-1}$	0.50	0.50	kW K^{-1}
CC Evaporator – Glycol Side Heat Transfer Factor (Subscripts "c,evap" omitted)					
Heat transfer factor	$f_{h,g} = \left(\frac{\dot{m}_{g,off}}{\dot{m}_{g,base}} \right)^{0.6}$	$f_{h,g} = \left(\frac{2.67}{52.1} \right)^{0.6}$	0.17	0.17	-
CC Evaporator – Glycol Side Heat Transfer Scaling (Subscripts "p,recup" omitted)					
Hydraulic diameter	$D_{hyd} = \frac{4(2F_p - \delta_f)F_h}{(2F_h + 2(2F_p - \delta_f))}$	Values omitted due to confidentiality	0.0019	0.0019	m

Parameter	Equation	Evaluated	EES Calc. Value	Hand Calc. Value	Units
Reynolds number	$Re_g = \frac{\dot{m}_{g,base}\left(\frac{D_{hyd}}{A_{cross}}\right)}{\mu_{g,base}}$	$Re_g = \frac{52.1\left(\frac{0.0019}{0.15}\right)}{0.0033}$	197.8	200	-
Nusselt number	Laminar flow table	Laminar flow table for a/b=4.0	5.33	5.33	-
Glycol side heat transfer coefficient	$h_g = \frac{Nu_g k_{g,base}}{D_{hyd}}$	$h_g = \frac{5.33(0.0004)}{0.0019}$	1.33	1.33	kW m^{-2} K^{-1}
CC Evaporator – Two-Phase Section Scaled UA (Subscripts "c,evap" omitted)					
Baseline glycol side resistance	$R_{tp,g} = h_g A_{g,total} A_{per,tp}$	$R_{tp,g} = 1.38(91.8)(0.98)$	119.4	119.6	kW K^{-1}
Baseline resistances	$UA_{tp,base} = \left(\frac{1}{R_{tp,f}} + \frac{1}{R_{tp,g}}\right)^{-1}$	$105.3 = \left(\frac{1}{R_{tp,f}} + \frac{1}{126.7}\right)^{-1}$	890.9	880.7	kW K^{-1}
Baseline Froude number	$Fr_{base} = \frac{\dot{m}^2_{c,base}}{\rho_{liq,base} g}$	$Fr_{base} = \frac{0.92^2}{923.7(9.81)}$	9.3E-5	9.3E-5	-
Baseline Boiling number	$Bo_{base} = \frac{\dot{Q}_{tp,base}}{\dot{m}_{c,base} h_{fg,base}}$	$Bo_{base} = \frac{248.2}{0.92(290.1)}$	0.93	0.93	-
Baseline liquid heat transfer coefficient	$h_{liq,base} = \left(\frac{\dot{m}_{c,base}}{\mu_{liq,base}}\right)^{0.8} Pr_{liq,base}^{0.4} k_{liq,base}$	$h_{liq,base} = \left(\frac{0.92}{0.00018}\right)^{0.8} 0.003^{0.4} 0.11$	9.55	9.98	W m$^{-0.2}$ K^{-1}
Baseline H_1 factor	$H_{1,base} = 1 + 3000 Bo_{base}^{0.86} Fr_{base}^{(0.1-2Fr_{base})}$	$H_{1,base} = 1 + 3000\left(0.93^{0.86}\right)\left(9.3\times10^{-5}\right)^{\left(0.1-2\left(9.3\times10^{-5}\right)\right)}$	1117	1117	-
Baseline H_2 factor	$H_{2,base} = 1.12 Fr_{base}^{0.5}\left[\frac{x}{1-x}\right]^{0.75}\left[\frac{\rho_{l,base}}{\rho_{g,base}}\right]^{0.41}$	$H_{2,base} = 1.12\left(9.3\times10^{-5}\right)^{0.5}\left[\frac{0.5}{1-0.5}\right]^{0.75}\left[\frac{923.7}{13.7}\right]^{0.41}$	0.06	0.06	-

Parameter	Equation	Evaluated	EES Calc. Value	Hand Calc. Value	Units
Baseline two-phase heat transfer coefficient	$h_{\mathrm{TP,base}} = \left(H_{1,\mathrm{base}} + H_{2,\mathrm{base}}\right) h_{\mathrm{liq,base}}$	$h_{\mathrm{TP,base}} = \left(1117 + 0.06\right) 9.98$	10670	11148	W m$^{-0.2}$ K^{-1}
Off-design Froude number	$Fr_{\mathrm{off}} = \dfrac{\dot{m}_{\mathrm{p,off}}^2}{\rho_{\mathrm{liq,off}} g}$	$Fr_{\mathrm{off}} = \dfrac{0.74^2}{1210\left(9.81\right)}$	4.6E-5	4.6E-5	-
Off-design Boiling number	$Bo_{\mathrm{off}} = \dfrac{\dot{Q}_{\mathrm{tp,off}}}{\dot{m}_{\mathrm{c,off}} h_{\mathrm{fg,off}}}$	$Bo_{\mathrm{off}} = \dfrac{128.7}{0.74\left(172.4\right)}$	1.0	1.0	-
Off-design liquid heat transfer coefficient	$h_{\mathrm{liq,off}} = \left(\dfrac{\dot{m}_{\mathrm{c,off}}}{\mu_{\mathrm{liq,off}}}\right)^{0.8} \mathrm{Pr}_{\mathrm{liq,off}}{}^{0.4} k_{\mathrm{liq,off}}$	$h_{\mathrm{liq,off}} = \left(\dfrac{0.74}{0.0002}\right)^{0.8} 0.0033^{0.4} 0.084$	6.09	6.09	W m$^{-0.2}$ K^{-1}
Off-design H_1 factor	$H_{1,\mathrm{off}} = 1 + 3000 Bo_{\mathrm{off}}^{0.86} Fr_{\mathrm{off}}^{\left(0.1-2Fr_{\mathrm{off}}\right)}$	$H_{1,\mathrm{off}} = 1 + 3000\left(1\right)^{0.86} \left(4.6\times10^{-5}\right)^{\left(0.1-2\left(4.6\times10^{-5}\right)\right)}$	1117	1107	-
Off-design H_2 factor	$H_{2,\mathrm{off}} = 1.12 Fr_{\mathrm{off}}^{0.5} \left[\dfrac{x}{1-x}\right]^{0.75} \left[\dfrac{\rho_{\mathrm{l,off}}}{\rho_{\mathrm{g,off}}}\right]^{0.41}$	$H_{2,\mathrm{off}} = 1.12\left(4.6\times10^{-5}\right)^{0.5} \left[\dfrac{0.5}{1-0.5}\right]^{0.75} \left[\dfrac{1210}{34.6}\right]^{0.41}$	0.033	0.033	-
Off-design two-phase heat transfer coefficient	$h_{\mathrm{TP,off}} = \left(H_{1,\mathrm{off}} + H_{2,\mathrm{off}}\right) h_{\mathrm{liq,off}}$	$h_{\mathrm{TP,off}} = \left(1107 + 0.033\right) 6.09$	6922	6963	W m$^{-0.2}$ K^{-1}
Heat transfer factor	$f_{\mathrm{h,tp}} = \dfrac{h_{\mathrm{TP,off}}}{h_{\mathrm{TP,base}}}$	$f_{\mathrm{h,tp}} = \dfrac{6922}{11148}$	0.649	0.62	-
Area factor	$f_{\mathrm{A,tp}} = \left(\dfrac{\dfrac{\dot{Q}_{\mathrm{tp,off}}}{\dot{Q}_{\mathrm{total,off}}}}{\dfrac{\dot{Q}_{\mathrm{tp,base}}}{\dot{Q}_{\mathrm{total,base}}}}\right) f_{\mathrm{h,tp}}$	$f_{\mathrm{A,tp}} = \left(\dfrac{\dfrac{128.7}{142.9}}{\dfrac{248.2}{250.8}}\right) 0.62$	0.59	0.56	-

Parameter	Equation	Evaluated	EES Calc. Value	Hand Calc. Value	Units
UA	$UA_{\text{tp,off}} = \left(\frac{1}{R_{\text{tp,f}} f_{\text{h,tp}} f_{\text{A,tp}} f_{\text{f}}} + \frac{1}{R_{\text{tp,a}} f_{\text{h,g}} f_{\text{A,tp}} f_{\text{f}}} \right)^{-1}$	$UA_{\text{tp,off}} = \left(\frac{1}{880.7(0.62)0.56(0.66)} + \frac{1}{119.6(0.17)0.56(0.66)} \right)^{-1}$	7.54	7.54	kW K^{-1}
CC Evaporator –Superheated Section Scaled UA (Subscripts "c,evap" omitted)					
Baseline resistances	$R_{\text{sh,g}} = h_{\text{g}} A_{\text{g,total}} A_{\text{per,sh}}$	$R_{\text{sh,g}} = 1.38(91.8)(0.02)$	2.65	2.53	kW K^{-1}
Baseline resistances	$UA_{\text{sh,base}} = \left(\frac{1}{R_{\text{sh,f}}} + \frac{1}{R_{\text{sh,g}}} \right)^{-1}$	$1.53 = \left(\frac{1}{R_{\text{sh,f}}} + \frac{1}{2.53} \right)^{-1}$	3.63	3.87	kW K^{-1}
Heat transfer factor	$f_{\text{h,sh}} = \left(\frac{\frac{\dot{m}_{\text{c,off}}}{\mu_{\text{vap,off}}}}{\frac{\dot{m}_{\text{c,base}}}{\mu_{\text{vap,base}}}} \right)^{0.8} \left(\frac{Pr_{\text{vap,off}}}{Pr_{\text{vap,base}}} \right)^{0.3}$	$f_{\text{h,sh}} = \left(\frac{\frac{0.74}{1.3\times10^{-5}}}{\frac{0.92}{1.0\times10^{-5}}} \right)^{0.8} \left(\frac{0.0008}{0.00069} \right)^{0.3}$	0.72	0.71	-
Area factor	$f_{\text{A,sh}} = \left(\frac{\frac{\dot{Q}_{\text{sh,off}}}{\dot{Q}_{\text{total,off}}}}{\frac{\dot{Q}_{\text{sh,base}}}{\dot{Q}_{\text{total,base}}}} \right) f_{\text{h,sh}}$	$f_{\text{A,sh}} = \left(\frac{\frac{14.21}{142.9}}{\frac{2.65}{250.8}} \right) 0.71$	6.78	6.68	-
UA	$UA_{\text{sh,off}} = \left(\frac{1}{R_{\text{sh,f}} f_{\text{h,sh}} f_{\text{A,sh}} f_{\text{f}}} + \frac{1}{R_{\text{sh,a}} f_{\text{h,g}} f_{\text{A,sh}} f_{\text{f}}} \right)^{-1}$	$UA_{\text{sh,off}} = \left(\frac{1}{3.06(0.71)6.68(0.66)} + \frac{1}{3.06(0.17)6.68(0.66)} \right)^{-1}$	1.7	1.8	kW K^{-1}
Summation of UA's					
PC Boiler SC+TP	$UA_{\text{p,b,sc+tp,off}} = UA_{\text{p,b,sc,off}} + UA_{\text{p,b,tp,off}}$	$UA_{\text{p,b,sc+tp,off}} = 0.34 + 2.79$	3.26	3.13	kW K^{-1}
PC Condenser TP + SH	$UA_{\text{p,cond,tp+sh,off}} = UA_{\text{p,cond,tp,off}} + UA_{\text{p,cond,sh,off}}$	$UA_{\text{p,cond,tp+sh,off}} = 5.59 + 0.39$	5.99	5.98	kW K^{-1}
CC Condenser TP + SH	$UA_{\text{c,cond,tp+sh,off}} = UA_{\text{c,cond,tp,off}} + UA_{\text{c,cond,sh,off}}$	$UA_{\text{c,cond,tp+sh,off}} = 32.7 + 1.86$	36.7	34.6	kW K^{-1}

Table A-8. Hand calculations to support EES evaluation of thermodynamic off-design performance calculations.

Parameter	Equation	Evaluated	EES Calc. Value	Hand Calc. Value	Units
Cross-Flow Heat Exchanger Areas					
PC Boiler SH area percent	$A_{\text{per,p,b,sh,off}} = f_{\text{A,p,b,sh}} A_{\text{per,p,b,sh,base}}$	$A_{\text{per,p,b,sh,off}} = 1.57(0.36)$	57.2	56.6	%
PC Boiler TP area percent	$A_{\text{per,p,b,tp,off}} = f_{\text{A,p,b,tp}} A_{\text{per,p,b,tp,base}}$	$A_{\text{per,p,b,tp,off}} = 0.848(0.486)$	41.2	41.2	%
PC Boiler SC area percent	$A_{\text{per,p,b,sc,off}} = f_{\text{A,p,b,sc}} A_{\text{per,p,b,sc,base}}$	$A_{\text{per,p,b,sc,off}} = 0.10(0.15)$	1.6	1.5	%
PC Condenser SH area percent	$A_{\text{per,p,cond,sh,off}} = f_{\text{A,p,cond,sh}} A_{\text{per,p,cond,sh,base}}$	$A_{\text{per,p,cond,sh,off}} = 16.8(0.02)$	36	33.6	%
PC Condenser TP area percent	$A_{\text{per,p,cond,tp,off}} = f_{\text{A,p,cond,tp}} A_{\text{per,p,cond,tp,base}}$	$A_{\text{per,p,cond,tp,off}} = 0.62(0.91)$	56	56	%
PC Condenser SC area percent	$A_{\text{per,p,cond,sc,off}} = f_{\text{A,p,cond,sc}} A_{\text{per,p,cond,sc,base}}$	$A_{\text{per,p,cond,sc,off}} = 1.14(0.07)$	8	8	%
CC Condenser SH area percent	$A_{\text{per,c,cond,sh,off}} = f_{\text{A,c,cond,sh}} f_{\text{f}} A_{\text{per,c,cond,sh,base}}$	$A_{\text{per,c,cond,sh,off}} = 2.25(0.66)0.024$	3.5	3.6	%
CC Condenser TP area percent	$A_{\text{per,c,cond,tp,off}} = f_{\text{A,c,cond,tp}} f_{\text{f}} A_{\text{per,c,cond,tp,base}}$	$A_{\text{per,c,cond,tp,off}} = 0.61(0.66)0.87$	35.1	35.2	%
CC Condenser SC area percent	$A_{\text{per,c,cond,sc,off}} = f_{\text{A,c,cond,sc}} f_{\text{f}} A_{\text{per,c,cond,sc,base}}$	$A_{\text{per,c,cond,sc,off}} = 8.81(0.66)0.11$	61.4	63.9	%
Cooling Cycle State Points					
CC heat duty	$\dot{Q}_{\text{c,evap}} = \dot{m}_{\text{c}} \left(h_{\text{c,3}} - h_{\text{c,1}} \right)$	$\dot{Q}_{\text{c,evap}} = 0.74(434 - 240.8)$	142.9	142.9	kW
CC evaporator TP heat duty	$\dot{Q}_{\text{c,evap,tp}} = \dot{m}_{\text{c}} \left(h_{\text{c,2}} - h_{\text{c,1}} \right)$	$\dot{Q}_{\text{c,evap,tp}} = 0.74(414.8 - 240.8)$	128.7	128.8	kW
CC evaporator SH heat duty	$\dot{Q}_{\text{c,evap,sh}} = \dot{m}_{\text{c}} \left(h_{\text{c,3}} - h_{\text{c,2}} \right)$	$\dot{Q}_{\text{c,evap,sh}} = 0.74(434 - 414.8)$	14.21	14.2	kW
Compressor outlet enthalpy	$\eta_{\text{c,comp}} = \dfrac{\left(h_{\text{c,s,5}} - h_{\text{c,4}} \right)}{\left(h_{\text{c,5}} - h_{\text{c,4}} \right)}$	$0.78 = \dfrac{(438.4 - 434)}{\left(h_{\text{c,5}} - 434 \right)}$	439.4	439.6	kJ kg^{-1}

Parameter	Equation	Evaluated	EES Calc. Value	Hand Calc. Value	Units
Compressor work	$\dot{W}_{c,comp} = \dot{m}_c \left(h_{c,5} - h_{c,4} \right)$	$\dot{W}_{c,comp} = 0.74\left(439.4 - 434 \right)$	4.03	4.0	kg s^{-1}
CC condenser heat duty	$\dot{Q}_{c,cond} = \dot{m}_c \left(h_{c,6} - h_{c,9} \right)$	$\dot{Q}_{c,cond} = 0.74\left(439.4 - 240.8 \right)$	147	147	kW
CC condenser SC heat duty	$\dot{Q}_{c,cond,sc} = \dot{m}_c \left(h_{c,8} - h_{c,9} \right)$	$\dot{Q}_{c,cond,sc} = 0.74\left(250.9 - 240.8 \right)$	5.06	7.5	kW
CC condenser TP heat duty	$\dot{Q}_{c,cond,tp} = \dot{m}_c \left(h_{c,7} - h_{c,8} \right)$	$\dot{Q}_{c,cond,tp} = 0.74\left(417.8 - 250.9 \right)$	125.9	123.5	kW
CC condenser SH heat duty	$\dot{Q}_{c,cond,sh} = \dot{m}_c \left(h_{c,6} - h_{c,7} \right)$	$\dot{Q}_{c,cond,sh} = 0.74\left(439.4 - 417.8 \right)$	16.0	16.0	kW
CC condenser air mass flow rate	$\dot{m}_{c,cond,a} = \dot{V}_{c,cond,a} \rho_{amb}$	$\dot{m}_{c,cond,a} = \frac{190000\left(0.98 \right)}{3600}$	51.9	51.7	kg s^{-1}
Compressor Equivalent Conditions and Map Correction Factors					
Off-design pressure ratio	$\delta_{comp} = \frac{P_{c,4}}{P_{comp,ref}}$	$\delta_{comp} = \frac{765.6}{420.7}$	1.82	1.82	-
Reference critical velocity	$V_{cr,comp,ref} = \sqrt{\frac{2\gamma_{comp,ref}}{\gamma_{comp,ref}+1} g_c Z R_{comp,ref} T_{comp,ref}}$	$V_{cr,comp,ref} = \sqrt{\frac{2\left(1.09 \right)}{1.09+1} 9.81\left(0.11 \right) 289.4}$	18.2	18.1	m s^{-1}
Actual specific gas constant	$R_{comp,act} = \frac{R_{univ}}{MW_c}$	$R_{comp,act} = \frac{8.314}{102}$	0.081	0.081	kJ kg^{-1} K^{-1}
Actual compressibility factor	$Z_{comp,act} = \frac{P_{c,4} \upsilon_{c,4}}{R_{univ} T_{c,4}}$	$Z_{comp,act} = \frac{755.6\left(3.04 \right)}{8.314\left(321.6 \right)}$	0.87	0.86	-
Actual specific heat ratio	$\gamma_{comp,act} = \frac{Cp_{c,4}}{Cv_{c,4}}$	$\gamma_{comp,act} = \frac{102.9}{89.4}$	1.19	1.15	-
Actual critical velocity	$V_{cr,comp,act} = \sqrt{\frac{2\gamma_{comp,act}}{\gamma_{comp,act}+1} g_c Z_{comp,act} R_{comp,act} T_{comp,act}}$	$V_{cr,comp,act} = \sqrt{\frac{2\left(1.15 \right)}{1.15+1} 9.81\left(0.86 \right) 0.081\left(321.6 \right)}$	15.61	15.4	m s^{-1}

Parameter	Equation	Evaluated	EES Calc. Value	Hand Calc. Value	Units
Critical velocity ratio	$\theta_{comp} = \left(\frac{V_{cr,comp,act}}{V_{cr,comp,ref}} \right)^2$	$\theta_{comp} = \left(\frac{15.4}{18.1} \right)^2$	0.73	0.72	-
Compressibility factor	$\varepsilon_{comp} = \frac{\gamma_{comp,ref} \left(\frac{2}{\gamma_{comp,ref}+1} \right)^{\frac{\gamma_{comp,ref}}{\gamma_{comp,ref}-1}}}{\gamma_{comp,act} \left(\frac{2}{\gamma_{comp,act}+1} \right)^{\frac{\gamma_{comp,act}}{\gamma_{comp,act}-1}}}$	$\varepsilon_{comp} = \frac{1.09 \left(\frac{2}{1.09+1} \right)^{\frac{1.09}{1.09-1}}}{1.15 \left(\frac{2}{1.15+1} \right)^{\frac{1.15}{1.15-1}}}$	0.95	0.95	-
Corrected mass flow rate	$\dot{m}_{c,comp,eq} = \frac{\dot{m}_c \varepsilon_{comp} \sqrt{\theta_{comp}}}{\delta_{comp}}$	$\dot{m}_{c,comp,eq} = \frac{0.74(0.95)\sqrt{0.72}}{1.82}$	0.33	0.33	kg s^{-1}
Corrected ideal enthalpy rise	$\Delta h_{c,comp,eq} = \frac{(h_{c,s,5} - h_{c,5})}{\theta_{comp}}$	$\Delta h_{c,comp,eq} = \frac{(438.4 - 434)}{0.72}$	5.82	6.1	kJ kg^{-1}
Map efficiency	$\eta_{c,comp}$	$\eta_{c,comp}$	0.78	0.78	%
Map corrected speed	$N_{c,comp,eq}$	$N_{c,comp,eq}$	20871	20871	RPM
Actual compressor speed	$N_{c,comp} = N_{c,comp,eq} \sqrt{\theta_{comp}}$	$N_{c,comp} = 20871\sqrt{0.72}$	17853	17809	RPM
Turbine Equivalent Conditions and Map Correction Factors					
Off-design pressure ratio	$\delta_t = \frac{P_{p,1}}{P_{t,ref}}$	$\delta_t = \frac{348}{569.9}$	0.61	0.61	-
Reference critical velocity	$V_{cr,t,ref} = \sqrt{\frac{2\gamma_{t,ref}}{\gamma_{t,ref}+1} g_c Z R_{t,ref} T_{t,ref}}$	$V_{cr,t,ref} = \sqrt{\frac{2(0.89)}{0.89+1} 9.81(0.035) 376.6}$	11.01	11.0	m s^{-1}
Actual specific gas constant	$R_{t,act} = \frac{R_{univ}}{MW_t}$	$R_{t,act} = \frac{8.314}{200.1}$	0.042	0.042	kJ kg^{-1} K^{-1}

Parameter	Equation	Evaluated	EES Calc. Value	Hand Calc. Value	Units
Actual	$Z_{t,act} = \frac{P_{p,1}\upsilon_{p,1}}{R_{univ}T_{p,1}}$	$Z_{t,act} = \frac{348(8.127)}{8.314(375.5)}$	0.91	0.91	-
Actual specific heat ratio	$\gamma_{t,act} = \frac{Cp_{p,1}}{Cv_{p,1}}$	$\gamma_{t,act} = \frac{212}{198.2}$	1.07	1.07	-
Actual critical velocity	$V_{cr,t,act} = \sqrt{\frac{2\gamma_{t,act}}{\gamma_{t,act}+1} g_c Z_{t,act} R_{t,act} T_{t,act}}$	$V_{cr,t,act} = \sqrt{\frac{2(1.07)}{1.07+1} 9.81(0.91)0.042(375.5)}$	11.97	12.0	m s^{-1}
Critical velocity ratio	$\theta_t = \left(\frac{V_{cr,t,act}}{V_{cr,t,ref}}\right)^2$	$\theta_t = \left(\frac{12.0}{11.0}\right)^2$	1.18	1.19	-
Compressibility factor	$\varepsilon_t = \frac{\gamma_{t,ref}\left(\frac{2}{\gamma_{t,ref}+1}\right)^{\frac{\gamma_{t,ref}}{\gamma_{t,ref}-1}}}{\gamma_{t,act}\left(\frac{2}{\gamma_{t,act}+1}\right)^{\frac{\gamma_{t,act}}{\gamma_{t,act}-1}}}$	$\varepsilon_t = \frac{0.89\left(\frac{2}{0.89+1}\right)^{\frac{0.89}{0.89-1}}}{1.07\left(\frac{2}{1.07+1}\right)^{\frac{1.07}{1.07-1}}}$	0.89	0.89	-
Actual turbine speed	$N_{c,comp} = N_{p,t}$	$N_{c,comp} = N_{p,t}$	17853	17853	RPM
Corrected speed	$N_{p,t,eq} = \frac{N_{p,t}}{\sqrt{\theta_t}}$	$N_{p,t,eq} = \frac{17853}{\sqrt{1.19}}$	16423	16366	RPM
Corrected ideal enthalpy rise	$\Delta h_{p,t,eq} = \frac{(h_{t,1} - h_{t,s,2})}{\theta_t}$	$\Delta h_{p,t,eq} = \frac{(438.1 - 424.4)}{1.19}$	11.64	11.5	kJ kg^{-1}
Map efficiency	$\eta_{p,t}$	$\eta_{p,t}$	0.79	0.79	%
Map x-axis value	$\dot{m}_{p,t,axis}$	$\dot{m}_{p,t,axis}$	1.04	1.04	kg s^{-1} RPM

Parameter	Equation	Evaluated	EES Calc. Value	Hand Calc. Value	Units
Corrected mass flow rate	$\dot{m}_{p,t,axis} = \frac{\dot{m}_{p,t,eq} N_{p,t,eq}}{10,000}$	$1.04 = \frac{\dot{m}_{p,t,eq} 16423}{10,000}$	0.64	0.63	kg s^{-1}
PC mass flow rate	$\dot{m}_{p,t,eq} = \frac{\dot{m}_p \varepsilon_t \sqrt{\theta_t}}{\delta_t}$	$0.63 = \frac{\dot{m}_p 0.89\sqrt{1.19}}{0.61}$	0.4	0.4	kg s^{-1}
Power Cycle State Points					
Turbine outlet enthalpy	$\eta_t = \frac{\left(h_{p,1} - h_{p,2}\right)}{\left(h_{p,1} - h_{p,s,2}\right)}$	$0.79 = \frac{\left(438.1 - h_{p,2}\right)}{\left(438.1 - 424.4\right)}$	427.2	427.3	kJ kg^{-1}
Turbine work	$\dot{W}_{p,t} = \dot{m}_p \left(h_{p,1} - h_{p,2}\right)$	$\dot{W}_{p,t} = 0.4\left(438.1 - 427.3\right)$	4.33	4.32	kW
Turbine work	$\dot{W}_{p,t} = \frac{\dot{W}_{c,comp}}{\eta_{shaft}}$	$\dot{W}_{p,t} = \frac{4.03}{0.93}$	4.33	4.33	kW
Power cycle mass flow rate	$\dot{W}_t = \dot{m}_p \left(h_{p,1} - h_{p,2}\right)$	$4.32 = \dot{m}_p \left(438.1 - 427.3\right)$	0.4	0.4	kW
Recuperator heat duty	$\dot{Q}_{p,recup} = \dot{m}_p \left(h_{p,3} - h_{p,4}\right)$	$\dot{Q}_{p,recup} = 0.4\left(427.2 - 386\right)$	16.5	16.5	kW
PC condenser SC heat duty	$\dot{Q}_{p,cond,sc} = \dot{m}_p \left(h_{p,7} - h_{p,8}\right)$	$\dot{Q}_{p,cond,sc} = 0.4\left(246.4 - 244.8\right)$	0.63	0.64	kW
PC condenser TP heat duty	$\dot{Q}_{p,cond,tp} = \dot{m}_p \left(h_{p,6} - h_{p,7}\right)$	$\dot{Q}_{p,cond,tp} = 0.4\left(380.2 - 246.4\right)$	49.0	53.5	kW
PC condenser SH heat duty	$\dot{Q}_{p,cond,sh} = \dot{m}_p \left(h_{p,5} - h_{p,6}\right)$	$\dot{Q}_{p,cond,sh} = 0.4\left(386 - 380.2\right)$	6.86	2.32	kW
PC condenser heat duty	$\dot{Q}_{p,cond} = \dot{m}_p \left(h_{p,5} - h_{p,8}\right)$	$\dot{Q}_{p,cond} = 0.4\left(386 - 244.8\right)$	56.5	56.5	kW
PC condenser air mass flow rate	$\dot{m}_{p,cond,a} = \dot{V}_{p,cond,a} \rho_{amb}$	$\dot{m}_{p,cond,a} = \frac{60000\left(0.98\right)}{3600}$	16.4	16.3	kg s^{-1}
Pump work	$\dot{W}_{p,pump} = \dot{m}_p \left(h_{p,10} - h_{p,9}\right)$	$\dot{W}_{p,pump} = 0.4\left(245.3 - 244.8\right)$	0.22	0.2	kW

Parameter	Equation	Evaluated	EES Calc. Value	Hand Calc. Value	Units
PC boiler heat duty	$\dot{Q}_{p,b} = \dot{m}_p \left(h_{p,16} - h_{p,13} \right)$	$\dot{Q}_{p,b} = 0.4\left(438.1 - 286.5\right)$	60.6	60.6	kW
PC boiler SC heat duty	$\dot{Q}_{p,b,sc} = \dot{m}_p \left(h_{p,14} - h_{p,13} \right)$	$\dot{Q}_{p,b,sc} = 0.4\left(291.9 - 286.5\right)$	2.15	2.16	kW
PC boiler TP heat duty	$\dot{Q}_{p,b,tp} = \dot{m}_p \left(h_{p,15} - h_{p,14} \right)$	$\dot{Q}_{p,b,tp} = 0.4\left(407.5 - 291.9\right)$	46.24	46.24	kW
PC boiler SH heat duty	$\dot{Q}_{p,b,sh} = \dot{m}_p \left(h_{p,16} - h_{p,15} \right)$	$\dot{Q}_{p,b,sh} = 0.4\left(438.1 - 407.5\right)$	9.58	12.2	kW
PC boiler fan power	$\dot{W}_{p,bf} = \frac{\dot{V}_{p,bf} \Delta P_{p,bf}}{\eta_{p,bf}}$	$\dot{W}_{p,bf} = \frac{23294\left(0.2\right)}{0.19}$	6.81	6.81	kW
PC condenser fan power	$\dot{W}_{p,cf} = N_{p,cf} \times 0.915[\text{kW}]$	$\dot{W}_{p,cf} = 2 \times 1.1[\text{kW}]$	2.2	2.2	kW
CC condenser fan power	$\dot{W}_{c,cf} = N_{p,cf} \times 1.13[\text{kW}]$	$\dot{W}_{c,cf} = 6 \times 1.4[\text{kW}]$	8.4	8.4	kW
Glycol pump power	$\dot{W}_{c,gp} = \frac{\dot{V}_{c,gp} \Delta P_{c,gp}}{\eta_{c,gp}}$	$\dot{W}_{c,gp} = \frac{42[\text{GPM}]\left(30.2\right)}{0.45}$	0.18	0.18	kW
Auxiliary power consumption	$\dot{W}_{aux} = \dot{W}_{p,bf} + \dot{W}_{p,cf} + \dot{W}_{c,cf} + \dot{W}_{c,gp}$	$\dot{W}_{aux} = 6.81 + 2.2 + 8.4 + 0.18$	17.6	17.6	kW
COP	$COP = \frac{\dot{Q}_{c,evap}}{\dot{Q}_{p,b} + \dot{W}_{p,pump} + \dot{W}_{aux}}$	$COP = \frac{142.9}{60.6 + 0.2 + 17.6}$	1.82	1.82	-

Table A-9. Input parameters for evaluation of test data parameter reduction and analysis.

Parameter	Value	Units
PC turbine differential pressure ($\Delta P_{p,t}$ – I005)	221	kPa
PC boiler inlet pressure ($P_{p,13}$ – I015)	381	kPa
PC boiler outlet pressure ($P_{p,16}$ – I017)	368	kPa
PC condenser inlet pressure ($P_{p,5}$ – I018)	138	kPa
PC condenser outlet pressure ($P_{p,8}$ – I019)	143	kPa
CC compressor inlet pressure ($P_{c,4}$ – I021)	791	kPa
CC compressor outlet pressure & CC condenser inlet pressure ($P_{c,5}$ & $P_{c,6}$ – I022)	936	kPa
CC condenser outlet pressure ($P_{c,9}$ – I023)	939	kPa
CC chiller inlet pressure ($P_{c,1}$ – I025)	810	kPa
CC chiller outlet pressure ($P_{c,3}$ – I026)	783	kPa
PC boiler inlet temperature ($T_{p,13}$ – I037)	66.0	°C
PC boiler 1 outlet temperature ($T_{p,16,1}$ – I038)	96.9	°C
PC boiler 2 outlet temperature ($T_{p,16,2}$ – I039)	113	°C
PC turbine inlet temperature ($T_{p,1}$ – I042)	98.5	°C
PC turbine outlet temperature ($T_{p,2}$ – I043)	86.4	°C
PC condenser inlet temperature ($T_{p,5}$ – I045)	46.4	°C
PC condenser 1 outlet temperature ($T_{p,8,1}$ – I046)	31.0	°C
PC condenser 2 outlet temperature ($T_{p,8,2}$ – I047)	28.8	°C
PC condenser 3 outlet temperature ($T_{p,8,3}$ – I048)	28.0	°C
PC compressor inlet temperature ($T_{c,4}$ – I059)	49.9	°C

Parameter	Value	Units
CC compressor outlet temperature & CC condenser inlet temperature ($T_{c,5}$ & $T_{c,6}$ – I060)	57.2	°C
CC condenser 1 outlet temperature ($T_{c,9,1}$ – I062)	30.3	°C
CC condenser 2 outlet temperature ($T_{c,9,2}$ – I063)	30.0	°C
CC condenser 3 outlet temperature ($T_{c,9,3}$ – I064)	28.8	°C
CC condenser 4 outlet temperature ($T_{c,9,4}$ – I065)	28.2	°C
CC condenser 5 outlet temperature ($T_{c,9,5}$ – I066)	25.9	°C
CC condenser 6 outlet temperature ($T_{c,9,6}$ – I067)	24.6	°C
CC chiller inlet temperature ($T_{c,1}$ – I082)	28.6	°C
CC chiller outlet temperature ($T_{c,3}$ – I086)	49.8	°C
PC mass flow rate ($\dot{m}_p$ – I116)	0.40	kg s^{-1}
CC mass flow rate 1 ($\dot{m}_{c,1}$ – I117)	0.74	kg s^{-1}
CC mass flow rate 2 ($\dot{m}_{c,2}$ – I118)	0	kg s^{-1}
PC boiler fan power ($\dot{W}_{p,bf}$ – I119)	6.42	kW
PC pump power ($\dot{W}_{p,p}$ – I121)	0.50	kW
PC condenser 1 fan power ($\dot{W}_{p,cf1}$ – I122)	0.89	kW
PC condenser 2 fan power ($\dot{W}_{p,cf2}$ – I123)	1.38	kW
CC condenser 1 fan power ($\dot{W}_{c,cf1}$ – I124)	1.51	kW
CC condenser 2 fan power ($\dot{W}_{c,cf2}$ – I125)	1.49	kW

Parameter	Value	Units
CC condenser 3 fan power ($\dot{W}_{c,cf3}$ – I126)	1.46	kW
CC condenser 4 fan power ($\dot{W}_{c,cf4}$ – I127)	1.49	kW
CC condenser 5 fan power ($\dot{W}_{c,cf5}$ – I128)	0.98	kW
CC condenser 6 fan power ($\dot{W}_{c,cf6}$ – I129)	1.45	kW

Table A-10. Hand calculations to support EES evaluation of test data parameter reduction and analysis.

Parameter	Equation	Evaluated	EES Calc. Value	Hand Calc. Value	Units
Turbo-machine parameters					
Turbine power	$\dot{W}_{p,t} = \dot{m}_p \left(h_{p,1} - h_{p,2}\right)$	$\dot{W}_{p,t} = 0.4\left(433.5 - 425\right)$	3.38	3.4	kW
Compressor power	$\dot{W}_{c,comp} = \dot{m}_c \left(h_{c,5} - h_{c,4}\right)$	$\dot{W}_{c,comp} = 0.74\left(439.8 - 434.9\right)$	3.59	3.62	kW
Turbine efficiency	$\eta_t = \frac{\left(h_{p,1} - h_{p,2}\right)}{\left(h_{p,1} - h_{p,s,2}\right)}$	$\eta_t = \frac{\left(433.5 - 425\right)}{\left(433.5 - 420.6\right)}$	0.66	0.66	-
Compressor efficiency	$\eta_{c,comp} = \frac{\left(h_{c,s,5} - h_{c,4}\right)}{\left(h_{c,5} - h_{c,4}\right)}$	$\eta_{c,comp} = \frac{\left(438.8 - 434.4\right)}{\left(439.8 - 434.4\right)}$	0.79	0.81	-
Shaft efficiency	$\eta_{shaft} = \frac{\dot{W}_{c,comp}}{\dot{W}_{p,t}}$	$\eta_{shaft} = \frac{3.62}{3.4}$	1.06	1.06	-
Heat Exchanger Heat Duties and *COP*					
PC recuperator heat duty	$\dot{Q}_{p,recup} = \dot{m}_p \left(h_{p,3} - h_{p,4}\right)$	$\dot{Q}_{p,recup} = 0.4\left(425.1 - 385.9\right)$	15.6	15.7	kW
PC condenser heat duty	$\dot{Q}_{p,cond} = \dot{m}_p \left(h_{p,5} - h_{p,8}\right)$	$\dot{Q}_{p,cond} = 0.4\left(385.9 - 235.5\right)$	59.8	60.2	kW
CC condenser heat duty	$\dot{Q}_{c,cond} = \dot{m}_c \left(h_{c,6} - h_{c,9}\right)$	$\dot{Q}_{c,cond} = 0.74\left(440.8 - 238.8\right)$	148.7	149.5	kW
CC chiller heat duty	$\dot{Q}_{c,evap} = \dot{m}_c \left(h_{c,3} - h_{c,1}\right)$	$\dot{Q}_{c,evap} = 0.74\left(434.9 - 237.5\right)$	145.3	146.1	kW
PC boiler heat duty	$\dot{Q}_{p,b} = \dot{m}_p \left(h_{p,16} - h_{p,13}\right)$	$\dot{Q}_{p,b} = 0.4\left(440.6 - 281.9\right)$	63.1	63.5	kW
PC condenser fan power	$\dot{W}_{p,cf} = \dot{W}_{p,cf1} + \dot{W}_{p,cf2}$	$\dot{W}_{p,cf} = 0.89 + 1.38$	2.27	2.27	kW
CC condenser fan power	$\dot{W}_{c,cf} = \dot{W}_{c,cf1} + \dot{W}_{c,cf2} + \dot{W}_{c,cf3} + \dot{W}_{c,cf4} + \dot{W}_{c,cf5} + \dot{W}_{c,cf6}$	$\dot{W}_{c,cf} = 1.51 + 1.49 + 1.46 + 1.49 + 0.98 + 1.45$	8.36	8.36	kW

Parameter	Equation	Evaluated	EES Calc. Value	Hand Calc. Value	Units
Auxiliary power consumption	$\dot{W}_{aux} = \dot{W}_{p,bf} + \dot{W}_{p,cf} + \dot{W}_{c,cf}$	$\dot{W}_{aux} = 6.42 + 2.27 + 8.36$	17.0	17.1	kW
COP	$COP = \frac{\dot{Q}_{c,evap}}{\dot{Q}_{p,b} + \dot{W}_{p,pump} + \dot{W}_{aux}}$	$COP = \frac{146.1}{63.5 + 0.5 + 17.1}$	1.80	1.80	-

APPENDIX B. PIPING AND INSTRUMENTATION DIAGRAM

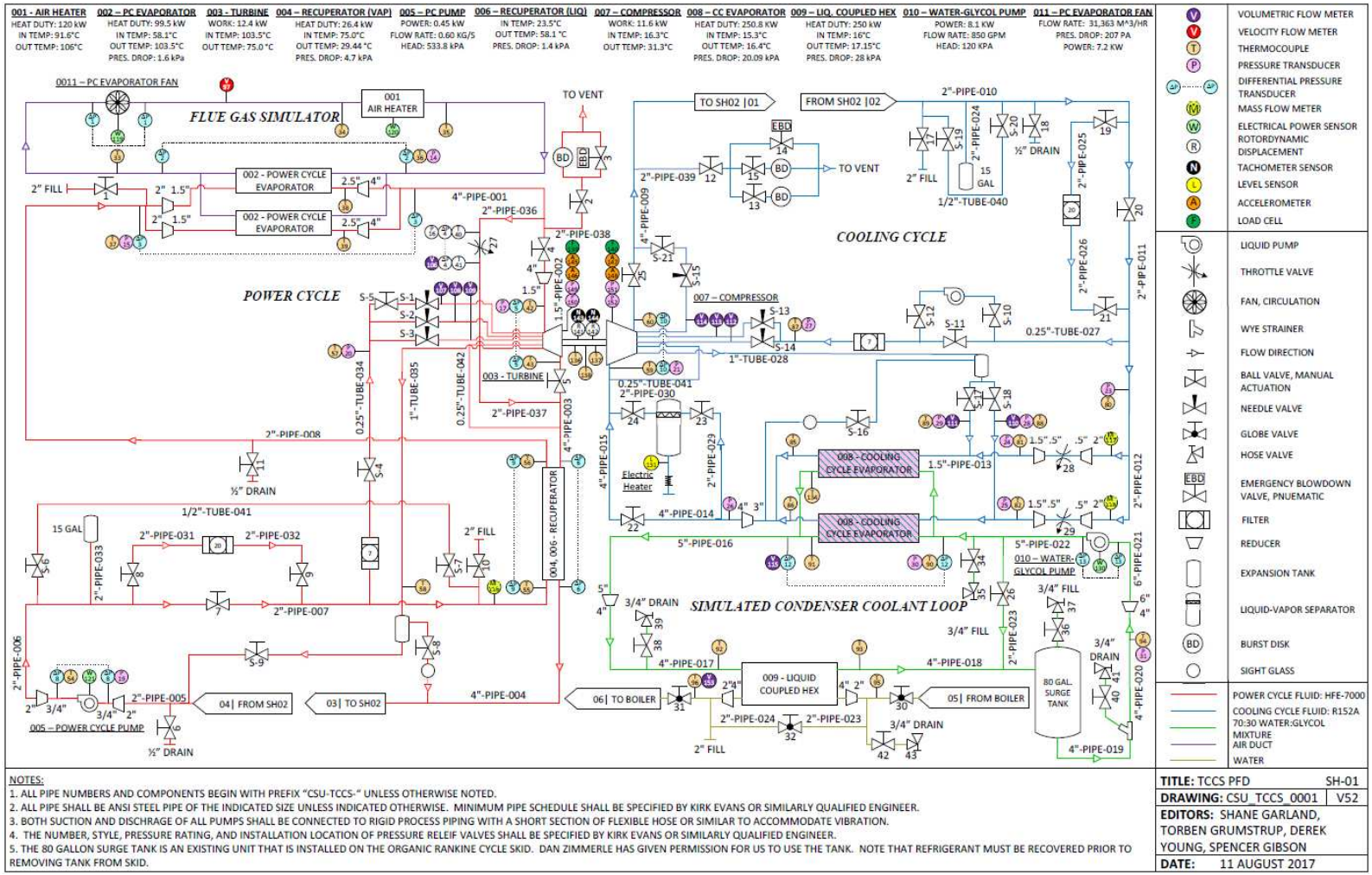

Figure B-1. TCCS Piping and Instrumentation Diagram Page 1.

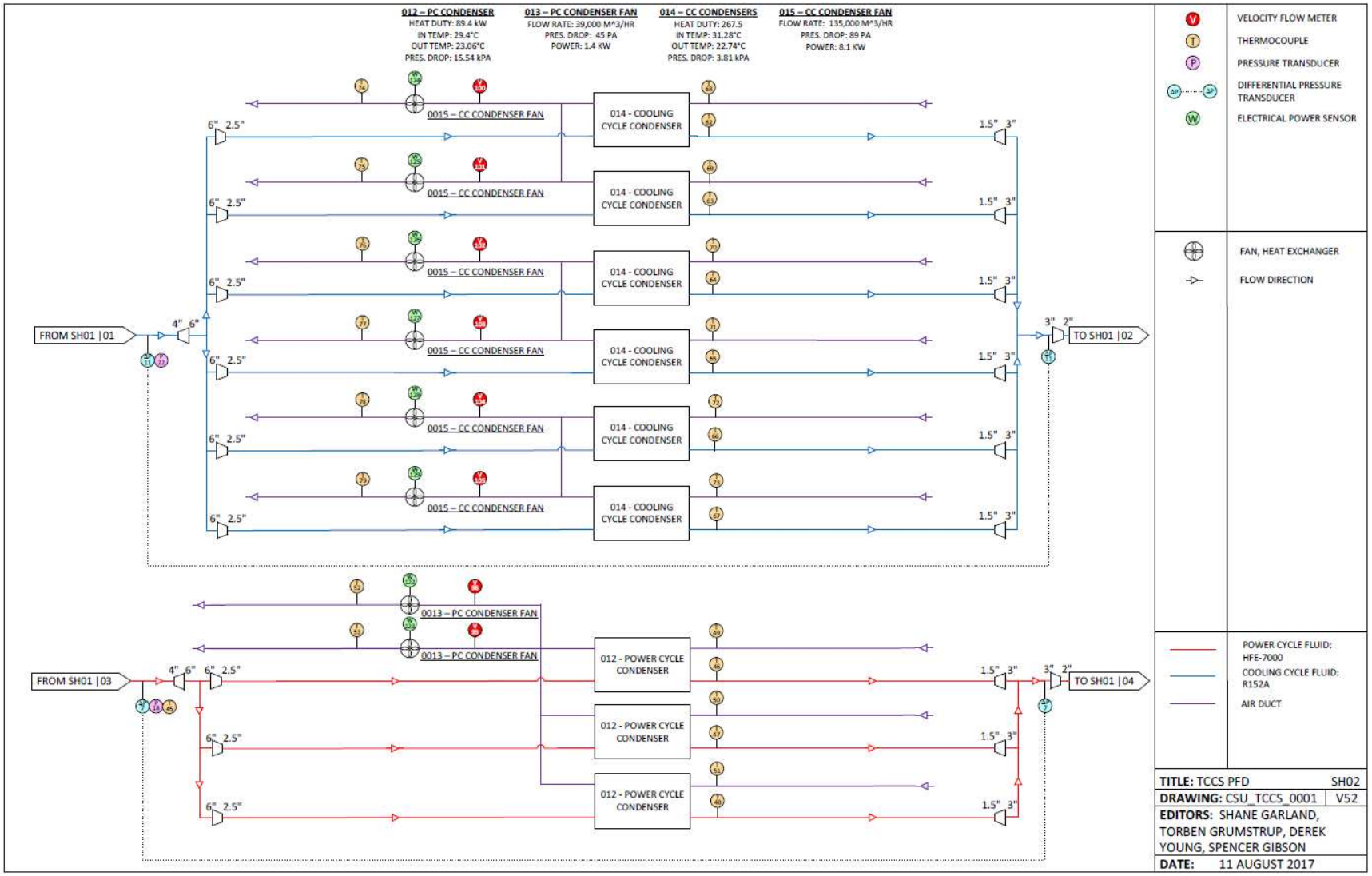

Figure B-2. TCCS Piping and Instrumentation Diagram Page 2.

APPENDIX C.TEST FACILITY EQUIPMENT LIST

Table C-1. TCCS equipment list.

QTY	DESCRIPTION	MANUFACTURER	SUPPLIER	PART NUMBER	LOC.
1	TURBO-COMPRESSOR	BARBER-NICHOLS	BARBER-NICHOLS	BNTC-07-000	PC/CC
1	RECUPERATOR	MODINE	MODINE	PR0444040200	PC
3	CONDENSER	MODINE	MODINE	PR0444190101	PC
1	RIGHT SIDE BOILER	MODINE	MODINE	PR0444190301	PC
1	LEFT SIDE BOILER	MODINE	MODINE	PR0444190201	PC
6	CONDENSER	MODINE	MODINE	PR0444190001	CC
1	RIGHT SIDE CHILLER	MODINE	MODINE	PR0444040300	CC
1	LEFT SIDE CHILLER	MODINE	MODINE	PR0444040400	CC
1	AIR RESISTANCE COIL HEATER	WINAIR	WINAIR	NA	FLUE
1	VANEAXIAL FAN	AEROVENT	CENTENNIAL EQUIPMENT	VWMD-43W7	FLUE
1	FAN MOTOR	NA	CENTENNIAL EQUIPMENT	TEFC-PREMIUM	FLUE
1	ALTIVAR 212 - FAN VFD	SCHNEIDER ELECTRIC	GRAINGER	ATV212HD11N4	ELEC.
1	SUCTION PUMP	GOULDS PUMPS	WATER TECH. GROUP	3804	GLYCOL
1	PUMP MOTOR	MARATHON MOTORS	WATER TECH. GROUP	254TTDCA6026	GLYCOL
1	80 GAL TANK	MCMASTER	ZIMMERLEE GROUP	4376K12	GLYCOL
1	PLATE AND FRAME HEX	ALFA LAVAL	ZIMMERLEE GROUP	M10M-FG	GLYCOL
1	WYE STRAINER	WATTS WATER	WINNELSON COMPANY	77F-CSI	GLYCOL
1	POWER CYCLE PUMP	LIQUIFLO	BF SALES ENGINEERING	H7F	PC
1	ALTIVAR 312 - PUMP VFD	SCHNEIDER ELECTRIC	GRAINGER	ATV312HU15M2	ELEC.
1	BALDOR PUMP MOTOR	BALDOR	BF SALES ENGINEERING	VEM3554	PC
2	CONDENSER FAN	ZIEHL-ABEGG	ZIEHL-ABEGG	ZN091-ZIQ.GL.V5P1	PC
6	CONDENSER FAN	ZIEHL-ABEGG	ZIEHL-ABEGG	ZN091-ZIQ.GL.V5P1	CC

QTY	DESCRIPTION	MANUFACTURER	SUPPLIER	PART NUMBER	LOC.
4	FAN CONTROLLERS	ZIEHL-ABEGG	ZIEHL-ABEGG	CXE/AV(E)	ELEC.
2	FILTER-DRIER	PARKER-HANNIFIN	PARKER-HANNIFIN	P9617-400716	PC/CC
4	FILTER-DRIER CORE	PARKER-HANNIFIN	PARKER-HANNIFIN	PFE-48BF 031858-00	PC/CC
1	ACCUMULATOR	PARKER-HANNIFIN	MOTION & FLOW CONTROL	BA15B3T01P2	PC
1	ACCUMULATOR	ACCUMULATORS, INC	INTEGRITY CONTOLS	A15TR3100WS	CC
1	LIQUID VAPOR SEPARATOR	EATON	INTERITY CONTROLS	2T150C	CC
1	LIQ-VAP REFRIGERANT HEATER	TEMPCO	MCMASTER-CARR	3656K365	CC
1	FLOAT SWITCH	DWYER INSTRUMENTS	MCMASTER-CARR	48255K31	CC
1	BEARING PUMP (GEAR)	MICROPUMP	TESCO PUMPS	GB-P35.JVS.A-B1	BEARING
1	VARIABLE SPEED PUMP DRIVE	COLE PARMER	COLE PARMER	EW-75211-10	BEARING
2	FILTER	SWAGELOK	SWAGELOK	SS-4TF-7	BEARING
2	1 GAL. BEARING DRAIN TANK	MANCHESTER TANK	MCMASTER-CARR	1733608	BEARING
2	SIGHT GLASS	NA	MCMASTER-CARR	1079K44	BEARING
1	PLATINUM SERIES VACUUM PUMP	JB INDUSTRIES	BASEMENT LAB	DV-85N	FILL
1	ULTRA GRADE 19 OIL	EDWARDS	BASEMENT LAB	H11025013	FILL
1	ROTARY VANE PUMP	FILL-RITE	GRAINGER	FR610G	FILL
1	SERIES GB GEAR PUMP	MICROPUMP	TESCO PUMPS	GB-P35.JVS.A-B1	FILL
1	A-MOUNT CONSOLE DRIVE	COLE PARMER	COLE PARMER	EW-75211-10	FILL
1	GFK CHECKWEIGHING SCALE	ADAM EQUIPMENT, INC	STOVES LAB	GFK 330aH	FILL
1	REFRIGERANT RECOVERY PUMP	CM REFRIGERATION	BEST VALUE VACS.	CMEP-OL	DRAIN
1	OIL BATH	MEMMERT	COLE PARMER	ONE 29	CAL
1	OIL BATH OIL	BOSS PRODUCTS	COLE PARMER	01894CL01	CAL
1	REFERENCE THERMOMETER	DIGISENSE	COLE PARMER	EW-37804-04	CAL
1	COMPACT RIO	NATIONAL INSTRUMENTS	NATIONAL INSTRUMENTS	cRIO-9066	DAQ

QTY	DESCRIPTION	MANUFACTURER	SUPPLIER	PART NUMBER	LOC.
1	CRIO 8-SLOT ADDITIONAL CHASSIS	NATIONAL INSTRUMENTS	NATIONAL INSTRUMENTS	NI 9149	DAQ
4	16 CH. TEMPERATURE INPUT MODULE	NATIONAL INSTRUMENTS	NATIONAL INSTRUMENTS	NI 9213	DAQ
3	32 CH. ANALOG INPUT MODULE	NATIONAL INSTRUMENTS	NATIONAL INSTRUMENTS	NI 9205	DAQ
1	32 CH. COUNTER INPUT MODULE	NATIONAL INSTRUMENTS	NATIONAL INSTRUMENTS	NI 9361	DAQ
2	VIBRATION INPUT MODULE	NATIONAL INSTRUMENTS	NATIONAL INSTRUMENTS	NI 9230	DAQ
1	± 10 VDC SIGNAL SUPPLY	NATIONAL INSTRUMENTS	NATIONAL INSTRUMENTS	NI 9263	DAQ
2	RTD SIGNAL CONDITIONERS	OMEGA	OMEGA	iDRX	DAQ
6	PROCESS SIGNAL CONDITIONER	RED LION	GRAINGER	IFMA0035	DAQ
2	PROXIMITY DRIVER	METRIX	METRIX	MX2033	DAQ
1	24 VDC POWER SUPPLY	NATIONAL INSTRUMENTS	NATIONAL INSTRUMENTS	NI PS-15	DAQ
1	-24VDC POWER SUPPLY	BEL-POWER	DIGIKEY	179-2319-ND	DAQ
1	12 VDC POWER SUPPLY	PULS	GRAINGER	ML15.121	DAQ
4	37-PIN DSUB SCREW TERMINAL BLOCK	NATIONAL INSTRUMENTS	NATIONAL INSTRUMENTS	778673-01	DAQ
3	COLLECTION ADAPTOR	EGAUGE	EGAUGE	EG3000	DAQ
2	SOLENOID VALVE	ASCO	GRAINGER	8321G001	SAFETY
1	24 V POWER SUPPLY	OMRON	GRAINGER	S8VK-G12024	SAFETY
1	UNINTERRUPTED POWER SUPPLY	DIRECTUPS	NEWEGG	VP2000	SAFETY
2	2 GAL. AIR STROAGE TANK	AMALGA COMPOSITES INC	MCMASTER-CARR	ACI2102	SAFETY
2	BURST DISK - 175 PSI	MERSEN	MCMASTER-CARR	4858K505	SAFETY
1	BURST DISK - 200 PSI	MERSEN	MCMASTER-CARR	4858K506	SAFETY
2	POLYTRON 5000 LEAK DETECTORS	DRAEGER SAFETY	FRONTIER CONTROLS	4544221	SAFETY
2	POLYTRON 5000 STATUS INDICATORS	DRAEGER SAFETY	FRONTIER CONTROLS	6811625	SAFETY

QTY	DESCRIPTION	MANUFACTURER	SUPPLIER	PART NUMBER	LOC.
1	SWITCHBOARD	EATON INC	EATON INC	POW-R-LINE C	ELEC.
1	40 AMP BREAKER	SQUARE D	CED	EDB34040	ELEC.
1	60 AMP BREAKER	SQUARE D	CED	EDB34060	ELEC.
4	15 AMP BREAKER	SQUARE D	CED	EDB34015	ELEC.
1	STEP-DOWN TRANSFORMER	SQUARE D	GRAINGER	EX15T6HCT	ELEC.
1	HEATER DISCONNECT	SQUARE D	CED	H364	ELEC.
3	200 AMP FUSES	BUSSMANN	CED	FRS-R-200	ELEC.
3	200 AMP CURRENT TRANSFORMER	EGAUGE	EGAUGE	ML-SCT-200-010	ELEC.
6	20 AMP CURRENT TRANSFORMER	EGAUGE	EGAUGE	ML-SCT-020-010	ELEC.
24	10 AMP CURRENT TRANSFORMER	EGAUGE	EGAUGE	ML-SCT-010-010	ELEC.
3	5 AMP CURRENT TRANSFORMAER	EGAUGE	EGAUGE	ML-SCT-005-010	ELEC.
1	CRANE	ABELL-HOWE	MCMASTER-CARR	J-906-FCT-1F1A	MEZZ.
1	TROLLEY	DAYTON	GRAINGER	3MB60	MEZZ.
1	HOIST	DAYTON	GRAINGER	1VW57	MEZZ.

APPENDIX D.TEST FACILITY VALVE LISTS

Table D-1. Pipe valves in the TCCS.

VALVE NUMBER	VALVE SIZE	VALVE TYPE	APPLICATION	CYCLE	SUPPLIER
1	2 INCH	BALL	FILL PORT	POWER	TRIAC
2	2 INCH	BALL	VENT LINE	POWER	TRIAC
3	2 INCH	EBV	EMERGENCY BLOWDOWN	POWER	TRIAC
4	4 INCH	BALL	TURBINE ISOLATION	POWER	TRIAC
5	4 INCH	BALL	TURBINE ISOLATION	POWER	TRIAC
6	1/2 INCH	BALL	DRAIN PORT	POWER	TRIAC
7	2 INCH	BALL	FILTER ISOLATION	POWER	TRIAC
8	2 INCH	BALL	FILTER ISOLATION	POWER	TRIAC
9	2 INCH	BALL	FILTER ISOLATION	POWER	TRIAC
10	2 INCH	BALL	FILL PORT	POWER	TRIAC
11	1/2 INCH	BALL	DRAIN PORT	POWER	TRIAC
12	2 INCH	BALL	VENT LINE	COOLING	TRIAC
13	2 INCH	BALL	BURST DISK 1	COOLING	TRIAC
14	2 INCH	EBV	EMERGENCY BLOWDOWN	COOLING	TRIAC
15	2 INCH	BALL	BURST DISK 2	COOLING	TRIAC
17	2 INCH	BALL	FILL PORT	COOLING	TRIAC
18	1/2 INCH	BALL	DRAIN PORT	COOLING	TRIAC
19	2 INCH	BALL	FILTER ISOLATION	COOLING	TRIAC
20	2 INCH	BALL	FILTER ISOLATION	COOLING	TRIAC
21	2 INCH	BALL	FILTER ISOLATION	COOLING	TRIAC
22	4 INCH	BALL	LIQ-VAP ISOLATION	COOLING	TRIAC
23	2 INCH	BALL	LIQ-VAP ISOLATION	COOLING	TRIAC
24	2 INCH	BALL	LIQ-VAP ISOLATION	COOLING	TRIAC
25	4 INCH	BALL	COMPRESSOR ISOLATION	COOLING	TRIAC
26	2 INCH	BALL	GLYCOL BYPASS	GLYCOL	TRIAC
27	1.5 INCH	GLOBE	TURBINE THROTTLE VALVE	POWER	WILLIAMS
28	1/2 INCH	GLOBE	THROTTLE VALVE	COOLING	WILLIAMS
29	1/2 INCH	GLOBE	THROTTLE VALVE	COOLING	WILLIAMS
30	2 INCH	GLOBE	BOILER WATER INLET	GLYCOL	MILWAUKEE
31	2 INCH	GLOBE	BOILER WATER RETURN	GLYCOL	MILWAUKEE
32	2 INCH	GLOBE	GLYCOL HEX BYPASS	GLYCOL	ACE
33	1/2 INCH	BALL	DRAIN VALVE FOR VAC	COOLING	MCMASTER
34	3/4 INCH	BALL	FILL PORT	GLYCOL	ACE
35	3/4 INCH	HOSE	FILL PORT	GLYCOL	ACE
36	3/4 INCH	BALL	FILL PORT	GLYCOL	ACE
37	3/4 INCH	HOSE	FILL PORT	GLYCOL	ACE
38	3/4 INCH	BALL	DRAIN PORT	GLYCOL	ACE
39	3/4 INCH	HOSE	DRAIN PORT	GLYCOL	ACE
40	1-1/2 INCH	BALL	DRAIN PORT	GLYCOL	MCMASTER
41	3/4 INCH	HOSE	DRAIN PORT	GLYCOL	ACE
42	2 INCH	BALL	DRAIN PORT	GLYCOL	MCMASTER
43	3/4 INCH	HOSE	DRAIN PORT	GLYCOL	ACE

Table D-2. Swagelok valves in the TCCS.

VALVE NUMBER	VALVE SIZE	VALVE TYPE	APPLICATION	CYCLE	SWAGELOK PART #
S1	1/4 INCH	METERING	MAG COUPLING INLET	POWER	SS-SS4
S2	1/4 INCH	METERING	BEARING INLET	POWER	SS-SS4
S3	1/4 INCH	METERING	BEARING INLET	POWER	SS-SS4
S4	1/4 INCH	BALL	COOLING INLET LINE	POWER	SS-43GS4
S5	1/4 INCH	BALL	MAG COUPLING COOLING LINE	POWER	SS-43GS4
S6	1/2 INCH	BALL	FILL LEVEL SIGHT TUBE	POWER	SS-45S8
S7	1/2 INCH	BALL	FILL LEVEL SIGHT TUBE	POWER	SS-45S8
S8	1 INCH	BALL	VAPOR OUTLET BEARING ACCUM	POWER	SS-65TS16
S9	1 INCH	BALL	LIQUID OUTLET BEARING ACCUM	POWER	SS-65TS16
S10	1/4 INCH	BALL	BEARING PUMP INLET	COOLING	SS-43GS4
S11	1/4 INCH	BALL	BEARING PUMP BYPASS	COOLING	SS-43GS4
S12	1/4 INCH	BALL	BEARING PUMP OUTLET	COOLING	SS-43GS4
S13	1/4 INCH	METERING	BEARING INLET	COOLING	SS-SS4
S14	1/4 INCH	METERING	BEARING INLET	COOLING	SS-SS4
S15	1/4 INCH	METERING	COMPRESSOR RECIRC	COOLING	SS-SS4
S16	1 INCH	BALL	VAPOR OUTLET BEARING ACCUM	COOLING	SS-65TS16
S17	1 INCH	BALL	LIQUID OUTLET BEARING ACCUM	COOLING	SS-65TS16
S18	1 INCH	BALL	LIQUID OUTLET BEARING ACCUM	COOLING	SS-65TS16
S19	1/2 INCH	BALL	FILL LEVEL SIGHT TUBE	COOLING	SS-45S8
S20	1/2 INCH	BALL	FILL LEVEL SIGHT TUBE	COOLING	SS-45S8
S21	1/4 INCH	BALL	COMPRESSOR RECIRC	COOLING	SS-43GS4
S22	3/4 INCH	BALL	TURBINE FILL LINE	POWER	SS-45S12
S23	3/4 INCH	BALL	COMPRESSOR FILL LINE	COOLING	SS-45S12
S24	3/4 INCH	BALL	VACUUM PUMP	POWER	SS-45S12
S25	3/4 INCH	BALL	HFE7000 FUEL PUMP	POWER	SS-45S12
S26	3/4 INCH	BALL	VACUUM PUMP	COOLING	SS-45S12
S27	3/4 INCH	BALL	REFRIGERANT GEAR PUMP	COOLING	SS-45S12
S28	1/4 INCH	BALL	TURBINE VENT LINE	POWER	SS-43GS4
S29	1/4 INCH	BALL	COMPRESSOR VENT LINE	COOLING	SS-43GS4
S30	1/4 INCH	BALL	REFRIGERANT TANK	COOLING	SS-43GS4
S31	1/2 INCH	BALL	DRAIN REFRIGERANT TANK	COOLING	SS-45S8

APPENDIX E. TEST FACILITY INSTRUMENT LIST

Table E-1. TCCS instrumentation list.

INST #	LOCATION	TYPE	SCALE	SIGNAL	SUPPLIER	PART #
1	FLUE GAS LOOP FAN	DIFFERENTIAL PRESSURE TRANSDUCER	0-4 INCHES OF WATER	4 to 20mA	ASHCROFT	GC52-7-F02-42-CD-4IW
2	PC EVAP AIR SIDE	DIFFERENTIAL PRESSURE TRANSDUCER	0-4 INCHES OF WATER	4 to 20mA	ASHCROFT	GC52-7-F02-42-CD-4IW
3	PC EVAP FLUID SIDE	DIFFERENTIAL PRESSURE TRANSDUCER	0-20 INCHES OF WATER	4 to 20mA	ASHCROFT	GC52-7-F02-42-CD-20IW
4	TURBINE BYPASS LINE	DIFFERENTIAL PRESSURE TRANSDUCER	100 PSI	4 to 20mA	DWYER	629-05-CH-P2-E5-S1
5	TURBINE	DIFFERENTIAL PRESSURE TRANSDUCER	100 PSI	4 to 20mA	DWYER	629-05-CH-P2-E5-S1
6	RECUP. VAPOR SIDE	DIFFERENTIAL PRESSURE TRANSDUCER	40 INCHES OF WATER	4 to 20mA	ASHCROFT	GC52-7-F02-42-CD-40IW
7	PC CONDENSERS	DIFFERENTIAL PRESSURE TRANSDUCER	200 INCHES OF WATER	4 to 20mA	ASHCROFT	GC52-7-F02-42-CD-200IW
8	POWER CYCLE PUMP	DIFFERENTIAL PRESSURE TRANSDUCER	100 PSI	4 to 20mA	DWYER	629-05-CH-P2-E5-S1
9	RECUP. LIQUID SIDE	DIFFERENTIAL PRESSURE TRANSDUCER	0-10 INCHES OF WATER	4 to 20mA	ASHCROFT	GC52-7-F02-42-CD-20IW
10	COMPRESSOR	DIFFERENTIAL PRESSURE TRANSDUCER	75 PSI	4 to 20mA	ASHCROFT	GC55-7-F02-42-CD-75#
11	CC CONDENSERS	DIFFERENTIAL PRESSURE TRANSDUCER	40 INCHES OF WATER	4 to 20mA	ASHCROFT	GC52-7-F02-42-CD-40IW
12	CC EVAP GLYCOL SIDE	DIFFERENTIAL PRESSURE TRANSDUCER	400 INCHES OF WATER	4 to 20mA	ASHCROFT	GC52-7-F02-42-CD-400IW
13	GLYCOL LOOP PUMP	DIFFERENTIAL PRESSURE TRANSDUCER	75 PSI	4 to 20mA	ASHCROFT	GC55-7-F02-42-CD-75#
14	PC EVAP AIR SIDE INLET	PRESSURE TRANSDUCER	15 PSI	4 to 20mA	ASHCROFT	K1-7-MO2-42-C1-15#-XFM

INST #	LOCATION	TYPE	SCALE	SIGNAL	SUPPLIER	PART #
15	PC EVAP FLUID SIDE INLET	PRESSURE TRANSDUCER	200 PSI	4 to 20mA	ASHCROFT	G2-7-M02-42-M1-200#
16	TURBINE BYPASS INLET	PRESSURE TRANSDUCER	200 PSI	4 to 20mA	ASHCROFT	G2-7-M02-42-M1-200#
17	TURBINE INLET	PRESSURE TRANSDUCER	200 PSI	4 to 20mA	ASHCROFT	G2-7-M02-42-M1-200#
18	PC CONDENSER INLET	PRESSURE TRANSDUCER	100 PSI	4 to 20mA	ASHCROFT	G2-7-M02-42-M1-100#
19	PC PUMP INLET	PRESSURE TRANSDUCER	100 PSI	4 to 20mA	ASHCROFT	G2-7-M02-42-M1-100#
20	PC BEARING INLET	PRESSURE TRANSDUCER	200 PSI	4 to 20mA	ASHCROFT	G2-7-M02-42-M1-200#
21	COMPRESSOR INLET	PRESSURE TRANSDUCER	300 PSI	4 to 20mA	OMEGA	PX319-300AI
22	CC CONDENSER INLET	PRESSURE TRANSDUCER	300 PSI	4 to 20mA	ASHCROFT	G2-7-M02-42-M1-300#
23	CC THROTTLE VALVE INLET	PRESSURE TRANSDUCER	300 PSI	4 to 20mA	ASHCROFT	G2-7-M02-42-M1-300#
24	CC THROTTLE VALVE OUTLET	PRESSURE TRANSDUCER	300 PSI	4 to 20mA	ASHCROFT	G2-7-M02-42-M1-300#
25	CC THROTTLE VALVE OUTLET	PRESSURE TRANSDUCER	300 PSI	4 to 20mA	ASHCROFT	G2-7-M02-42-M1-300#
26	CC EVAP. OUTLET	PRESSURE TRANSDUCER	300 PSI	4 to 20mA	ASHCROFT	G2-7-M02-42-M1-300#
27	CC BEARING LINE INLET	PRESSURE TRANSDUCER	300 PSI	4 to 20mA	ASHCROFT	G2-7-M02-42-M1-300#
28	CC BEARING DRAIN OUTLET	PRESSURE TRANSDUCER	300 PSI	4 to 20mA	ASHCROFT	G2-7-M02-42-M1-300#
29	CC BEARING DRAIN OUTLET	PRESSURE TRANSDUCER	300 PSI	4 to 20mA	ASHCROFT	G2-7-M02-42-M1-300#
30	GLYCOL LOOP EVAP. INLET	PRESSURE TRANSDUCER	15 PSI	4 to 20mA	ASHCROFT	K1-7-M02-42-C1-15#-XFM
31	GLYCOL LOOP TANK	PRESSURE TRANSDUCER	15 PSI	4 to 20mA	ASHCROFT	K1-7-M02-42-C1-15#-XFM
32	ATOMOSPHERIC	BAROMETRIC PRESSURE TRANSDUCER	0 – 29.9 INHG	4 to 20mA	BARKSDALE	425H5-23
33	PC EVAP OUTLET AIR	THERMOCOUPLE WIRE	T-TYPE WIRE	VOLTS	OMEGA	TT-T-24-50

INST #	LOCATION	TYPE	SCALE	SIGNAL	SUPPLIER	PART #
34	PC AIR HEATER INLET	THERMOCOUPLE WIRE	T-TYPE WIRE	VOLTS	OMEGA	TT-T-24-50
35	PC AIR HEATER OUTLET	THERMOCOUPLE WIRE	T-TYPE WIRE	VOLTS	OMEGA	TT-T-24-50
36	PC EVAP INLET AIR	THERMOCOUPLE WIRE	T-TYPE WIRE	VOLTS	OMEGA	TT-T-24-50
37	PC EVAP INLET FLUID	THERMOCOUPLE 2 INCH	T-TYPE	VOLTS	OMEGA	TQSS-18U-4
38	PC EVAP LEFT OUTLET FLUID	THERMOCOUPLE 4 INCH	T-TYPE	VOLTS	OMEGA	TQSS-18U-6
39	PC EVAP RIGHT OUTLET FLUID	THERMOCOUPLE 4 INCH	T-TYPE	VOLTS	OMEGA	TQSS-18U-6
40	TURBINE BYPASS INLET	THERMOCOUPLE 2 INCH	T-TYPE	VOLTS	OMEGA	TQSS-18U-4
41	TURBINE BYPASS OUTLET	THERMOCOUPLE 2 INCH	T-TYPE	VOLTS	OMEGA	TQSS-18U-4
42	TURBINE INLET	THERMOCOUPLE 4 INCH PIPE	T-TYPE	VOLTS	OMEGA	TQSS-18U-6
43	TURBINE OUTLET	THERMOCOUPLE 4 INCH PIPE	T-TYPE	VOLTS	OMEGA	TQSS-18U-6
45	PC CONDENSER INLET	THERMOCOUPLE 4 INCH PIPE	T-TYPE	VOLTS	OMEGA	TQSS-18U-6
46	PC CONDENSER 1 OUTLET	THERMOCOUPLE 2 INCH	T-TYPE	VOLTS	OMEGA	TQSS-18U-4
47	PC CONDENSER 2 OUTLET	THERMOCOUPL 2 INCH	T-TYPE	VOLTS	OMEGA	TQSS-18U-4
48	PC CONDENSER 3 OUTLET	THERMOCOUPLE 2 INCH	T-TYPE	VOLTS	OMEGA	TQSS-18U-4
49	PC CONDENSER 1 AIR SIDE INLET	THERMOCOUPLE WIRE	T-TYPE WIRE	VOLTS	OMEGA	PP-T-24-100
50	PC CONDENSER 2 AIR SIDE INLET	THERMOCOUPLE WIRE	T-TYPE WIRE	VOLTS	OMEGA	PP-T-24-100
51	PC CONDENSER 3 AIR SIDE INLET	THERMOCOUPLE WIRE	T-TYPE WIRE	VOLTS	OMEGA	PP-T-24-100
52	PC CONDENSER LEFT AIR SIDE OUTLET	THERMOCOUPLE WIRE	T-TYPE WIRE	VOLTS	OMEGA	PP-T-24-100
53	PC CONDENSER RIGHT AIR SIDE OUTLET	THERMOCOUPLE WIRE	T-TYPE WIRE	VOLTS	OMEGA	PP-T-24-100
54	PC PUMP INLET	THERMOCOUPLE 2 INCH	T-TYPE	VOLTS	OMEGA	TQSS-18U-4
55	RECUPERATOR LIQUID SIDE INLET	THERMOCOUPLE 2 INCH	T-TYPE	VOLTS	OMEGA	TQSS-18U-4

INST #	LOCATION	TYPE	SCALE	SIGNAL	SUPPLIER	PART #
56	RECUPERATOR LIQUID SIDE OUTLET	THERMOCOUPLE 2 INCH	T-TYPE	VOLTS	OMEGA	TQSS-18U-4
57	PC BEARING INLET	THERMOCOUPLE TUBE	T-TYPE	VOLTS	OMEGA	TQSS-116U-3
58	PC BEARING OUTLET	THERMOCOUPLE TUBE	T-TYPE	VOLTS	OMEGA	TQSS-116U-3
59	COMPRESSOR INLET	THERMOCOUPLE 4 INCH PIPE	T-TYPE	VOLTS	OMEGA	TQSS-18U-6
60	COMPRESSOR OUTLET	THERMOCOUPLE 4 INCH PIPE	T-TYPE	VOLTS	OMEGA	TQSS-18U-6
62	CC CONDENSER 1 OUTLET	THERMOCOUPLE 2 INCH	T-TYPE	VOLTS	OMEGA	TQSS-18U-4
63	CC CONDENSER 2 OUTLET	THERMOCOUPLE 2 INCH	T-TYPE	VOLTS	OMEGA	TQSS-18U-4
64	CC CONDENSER 3 OUTLET	THERMOCOUPLE 2 INCH	T-TYPE	VOLTS	OMEGA	TQSS-18U-4
65	CC CONDENSER 4 OUTLET	THERMOCOUPLE 2 INCH	T-TYPE	VOLTS	OMEGA	TQSS-18U-4
67	CC CONDENSER 6 OUTLET	THERMOCOUPLE 2 INCH	T-TYPE	VOLTS	OMEGA	TQSS-18U-4
68	CC CONDENSER 1 AIR INLET	THERMOCOUPLE WIRE	T-TYPE WIRE	VOLTS	OMEGA	PP-T-24-100
69	CC CONDENSER 2 AIR INLET	THERMOCOUPLE WIRE	T-TYPE WIRE	VOLTS	OMEGA	PP-T-24-100
70	CC CONDENSER 3 AIR INLET	THERMOCOUPLE WIRE	T-TYPE WIRE	VOLTS	OMEGA	PP-T-24-100
71	CC CONDENSER 4 AIR INLET	THERMOCOUPLE WIRE	T-TYPE WIRE	VOLTS	OMEGA	PP-T-24-100
72	CC CONDENSER 5 AIR INLET	THERMOCOUPLE WIRE	T-TYPE WIRE	VOLTS	OMEGA	PP-T-24-100
73	CC CONDENSER 6 AIR INLET	THERMOCOUPLE WIRE	T-TYPE WIRE	VOLTS	OMEGA	PP-T-24-100
74	CC CONDENSER 1 AIR OUTLET	THERMOCOUPLE WIRE	T-TYPE WIRE	VOLTS	OMEGA	PP-T-24-100
75	CC CONDENSER 2 AIR OUTLET	THERMOCOUPLE WIRE	T-TYPE WIRE	VOLTS	OMEGA	PP-T-24-100
76	CC CONDENSER 3 AIR OUTLET	THERMOCOUPLE WIRE	T-TYPE WIRE	VOLTS	OMEGA	PP-T-24-100
77	CC CONDENSER 4 AIR OUTLET	THERMOCOUPLE WIRE	T-TYPE WIRE	VOLTS	OMEGA	PP-T-24-100
78	CC CONDENSER 5 AIR OUTLET	THERMOCOUPLE WIRE	T-TYPE WIRE	VOLTS	OMEGA	PP-T-24-100
79	CC CONDENSER 6 AIR OUTLET	THERMOCOUPLE WIRE	T-TYPE WIRE	VOLTS	OMEGA	PP-T-24-100
80	CC THROTTLE VALVE INLET	THERMOCOUPLE 2 INCH PIPE	T-TYPE	VOLTS	OMEGA	TQSS-18U-4
81	CC THROTTLE VALVE OUTLET	THERMOCOUPLE 2 INCH PIPE	T-TYPE	VOLTS	OMEGA	TQSS-18U-4

INST #	LOCATION	TYPE	SCALE	SIGNAL	SUPPLIER	PART #
82	CC THROTTLE VALVE OUTLET	THERMOCOUPLE 2 INCH PIPE	T-TYPE	VOLTS	OMEGA	TQSS-18U-4
85	CC EVAPORATOR OUTLET	THERMOCOUPLE 4 INCH PIPE	T-TYPE	VOLTS	OMEGA	TQSS-18U-6
86	CC EVAPORATOR OUTLET	THERMOCOUPLE 4 INCH PIPE	T-TYPE	VOLTS	OMEGA	TQSS-18U-6
87	CC BEARING LINE INLET	THERMOCOUPLE TUBE	T-TYPE	VOLTS	OMEGA	TQSS-116U-3
88	CC BEARING LINE OUTLET	THERMOCOUPLE TUBE	T-TYPE	VOLTS	OMEGA	TQSS-116U-3
89	CC BEARING LINE OUTLET	THERMOCOUPLE TUBE	T-TYPE	VOLTS	OMEGA	TQSS-116U-3
90	GLYCOL SKID EVAPORATOR INLET	THERMOCOUPLE 5 INCH PIPE	T-TYPE	VOLTS	OMEGA	TQSS-18U-6
91	GLYCOL SKID EVAPORATOR OUTLET	THERMOCOUPLE 5 INCH PIPE	T-TYPE	VOLTS	OMEGA	TQSS-18U-6
92	GLYCOL SKID HEX INLET	THERMOCOUPLE 4 INCH PIPE	T-TYPE	VOLTS	OMEGA	TQSS-18U-6
93	GLYCOL SKID HEX OUTLET	THERMOCOUPLE 4 INCH PIPE	T-TYPE	VOLTS	OMEGA	TQSS-18U-6
94	GLYCOL SKID SURGE TANK	THERMOCOUPLE 4 INCH PIPE	T-TYPE	VOLTS	OMEGA	TQSS-18U-6
95	BASEMENT LOOP HEX INLET	THERMOCOUPLE 2 INCH PIPE	T-TYPE	VOLTS	OMEGA	TQSS-18U-4
96	BASEMENT LOOP HEX OUTLET	THERMOCOUPLE 2 INCH PIPE	T-TYPE	VOLTS	OMEGA	TQSS-18U-4
97	FLUE GAS LOOP	VELOCITY FLOW METER	0.4 - 50 m/s	NA	KANOMAX	6162-0204-04
98	LEFT POWER CYCLE FAN	VELOCITY FLOW METER	0-20 m/s	4 to 20 mA	ZIEHL-ABEGG	MAL10
99	RIGHT POWER CYCLE FAN	VELOCITY FLOW METER	0-20 m/s	4 to 20 mA	ZIEHL-ABEGG	MAL10
100	CC CONDENSER 1	VELOCITY FLOW METER	0-20 m/s	4 to 20 mA	ZIEHL-ABEGG	MAL10
101	CC CONDENSER 2	VELOCITY FLOW METER	0-20 m/s	4 to 20 mA	ZIEHL-ABEGG	MAL10
102	CC CONDENSER 3	VELOCITY FLOW METER	0-20 m/s	4 to 20 mA	ZIEHL-ABEGG	MAL10
103	CC CONDENSER 4	VELOCITY FLOW METER	0-20 m/s	4 to 20 mA	ZIEHL-ABEGG	MAL10
104	CC CONDENSER 5	VELOCITY FLOW METER	0-20 m/s	4 to 20 mA	ZIEHL-ABEGG	MAL10

INST #	LOCATION	TYPE	SCALE	SIGNAL	SUPPLIER	PART #
105	CC CONDENSER 6	VELOCITY FLOW METER	0-20 m/s	4 to 20 mA	ZIEHL-ABEGG	MAL10
106	TURBINE BYPASS LINE	VOLUMETRIC FLOW METER, 2 INCH PIPE	20-160 GPM	4 to 20 mA	BADGER METER	XMTR - PFT420/2
107	PC BEARING INLET LINE 1	VOLUMETRIC FLOW METER, 1/4 INCH TUBE	50-500 mL/min	4 to 20 mA	MCMILLAN FLOW	107-5
108	PC BEARING INLET LINE 2	VOLUMETRIC FLOW METER, 1/4 INCH TUBE	50-500 mL/min	4 to 20 mA	MCMILLAN FLOW	107-5
109	PC BEARING INLET LINE 3	VOLUMETRIC FLOW METER, 1/4 INCH TUBE	50-500 mL/min	4 to 20 mA	MCMILLAN FLOW	107-5
110	CC BEARING DRAIN LINE 1	VOLUMETRIC FLOW METER, 1 INCH TUBE	2 GPM	4 to 20 mA	OMEGA	FLMH-1002SS-MA
111	CC BEARING DRAIN LINE 2	VOLUMETRIC FLOW METER, 1 INCH TUBE	2 GPM	4 to 20 mA	OMEGA	FLMH-1002SS-MA
112	CC BEARING INLET	VOLUMETRIC FLOW METER, 1/4 INCH TUBE	50-500 mL/min	4 to 20 mA	MCMILLAN FLOW	107-5
113	CC BEARING INLET	VOLUMETRIC FLOW METER, 1/4 INCH TUBE	50-500 mL/min	4 to 20 mA	MCMILLAN FLOW	107-5
114	CC MAG COUPLING COOLING	VOLUMETRIC FLOW METER, 1/4 INCH TUBE	50-500 mL/min	4 to 20 mA	MCMILLAN FLOW	107-5
115	GLYCOL LOOP EVAPORATOR OUTLET	VOLUMETRIC FLOW METER, 5 INCH PIPE	0.15 – 6.1 m/s	4 to 20 mA	OMEGA	SDI1D1N10-0200
116	PC MASS FLOW METER	MASS FLOW METER	0 - 7.5 kg/s	4 to 20 mA	INSTRUMART	OPTIMASS 1400
117	CC MASS FLOW METER	MASS FLOW METER	0 - 7.5 kg/s	4 to 20 mA	INSTRUMART	OPTIMASS 1400
118	CC MASS FLOW METER	MASS FLOW METER	0 - 7.5 kg/s	4 to 20 mA	INSTRUMART	OPTIMASS 1400
119	FLUE GAS LOOP FAN	POWER METER (CT)	0 - 20 AMPS	NA	EGAUGE	ML-SCT-020-010
120	AIR HEATER	POWER METER (CT)	0 - 200 AMPS	NA	EGAUGE	ML-SCT-200-010
121	PC PUMP	POWER METER (CT)	0 - 5 AMP	NA	EGAUGE	ML-SCT-005-010
122	PC CONDENSER FAN 1	POWER METER (CT)	0 - 10 AMP	NA	EGAUGE	ML-SCT-010-010
123	PC CONDENSER FAN 2	POWER METER (CT)	0 - 10 AMP	NA	EGAUGE	ML-SCT-010-010

INST #	LOCATION	TYPE	SCALE	SIGNAL	SUPPLIER	PART #
124	CC CONDENSER FAN 1	POWER METER (CT)	0 - 10 AMP	NA	EGAUGE	ML-SCT-010-010
125	CC CONDENSER FAN 2	POWER METER (CT)	0 - 10 AMP	NA	EGAUGE	ML-SCT-010-010
126	CC CONDENSER FAN 3	POWER METER (CT)	0 - 10 AMP	NA	EGAUGE	ML-SCT-010-010
127	CC CONDENSER FAN 4	POWER METER (CT)	0 - 10 AMP	NA	EGAUGE	ML-SCT-010-010
128	CC CONDENSER FAN 5	POWER METER (CT)	0 - 10 AMP	NA	EGAUGE	ML-SCT-010-010
129	CC CONDENSER FAN 6	POWER METER (CT)	0 - 10 AMP	NA	EGAUGE	ML-SCT-010-010
130	GLYCOL LOOP PUMP	POWER METER (CT)	0 - 20 AMP	NA	EGAUGE	ML-SCT-020-010
131	LIQUID VAPOR SEPARATOR	LEVEL SENSOR	NA	NA	MCMASTER	46515K71
134	GLYCOL SKID EVAPORATOR OUTLET	THERMOCOUPLE5 INCH PIPE	T-TYPE	VOLTS	OMEGA	TQSS-18U-6
136	PC BEARING TEMPERATURE	2 WIRE RTD	0 - 200°C	0 to 5 V	HONEYWELL	HEL-705-U-1-12-00
137	CC BEARING TEMPERATURE	2 WIRE RTD	0 - 200°C	0 to 5 V	HONEYWELL	HEL-705-U-1-12-00
138	FEMALE MAG COUPLING	THERMOCOUPLE	K-Type	VOLTS	OMEGA	KQSS-18U-12
139	TURBINE WHEEL SIDE	4 WIRE LOAD CELL	0 - 500 lbf	2 mV/V	OMEGA	LC8200-1.00-500
140	COMPRESSOR WHEEL SIDE	4 WIRE LOAD CELL	0 - 500 lbf	2 mV/V	OMEGA	LC8200-1.00-500
141	TURBINE SHAFT	PROX PROBE	10 to 90 mil	4 to 20 mA	METRIX	10026-925-10-02
142	COMPRESSOR SHAFT	PROX PROBE	10 to 90 mil	4 to 20 mA	METRIX	10026-925-10-02
143	TURBINE SHAFT	SPEED PROBE	10 to 90 mil	4 to 20 mA	METRIX	10026-925-10-02
144	COMPRESSOR SHAFT	SPEED PROBE	10 to 90 mil	4 to 20 mA	METRIX	10026-925-10-02
145	TOP TURBINE	ACCELEROMETER	0-80G	100 mV/g (0-8V)	OMEGA	ACC793
146	SIDE TURBINE	ACCELEROMETER	0-80G	100 mV/g (0-8V)	OMEGA	ACC793
147	TOP COMPRESSOR	ACCELEROMETER	0-80G	100 mV/g (0-8V)	OMEGA	ACC793

INST #	LOCATION	TYPE	SCALE	SIGNAL	SUPPLIER	PART #
148	SIDE COMPRESSOR	ACCELEROMETER	0-80G	100 mV/g (0-8V)	OMEGA	ACC793
149	TURBINE SIDE INLET	PRESSURE TRANSDUCER	0-200 PSI	4 to 20mA	OMEGA	PX219-200AI
150	TURBINE SIDE DISCHARGE	PRESSURE TRANSDUCER	0-100 PSI	4 to 20mA	OMEGA	PX219-100AI
151	COMPRESSOR SIDE INLET	PRESSURE TRANSDUCER	0-300 PSI	4 to 20mA	OMEGA	PX219-300AI
152	COMPRESSOR SIDE DISCHARGE	PRESSURE TRANSDUCER	0-300 PSI	4 to 20mA	OMEGA	PX219-300AI
153	GLYCOL LOOP EVAPORATOR OUTLET	VOLUMETRIC FLOW METER, 4 INCH PIPE	0.15 – 6.1 m/s	4 to 20mA	OMEGA	SDI1D1N1 0-0200

Table E-2. Instrument wiring list.

INST #	DAQ CHANNEL	LOCATION	INSTRUMENT TYPE
Analog Input Module 9205 #2, Channels 00-31			
153	9205-2,00	BASEMENT BOILER LOOP	VOLUMETRIC FLOW METER 4 INCH PIPE
143	9205-2,01	TURBINE SPEED	PROX PROBE
144	9205-2,02	COMPRESSOR SPEED	PROX PROBE
136	9205-2,03	PC BEARING TEMPERATURE	2 WIRE RTD
137	9205-2,04	CC BEARING TEMPERATURE	2 WIRE RTD
111	9205-2,05	CC BEARING DRAIN LINE 2	VOLUMETRIC FLOW METER 1 INCH TUBE
110	9205-2,06	CC BEARING DRAIN LINE 1	VOLUMETRIC FLOW METER 1 INCH TUBE
115	9205-2,07	GLYCOL LOOP EVAPORATOR OUTLET	VOLUMETRIC FLOW METER 5 INCH PIPE
114	9205-2,08	CC MAG COUPLING COOLING	VOLUMETRIC FLOW METER 1/4 INCH TUBE
113	9205-2,09	CC BEARING INLET	VOLUMETRIC FLOW METER 1/4 INCH TUBE
112	9205-2,10	CC BEARING INLET	VOLUMETRIC FLOW METER 1/4 INCH TUBE
109	9205-2,11	MAG COUPLING COOLING	VOLUMETRIC FLOW METER 1/4 INCH TUBE
108	9205-2,12	BEARING LUBRICATION	VOLUMETRIC FLOW METER 1/4 INCH TUBE
104	9205-2,17	CC CONDENSER 5	VELOCITY FLOW METER
103	9205-2,18	CC CONDENSER 4	VELOCITY FLOW METER
102	9205-2,19	CC CONDENSER 3	VELOCITY FLOW METER
101	9205-2,20	CC CONDENSER 2	VELOCITY FLOW METER
99	9205-2,21	RIGHT PC FAN	VELOCITY FLOW METER
105	9205-2,22	CC CONDENSER 6	VELOCITY FLOW METER
100	9205-2,23	CC CONDENSER 1	VELOCITY FLOW METER
98	9205-2,24	LEFT PC FAN	VELOCITY FLOW METER
116	9205-2,25	PC MASS FLOW METER	MASS FLOW METER
10	9205-2,26	COMPRESSOR	DIFFERENTIAL PRESSURE TRANSDUCER
32	9205-2,27	ATM PRESSURE TRANSDUCER	BAROMETRIC PRESSURE TRANSDUCER
11	9205-2,28	COOLING CYCLE CONDENSERS	DIFFERENTIAL PRESSURE TRANSDUCER

INST #	DAQ CHANNEL	LOCATION	INSTRUMENT TYPE
6	9205-2,29	RECUPERATOR VAPOR SIDE	DIFFERENTIAL PRESSURE TRANSDUCER
9	9205-2,30	RECUPERATOR LIQUID SIDE	DIFFERENTIAL PRESSURE TRANSDUCER
8	9205-2,31	PC PUMP	DIFFERENTIAL PRESSURE TRANSDUCER
Analog Input Module 9205 #3, Channels 00-31			
13	9205-3,00	GLYCOL LOOP PUMP	DIFFERENTIAL PRESSURE TRANSDUCER
N/A	9205-3,01	AI2-01	EMPTY
1	9205-3,02	FLUE GAS LOOP FAN	DIFFERENTIAL PRESSURE TRANSDUCER
2	9205-3,03	PC EVAP AIR SIDE	DIFFERENTIAL PRESSURE TRANSDUCER
3	9205-3,04	PC EVAP FLUID SIDE	DIFFERENTIAL PRESSURE TRANSDUCER
5	9205-3,05	TURBINE	DIFFERENTIAL PRESSURE TRANSDUCER
12	9205-3,06	CC EVAP GLYCOL SIDE	DIFFERENTIAL PRESSURE TRANSDUCER
4	9205-3,07	TURBINE BYPASS LINE	DIFFERENTIAL PRESSURE TRANSDUCER
7	9205-3,08	PC CONDENSERS	DIFFERENTIAL PRESSURE TRANSDUCER
30	9205-3,09	GLYCOL LOOP EVAPORATOR INLET	PRESSURE TRANSDUCER
N/A	9205-3,10	AI2-10	EMPTY
31	9205-3,11	GLYCOL LOOP TANK	PRESSURE TRANSDUCER
14	9205-3,12	PC EVAP AIR SIDE INLET	PRESSURE TRANSDUCER
149	9205-3,13	TURBINE SIDE INLET	PRESSURE TRANSDUCER
150	9205-3,14	TURBINE SIDE DISCHARGE	PRESSURE TRANSDUCER
151	9205-3,15	COMPRESSOR SIDE INLET	PRESSURE TRANSDUCER
152	9205-3,16	COMPRESSOR SIDE DISCHARGE	PRESSURE TRANSDUCER
23	9205-3,17	CC THROTTLE VALVE INLET	PRESSURE TRANSDUCER
27	9205-3,18	CC BEARING LINE INLET	PRESSURE TRANSDUCER
24	9205-3,19	CC THROTTLE VALVE OUTLET	PRESSURE TRANSDUCER
28	9205-3,20	CC BEARING DRAIN OUTLET	PRESSURE TRANSDUCER
20	9205-3,21	PCBEARING INLET	PRESSURE TRANSDUCER
25	9205-3,22	CC THROTTLE VALVE OUTLET	PRESSURE TRANSDUCER

INST #	DAQ CHANNEL	LOCATION	INSTRUMENT TYPE
29	9205-3,23	CC BEARING DRAIN OUTLET	PRESSURE TRANSDUCER
19	9205-3,24	PC PUMP INLET	PRESSURE TRANSDUCER
18	9205-3,25	PC CONDENSER INLET	PRESSURE TRANSDUCER
15	9205-3,26	PC EVAP FLUID SIDE INLET	PRESSURE TRANSDUCER
26	9205-3,27	CC EVAPORATOR OUTLET	PRESSURE TRANSDUCER
17	9205-3,28	TURBINE INLET	PRESSURE TRANSDUCER
21	9205-3,29	COMPRESSOR INLET	PRESSURE TRANSDUCER
16	9205-3,30	TURBINE BYPASS INLET	PRESSURE TRANSDUCER
22	9205-3,31	CC CONDENSER INLET	PRESSURE TRANSDUCER
Temperature Input Module 9213 #1, Channels 00-15			
37	9213-1,00	PC EVAP INLET FLUID	THERMOCOUPLE, 2 INCH
38	9213-1,01	PC EVAP LEFT OUTLET FLUID	THERMOCOUPLE, 4 INCH
39	9213-1,02	PC EVAP RIGHT OUTLET FLUID	THERMOCOUPLE, 4 INCH
40	9213-1,03	TURBINE BYPASS INLET	THERMOCOUPLE, 2 INCH
41	9213-1,04	TURBINE BYPASS OUTLET	THERMOCOUPLE, 2 INCH
42	9213-1,05	TURBINE INLET	THERMOCOUPLE, 4 INCH PIPE
46	9213-1,06	PC CONDENSER 1 OUTLET	THERMOCOUPLE, 2 INCH
48	9213-1,07	PC CONDENSER 3 OUTLET	THERMOCOUPLE, 2 INCH
59	9213-1,08	COMPRESSOR INLET	THERMOCOUPLE, 4 INCH PIPE
93	9213-1,09	GLYCOL SKID HEX OUTLET	THERMOCOUPLE, 4 INCH PIPE
76	9213-1,10	CC CONDENSER 3 AIR OUTLET	THERMOCOUPLE WIRE
92	9213-1,11	GLYCOL SKID HEX INLET	THERMOCOUPLE, 4 INCH PIPE
60	9213-1,12	COMPRESSOR OUTLET	THERMOCOUPLE, 4 INCH PIPE
57	9213-1,13	PC BEARING INLET	THERMOCOUPLE, TUBE
91	9213-1,14	GLYCOL SKID EVAPORATOR OUTLET	THERMOCOUPLE, 5 INCH PIPE
94	9213-1,15	GLYCOL SKID SURGE TANK	THERMOCOUPLE, 4 INCH PIPE
Temperature Input Module 9213 #2, Channels 00-15			
77	9213-2,00	CC CONDENSER 4 AIR OUTLET	THERMOCOUPLE WIRE
78	9213-2,01	CC CONDENSER 5 AIR OUTLET	THERMOCOUPLE WIRE
79	9213-2,02	CC CONDENSER 6 AIR OUTLET	THERMOCOUPLE WIRE
58	9213-2,03	PC BEARING OUTLET	THERMOCOUPLE, TUBE

INST #	DAQ CHANNEL	LOCATION	INSTRUMENT TYPE
43	9213-2,04	TURBINE OUTLET	THERMOCOUPLE, 4 INCH PIPE
90	9213-2,05	GLYCOL SKID EVAPORATOR INLET	THERMOCOUPLE, 5 INCH PIPE
95	9213-2,06	BASEMENT LOOP HEX INLET	THERMOCOUPLE, 2 INCH PIPE
89	9213-2,07	CC BEARING LINE OUTLET	THERMOCOUPLE, TUBE
88	9213-2,08	CC BEARING LINE OUTLET	THERMOCOUPLE, TUBE
54	9213-2,09	PC PUMP INLET	THERMOCOUPLE, 2 INCH
82	9213-2,10	CC THROTTLE VALVE OUTLET	THERMOCOUPLE, 2 INCH PIPE
134	9213-2,11	GLYCOL SKID EVAPORATOR OUTLET	THERMOCOUPLE, 5 INCH PIPE
47	9213-2,12	PC CONDENSER 2 OUTLET	THERMOCOUPLE, 2 INCH
87	9213-2,13	CC BEARING LINE INLET	THERMOCOUPLE, TUBE
51	9213-2,14	PC CONDENSER 3 AIR SIDE INLET	THERMOCOUPLE WIRE
67	9213-2,15	CC CONDENSER 6 OUTLET	THERMOCOUPLE, 2 INCH
Temperature Input Module 9213 #3, Channels 00-15			
50	9213-3,00	PC CONDENSER 2 AIR SIDE INLET	THERMOCOUPLE WIRE
53	9213-3,01	PC CONDENSER RIGHT AIR SIDE OUTLET	THERMOCOUPLE WIRE
49	9213-3,02	PC CONDENSER 1 AIR SIDE INLET	THERMOCOUPLE WIRE
45	9213-3,03	PC CONDENSER INLET	THERMOCOUPLE, 4 INCH PIPE
55	9213-3,04	RECUPERATOR LIQUID SIDE INLET	THERMOCOUPLE, 2 INCH
56	9213-3,05	RECUPERATOR LIQUID SIDE OUTLET	THERMOCOUPLE, 2 INCH
52	9213-3,06	PC CONDENSER LEFT AIR SIDE OUTLET	THERMOCOUPLE WIRE
62	9213-3,07	CC CONDENSER 1 OUTLET	THERMOCOUPLE, 2 INCH
63	9213-3,08	CC CONDENSER 2 OUTLET	THERMOCOUPLE, 2 INCH
64	9213-3,09	CC CONDENSER 3 OUTLET	THERMOCOUPLE, 2 INCH
65	9213-3,10	CC CONDENSER 4 OUTLET	THERMOCOUPLE, 2 INCH
66	9213-3,11	CC CONDENSER 5 OUTLET	THERMOCOUPLE, 2 INCH
80	9213-3,12	CC THROTTLE VALVE INLET	THERMOCOUPLE, 2 INCH PIPE
81	9213-3,13	CC THROTTLE VALVE OUTLET	THERMOCOUPLE, 2 INCH PIPE
85	9213-3,14	CC EVAPORATOR OUTLET	THERMOCOUPLE, 4 INCH PIPE
86	9213-3,15	CC EVAPORATOR OUTLET	THERMOCOUPLE, 4 INCH PIPE

INST #	DAQ CHANNEL	LOCATION	INSTRUMENT TYPE
Temperature Input Module 9213 #4, Channels 00-15			
N/A	9213-4,00	TC4-00	EMPTY
75	9213-4,01	CC CONDENSER 2 AIR OUTLET	THERMOCOUPLE WIRE
74	9213-4,02	CC CONDENSER 1 AIR OUTLET	THERMOCOUPLE WIRE
73	9213-4,03	CC CONDENSER 6 AIR INLET	THERMOCOUPLE WIRE
72	9213-4,04	CC CONDENSER 5 AIR INLET	THERMOCOUPLE WIRE
71	9213-4,05	CC CONDENSER 4 AIR INLET	THERMOCOUPLE WIRE
70	9213-4,06	CC CONDENSER 3 AIR INLET	THERMOCOUPLE WIRE
69	9213-4,07	CC CONDENSER 2 AIR INLET	THERMOCOUPLE WIRE
68	9213-4,08	CC CONDENSER 1 AIR INLET	THERMOCOUPLE WIRE
36	9213-4,09	PC EVAP INLET AIR	THERMOCOUPLE WIRE
35	9213-4,10	PC AIR HEATER OUTLET	THERMOCOUPLE WIRE
34	9213-4,11	PC AIR HEATER INLET	THERMOCOUPLE WIRE
33	9213-4,12	PC EVAP OUTLET AIR	THERMOCOUPLE WIRE
N/A	9213-4,13	TC4-13	EMPTY
N/A	9213-4,14	TC4-14	EMPTY
138	9213-4,15	FEMALE MAG COUPLING	THERMOCOUPLE
Power Meter E-3000 #1, Channel 113			
122	129.82.106.113	PC CONDENSER FAN 1	POWER METER
123	129.82.106.113	PC CONDENSER FAN 2	POWER METER
124	129.82.106.113	CC CONDENSER FAN 1	POWER METER
125	129.82.106.113	CC CONDENSER FAN 2	POWER METER
Power Meter E-3000 #2, Channel 114			
126	129.82.106.114	CC CONDENSER FAN 3	POWER METER
127	129.82.106.114	CC CONDENSER FAN 4	POWER METER
128	129.82.106.114	CC CONDENSER FAN 5	POWER METER
129	129.82.106.114	CC CONDENSER FAN 6	POWER METER
Power Meter E-3000 #3, Channel 114			
119	129.82.106.115	FLUE GAS LOOP FAN	POWER METER
120	129.82.106.115	AIR HEATER	POWER METER
121	129.82.106.115	PC PUMP	POWER METER
130	129.82.106.115	GLYCOL LOOP PUMP	POWER METER

INST #	DAQ CHANNEL	LOCATION	INSTRUMENT TYPE
Analog Input Module 9205 #1, Differential Channels 00-31			
139	9205-1,00-08	TURBINE WHEEL SIDE	4 WIRE LOAD CELL
140	9205-1,01-09	COMPRESSOR WHEEL SIDE	4 WIRE LOAD CELL
Vibration Input Module 9230 #1, Channels 00-02			
148	9230-1,00	SIDE COMPRESSOR	ACCELEROMETER
145	9230-1,01	TOP TURBINE	ACCELEROMETER
146	9230-1,02	SIDE TURBINE	ACCELEROMETER
Vibration Input Module 9230 #2, Channels 00-02			
147	9230-2,00	TOP COMPRESSOR	ACCELEROMETER
N/A	9230-2,01	VIBE2-01	EMPTY
N/A	9230-2,02	VIBE2-02	EMPTY
Not Recorded			
96	NO RECORDING	BASEMENT LOOP HEX OUTLET	THERMOCOUPLE, 2 INCH PIPE
97	NO RECORDING	FLUE GAS LOOP	VELOCITY FLOW METER
141	NO RECORDING	TURBINE SHAFT	PROX PROBE
142	NO RECORDING	COMPRESSOR SHAFT	PROX PROBE

APPENDIX F. TEST FACILITY PROCEDURES

This appendix describes information required to safely operate the 250 kW_{th} scale TCCS test facility. The first section presents the safety hazards involved with operation and the relevant emergency scenario mitigation techniques. The next section describes the charge procedure for each of the three fluid systems: power cycle, cooling cycle, glycol loop. Section F.4 describes system operation procedure including emergency shut-down procedures. Finally, Section F.5 describes the drain procedures for the three fluid systems.

F.1. System Safety Information

The TCCS has several systems to ensure safe operation and mitigate any potential hazards in emergency scenarios. The scenarios and safety systems are also summarized in the document "TCCS_SAFETY_SYSTEMS". This section includes safety warnings shown in the formats shown in Figure F-1. To maintain personal and product safety, read, understand, and follow all safety messages.

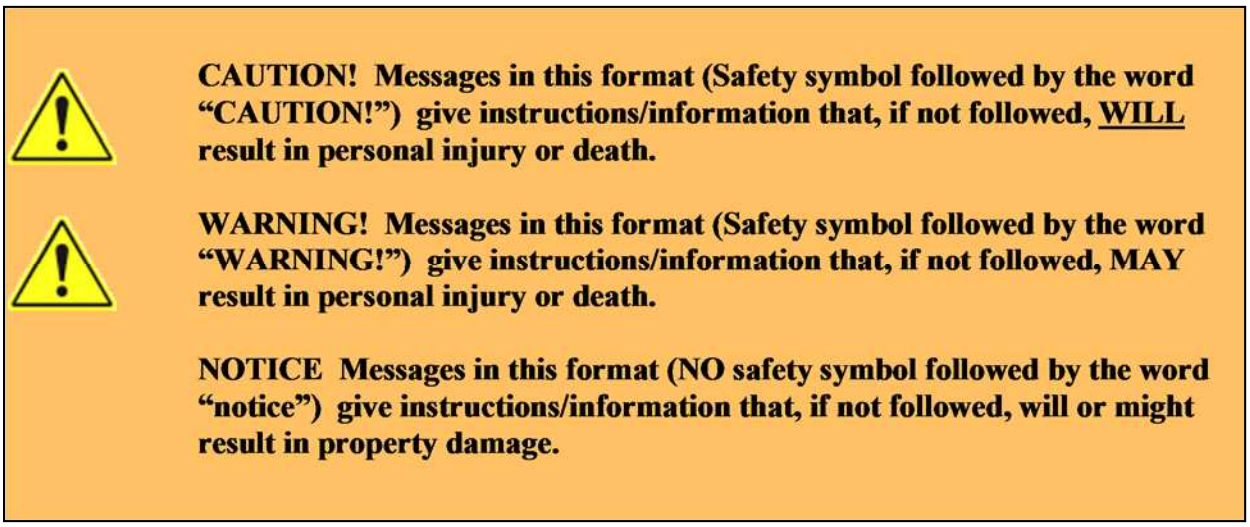

Figure F-1. Safety messages used in this manual.

F.1.1 Emergency Procedures

Four principle hazards have been identified with the potential to cause catastrophic damage to the TCCS and the Powerhouse: fire and or detonation, asphyxiation, explosion, and electrocution. In some cases the emergency scenario could cause serious injury or death.

F.1.1.1. Fire and or Detonation

A major fire and or detonation risk is associated with operating the TCCS due to the flammability of the cooling cycle fluid, R152a. Two high performance refrigerant monitoring probes (Draeger Part # 4544221) are installed in the TCCS. One monitor is located above while the other is below the facility. Fire extinguishers are available for small fires and the Powerhouse thermally-activated sprinkler system is available in case of large fire. The specific actions in an emergency event are shown in Table F-1.

Table F-1. Action steps in various leak level scenarios.

Monitor State	Action
10% Lower Explosive Limit	• Low level alarm • Yellow strobe, horn • Powerhouse staff text • Plant moves to safe shutdown
50% Lower Explosive Limit	• High level alarm • Red strobe, horn • Building evacuation alarm activation • Powerhouse staff text • R152 emergency blowdown activation • Immediate system shutdown

F.1.1.2. Asphyxiation

There is a significant asphyxiation risk by operating the TCCS due to the large amount of refrigerant present in both the cooling and power cycles. In a large refrigerant leak, the air could become flooded with refrigerant vapor which would displace the oxygen available: persons within that area would be at risk of asphyxiation. Do not continue working on the TCCS if there are any

symptoms of asphyxia including: difficulty breathing, rapid pulse, high blood pressure, bluish coloration of the face, swollen veins in the head or neck, convulsions, paralysis, or slow loss of consciousness. Should any of these symptoms manifest themselves, leave the facility immediately.

WARNING! Refrigerants are denser than air. If a significant leak is detected, persons operating the TCCS should not be on or below the mezzanine. Failure to comply with these warnings could result in asphyxiation which leads to difficulty breathing, loss of consciousness, and death.

F.1.1.3. Explosion

The main risk of explosion is due to over-pressurization of the power or cooling cycles which could cause a rupture of process piping or pressure vessels. To mitigate the risk of over-pressurization, actively monitor the pressure in each loop through the DAQ system. There are varying actions required at different pressurization states shown in Table F-2 depending on the max allowable working pressure (MAWP) for each loop. The MAWP is based on the system operating conditions (in off-design conditions, the cooling cycle may reach a MAWP as high as 1061 kPa or 154 psi). If the system becomes over-pressurized, immediate steps should be taken to safely shutdown the system. Follow the operating procedures located in Section F.4.

Table F-2. Action steps in various over-pressurizations scenarios.

Pressurization State	Action
105% MAWP	• DAQ issues low level alarm • Yellow strobe
120% MAWP	• DAQ issues high level alarm • Red strobe, horn • Plant moves to safe shutdown
150% MAWP	• DAQ issues high level alarm • Red stobe, horn • Emergency pneumatic blowdown valve actuated
200% MAWP	• DAQ issues high level alarm • Red stobe, horn • Rupture disk breaks, causing immediate blow down

F.1.1.4. Electrocution

Electrocution is a hazard associated with the TCCS due to high voltage and current electrical feeds required to power several electrical devices. Table F-3 shows a list of the power feeds used by the TCCS. To accommodate the danger associated with the electrical power, all electrical installations adhere to relevant NEC code and were installed by Collins Control & Electrical Inc. The system has been designed with extensive overcurrent protection and fuses/breakers that have been appropriately sized.

WARNING! An electrical fire-rated fire extinguisher should always be present while operating the TCCS. If an electrical fire should occur, use the extinguisher if safe to do so. Do not use a non-electrically rated extinguisher as that could make the fire worse. Failure to comply with these warnings could result in personal injury or death.

Table F-3. Power feed list for electrical components in the TCCS.

Feed From	Feed To	Power Feed
Powerhouse Switchboard	TCCS Switchboard	480 VAC 3-Phase, 800 Amp Breaker
TCCS Switchboard	Air Heater Disconnect	480 VAC 3-Phase, 200 Amp Breaker
TCCS Switchboard	Main Breaker Panel	480 VAC 3-Phase, 250 Amp Breaker
Main Breaker Panel	Step-Down Transformer	480 VAC 3-Phase, 40 Amp Breaker
Main Breaker Panel	Glycol Pump	480 VAC 3-Phase, 60 Amp Breaker
Main Breaker Panel	Power Cycle Pump	480 VAC 3-Phase, 15 Amp Breaker
Main Breaker Panel	Flue Loop Fan	480 VAC 3-Phase, 15 Amp Breaker
Main Breaker Panel	Power Meters	480 VAC 3-Phase, 15 Amp Breaker
Step-Down Transformer	Six Condenser Fans	240 VAC 3-Phase
Step-Down Transformer	Two Condenser Fans	240 VAC 3-Phase
Distribution Panel	DAQ System	120 VAC, 10 Amp Breaker
Distribution Panel	Four Fan Controllers	120 VAC, 10 Amp Breaker
Distribution Panel	Three Mass Flow Meters	120 VAC, 10 Amp Breaker
Distribution Panel	Bearing Line Pump Air Velocity Sensor UPS to Solenoid Valves	120 VAC, 10 Amp Breaker
Distribution Panel	Refrigerant Heater	120 VAC, 10 Amp Breaker

F.2. Using the LabVIEW Interface

LabVIEW is the National Instruments monitoring and control program which directly interfaces with the National Instruments data acquisition hardware for the TCCS. Kirk Evans was the primary programmer of the LabVIEW interface.

To access the software, first make sure LabVIEW is properly installed on your machine. Open the LabVIEW project "CoolTurboDAQ Project2" and then open the Virtual Instrument (VI) "TurboCoolRT.vi". This VI controls the real time updating of the instruments: click "RUN" to start the VI. Next, open the "Main.vi" program which is the user interface to read and record the instruments: click "RUN" to start the VI. There are several tabs along the top of the "Main.vi" interface that show instruments located in different sections of the TCCS. The Overview tab displays a modified version of the process flow diagram. The Turbo-Compressor tab shows a model of the turbo-compressor and displays the inputs and output instruments. The Condensers tab shows the condensing heat exchangers and fans with the appropriate flow rates, power, and temperatures. The Flue Gas Simulator tab shows the pressures and temperatures within the flue gas loop. The Glycol Loop tab shows the conditions in the glycol loop. The Trends tab shows the instrument data changes over a short time interval. The tab labeled Page 7 is only used as a placeholder for the accelerometer logging button.

To record data, click the File/Record button located in the lower left corner of the "Main.vi" interface. The data rate and total time of log can be changed to any value, but a typical value is a 2 Hz data rate. After clicking the button, a pop-up window will appear to name the data file. To stop the log before the designated time, select the Stop Log button. To log accelerometer data simply click the Save button under the "Acc Data" label: the button will turn orange when pressed. The accelerometer data will save to the file location "Accelerometer Data" located in the "Data"

folder of the TCCS T: Dive. The accelerometer data will continuously record at 12.6 kS/s until the Save button is pressed a second time.

The flue gas loop air heater is the only control aspect integrated in the LabVIEW program. A slider bar controlling the percentage power of the heater is shown on the left side of the screen near the logger section. Simply adjust the heater output by percentage to control the air heater power input. There is also an automation option for controlling the air heater, operating by using the loop temperature as a set point. Input the desired air temperature into the boiler and select the "Heater Automation" button to start the heater automation.

F.2.1 Changing Calibration Parameters

If an instrument is replaced or requires re-calibration, the following section will provide the steps to adjust the calibration parameters.

Step 1: Open an Internet Explorer browser (other browsers not supported)

Step 2: Go to the address 129.82.106.111 and click login. The standard user name and password combination is 'Admin' and Test430$, respectively.

Step 3: Go to the file explorer section, and click C: drive folder so the pressure and temperature calibration factor files appear. Open the text files to view the calibration details.

Step 4: Enter in the scaling for the desired instrument in mx+b format based on column

Instrument # Channel # m b

Example: If the instrument outputs a 0-5 V source over a range of 0-15 m/s, calculate the "m" value by taking the instrument range and dividing it by the voltage range.

$$\frac{InstrumentRange}{VoltageRange} = \frac{15 \, m/s}{5V} = 3 \frac{m/s}{V}$$

Then find the "b" value by using the point 0 V and 0 m/s to find a "b" of 0.

F.3. Charge Procedure

This section documents the steps to charge the cooling and power cycles with fluid. A document titled "CSU_FLUIDFILLPROCEDURE_V2" is located in the "TCCS Design Documents" folder on the TCCS T: Drive. The amount of fluid charge for each cycle depends on the current system configuration and fluid operating conditions. Table F-4 shows the amount of charge required (kg of fluid) for the baseline design condition and R134a design condition. The charge amounts were calculated by considering the fluid density and volume at each state point in the loop. The two-phase heat exchangers were assumed to have an even distribution of liquid and vapor.

Table F-4. Charge amount for the baseline and R134a design conditions

	Baseline Design Point	**R134a Design**
Power Cycle		
Piping	76.8	76.8
Component	113.3	113.3
Total	190.1	190.1
Cooling Cycle		
Piping	59.8	59.8
Component	131.6	176.9
Total	191.4	258.1

F.3.1 Cooling Cycle Fill Procedure

The following steps should be followed to successfully fill the cooling cycle with refrigerant. Place each refrigerant tank on the mass scale (Part # GFK 330aH).

Step 1: Attach fill line to flange top

Ensure the connections are properly tightened at the fill port. Open Valve 17 (cooling cycle system fill port) and the fill line swage valve (Valve S23).

Step 2: Attach vacuum pump to port tee

The fill line follows the emergency vent piping next to the flue loop and stop at the third floor balcony. The line will have a tee. Take one side of the tee and connect it to the vacuum pump, Model DV-85N (JB Industries), by attaching the line to Valve S26 and then continuing to the pump with appropriate fittings. Ensure there is enough oil in the vacuum pump and that the oil is clear. If the oil is cloudy, water vapor is trapped in the oil tank. If there is vapor, drain the oil tank and refill before operating the vacuum pump. Use Ultra Grade 19 Oil (H11025013) made especially for vacuum pumps by Edwards Vacuum.

Step 3: Attach gear pump and refrigerant tank to other side of tee

Connect the gear pump to the tube extending from Valve S27. The gear pump is a Series GB Micropump (Part# GB-P35.JVS.A-B1) driven by an A-Mount Console Drive manufactured by Cole Parmer (Part#EW-75211-10). Connect the other side ofo the pump to Valve 30.

The cooling cycle should be filled with liquid to expedite the filling and keep the system pressure low. The best way to fill with only liquid is to invert the tank and attach the fill line to the vapor outlet. With the refrigerant tank standing upright, slide the metal tank stand over the top so the base of the stand is at the outlet of the tank. Tilt the tank horizontally and rest it on the floor. Now lift the opposite end of the stand so the base of the stand is on the floor and the tank is inverted. Use a strap to compress the stand legs to the tank. Place the tank/stand on the scale. Connect the tube outlet from Valve S30 to the vapor outlet of the tank.

Step 4: Operate vacuum pump

Ensure Valve S27 (before gear pump) is closed and S26 is open (vacuum pump). Power on the vacuum pump to draw vacuum on the cooling cycle. Use the vacuum pressure gauge located on instrument port 11 (after the cooling cycle liquid manifold) to measure vacuum in the cooling cycle. When vacuum pressure gauge reads approximately -85 kPa (-25 in Hg) then the cooling cycle is at vacuum. Close Valve S26 (vacuum pump) and shut off the vacuum pump. Disconnect the pump by unthreading the Swagelok tube port from the un-vacuumed side of Valve S26.

Step 5: Fill system with refrigerant

With the tank on the mass scale and the scale powered on, record the initial weight of the tank plus stand. Ground the scale, tank, and stand setup to the building by connecting a metal wire to a metal source on the building to prevent static buildup.

WARNING! Ground the scale/tank to the Powerhouse to prevent static electricity buildup. The static electricity has the potential to build-up enough charge to cause sparking. If R152a is being used, the fluid could ignite or explode causing injury or death.

Ensure Valve S27 and S30 are open. Since the tank is upside down, open the vapor valve on the refrigerant tank to start the liquid flow into the system. The mass of the tank will start dropping. When flow begins to slow down, turn on the gear pump to draw liquid into the cooling cycle. Continue to add liquid into the system until the desired mass is reached, then close the refrigerant tank vapor valve. Watch as the pump pulls the remaining liquid from the line (1-2 seconds) and then in sequence: close Valve S30, turn off the pump,

and close Valve S27. It is generally recommended to add 50 kg of liquid from each 125 lb size refrigerant tank.

If the desired mass is not achieved, proceed to step 6, if it has been reached, go to Step 7.

Step 6: Replace refrigerant tank if necessary

If more charge is required in the cooling cycle, the following steps show how to switch tanks and continue filling. Record the current amount of mass in the system by reading the difference between the initial tank mass and the final tank mass. Ensure Valve S30 is closed. Unthread the Swagelok tube connector from the refrigerant tank. Remove the tank stand from the scale and lower it horizontally to the ground. Release the strap and slide the tank out of the stand. Follow the second part of step 3 to load the new refrigerant tank onto the scale. Once the new tank is on the scale, record the mass and follow step 5 to continue filling. The pump will be required to add liquid into the system.

Step 7: Shut and close the fill lines

If the desired system charge is achieved, close Valve 17 and Valve S23 to close the fill port. Some refrigerant may be present in the short line that runs between Valves S27 and S30 through the gear pump. Drain this refrigerant into a tank or bucket by opening valve S30 and directing the flow into the bucket. Any liquid refrigerant will immediately vaporize.

WARNING! This step includes exposure to hazardous refrigerant. Do not inhale any portion of drained refrigerant. Wear a respirator to reduce the chance of inhaling evaporating refrigerant. Wear protective gloves to avoid frostbite from handling refrigerant. If R152a is being used, do not drain fluid

around any ignition source and do not allow any sparking. Failure to comply with these warning could cause personal injury or death.

Disconnect the vacuum pump and gear pump by unthreading the tube connectors from the unfilled sides of Valves S26 and S27.

F.3.2 Power Cycle Fill Procedure

The following steps should be taken to fill the power cycle with fluid. Place the HFE-7000 tank on the mass scale (Part # GFK 330aH).

Step 1: Attach fill line to fill port flange top

Ensure connections are properly tightened at the fill port. Open Valve 1 (power cycle fill port) and the fill line swage valve (Valve S22).

Step 2: Attach vacuum pump to port tee

The fill line follows the emergency vent piping next to the flue loop and stop at the third floor balcony. The line will have a tee. Take one side of the tee and connect it to the vacuum pump Model DV-85N (JB Industries) by attaching it through Valve S25. Ensure there is a proper level of oil in the vacuum pump and that the oil is clear. If the oil is cloudy, there is most likely water vapor trapped in the oil tank. If there is vapor, drain the oil tank and refill before pump operation. Use Ultra Grade 19 Oil (H11025013) made especially for vacuum pumps by Edwards Vacuum.

Step 3: Attach Fill-Rite rotary vane pump hose outlet

Open the 2 inch cap on the HFE-7000 fuel tank. Be cautious of pressure buildup within the tank if the ambient temperature is warm: opening the tank after a prolonged period could result in HFE-7000 gas build-up in the tank. Extend the dip stick on the Fill-Rite Rotary Vane Pump (Part # FR610G) all the way and plunge it into the tank. Thread

the pump onto the outlet port of the tank. Finally, attach Valve S24 to the Swagelok tube connector on the outlet of the pump.

Step 4: Operate vacuum pump

Ensure Valve S24 (before HFE-7000 fuel pump) is closed and S25 is open (vacuum pump). Power on the vacuum pump to pull the air from the power cycle. Use the vacuum pressure gauge located on instrument port 8 (just before power cycle pump) to measure vacuum in the power cycle. When the pressure gauge reads approximately -85 kPa (-25 in H2O) then the power cycle is at vacuum. Close Valve S25 (vacuum pump) and shut off the vacuum pump. Disconnected the pump by unthreading the Swagelok tube connector from the un-vacuumed side of Valve S25.

Step 5: Fill system with HFE-7000

Record the initial weight of the tank using the mass scale. Open the vent port on the HFE-7000 tank. Open Valve S24. The liquid will syphon liquid into the loop. When the syphon slows, power on the Fill-Rite pump to force liquid into the system. Continue adding liquid until the desired mass is reached, then shut off the pump and close Valve S24. The lower mass limit for each tank (including pump weight) is approximately 35 kg.

NOTICE! Do not operate the pump below the 35 kg limit because the pump will start drawing air into the loop and obliterate the vacuum level in the loop, severely hampering the operation of the system.

If the desired power cycle charge is not achieved, proceed to step 6, if it has been reached, go to Step 7.

Step 6: Swap HFE-7000 tanks if necessary

If the power cycle requires more mass after the initial tank fill, follow these steps to switch tanks and continue filling. Record the current amount of mass in the system by reading the difference between the initial and final tank masses. Ensure Valve S24 is closed. Replace the vent cap on the HFE-7000 tank. Disconnect the HFE-7000 pump by unthreading the Swagelok tube connector from the unfilled side of Valve S24. Remove the pump from the tank by unthreading and lifting it out of the tank. Replace the cap on the HFE-7000 tank to prevent vapor escape. Remove the tank from the scale and replace with the full tank. Attach the pump to the new tank by removing the tank cap, threading the pump on, and attaching Valve S24. Follow Step 5 to complete the fill procedure.

Step 7: Shut and close the fill lines

If the desired system charge is achieved, close Valve 1 and Valve S22. Disconnect the vacuum pump and Fill-Rite pump by unthreading the tube connectors from the unfilled sides of Valves S24 and S25.

F.3.3 Glycol Loop Fill Procedure

Take the following steps to fill the glycol loop with 30:70 propylene glycol: water.

Step 1: Prepare propylene glycol fluid

A mixture of 30:70 propylene glycol:water should be used in the glycol loop. Use either premixed fluid or create a new mixture with propylene glycol concentrate. The propylene glycol is Dowfrost Heat Transfer Fluid manufactured by the Dow Chemical Company and purchased through Chempoint was used for the glycol loop.

Step 2: Attach pump to glycol drum

Extend the dip stick on the Fill-Rite Rotary Vane Pump (Part # FR610G) all the way and plunge it into the tank. Thread the pump onto the outlet port of the premixed propylene glycol drum. Attach tubing or hose from the outlet of the pump to the fill port valve (Valves 36 and 37) on top of the glycol surge tank and open those valves.

Step 3: Operate glycol pump

Open Valve 34 and 35 at the top of the heat exchangers to allow air to vent as the loop is filled. Open the vent cap on the propylene glycol drum. Power on the rotary vane pump to fill the glycol loop. Continue filling the glycol tank until the liquid level is halfway in the highest sight glass in the tank. Continue filling until either the desired fill level is achieved or the propylene glycol drum is empty. If the desired level is reached go to step 5, if the drum is empty go to step 4.

Step 4: Swap glycol drums if necessary

Power off the pump and allow the glycol in the fill line to drain back into the drum. Unthread the pump from the drum and reattach it to the next premixed drum. Repeat step 3 with the new drum.

Step 5: Detach fill lines and close valves

Power off the pump and allow the glycol in the fill line to drain back into the drum. Close Valves 34 – 37 to close the glycol loop. Detach the fill lines. The glycol loop is now ready for operation.

F.4. Operation Procedure

The following section outlines the steps to successfully operate the TCCS.

WARNING! One operator should monitor the LabVIEW data acquisition program at all times during TCCS operation. Record data during any operating event and properly label the data in the TCCS "DATA" folder on the TCCS T: Drive. Failure to monitor or record data could result in system failure leading to any of the safety hazards listed in Section F.1.

F.4.1 Turbo-Compressor Operating and Maintenance Hazards

The turbo-compressor is a rotating machine that has several operating and maintenance hazards. Damage to the machine or operator injury could occur if the proper procedures are not followed while operating the turbo-machine.

Before operating the turbomachinery, perform the following checks and operations:

1. Be sure there are no loose objects or large particles in the upstream piping that could get caught in the impeller clearances and cause damage to the pump.
2. Ensure that all pump mounting bolts are securely fastened.
3. The turbomachinery was not designed to operate under piping loads or shock loading (thermal or impact). Ensure that piping loads and heavy shock loads are not encountered in service.
4. The turbomachinery maximum design speed is 30,000 rpm. The customer is responsible for ensuring rotating machinery speeds do not exceed maximum speed.
5. Successful operation of the turbomachine assumes that various components see design conditions (gas only in compressor wheel, gas only in turbine wheel, sufficient bearing lubrication, etc.). If off design conditions are experienced, the turbomachine may see some

form of mechanical damage. Table F-5 presents hypothetical implications to off design conditions. The customer is responsible for monitoring and controlling critical variables to ensure safe machine operation.

6. Operating at speeds in excess of design speed will reduce bearing life and is not recommended. Operating at speeds less than design speed will extend the life of the bearings.

WARNING! Turbine housing will exceed 200 F. Failure to wear personal protective equipment may result in personal injury.

WARNING! Before performing any maintenance on the unit, ensure that the loop is depressurized and is safe to touch. Ensure adequate ventilation as there is an asphyxiation risk.

It is recommended that any maintenance on the BNTC-07-000 turbomachine is performed by Barber-Nichols personnel. Please contact Barber-Nichols if there is a need to perform maintenance. Table F-5 below shows some of the turbo-machine operational issues that may occur and the possible mitigation strategies to overcome those difficulties.

F.4.2 Start-Up

Prior to start-up of the TCCS, the Swagelok and pipe valves should be oriented in the positions shown in Table F-6 and Table F-7. Refer to the PFD in Appendix B for valve location.

Step 1: Turn on component "011-PC Evaporator Fan"

The flue gas loop fan VWBD 43W7, manufactured by Aerovent has a 15 HP motor powered and controlled by an "Altivar 212" Variable Speed Drive (VFD) manufactured by

Table F-5. Turbo-machine off-design operation implications.

	Situation	Result	Mitigation
1	Insufficient bearing lubrication / cooling	Damaged or overheated bearing	Ensure bearing lines has filter, sufficient flow, and driving pressure
2	Liquid in turbine	Limited achievable design speed	Monitor pressure and temperature entering turbine. Install liquid trap upstream of turbine.
3	Excessive compressor load due to liquid in compressor wheel or mechanical rub	Overspeed turbine shaft	Monitor turbine and compressor speed at all times. Bypass line on turbine or quick method to unload turbine wheel
4	Female magnetic coupling overheat	Loss of torque transfer. Compressor overspeed.	Monitor coupling cavity temperature. Employ coupling liquid cooling if required. Monitor flow, coupling cavity temperature, and speed to ensure adequate balance of cooling versus turbomachine performance
5	Male magnetic coupling overheat	Loss of torque transfer. Compressor overspeed.	Ensure male mag coupling cooling line is open at all times. Consult Barber-Nichols for any changes to limit male mag coupling cooling.
6	Overpressure	Mechanical damage to components	Monitor pressures and temperatures in and around machine at all times. Set pressure relief valves accordingly to ensure system safety. Note: the barrier can requires attention to detail with regards to allowable pressure delta.

Schneider Electric. More information for the fan and VFD combination is located in Section 4.1.2 or in the Equipment Data Sheets folder located on the TCCS T: Drive. The VFD has a 15 amp breaker in the Distribution Panel which should be in the "ON" position. The power switch for the fan is located in the CT Enclosure box: turn the switch to the "ON" configuration. The Altivar 212 VFD, located in the Flue Loop Fan box, will be powered on. Ensure the green LED light above the LOC/REM button is lit. If it is not lit, press the LOC/REM button: this configures the fan to local operation mode. Finally, to turn the fan on, press the Run button, and the fan will begin to ramp up.

Table F-6. Swagelok valve configuration at start-up operation.

VALVE NUMBER	VALVE POSITION	VALVE SIZE	VALVE TYPE	APPLICATION	CYCLE
S1	CLOSED	1/4 INCH	METERING	MAG COUPLING INLET	POWER
S2	CLOSED	1/4 INCH	METERING	BEARING INLET	POWER
S3	CLOSED	1/4 INCH	METERING	BEARING INLET	POWER
S4	CLOSED	1/4 INCH	BALL	COOLING INLET LINE	POWER
S5	CLOSED	1/4 INCH	BALL	MAG COUPLING INLET SHUTOFF	POWER
S6	CLOSED	1/2 INCH	BALL	FILL LEVEL SIGHT TUBE	POWER
S7	CLOSED	1/2 INCH	BALL	FILL LEVEL SIGHT TUBE	POWER
S8	CLOSED	1 INCH	BALL	VAPOR OUTLET BEARING ACCUM	POWER
S9	OPEN	1 INCH	BALL	LIQUID OUTLET BEARING ACCUM	POWER
S10	OPEN	1/4 INCH	BALL	BEARING PUMP INLET	COOLING
S11	CLOSED	1/4 INCH	BALL	BEARING PUMP BYPASS	COOLING
S12	OPEN	1/4 INCH	BALL	BEARING PUMP OUTLET	COOLING
S13	OPEN	1/4 INCH	METERING	BEARING INLET	COOLING
S14	OPEN	1/4 INCH	METERING	BEARING INLET	COOLING
S15	CLOSED	1/4 INCH	METERING	COMPRESSOR RECIRC	COOLING
S16	CLOSED	1 INCH	BALL	VAPOR OUTLET BEARING ACCUM	COOLING
S17	OPEN	1 INCH	BALL	LIQUID OUTLET BEARING ACCUM	COOLING
S18	OPEN	1 INCH	BALL	LIQUID OUTLET BEARING ACCUM	COOLING
S19	CLOSED	1/2 INCH	BALL	FILL LEVEL SIGHT TUBE	COOLING
S20	CLOSED	1/2 INCH	BALL	FILL LEVEL SIGHT TUBE	COOLING
S21	CLOSED	1/4 INCH	BALL	COMPRESSOR RECIRC	COOLING
S22	CLOSED	3/4 INCH	BALL	TURBINE FILL LINE	POWER
S23	CLOSED	3/4 INCH	BALL	COMPRESSOR FILL LINE	COOLING
S24	CLOSED	3/4 INCH	BALL	VACUUM PUMP	POWER
S25	CLOSED	3/4 INCH	BALL	HFE7000 FUEL PUMP	POWER
S26	CLOSED	3/4 INCH	BALL	VACUUM PUMP	COOLING
S27	CLOSED	3/4 INCH	BALL	REFRIGERANT GEAR PUMP	COOLING
S28	OPEN	1/4 INCH	BALL	TURBINE VENT LINE	POWER
S29	OPEN	1/4 INCH	BALL	COMPRESSOR VENT LINE	COOLING
S30	CLOSED	1/4 INCH	BALL	REFRIGERANT TANK	COOLING
S31	CLOSED	1/2 INCH	BALL	DRAIN REFRIGERANT TANK	COOLING

Table F-7. Pipe valve configuration at start-up operation.

VALVE NUMBER	VALVE POSITION	VALVE SIZE	VALVE TYPE	APPLICATION	CYCLE
1	CLOSED	2 INCH	BALL	FILL PORT	POWER
2	OPEN	2 INCH	BALL	VENT LINE	POWER
3	CLOSED	2 INCH	EBV	EMERGENCY BLOWDOWN	POWER
4	CLOSED	4 INCH	BALL	TURBINE ISOLATION	POWER
5	CLOSED	4 INCH	BALL	TURBINE ISOLATION	POWER
6	CLOSED	1/2 INCH	BALL	DRAIN PORT	POWER
7	CLOSED	2 INCH	BALL	FILTER ISOLATION	POWER
8	OPEN	2 INCH	BALL	FILTER ISOLATION	POWER
9	OPEN	2 INCH	BALL	FILTER ISOLATION	POWER
10	CLOSED	2 INCH	BALL	FILL PORT	POWER
11	CLOSED	1/2 INCH	BALL	DRAIN PORT	POWER
12	OPEN	2 INCH	BALL	VENT LINE	COOLING
13	OPEN	2 INCH	BALL	BURST DISK 1	COOLING
14	CLOSED	2 INCH	EBV	EMERGENCY BLOWDOWN	COOLING
15	CLOSED	2 INCH	BALL	BURST DISK 2	COOLING
17	CLOSED	2 INCH	BALL	FILL PORT	COOLING
18	CLOSED	1/2 INCH	BALL	DRAIN PORT	COOLING
19	OPEN	2 INCH	BALL	FILTER ISOLATION	COOLING
20	CLOSED	2 INCH	BALL	FILTER ISOLATION	COOLING
21	OPEN	2 INCH	BALL	FILTER ISOLATION	COOLING
22	CLOSED	4 INCH	BALL	LIQ-VAP ISOLATION	COOLING
23	OPEN	2 INCH	BALL	LIQ-VAP ISOLATION	COOLING
24	OPEN	2 INCH	BALL	LIQ-VAP ISOLATION	COOLING
25	OPEN	4 INCH	BALL	COMPRESSOR ISOLATION	COOLING
26	OPEN	2 INCH	BALL	GLYCOL BYPASS	GLYCOL
27	OPEN	1.5 INCH	GLOBE	TURBINE THROTTLE VALVE	POWER
28	OPEN	1/2 INCH	GLOBE	THROTTLE VALVE	COOLING
29	OPEN	1/2 INCH	GLOBE	THROTTLE VALVE	COOLING
30	CLOSED	2 INCH	BALL	BOILER WATER INLET	GLYCOL
31	CLOSED	2 INCH	BALL	BOILER WATER RETURN	GLYCOL
32	CLOSED	2 INCH	BALL	BASEMENT WATER FILL	GLYCOL
33	CLOSED	1/2 INCH	BALL	DRAIN VALVE FOR VAC	COOLING
34	CLOSED	3/4 INCH	BALL	FILL PORT	GLYCOL
35	CLOSED	3/4 INCH	HOSE	FILL PORT	GLYCOL
36	CLOSED	3/4 INCH	BALL	FILL PORT	GLYCOL
37	CLOSED	3/4 INCH	HOSE	FILL PORT	GLYCOL
38	CLOSED	3/4 INCH	BALL	DRAIN PORT	GLYCOL
39	CLOSED	3/4 INCH	HOSE	DRAIN PORT	GLYCOL
40	CLOSED	1-1/2 INCH	BALL	DRAIN PORT	GLYCOL
41	CLOSED	3/4 INCH	HOSE	DRAIN PORT	GLYCOL
42	CLOSED	2 INCH	BALL	DRAIN PORT	GLYCOL
43	CLOSED	3/4 INCH	HOSE	DRAIN PORT	GLYCOL

The VFD is programmed with an upper limit frequency of 60 Hz, but is set to 58 Hz to achieve the design point flow rate in the loop of 2.35 m/s. If a different frequency is required, press the UP/DOWN arrows to adjust the frequency. To measure the air flow rate, power on the Anemomaster main unit located above the uninterrupted power supply. The flow-rate read-out is meters per second. Adjust the fan frequency until the desired air flow rate is achieved. The current maximum frequency is set to 60 Hz, but, if required, the VFD can provide a higher frequency rating by reprogramming the Upper Frequency Limit (UL) and Maximum Allowed Frequency (FH). If further programming is required, refer to document "ATV212_programming_manual_EN_S1A53832_03 - FlueFanVFD".

Step 2: Turn on component "001-Air Heater"

The air heater in the flue gas loop, manufactured by Winair Company, is powered by its own 200 amp 480 VAC 3-phase power source directly fed from the switchboard. Switch the air heater electrical disconnect to the "ON" configuration.

The heater load is controlled through the LabVIEW VI. On the left side of the "Main" page is a slider bar labeled "Heater Output". Slide the bar or enter a designated percentage to adjust the power output of the heater. Start the heater at 75-100% during ramping phase and adjust the percentage as necessary until the temperature within the loop reaches 106°C. As the system operates, adjust the heater power accordingly to maintain an entering temperature of 106°C into the boiler heat exchanger.

To automate the air heater, set the desired boiler input temperature by typing it into the window. Select the "Heater Automation" button to automate the heater. The control button will adjust the heater power to match I36 to the desired temperature. To return to normal heater operation, press the "Heater Automation" button.

NOTICE! If the heater control malfunctions, the temperatures in the flue duct could increase rapidly. See Table F-10 to prevent damage to the facility.

Step 3: Turn on two components "013-PC Condenser Fan"

The power cycle fans (model ZN091-ZIQ.GG, manufactured by Ziehl-Abegg, Inc) are powered through the electrical step-down transformer which converts 480VAC 3-phase power to 240VAC 3-phase power.

To supply power to the fans, ensure the 40 amp breaker in the Distribution Panel is set to the "ON" position. Next, turn on the transformer by throwing the Transformer Disconnect switch to the "ON" position. Turn the two switches in the CT Enclosure box to start the fans. The fans activate at 100% load which corresponds to a flow rate through the heat exchangers of 24.4 m^3/s. For different flow rates, adjust the percentage level while monitoring the velocity readings shown in the LabVIEW VI for instruments I98 and I99.

Step 4: Turn on component "005-Power Cycle Pump"

The power cycle pump is a gear pump model H7F, manufactured by Liquiflo with a 1.5 hp magnetically driven motor. The motor is powered by an "Altivar 312" VFD manufactured by Schneider Electric.

Before starting the pump, ensure there is liquid between the pump and the boiler so there is enough charge to begin operation (see step 1). If there is not enough liquid the pump will run dry and will not be able to circulate fluid through the loop.

Wait for the air temperature at the entrance of the boiler to be approximately 106°C and the pressure in the power cycle loop to be higher than ambient. The fluid temperature at the outlet of the boiler should be above 50°C.

Switch the 15 amp breaker powering the pump VFD to the "ON" position. The switch for the pump is located in the CT Enclosure: turn the switch to the "ON" configuration. Now, within the Power Pump electrical box, the VFD will have power. Ensure the VFD is in local operation mode: the three red LED lights on the left side of the display will cycle if this is correct. If the VFD is not in local operation mode, hold the "MODE" button for three seconds. The dial can now be spun to any given frequency (Up to 60Hz) for pump operation. Press the "RUN" button to start the pump at the desired frequency. A typical frequency during startup operations is 20 Hz and corresponds to an unobstructed 0.25 kg/s mass flow rate.

As the pump operates there will be a spike in mass flow followed by a gradual decrease to a fairly low flow. The mass flow and the pump outlet pressure will gradually increase while the pump inlet pressure will gradually decrease.

NOTICE! If the mass flow rate drops very low or the pump begins to vibrate excessively, the pump is running dry. Shut the pump off and diagnose the problem. One possible solution is to add more fluid to the system during startup.

Step 5: Adjust Valve 27 (turbine bypass) to achieve state conditions for turbine inlet flow

Check the pressure and temperature of the power cycle fluid at the inlet of the bypass expansion valve to ensure superheat. Set the desired state conditions of the power cycle by adjusting the pump speed and turbine bypass valve. If the bypass valve is closed too much, the mass flow rate will decrease and could cause pump backpressure problems.

Step 6: Start hot water flow from basement glycol loop

The basement glycol loop valves are located in the Interdisciplinary Thermal Science basement lab. Open those two valves to start the flow of hot glycol to the

mezzanine. Adjust Valves 30 and 31 at the TCCS mezzanine level to control the glycol flow rate.

Step 7: Turn on component "010-Water-Glycol Pump"

The water-glycol pump simulates the cooling load and needs to be operating. The water-glycol pump is a suction pump manufactured by Goulds with a 15 hp motor. The motor is connected directly to 480VAC 3-Phase power and is started through a motor starter.

The power is routed through a 60 amp breaker in the distribution panel. Switch that breaker to the "ON" configuration. Next, turn on the motor using the motor starter located in the "CT Enclosure" electrical box. Once the switch is activated, the pump will turn on and ramp-up to the fixed revolution rate based on the power level. To control the flow rate of fluid entering the evaporators, adjust the position of Valve 26 while monitoring the flow rate measured from I115 on the LabVIEW VI. Adjust the valve until the desired flow rate is achieved.

Step 8: Turn on six of six components "015-CC Condenser Fan"

The cooling cycle fans (model ZN0910ZIQ.GG/L.V5P1, manufactured by Ziehl-Abegg, Inc.) are powered through the electrical step-down transformer which converts 480VAC 3-phase power to 240VAC 3-phase power.

Since the power cycle fans are already operating, the 40 amp breaker in the Distribution Panel and the transformer are already "ON". Open the CT Enclosure box and switch the fans to the "ON" configuration to activate the fans. The fans are set to activate at 100% load which corresponds to the flow rate through the heat exchangers of 49.4 m^3/s.

For any different flow rates, adjust the percentage level while monitoring the velocity readings shown in the LabVIEW VI for instruments I100 through I106.

Step 9: Turn on component "016-CC Bearing Pump"

The cooling cycle bearing pump is a magnetically driven gear pump (model GB-P35.JVS.A-B1) manufactured by Micropump. Power on the electric console drive and adjust the flow rate of the pump by turning the frequency knob on the drive. Monitor the pressure at I27 and the flow rates at I113 and I112 to meet the desired flow conditions. Do not increase the flow rate too high or the bearing line pressure could increase beyond the 150 psi pressure rating.

Step 10: Start Turbine Flow

Before opening the turbine valves, check if both the outlet of the cooling cycle chiller and the inlet of the power cycle bypass valve are completely superheated. If either is not superheated, do not open the turbine valves.

NOTICE! Do not begin Step 12 without confirming the fluid exiting the boiler is completely vapor. Allowing liquid slugs to enter the turbine will cause damage to the blades.

To start turbine operation, open Valve 4 (turbine inlet) slowly to allow the turbine to fill with vapor from the boiler. It is not necessary to open the valve fully, a slight opening will allow enough flow to enter the turbine. Wait for 10-20 seconds to confirm the temperature and pressure is increasing in the turbine. Now open Valve 5 (turbine outlet) slowly to allow the turbine to begin spinning.

NOTICE! As the turbine spins, carefully monitor the speed to ensure no over-speed scenarios occur. Failure to monitor the turbine speed could result in damage to the turbo-compressor.

Note, the compressor will also begin spinning, thus starting the cooling cycle. The turbine will now be operating in parallel flow with the turbine bypass line. Slowly close Valve 27 (turbine bypass), sending all of the flow to the turbine. Again, be careful to monitor the rotational speed of the shaft as the turbine spins. Valve 27 (turbine bypass) does not close all the way, however, so some flow will always bypass the turbine.

Step 11: Adjust conditions on cooling cycle

The cooling cycle will be in full operation, but the saturation conditions on the evaporator may not be correct. Adjust Valves 28 and 29 to achieve proper flow conditions by monitoring temperature and pressure instruments I24, I25, I81, and I82 at the inlet of the evaporator, as well as outlet temperatures I85 and I86. The mass flow rates and flow conditions through both lines should be similar.

The temperature at the chiller outlet is controlled by adjusting globe Valves 30 and 31 to increase or decrease the flow of the hot glycol entering the glycol loop. The flow rate of the glycol loop is adjusted by the position of glycol bypass (Valve 26). Check the pressure and temperature at the chiller outlet to ensure superheat at the chiller exit.

Step 12: Close power cycle filter flow

The power cycle is now in full operation, but to decrease the pressure drop through the system, the filter lines should be closed. Open Valve 7 to start power cycle parallel filter flow and then close Valves 8 and 9 to stop filter bypass flow.

Step 13: Close cooling cycle filter flow

The cooling cycle is now in full operation, but to decrease the pressure drop through the system, the filter lines should be closed. Open Valve 20 to start cooling cycle parallel filter flow and then close Valves 19 and 21 to stop filter bypass.

Step 14: Stop component "016-CC Bearing Pump"

The compressor will have enough energy to provide the flow into its own bearing lines, allowing the bearing pump to be shut-off. Open Valve S11 to start bearing parallel flow. Turn off the pump and then close Valve S10 and S12 to stop bearing bypass.

Step 15: Stop liquid-vapor separator bypass

Check the pressure and temperature at cooling cycle evaporator to determine if completely vapor. Slowly open Valve 22 to start liquid-vapor separator parallel flow. Monitor the conditions entering the compressor to ensure superheat. Close Valves 23 and 24 to stop liquid-vapor separator bypass.

The TCCS is now in full operation

Steady state data can be recorded and the conditions of both cycles should be adjusted to achieve the data conditions required. The new valve configuration for Swagelok and pipe valves is shown in Table F-8 and Table F-9, respectively.

F.4.3 Standard Shutdown Procedure

The shutdown procedure detailed below should be used during any scenario where standard shutdown is possible. If an emergency shutdown is required, follow the procedures listed in Section F.4.4. The shutdown procedure is listed in order of starting from a system at full scale operation. To shut down the system before full scale operation, simply skip the steps that do not apply to the current state of operation.

Step 1: Start liquid-vapor separator bypass

Open Valves 23 and 24 to start liquid vapor separator bypass. Slowly close Valve 22 to direct all flow into the liquid vapor separator.

Table F-8. Swagelok valve configuration at steady state operation.

VALVE NUMBER	VALVE POSITION	VALVE SIZE	VALVE TYPE	APPLICATION	CYCLE
S1	CLOSED	1/4 INCH	METERING	MAG COUPLING INLET	POWER
S2	OPEN	1/4 INCH	METERING	BEARING INLET	POWER
S3	OPEN	1/4 INCH	METERING	BEARING INLET	POWER
S4	OPEN	1/4 INCH	BALL	COOLING INLET LINE	POWER
S5	CLOSED	1/4 INCH	BALL	MAG COUPLING COOLING LINE	POWER
S6	CLOSED	1/2 INCH	BALL	FILL LEVEL SIGHT TUBE	POWER
S7	CLOSED	1/2 INCH	BALL	FILL LEVEL SIGHT TUBE	POWER
S8	CLOSED	1 INCH	BALL	VAPOR OUTLET BEARING ACCUM	POWER
S9	OPEN	1 INCH	BALL	LIQUID OUTLET BEARING ACCUM	POWER
S10	CLOSED	1/4 INCH	BALL	BEARING PUMP INLET	COOLING
S11	OPEN	1/4 INCH	BALL	BEARING PUMP BYPASS	COOLING
S12	CLOSED	1/4 INCH	BALL	BEARING PUMP OUTLET	COOLING
S13	OPEN	1/4 INCH	METERING	BEARING INLET	COOLING
S14	OPEN	1/4 INCH	METERING	BEARING INLET	COOLING
S15	CLOSED	1/4 INCH	METERING	COMPRESSOR RECIRC	COOLING
S16	OPEN	1 INCH	BALL	VAPOR OUTLET BEARING ACCUM	COOLING
S17	OPEN	1 INCH	BALL	LIQUID OUTLET BEARING ACCUM	COOLING
S18	OPEN	1 INCH	BALL	LIQUID OUTLET BEARING ACCUM	COOLING
S19	CLOSED	1/2 INCH	BALL	FILL LEVEL SIGHT TUBE	COOLING
S20	CLOSED	1/2 INCH	BALL	FILL LEVEL SIGHT TUBE	COOLING
S21	CLOSED	1/4 INCH	BALL	COMPRESSOR RECIRC	COOLING
S22	CLOSED	3/4 INCH	BALL	TURBINE FILL LINE	POWER
S23	CLOSED	3/4 INCH	BALL	COMPRESSOR FILL LINE	COOLING
S24	CLOSED	3/4 INCH	BALL	VACUUM PUMP	POWER
S25	CLOSED	3/4 INCH	BALL	HFE7000 FUEL PUMP	POWER
S26	CLOSED	3/4 INCH	BALL	VACUUM PUMP	COOLING
S27	CLOSED	3/4 INCH	BALL	REFRIGERANT GEAR PUMP	COOLING
S28	OPEN	1/4 INCH	BALL	TURBINE VENT LINE	POWER
S29	OPEN	1/4 INCH	BALL	COMPRESSOR VENT LINE	COOLING
S30	CLOSED	1/4 INCH	BALL	REFRIGERANT TANK	COOLING
S31	CLOSED	1/2 INCH	BALL	DRAIN REFRIGERANT TANK	COOLING

Table F-9. Pipe valve configuration at steady state operation.

VALVE NUMBER	VALVE POSITION	VALVE SIZE	VALVE TYPE	APPLICATION	CYCLE
1	CLOSED	2 INCH	BALL	FILL PORT	POWER
2	OPEN	2 INCH	BALL	VENT LINE	POWER
3	CLOSED	2 INCH	EBV	EMERGENCY BLOWDOWN	POWER
4	OPEN	4 INCH	BALL	TURBINE ISOLATION	POWER
5	OPEN	4 INCH	BALL	TURBINE ISOLATION	POWER
6	CLOSED	1/2 INCH	BALL	DRAIN PORT	POWER
7	OPEN	2 INCH	BALL	FILTER ISOLATION	POWER
8	CLOSED	2 INCH	BALL	FILTER ISOLATION	POWER
9	CLOSED	2 INCH	BALL	FILTER ISOLATION	POWER
10	CLOSED	2 INCH	BALL	FILL PORT	POWER
11	CLOSED	1/2 INCH	BALL	DRAIN PORT	POWER
12	OPEN	2 INCH	BALL	VENT LINE	COOLING
13	OPEN	2 INCH	BALL	BURST DISK 1	COOLING
14	CLOSED	2 INCH	EBV	EMERGENCY BLOWDOWN	COOLING
15	CLOSED	2 INCH	BALL	BURST DISK 2	COOLING
17	CLOSED	2 INCH	BALL	FILL PORT	COOLING
18	CLOSED	1/2 INCH	BALL	DRAIN PORT	COOLING
19	CLOSED	2 INCH	BALL	FILTER ISOLATION	COOLING
20	OPEN	2 INCH	BALL	FILTER ISOLATION	COOLING
21	CLOSED	2 INCH	BALL	FILTER ISOLATION	COOLING
22	OPEN	4 INCH	BALL	LIQ-VAP ISOLATION	COOLING
23	CLOSED	2 INCH	BALL	LIQ-VAP ISOLATION	COOLING
24	CLOSED	2 INCH	BALL	LIQ-VAP ISOLATION	COOLING
25	OPEN	4 INCH	BALL	COMPRESSOR ISOLATION	COOLING
26	OPEN	2 INCH	BALL	GLYCOL BYPASS	GLYCOL
27	CLOSED	1.5 INCH	GLOBE	TURBINE THROTTLE VALVE	POWER
28	OPEN	1/2 INCH	GLOBE	THROTTLE VALVE	COOLING
29	OPEN	1/2 INCH	GLOBE	THROTTLE VALVE	COOLING
30	OPEN	2 INCH	BALL	BOILER WATER INLET	GLYCOL
31	OPEN	2 INCH	BALL	BOILER WATER RETURN	GLYCOL
32	CLOSED	2 INCH	BALL	BASEMENT WATER FILL	GLYCOL
33	CLOSED	1/2 INCH	BALL	DRAIN VALVE FOR VAC	COOLING
34	CLOSED	3/4 INCH	BALL	FILL PORT	GLYCOL
35	CLOSED	3/4 INCH	HOSE	FILL PORT	GLYCOL
36	CLOSED	3/4 INCH	BALL	FILL PORT	GLYCOL
37	CLOSED	3/4 INCH	HOSE	FILL PORT	GLYCOL
38	CLOSED	3/4 INCH	BALL	DRAIN PORT	GLYCOL
39	CLOSED	3/4 INCH	HOSE	DRAIN PORT	GLYCOL
40	CLOSED	1-1/2 INCH	BALL	DRAIN PORT	GLYCOL
41	CLOSED	3/4 INCH	HOSE	DRAIN PORT	GLYCOL
42	CLOSED	2 INCH	BALL	DRAIN PORT	GLYCOL
43	CLOSED	3/4 INCH	HOSE	DRAIN PORT	GLYCOL

Step 2: (Optional in shutdown) Open cooling cycle filter flow

Opening the filter lines is not critical for shutdown of the system, but is recommended.

Open Valves 19 and 21 to start filter bypass flow and then close Valve 20 to stop cooling cycle parallel filter flow.

Step 3: (Optional in shutdown) Open power cycle filter flow

Opening the filter lines is not critical for system shutdown, but is recommended. Open Valves 8 and 9 to start filter bypass flow and then close Valve 7 to stop parallel filter flow.

Step 4: Stop turbine flow

Ensure the turbine bypass line (Valve 27) is open by checking the flow rate through the I106. If there is low or minimal flow, open Valve 27 further.

Slowly close Valve 4 to stop the flow through the turbine, directing it into the turbine bypass line.

Close Valve 5 to prevent back flow of fluid. By closing Valve 4, the cooling cycle will also stop operation due to the coupling of the cycles.

Step 5: Stop power cycle pump

Press the red "Stop" button on the pump VFD located in the "Power Pump" electrical box.

Step 6: Shut-off the flue gas loop air heater

Power off the heater by adjusting the slider bar in the LabVIEW program to 0% and then throwing the electrical disconnect switch to the "OFF" position. If the air heater

was in automatic operation mode, press the “Heater Automation” button prior to shutting off the heater.

Step 7: Shut-off the water-glycol pump

Power off the water-glycol pump by switching the power switch located in the “CT enclosure” electrical box to the “OFF” position. The flow of water-glycol will stop.

Step 8: Shut-off the basement boiler hot glycol loop

Shut-off the hot glycol loop from the basement by turning the two valves in the ITS basement lab to the “OFF” position.

Step 9: Turn off component “011-PC Evaporator Fan”

It is recommended for the fan to circulate the hot air to help with cooling of the loop, but it is not necessary for shutdown. Press the “STOP” button on the PC Evaporator VFD located in the “Flue Loop Fan” electrical box to ramp down the power cycle fan.

Step 10: Turn off condenser cooling fans

It is recommended to allow the condenser fan to continue operation after shutdown to provide cooling for the cycles. Monitor the temperatures and pressures of the cycles on the LabVIEW program, and, when the temperatures have dropped significantly, power off the condensers. Open the “CT Enclosure” electrical box and power off each fan by turning the individual switches to the “OFF” position. Throw the electrical disconnect switch for the 240 VAC transformer to the “OFF” position.

The TCCS is now shutdown

F.4.4 Emergency Shutdown

This section list the procedures for emergency scenarios such as those listed in Section F.1. The following procedure is the fastest way to shut down the TCCS without venting the cycle,

but is not the most optimal because it skips several standard shutdown steps. In very extreme scenarios, the emergency shut-down procedure may not be fast enough to shut down the system – in those situations, press the emergency blow-down buttons to evacuate the cycles quickly.

CAUTION! If an over-pressurization situation develops rapidly in the either cycle, do not follow the emergency shutdown procedure, but instead press the emergency blow-down buttons to vent the fluid from the loop to avoid an explosion.

Step 1: Stop power cycle pump

The three options below present the three possibilities to shut off the pump. Execute the option which can be performed quickest to rapidly stop the power cycle pump.

Option 1: Press the red "Stop" button on the power cycle VFD located in the "Power Pump" electrical box.

Option 2: Switch the power switch associated with the power cycle pump located in the "CT Enclosure" to the "OFF" configuration.

Option 3: Switch the 15 amp breaker associated with the power cycle pump in the Main Breaker Panel to the "OFF" configuration.

Step 2: Close turbine inlet valve

Close Valve 4 to immediately stop the flow entering the turbine. This will cause the turbo-compressor to stop spinning and thus transferring power.

Step 3: Shut-off the flue gas loop air heater

Power off the heater by adjusting the slider bar in the LabVIEW program to 0% and then throwing the electrical disconnect switch to the "OFF" position. If the air heater

was in automatic operation mode, press the “Heater Automation” button prior to shutting off the heater.

The facility will be powered off after three steps. To complete TCCS shutdown, follow the steps shown in Section F.4.3.

F.5. System Drain Procedures

The following instructions list the procedure for draining the power, cooling, and glycol loops.

F.5.1 Power Cycle Drain Procedure

Use the following steps to drain the power cycle. There are two draining methods: one passive and one active. The passive method is outlined in steps 1 - 4 and the active method in steps 5 - 8. The best strategy might be to use the active method to drain as much fluid as possible, allow the cycle to cool and settle, then use the passive method to remove any residual fluid. Both methods require an empty HFE-7000 drum and a mass scale (Part # GFK 330aH). Record the total mass removal for each tank to calculate the amount of liquid remaining in the loop.

Passive Method: Gravity Drain

The passive method is slow and does not work well when the ambient temperature is high. When the ambient temperature is higher than 30°C the HFE-7000 will vaporize as it travels down the tubing, causing a large loss of fluid in the vapor form. When attempting the passive method it is prudent to place the entire drum in a bucket of ice to condense the vapor.

Step 1: Connect tank to drain port

Place an empty HFE-7000 drum and scale on the first floor. Route tubing from the drain port (Valve 6), protruding through the mezzanine, to the HFE-7000 drum.

Step 2: Drain HFE-7000

Open the vent on the HFE-7000 drum by unscrewing the vent cap. Also open the power cycle vent by opening Valves 2 and 3. Open Valve 6 to start the flow of liquid into the drum. Fill the tank until the total weight of the drum is approximately 150 kg (or until flow stops), then close Valve 6, and replace the vent cap.

Step 3: Switch tanks as necessary

As the HFE-7000 drums fill, it will be required to switch drums. Close Valve 6 when 150 kg of liquid is in the drum. Wait for the liquid to drain out of the fill line before removing the tubing from the top of the filled drum. After removing the tubing, switch the filled and empty drums, and then repeat steps 1 and 2 to fill the new drum.

Step 4: Attach drain lines to second port

Place a HFE-7000 drum and scale on the mezzanine level. Route tubing from the outlet of the secondary drain port (Valve 11) to the HFE-7000 drum. With Valves 2 and 3 still open, open Valve 11 to start draining from the second port. Fill the tank until the total weight of the drum is approximately 150 kg (or until flow stops), then close Valve 11, and replace the vent cap. Follow step 3 if the mass limit of the tank is reached.

Active Method: Power Cycle Operation

The active method is fast but will not drain all of the fluid and has the potential for fluid loss in the form of escaping vapor.

Step 5: Operate power cycle

Follow the first 5 steps of the start-up procedure (Section F.4.1) to get the power cycle into steady state operation mode.

Step 6: Drain the excess power cycle fluid

Make sure the mass flow rate and high side system pressure are stabilized and that the cycle is performing normally. If neither the mass flow nor pressure increase sufficiently or stabilize well, adjust the turbine bypass valve accordingly (Valve 27).

One operator should stand at the power cycle fill port (Valve 1), another monitoring the LabVIEW program, and a third on the third floor balcony above the TCCS. The operator on the third floor should place the HFE7000 drum on the scale and record the weight. With the fill lines attached to the top of the HFE7000 pump, open the vent by unscrewing the cap on the drum. Be careful of any pressure that may have built up.

WARNING! Breathing excess amounts of HFE7000 could have adverse health effects. During draining some vapor will escape from the drum. Wear a respirator with a proper filter to prevent inhaling HFE7000 vapor.

Ensure Valve S24 is closed. Next, open Valve S25 fully. Crack open Valve 1 to allow the power cycle pump to push liquid HFE-7000 into the drum. Continue draining until either the mass off the drum increases to 150 kg or the pump fails to deliver liquid. If the mass of the drum reaches the 150 kg limit, proceed to step 7. If the pump fails to deliver liquid, proceed to Step 8.

Step 7: Switch HFE-7000 drums as necessary

Close Valves 1 and S25 to stop the liquid flow. Keep the power cycle operating and make adjustments to the turbine bypass valve (Valve 27) as necessary. Re-screw the vent cap onto the HFE-7000 drum. Detach the Fill-Rite pump from the HFE-7000 drum, record the mass, and remove the drum from the scale. Place the empty drum on the scale and

record the initial mass. Attach the Fill-Rite pump to the inlet port of the drum and open the vent cap. Follow step 6 to drain fluid into the new drum.

Step 8: Shut down power cycle

Close Valve S25 and move the power cycle into shut-down mode by following steps 5 – 10 in the standard shut-down procedure listed in Section F.4.3. Re-screw the vent cap onto the HFE-7000 drum. Wait for the loop to return to normal ambient temperatures and then begin the passive method to remove any residual fluid.

F.5.2 Cooling Cycle Drain Procedure

Use the following steps to drain the cooling cycle of fluid. Place an empty refrigerant tank in a bucket on the mass scale (Part # GFK 330aH). Record the total mass removed for each tank to calculate the amount of refrigerant remaining in the loop. Fill the bucket with ice to keep the refrigerant tank from overheating during the drain process.

Step 1: Vacuum the drain lines

Place the empty refrigerant tank, recovery device, and vacuum pump on the third floor. Attach tubing from the refrigerant fill port (Valve 17), to the tee connecting a ball valve, and the inlet of the refrigerant recovery device (CMEP-OL). The outlet of the refrigerant recovery device should be attached to the empty refrigerant tank. With Valve S30 closed, operate the vacuum pump (Part # VN-85N) to remove the air from the drain lines. When the tube is vacuumed, close the ball valve and shut off the vacuum pump.

Step 2: Drain refrigerant

Make sure there is an adequate ice level around the refrigerant tank around the tank. Add more ice if necessary.

CAUTION! The refrigerant recovery device compresses the fluid into the empty cylinder thus increasing the temperature and pressure. If the refrigerant tank is not surrounded by ice the tank could become dangerously over pressurized. Failure to keep the tank cool could result in violent explosion.

Open Valve 17 and allow the pressure to equalize in the tubing. Open the valves on the refrigerant recovery device. Turn on the recovery pump to compress vapor out of the system and into the empty refrigerant tank. Open Valve S30, S31 and the refrigerant tank valve. Continue operating the recovery device until the mass increases by 50 kg.

When the refrigerant tank increases by 50 kg, close Valve 17 and wait briefly as the pump starts to starve. When the recovery pump is pulling vacuum, turn off the refrigerant recovery pump, close Valves S30 and S31, and close the refrigerant tank valve. If there is more refrigerant in the loop proceed to Step 3, if the loop is empty, proceed to Step 4.

Step 3: Switch tanks as necessary

Unthread Valve S31 from the refrigerant tank and move the filled tank off the scale. Place an empty cylinder on the scale and tare the scale to zero. Attach Valve S31 to the refrigerant tank. Simply turn on the refrigerant recovery pump and open Valve S31 to continue the drain with the new tank.

WARNING! If R152a is being drained from the system, extreme caution should be used when switching tanks due to the high flammability of the fluid. Some gas will escape as valve S31 is unthreaded which has the potential to spark or explode.

Step 4: Evacuate the cooling cycle

Open the valves on the refrigerant recovery pump, Valve S31, and Valve 18. Allow the remaining refrigerant in the drain line to equilibrate with the loop by waiting for 5 – 10 minutes. Next, open the cooling cycle vent line by pressing the emergency blow-down button. Since the loop will be vacuumed, air from the outside will be pulled into the cycle, diluting the refrigerant remaining in the loop. Finally, attach a compressed air line to the loop and blow out the air refrigerant mix to finish the drain.

F.5.3 Glycol loop drain procedure

The following procedure should be used to drain glycol from the loop. Move an empty 55 gallon glycol tank to the first floor.

Step 1: Attach drain lines

Attach a short garden hose to Valve 39. Stretch that hose to the first floor and insert into the empty 55 gallon glycol drum.

Step 2: Drain glycol

Open Valves 38 and 39 to drain the glycol from the loop and into the 55 gallon drum. Open Valves 34 – 37 to allow air to escape out of the top of the loop. Continue draining until either the 55 gallon drum is full (go to step 3) or the glycol stops flowing (go to step 4).

Step 3: Switch tanks is necessary

Remove the hose from the filled drum and insert into an empty drum. Continue the draining process.

Step 4: Attach drain lines to second port

Attach the garden hose to Valve 41. Stretch the hose to the first floor and inset into a 55 gallon glycol drum. Open Valves 40 and 41 to drain the glycol. Continue draining until either the 55 gallon drum is full (go to step 3) or the glycol stops flowing. When the glycol stops flowing, the loop drain is complete.

Table F-10. Troubleshooting symptoms, problem, and actions for various problems encountered while operating the TCCS.

Symptom	Possible Problems	Recommended Action
Air heater stuck on – power reading does not change as percentage adjusted	Relay switch overheat	Press and hold far right relay switch button in air heater input box.
Load cells read much greater than 500 lbf	LabVIEW setting adjustment Load cell broken	From the "TurboCoolRT.vi" change the 9205 parameters on channel 0 and 1 to differential mode by clicking the "Change 9205 Settings" button. If changing the settings has no effect, the sensor is likely broken.
Temperature measurements read -267°C	NI-9149 disconnect	Press reset button on NI-9149 module. Restart LabVIEW program.
Accelerometers read 0 g's	LabVIEW error	Restart LabVIEW program.
Instruments read negative values or don't change	Blown fuse Power failure	Check fuses from 24 V power source to terminal blocks Check power at data acquisition system
Rapid fluid pressure drop	Burst disk failure	Move to system shutdown.
LabVIEW logger is unresponsive	LabVIEW error	Stop all VIs and restart LabVIEW program. Do not recover file.
Power cycle mass flow rate is lower than expected at pump frequency level	Bypass valve is too restrictive	Open the bypass valve to encourage flow
Excessive pump vibration	Pump is out of liquid Pressure head is too high	Shut off pump Shut off pump

Symptom	Possible Problems	Recommended Action
Turbine inlet superheat loss	Heater power too low	Increase heater power level
Compressor inlet superheat loss	Glycol loop heat too low CC expansion valves too open	Increase basement boiler heat exchanger heat duty by opening Valves 30 and 31 more Close CC expansion valves (Valves 28 and 29)
Power cycle pump cavitation	Power cycle pump saturation pressure too low	Turn down power cycle fans to increase power cycle saturation pressure
Fluid pressure spike	System over-pressurization	Hit associated E-stop button
Condenser fan controllers unresponsive	Modbus fan controller error	Restart fan controllers by flipping breaker 14 in South 120V distribution panel.

ABBREVIATIONS

Symbol	Description	Units
ACCUM	Accumulator	
BNI	Barber-Nichols, Inc.	
BTU	British Thermal Unit	
CC	Cooling cycle	
CFC	Chlorofluorocarbons	
COP	Coefficient of Performance	
DOE	Department of Energy	
EES	Engineering Equation Solver	
FS	Full scale	
HC	Hydrocarbon	
HFC	Hydrofluorocarbon	
HFE	Hydrofluoroether	
MAWP	Maximum allowable working pressure	
MV	Mean value	
NETL	National Energy Technology Laboratory	
NGCC	Natural Gas Combined Cycle	
NIST	National Institute of Standards and Technology	
ORC	Organic Rankine Cycle	
PC	Power cycle	
PFD	Process flow diagram	
P&ID	Piping and instrumentation diagram	

RECUP	Recuperator	
TCCS	Turbo-compression cooling system	
TMC	Transport Membrane Condenser	
VC	Vapor-Compression	
VFD	Variable Frequency Drive	
WHR	Waste heat recovery	